

HEAT TRANSFER STUDIES ON GAS TURBINE COMBUSTOR LINER COOLING

THESIS

Submitted in partial fulfillment of the requirement for the degree of

DOCTOR OF PHILOSOPHY

by

FELIX J

Reg.No. 135039ME13P02



DEPARTMENT OF MECHANICAL ENGINEERING
NATIONAL INSTITUTE OF TECHNOLOGY KARNATAKA
SURATHKAL, MANGALORE – 575025

JULY, 2019

*Reserved copyrights with supervisor of this thesis, “**Heat Transfer Studies on Gas Turbine Combustor Liner Cooling**” N.I.T.K, Surathkal. No part of this thesis can be reproduced in any form or by any means without prior written permission of the Supervisor and N.I.T.K. authorities.*

DECLARATION

by the Ph.D. Research Scholar

I hereby *declare* that the Research Thesis entitled “**Heat Transfer Studies on Gas Turbine Combustor Liner Cooling**” which is being submitted to the **National Institute of Technology Karnataka, Surathkal** in partial fulfillment of the requirements for the award of the Degree of **Doctor of Philosophy** in Mechanical Engineering is a *bonafide report of the research work carried out by me*. The material contained in this Research Thesis has not been submitted to any University or Institution for the award of any degree.

Place : NITK, Surathkal

Felix J

Date :

Reg. No.: 135039ME13P02
Department of Mechanical Engineering
NITK, Surathkal, Mangalore - 575025

CERTIFICATE

This is to *certify* that the Research Thesis entitled “**Heat Transfer Studies on Gas Turbine Combustor Liner Cooling**” submitted by **Felix J** (Register Number: 135039ME13P02) as the record of the research work carried out by him, is *accepted as the Research Thesis submission* in partial fulfillment of the requirements for the award of degree of Doctor of Philosophy.

Place : NITK, Surathkal

Date :

Research Guide

Dr. Kumar G.N

Associate Professor
Department of Mechanical Engineering
NITK, Surathkal, Mangalore – 575025.

Place : NAL, Bangalore

Date :

External Guide

Dr. R.Rajendran

Advisor (Technical)
CSIR-National Aerospace Laboratories &
Professor, Aeronautical Engineering Dept.
Dayananda Sagar College of Engineering,
Bangalore-560078.

Place : NITK, Surathkal

Date :

Chairman - DRPC

Department of Mechanical Engineering
NITK, Surathkal, Mangalore - 575025

ACKNOWLEDGEMENTS

First and foremost, I express my sincere, heartfelt thanks and deepest gratitude to my research guide Dr. Kumar G N, Associate Professor, Mechanical Engineering Department, National Institute of Technology Karnataka, Surathkal for his valuable guidance, constant inspiration and support throughout the course of my research work. I am expressing thanks to my external research guide Dr. R. Rajendran, Scientist (Retd) and former Joint Head of Propulsion Division, National Aerospace Laboratories, Bangalore for his painstaking efforts in guidance thoroughly throughout my research activities and improving the manuscript.

I am thankful to the RPAC members Dr. Arun M Isloor, Professor and HOD, Department of Chemistry and Dr. Gnanasekaran, Assistant Professor, Department of Mechanical Engineering, NITK for their valuable comments and critical suggestions to complete my research activities successfully.

It is my great pleasure in undertaking this research work at NITK, Surathkal, Mangalore and I sincerely express my gratitude to Director, NITK for providing this opportunity. I am also thankful to Dean (Academic) and Head, Department of Mechanical Engineering, NITK for providing the facilities, support and an opportunity to carry out my research work.

I extend special gratitude to Director, CSIR-National Aerospace Laboratories (NAL), Bangalore for granting the permission to carry out the experimental activities of my Ph.D. work at NAL. I also wish to thank my heat transfer group colleagues at NAL (Dr. Giridhara Babu Y, Mrs. Poornima, Mr. Maria Arockiam S., Mr. Sanmugantham M., and Mr. Pradeep K. A.) for their constant support during the experimental activities of my Ph.D. work at NAL.

Finally, I am very grateful to my wife Mrs. Darthik Sharmila for her constant support and continuous encouragement towards the completion of my research work effectively.

Felix J

ABSTRACT

This study deals with the combination of film cooling techniques in an effusion cooled test plate. Geometrical parameters of the effusion cooling test plate have holes of diameter 1 mm, hole angle of 27° and 7.2 mm pitch in both streamwise and spanwise directions. Effusion holes are placed in a staggered manner with 9 holes per row, and there are 13 rows in total. Experimental and numerical investigation of adiabatic cooling effectiveness and convective heat transfer coefficient on an effusion cooled test plate is carried out with and without machined ring geometries upstream. For these tests, the effusion cooling geometrical parameters are scaled up by 3 times. Tests are carried out at blowing ratio ranging from 0.5 to 2.5, coolant to mainstream density ratio of 1.3 and at a mainstream velocity of 20 m/s. The convective heat transfer coefficient investigations are carried out using a constant heat flux surface with coolant and mainstream at the same temperature. Test plate surface temperature measurements are recorded by an infrared camera. Effusion cooling along with machined ring geometries upstream shows higher adiabatic film cooling effectiveness and higher film heat transfer coefficients than effusion cooling alone at all the blowing ratios. Measurements of overall film cooling effectiveness are also carried out in stainless steel effusion cooling test plate of 2 mm thickness with and without machined ring geometries. This comparison result also shows that the overall cooling effectiveness increases significantly before the effusion cooling holes with the presence of machined ring geometries. Another combination of impingement with effusion cooling is studied for an effusion test plate having a 5.4 mm pitch in both the spanwise and streamwise directions. An impingement plate is kept backside of the effusion plate at a distance of 6 mm. The holes in the impingement plate are arranged in a staggered manner such that each effusion hole is surrounded by four impingement holes. The result shows that the effusion cooling with impingement gives higher overall cooling effectiveness than effusion cooling alone. The comparison is made between effusion cooling with impingement and effusion with machined ring geometries. The result shows that the effusion with machined ring geometries has higher overall cooling effectiveness than effusion cooling with impingement. Numerical analysis is performed using ANSYS workbench, and the methodology is validated against the experimental results. The numerical results are matching with the experimental results and the temperature contours obtained are compared with infrared camera images. A MATLAB program is

used to obtain the effectiveness contours for both the experimental and numerical results.

Key Words: Combustor liner cooling, Adiabatic film cooling effectiveness, Heat transfer coefficient, Overall cooling effectiveness, Combined film cooling techniques.

CONTENTS

	Page No.
ACKNOWLEDGEMENTS.....	i
ABSTRACT.....	ii
LIST OF FIGURES	viii
LIST OF TABLES.....	xvi
NOMENCLATURE	xvi
1 INTRODUCTION.....	1
1.1 Gas Turbine Engine	1
1.2 Gas Turbine Combustor.....	2
1.2.1 Primary Zone.....	2
1.2.2 Intermediate Zone	3
1.2.3 Dilution Zone	3
1.3 Combustor Liner and Need for Cooling	4
1.4 Heat Transfer through Uncooled Liner.....	6
1.5 Heat Transfer through Film Cooled Liner	7
1.6 Introduction to Computational Fluid Dynamics	9
1.6.1 Pre Processor	10
1.6.2 Solver	11
1.6.3 Post Processor	12
1.6.4 Equations Governing Fluid Flow and Heat Transfer	13
1.6.4.1 Three Dimensional Mass Conservation Equation	13
1.6.4.2 Momentum Equation in Three Dimensions.....	14
1.6.4.3 Three Dimensional Energy Equation	15
1.6.4.4 Navier- Stokes Equations for a Newtonian Fluid.....	15
1.6.5 Turbulence Models.....	16

1.6.5.1	Selecting a Suitable Turbulence Model.....	16
1.6.5.2	Realizable k- ϵ Model.....	16
1.6.5.3	Transport Equations for the Realizable k- ϵ Model.....	17
1.7	Organization of the Thesis	18
2	LITERATURE REVIEW.....	19
2.1	Slot Cooling	19
2.2	Effusion Cooling.....	20
2.3	Surface Temperature Measurements Techniques	21
2.4	Numerical Models.....	23
2.5	Slot/Effusion Combined Cooling.....	24
2.6	Impingement/Effusion Combined Cooling.....	24
2.7	Summary of the Literature Survey.....	25
2.8	Research Gap and Need for the Study	25
2.9	Scope of the Present Study	26
2.10	Objectives of the Work	28
3	EXPERIMENTAL SETUP AND METHODOLOGY	29
3.1	Experimental Setup.....	29
3.2	Test Plate Details	31
3.2.1	Geometric Details of Machined Ring.....	31
3.2.2	Geometric Details of Effusion Test Plate.....	34
3.3	Instrumentation Systems.....	40
3.3.1	Thermocouples	40
3.3.1.1	Thermocouple Calibration.....	40
3.3.2	Infrared Camera.....	41
3.3.2.1	Infrared Camera Calibration.....	41
3.3.3	Pressure Net Scanner.....	44

3.3.4	Orifice Plate.....	44
3.4	Experimental Procedure.....	45
3.4.1	Adiabatic Film Cooling Effectiveness Measurement.....	45
3.4.2	Convective Heat Transfer Coefficient Measurement.....	46
3.5	Error Estimate	50
4	COMPUTATIONAL METHODOLOGY	52
4.1	Modeling.....	52
4.2	Mesh Generation.....	55
4.3	Boundary Conditions	56
4.4	Turbulence Model Selection	57
4.5	Grid Independence Study.....	58
5	RESULTS AND DISCUSSION	60
5.1	Machined Ring 1.....	60
5.1.1	Adiabatic Film Cooling Effectiveness	60
5.1.2	Heat Transfer Coefficients	66
5.1.3	Net Heat Flux Reduction.....	71
5.2	Machined Ring 2.....	72
5.2.1	Adiabatic Film Cooling Effectiveness	72
5.2.2	Heat Transfer Coefficients	77
5.2.3	Net Heat Flux Reduction.....	80
5.3	Comparison Between Two Machined Ring Geometries	81
5.4	Effusion Cooling.....	85
5.4.1	Adiabatic Film Cooling Effectiveness	85
5.4.2	Heat Transfer Coefficients	91
5.4.3	Net Heat Flux Reduction.....	95

5.5	Effusion Cooling with MR1.....	95
5.5.1	Adiabatic Film Cooling Effectiveness	95
5.5.2	Heat Transfer Coefficients	100
5.5.3	Net Heat Flux Reduction.....	104
5.6	Effusion Cooling with MR2.....	105
5.6.1	Adiabatic Film Cooling Effectiveness	105
5.6.2	Heat Transfer Coefficients	109
5.6.3	Net Heat Flux Reduction.....	113
5.7	Comparison Between Effusion Cooling with and Without Machined Ring Geometries	114
5.8	Overall Cooling Effectiveness for Effusion Holes	119
5.8.1	Test plate with 7.2D Pitch.....	120
5.8.2	Test Plate with 5.4D Pitch.....	126
5.8.3	Effect of Pitch for effusion holes	128
5.9	Overall Cooling Effectiveness for Effusion Holes with Machined Ring Geometries	130
5.10	Overall Cooling Effectiveness for Effusion with Impingement Holes	138
5.11	Comparison Between Effusion with Impingement and Effusion with Machined Ring Geometries	144
6	CONCLUSIONS.....	146
6.1	Scope for Future Work.....	150
	REFERENCES	151
	APPENDIX I	157
I	MASS FLOW MEASUREMENTS	157
I.1	Machined Ring Geometries	158

I.2	Effusion Cooling – Adiabatic Test Plate	159
I.3	Effusion Cooling – SS Test Plate.....	159
APPENDIX II	162
II	UNCERTAINTY ANALYSIS.....	162
II.1	Blowing Ratio	163
II.2	Adiabatic Cooling Effectiveness.....	165
II.3	Heat Transfer Coefficient	166
II.4	Coolant Mass Flow Rate	167
List of Publications based on the Ph.D Work	169
BIODATA	171

LIST OF FIGURES

Fig. 1.1	Typical gas turbine engine.....	1
Fig. 1.2	P-V and T-S diagram of the gas turbine	2
Fig. 1.3	Components of a gas turbine combustor and its zones.....	3
Fig. 1.4	Liner cooling hole arrangements/schemes	4
Fig. 1.5	Schematic of film cooling concept	5
Fig. 1.6	Heat transfer through uncooled Liner.....	6
Fig. 1.7	Cooling film formation.....	7
Fig. 3.1	Photograph of the film/effusion cooling test setup.....	29
Fig. 3.2	Schematic layout of the film/effusion cooling test rig	30
Fig. 3.3	Schematic of machined ring geometries.....	31
Fig. 3.4	Schematic of the machined ring with one row of holes	32
Fig. 3.5	Schematic of the machined ring with two rows of holes.....	32

Fig. 3.6 Schematic of the machined ring test plate assembly	33
Fig. 3.7 Geometric details of the effusion test plate	34
Fig. 3.8 Schematic of the effusion test plate assembly	36
Fig. 3.9 Schematic of the effusion test plate with the machined ring assembly	36
Fig. 3.10 Geometrical details of the test plate for overall cooling effectiveness.....	37
Fig. 3.11 Photograph of the test plate for overall cooling effectiveness.....	38
Fig. 3.12 Schematic of effusion cooling with machined ring cooling flow along with the mainstream flow.....	39
Fig. 3.13 Photograph of the fabricated adiabatic effusion test plate.....	39
Fig. 3.14 Photograph of fabricated machined Ring 1 with one row of holes	40
Fig. 3.15 Photograph of fabricated machined Ring 2 with two rows of holes	40
Fig. 3.16 Variation of raw radiation values with respect to temperature.....	42
Fig. 3.17 Variation of temperature with respect to raw radiation values.....	42
Fig. 3.18 Comparison of thermocouple effectiveness and image effectiveness values	43
Fig. 3.19 Variation of voltage with respect to the current supplied for thin stainless steel sheet for machined ring geometries	48
Fig. 3.20 Variation of voltage with respect to the current supplied for thin stainless steel sheet with effusion cooling holes.....	48
Fig. 3.21 Conduction heat loss with respect to the temperature difference across the substrate used for machined ring geometry	49
Fig. 3.22 Conduction heat loss with respect to the temperature difference across the substrate used for effusion cooling holes.....	49
Fig. 3.23 Pictorial representation of error band for adiabatic film cooling effectiveness of effusion cooling holes.....	51
Fig. 4.1 Modeling of machined ring 1	52

Fig. 4.2 Modeling of machined ring 2	53
Fig. 4.3 Modeling of effusion cooling holes.....	53
Fig. 4.4 Modeling of effusion holes with machined ring 1	53
Fig. 4.5 Modeling of effusion holes with machined ring 2.....	54
Fig. 4.6 Computational domain for conjugate analysis of effusion cooling with boundary conditions.....	54
Fig. 4.7 Meshing details for machined ring 1	55
Fig. 4.8 Meshing details for effusion cooling	55
Fig. 4.9 Meshing details for effusion cooling with machined ring 1	56
Fig. 4.10 Different mesh sizes for grid independence study.....	58
Fig. 4.11 CFD overall film cooling effectiveness results at different mesh sizes in comparison with the experimental result	59
Fig. 5.1 Thermographic image of test plate during a machined ring test run	61
Fig. 5.2 Experimental adiabatic film cooling effectiveness distribution for machined ring 1	61
Fig. 5.3 CFD adiabatic film cooling effectiveness distribution for machined ring 1 ..	62
Fig. 5.4 CFD adiabatic test plate temperature contours for machined ring 1 at different blowing ratios.....	63
Fig. 5.5 CFD flow field temperature contours for machined ring 1 at different blowing ratios.....	64
Fig. 5.6 Comparison of experimental and CFD adiabatic film cooling effectiveness for machined ring 1 at different blowing ratios	65
Fig. 5.7 Mainstream heat transfer coefficient in the streamwise direction	67
Fig. 5.8 Experimental film heat transfer coefficient for machined ring 1	67
Fig. 5.9 Experimental heat transfer coefficient ratio for machined ring 1	69
Fig. 5.10 CFD film heat transfer coefficient for machined ring 1	69

Fig. 5.11 Comparison of experimental and CFD film heat transfer coefficient for machined ring 1 at different blowing ratios	70
Fig. 5.12 Effect of blowing ratio on NHFR distribution for machined ring 1	72
Fig. 5.13 Experimental adiabatic film cooling effectiveness distribution for machined ring 2	73
Fig. 5.14 CFD adiabatic film cooling effectiveness distribution for machined ring 2	73
Fig. 5.15 CFD adiabatic test plate temperature contours for machined ring 2 at different blowing ratios.....	75
Fig. 5.16 Comparison of experimental and CFD adiabatic film cooling effectiveness for machined ring 2 at different blowing ratios	76
Fig. 5.17 Experimental film heat transfer coefficient for machined ring 2	77
Fig. 5.18 Experimental heat transfer coefficient ratio for machined ring 2.....	78
Fig. 5.19 CFD film heat transfer coefficient for machined ring 2	78
Fig. 5.20 Comparison of experimental and CFD film heat transfer coefficients for machined ring 2 at different blowing ratios	79
Fig. 5.21 Effect of blowing ratio on NHFR distribution for machined ring 2.....	80
Fig. 5.22 Comparison of adiabatic film cooling effectiveness for machined ring 1 & 2 at different blowing ratios.....	82
Fig. 5.23 Comparison of film heat transfer coefficient for machined ring 1 & 2 at different blowing ratios.....	83
Fig. 5.24 Comparison of net heat flux reduction for machined ring 1 & 2 at different blowing ratios.....	84
Fig. 5.25 Thermographic image of effusion cooled test plate at 2.5 blowing ratio	85
Fig. 5.26 Experimental adiabatic film cooling effectiveness distribution for effusion cooling holes	86
Fig. 5.27 CFD adiabatic film cooling effectiveness distribution for effusion cooling holes	87

Fig. 5.28 CFD temperature contours for adiabatic effusion cooling holes.....	88
Fig. 5.29 CFD flow field contours for adiabatic effusion cooling holes	89
Fig. 5.30 Comparison of experimental and CFD adiabatic film cooling effectiveness for effusion cooling holes	90
Fig. 5.31 Experimental film heat transfer coefficient for effusion cooling holes.....	91
Fig. 5.32 Heat transfer coefficient ratio for effusion cooling holes.....	92
Fig. 5.33 CFD film heat transfer coefficient for effusion cooling holes.....	92
Fig. 5.34 Comparison of experimental and CFD film heat transfer coefficient for effusion cooling holes	94
Fig. 5.35 Effect of blowing ratio on NHFR distribution for effusion cooling holes ...	95
Fig. 5.36 Typical thermographic image of effusion cooling with MR1 at BR 2.5.....	96
Fig. 5.37 Experimental adiabatic film cooling effectiveness distribution for effusion cooling holes with machined ring geometry 1	97
Fig. 5.38 CFD adiabatic film cooling effectiveness for effusion cooling holes with machined ring geometry 1	97
Fig. 5.39 Comparison of experimental and CFD film cooling effectiveness for effusion cooling holes with machined ring geometry 1	99
Fig. 5.40 Experimental film heat transfer coefficient for effusion cooling holes with machined ring geometry 1	100
Fig. 5.41 CFD film heat transfer coefficient for effusion cooling holes with machined ring geometry 1	101
Fig. 5.42 Heat transfer coefficient ratio for effusion cooling holes with machined ring geometry 1	101
Fig. 5.43 Comparison of experimental and CFD film heat transfer coefficient for effusion cooling holes with machined ring geometry 1	103
Fig. 5.44 Effect of blowing ratio on NHFR distribution for effusion cooling holes with machined ring geometry 1	104

Fig. 5.45 Experimental adiabatic film cooling effectiveness distribution for effusion cooling holes with machined ring geometry 2	105
Fig. 5.46 CFD film cooling effectiveness for effusion cooling holes with machined ring geometry 2	106
Fig. 5.47 CFD temperature contour at blowing ratio of 2.5 for effusion cooling holes with machined ring geometry 2	107
Fig. 5.48 CFD flow field contour at blowing ratio of 2.5 for effusion cooling holes with machined ring geometry 2	107
Fig. 5.49 Comparison of experimental and CFD film cooling effectiveness for effusion cooling holes with machined ring geometry 2	108
Fig. 5.50 Experimental film heat transfer coefficient for effusion cooling holes with machined ring geometry 2	110
Fig. 5.51 CFD film heat transfer coefficient for effusion cooling holes with machined ring geometry 2	110
Fig. 5.52 Heat transfer coefficient ratio for effusion cooling holes with machined ring geometry 2	111
Fig. 5.53 Comparison of experimental and CFD film heat transfer coefficient for effusion cooling holes with machined ring geometry 2	112
Fig. 5.54 Effect of blowing ratio on NHFR distribution for effusion cooling holes with machined ring geometry 2	113
Fig. 5.55 Comparison of adiabatic film cooling effectiveness for effusion holes with and without machined ring geometries at different blowing ratios	116
Fig. 5.56 Comparison of film heat transfer coefficient for effusion holes with and without machined ring geometries at different blowing ratios	117
Fig. 5.57 Comparison of net heat flux reduction for effusion holes with and without machined ring geometries at different blowing ratios	118
Fig. 5.58 Effect of blowing ratio on experimental overall cooling effectiveness for 7.2D pitch effusion holes	121

Fig. 5.59 Effect of blowing ratio on CFD overall cooling effectiveness for 7.2D pitch effusion holes	122
Fig. 5.60 Comparison of experimental and CFD overall film cooling effectiveness at different blowing ratios.....	123
Fig. 5.61 Experimental and CFD overall film cooling temperature contours for 7.2D pitch effusion holes at a blowing ratio of 2.0.....	124
Fig. 5.62 Experimental overall cooling effectiveness contours at different blowing ratios for 7.2D pitch effusion holes.....	125
Fig. 5.63 CFD overall cooling effectiveness contours at different blowing ratios for 7.2D pitch effusion holes	125
Fig. 5.64 Effect of blowing ratio on the experimental overall cooling effectiveness for 5.4D pitch effusion holes	126
Fig. 5.65 Typical thermal image of overall cooling effectiveness effusion plate at a blowing ratio of 2.5.....	127
Fig. 5.66 Experimental overall cooling effectiveness contours for 5.4D pitch effusion holes at different blowing ratios	128
Fig. 5.67 Comparison of overall film cooling effectiveness for 7.2D and 5.4D pitch effusion holes at different blowing ratios	129
Fig. 5.68 Effect of blowing ratio on the overall cooling effectiveness for effusion holes with machined ring geometry 1	131
Fig. 5.69 CFD conjugate test plate temperature contours for effusion with machined ring 1 at different blowing ratios	132
Fig. 5.70 Effect of blowing ratio on the overall cooling effectiveness for machined ring geometry 2	133
Fig. 5.71 CFD conjugate streamwise temperature contours for effusion with machined ring 2 at different blowing ratios	135
Fig. 5.72 CFD conjugate test plate temperature contours for effusion with machined ring 2 at different blowing ratios	136

Fig. 5.73 Comparison of overall film cooling effectiveness for effusion holes with and without machined ring geometries at different blowing ratios	137
Fig. 5.74 Schematic of the effusion cooling test rig with the impingement test plate	138
Fig. 5.75 Geometrical details of the impingement plate	138
Fig. 5.76 Typical thermal image of effusion plate at a blowing ratio of 2.5 with impingement plate at the backside	139
Fig. 5.77 Experimental overall cooling effectiveness contours of effusion holes with impingement flow at different blowing ratios	140
Fig. 5.78 Effect of blowing ratio on the overall cooling effectiveness of effusion holes with impingement holes at the backside	140
Fig. 5.79 Effect of impingement on effusion cooling at different blowing ratios	142
Fig. 5.80 Effect of impingement on overall cooling effectiveness at different x locations for a blowing ratio of 2.5	143
Fig. 5.81 Overall cooling effectiveness comparison between effusion with impingement and effusion with machined ring geometries at different blowing ratios	145
Fig. I.1 Mass flow through the cooling holes for machined ring 1	158
Fig. I.2 Coefficient of discharge through the cooling holes for machined ring 1	159
Fig. I.3 Mass flow through the effusion cooling holes for the adiabatic test plate	160
Fig. I.4 Coefficient of discharge through the effusion cooling holes for the adiabatic test plate	160
Fig. I.5 Mass flow through the effusion cooling holes for SS test plate	161
Fig. I.6 Coefficient of discharge through the effusion cooling holes for SS test plate	161

LIST OF TABLES

Table 4.1 CFD boundary conditions	56
Table 4.2 Test matrix for heat transfer coefficient and adiabatic film cooling effectiveness measurements	57
Table II.1 Specifications of the instruments	162

NOMENCLATURE

A	-	Area (m^2)
c	-	Constant
Cd	-	Coefficient of discharge
D	-	Diameter of effusion cooling hole (mm)
d	-	Diameter of machined ring hole (mm)
Dp	-	Orifice pipe diameter (mm)
h	-	Heat transfer coefficient (W/m^2K)
I	-	Current (amps)
k	-	Thermal conductivity (W/mK)
L	-	Length of test plate (mm)
l	-	Length of the hole (mm)
\dot{m}	-	mass flow rate (kg/hr)
P	-	Pressure (N/m^2)
Q	-	Heat (W)
q	-	Heat flux (W/m^2)
q_{in}	-	Heat addition (W/m^2)
q_{out}	-	Heat removal (W/m^2)
s	-	Entropy
Sx	-	Streamwise pitch of effusion holes (mm)
Sy	-	Spanwise pitch of effusion holes (mm)
T	-	Temperature (K)
t	-	Thickness of effusion plate/liner wall (mm)

U	-	Velocity (m/s)
V	-	Voltage (volts)
v	-	Volume (m ³)
W	-	Width of test plate (mm)
X	-	Length along the flow direction / Streamwise direction (mm)
x	-	Machined ring hole pitch (mm)
y	-	Machined ring 2 row spacing (mm)
ΔA	-	Elemental surface area (m ²)
ΔP	-	Pressure difference across orifice (N/m ²)
ΔT	-	Temperature Difference (K)

Greek Symbols

β	-	Effusion hole angle
η	-	Overall cooling effectiveness
θ	-	Non-dimensional temperature
ρ	-	Density (kg/m ³)

Subscripts

1	-	liner wall section on the hot gas side
1f	-	liner wall section with film cooling holes on the hot gas side
2	-	liner wall section on the cold air side
a	-	Cold air
act	-	Actual
aw	-	Adiabatic wall
c	-	Coolant
cc	-	Coolant chamber/Plenum
down	-	Downstream of the orifice
e	-	Supplied
f	-	Film
g	-	Hot gas

L	-	Loss
m	-	Mainstream
ms	-	Mainstream static
net	-	Final/Total
o	-	Without film
s	-	Static mainstream
t	-	Total mainstream
theo	-	Theoretical
up	-	Upstream of the orifice
w	-	Wall

Abbreviations

BR	-	Blowing ratio
C	-	Convection
CFD	-	Computational fluid dynamics
DR	-	Density ratio
exp	-	Experimental
IR	-	Infrared
K	-	Conduction
MR1	-	Machined ring 1
MR2	-	Machined ring 2
NHFR	-	Net heat flux reduction
R	-	Radiation

CHAPTER 1

INTRODUCTION

1 INTRODUCTION

The life and durability of the gas turbine engine mainly depend on the temperature of its parts. To keep the temperature of the parts within the safe limit, cooling methods and an effective thermal barrier coating are used in the turbine airfoils and the combustors. For the cooling, secondary air is taken from the high-pressure compressor exit and used to cool the liners in the combustion chamber and also the turbine stator and rotor blades. The amount of secondary air used for this cooling purpose should be minimum. Otherwise, the gas turbine efficiency will go down. Film cooling is one of the cooling techniques used to cool the combustion chamber liner and turbine blade components.

1.1 Gas Turbine Engine

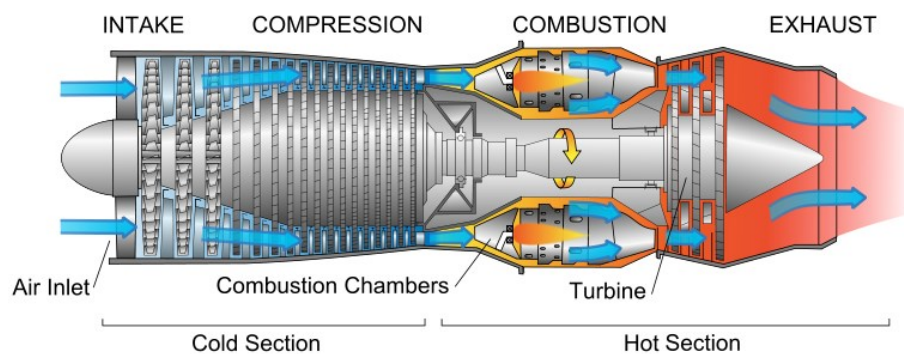


Fig. 1.1 Typical gas turbine engine

Source: (https://commons.wikimedia.org/wiki/File:Jet_engine.svg)

Fig. 1.1 shows the typical gas turbine engine and its components. It mainly consists of four parts: the compressor, combustion chamber, turbine, and nozzle. The compressor is used to increase the pressure and temperature of the incoming air from the intake section. Combustion chamber, in which fuel is injected into the high-pressure air as a fine spray and mixed with the air, which is burned inside the combustion chamber liner. The pressure remains nearly constant during combustion. In the turbine, the temperature rise during the combustion process is converted into rotational energy, which is used to drive the compressor. The exhaust nozzle produces a high-velocity exhaust jet by using the remaining energy added in the combustor. Gas turbine engines work on the Brayton cycle. Fig. 1.2 shows the P-V and T-S plots of the Brayton cycle.

The process 1-2 shows the compression, 2-3 combustion, 3-4 expansion in turbine and 4-1 shows the exhaust in the nozzle.

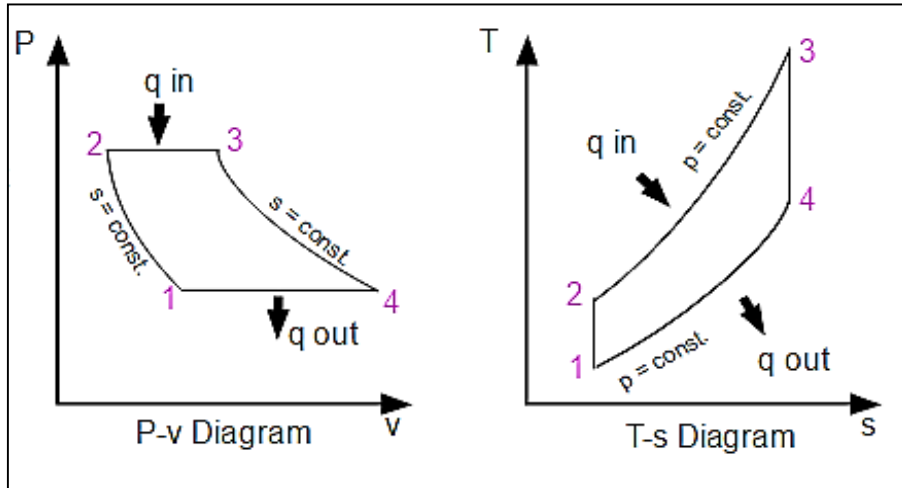


Fig. 1.2 P-V and T-S diagram of the gas turbine

Source: https://en.wikipedia.org/wiki/Brayton_cycle

1.2 Gas Turbine Combustor

The gas turbine combustor is a device in which combustion takes place by adding the fuel to air stream which is coming out from the compressor. Due to the combustion, the temperature rises inside the combustion chamber. The combustor is one of the main sub-systems of the engine in which highly three-dimensional flows with turbulent in nature, complex chemical reactions, and multidimensional heat transfer takes place. The compressor outlet conditions also dictate the design of the combustion system, and also it has to meet the turbine design requirements in terms of pattern factor for satisfactory operation and its desired life. Fig. 1.3 shows the components of a gas turbine combustor and its zones.

1.2.1 Primary Zone

The aim of the primary zone is to stable the flame and offer adequate time to attain complete combustion of the incoming air-fuel mixture. Many different types of flow patterns are engaged for the complete mixing of air and fuel which produces continuous ignition. These flow patterns create a toroidal flow reversal which recirculates a portion of the hot combustion gases for the continuous ignition. Air

swirlers are used in the modern combustors to create such type of flow pattern, whereas in olden days the air is fed through the holes drilled in the liner wall at the upstream end of the liner.

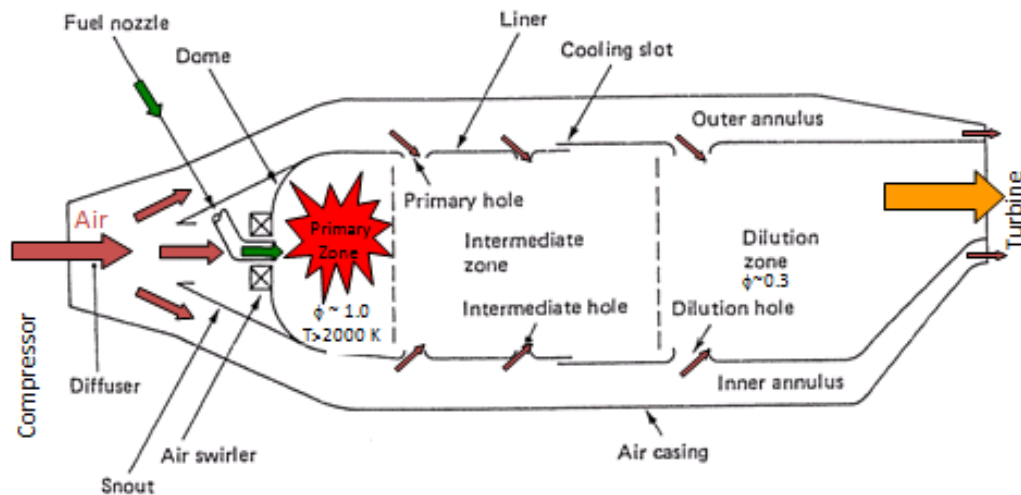


Fig. 1.3 Components of a gas turbine combustor and its zones

Source: Gas Turbine Combustion (Lefebvre and Ballal)

1.2.2 Intermediate Zone

If the primary-zone temperature is more than 2000 K, dissociation reactions will happen, and a significant amount of carbon monoxide (CO) and hydrogen (H₂) will emit in the efflux gases. If these gases passed to the dilution zone, it would be cooled quickly by the accumulation of a huge amount of air. The CO would be discharged from the combustor unburned which is a source of combustion inefficiency and a pollutant also. So, by adding a small amount of air in the intermediate zone enhances the burnout of soot and permits the CO and any other unburned hydrocarbons to progress for complete combustion.

1.2.3 Dilution Zone

In the dilution zone, the annulus air is fed into the main flow path through dilution holes to reduce the temperature of the outlet stream that is suitable to the turbine. This temperature distribution at the exit of the combustor section is generally described in terms of “pattern factor.”

1.3 Combustor Liner and Need for Cooling

The liner holds the combustion and introduces the airflow through the intermediate, dilution, and cooling holes for various purposes into the combustion zone. The combustor liner should be designed and withstand extended high-temperature cycles. Due to this reason superalloys like Hastelloy X, nimonic materials are used for the fabrication of liners. Even though high-performance alloys are used, it must be cooled with some amount of air flow. Some combustors will have thermal barrier coatings to reduce the heat flux. However, air cooling is still required. Various types of cooling arrangements were investigated to achieve better cooling effectiveness in the liner. Fig. 1.4 shows the different types of liner cooling arrangements.

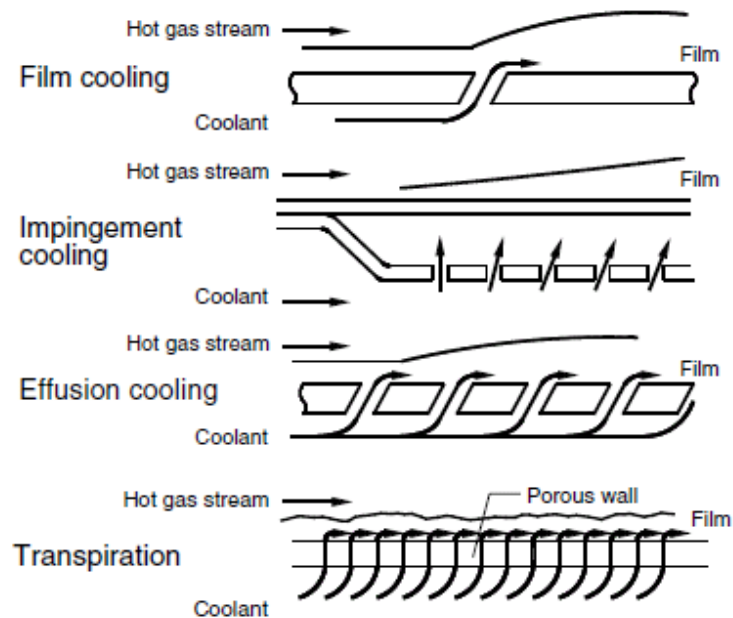


Fig. 1.4 Liner cooling hole arrangements/schemes

Film cooling works by injecting cold air from a slot/hole and forms a barrier in-between the hot gas and the liner wall which is shown in Fig. 1.5. This cold air creates a thin film that protects the liner surface, reducing the temperature of the liner significantly. The distinct nature of the film cooling holes does not offer a fully protected cooling film over the surface, and due to that the liner is not sufficiently safeguarded from the combustion gases. Even though if an excessive amount of coolant is sent through the film cooling holes, it leads the coolant jet to directly mix with the mainstream and induces vortices that can reduce the effectiveness. The region after

some distance from the film cooling holes is adequately cooled due to the reattachment of film. But in effusion-cooling, multiple numbers of holes are arranged closely together. Due to this, the lower impulse jets influence each other and do not go beyond into the main flow and remain within the coolant boundary layer. Thus the cooling effectiveness is increased by the tendency of the vortices to reattach to the wall. Effusion cooling which is multiple rows of film cooling holes which are closely packed together in spanwise and streamwise directions and it seems at least seven rows of cooling holes should be there for an effusion cooling geometry that captures all relevant phenomena. Therefore, most film-cooling research data cannot provide a valid meaning for effusion cooling. Also, the coolant flow through the effusion cooling holes produces a significant amount of convective cooling.

In impingement cooling, where the jets from the impingement holes cool the backside of the liner plate. The jets coming out from the impingement holes hits the liner plate and increases the local heat transfer coefficients significantly. For efficient impingement design the following parameters have to be considered: the layout of holes, jet to target spacing, the shape of the target surface, the shape of the jet nozzle, etc. Transpiration cooling in which the porous wall is used so that the continuous film formation happens and efficient cooling will be achieved. But due to the strength of the porous medium, this cooling method cannot be used in the combustor liner cooling.

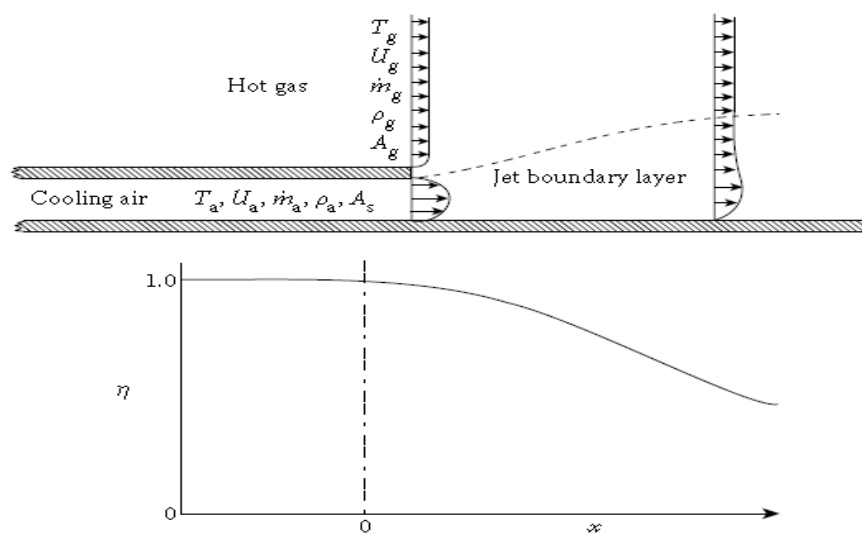


Fig. 1.5 Schematic of film cooling concept

Source: Gas Turbine Combustion (Lefebvre and Ballal)

1.4 Heat Transfer through Uncooled Liner

The heat-transfer model shown in Fig. 1.6 contains only the variation of properties in the axial direction. Around the circumference, all properties are assumed to be constant at the axial position. The rate of heat transfer into an element of a wall must be well-adjusted by the rate of heat transfer out at steady-state conditions. Therefore, the inside surface area ΔA_{w1} of an element is,

$$(R_1 + C_1) \Delta A_{w1} = (R_2 + C_2) \Delta A_{w2} = K_{1-2} \Delta A_{w1} \quad (1.1)$$

K is the liner wall heat conduction which is always negligible compared to the convection and radiation.

The liner wall thickness is thin; then we can consider $\Delta A_{w1} \cong \Delta A_{w2}$. Thus, the above equation can be simplified to

$$R_1 + C_1 = R_2 + C_2 = K_{1-2} \quad (1.2)$$

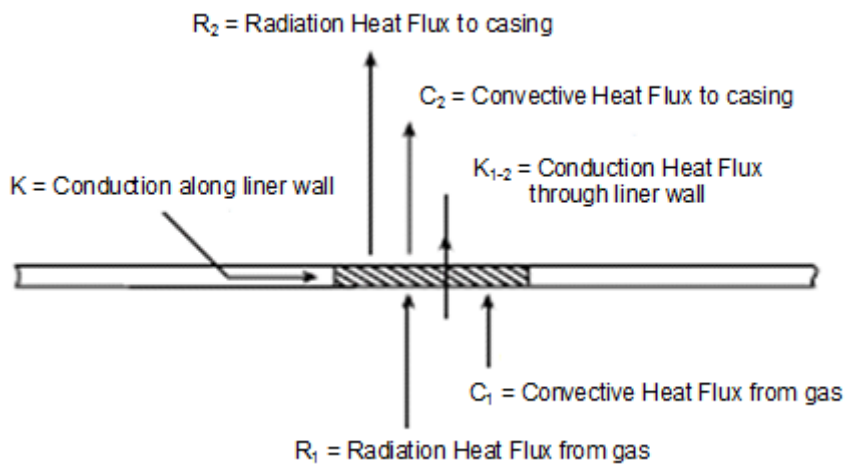


Fig. 1.6 Heat transfer through uncooled Liner

Source: Gas Turbine Combustion (Lefebvre and Ballal)

where K_{1-2} is the liner conduction heat transfer due to the temperature difference within the wall, i.e.,

$$K_{1-2} = k_w (T_{w1} - T_{w2}) / t_w \quad (1.3)$$

1.5 Heat Transfer through Film Cooled Liner

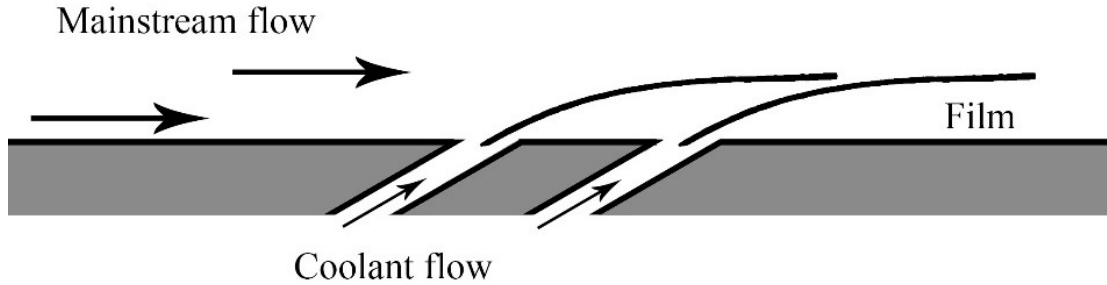


Fig. 1.7 Cooling film formation

The cooling film formation over a cooled surface by using secondary flow as coolant is shown in Fig. 1.7. In the calculation of film-cooled surface temperatures, the previous R_1 , R_2 , and C_2 equations remain the same, but the internal-convection component, C_1 , is different due to the introduction of coolant flow. The temperature and velocity of the hot gas near the wall are changed by the coolant coming out from the film cooled slot/holes. So the C_1 equation becomes,

$$C_{1f} = h_f (T_m - T_{aw}) \quad (1.4)$$

The mainstream heat transfer coefficient with effusion cooling holes is defined as

$$h_f = C_{1f} / (T_m - T_{aw}) \quad (1.5)$$

where T_{aw} is the adiabatic wall temperature and C_{1f} shows the convection heat rate between the effusion test plate and the mainstream flow with effusion holes.

The mainstream heat transfer coefficient without effusion cooling holes is defined as

$$h_0 = C_1 / (T_m - T_w) \quad (1.6)$$

where T_m is the mainstream static temperature, T_w is the wall temperature and C_1 shows the convection heat rate between the plate without effusion cooling holes and the mainstream flow.

Adiabatic cooling effectiveness is defined as

$$\eta_{aw} = (T_m - T_{aw}) / (T_m - T_c) \quad (1.7)$$

Net Heat Flux Reduction (NHFR) is a parameter that generally used to estimate the reduction of heat flux across a cooled surface. This parameter was defined as,

$$\text{NHFR} = 1 - (C_{1f} / C_1) = 1 - (h_f / h_0) * (1 - \eta_{aw}\theta) \quad (1.8)$$

Where θ represent the dimensionless temperature:

$$\theta = (T_m - T_c) / (T_m - T_w) \quad (1.9)$$

So it is important to find the adiabatic film cooling effectiveness and heat transfer coefficients with and without film cooling to get the NHFR values for a particular film cooling geometry. The film effectiveness measurements are normally carried out using an adiabatic surface with free stream and coolant at different temperatures. The heat transfer coefficient investigations are carried out using a constant heat flux or temperature surface with the coolant and free stream at the same temperature. A number of geometric and flow parameters influence the film cooling performance of a film cooling geometry. Lakshminarayana (1996) explained these parameters and their effect on film cooling. The main influencing geometric parameters of the film cooling hole are:

- Hole inclination angle.
- Hole pitch in a row.
- Row pitch.
- Hole Diameter.

The important flow parameters influence the film cooling performance are:

- Blowing ratio.
- Mainstream Reynolds number.
- Coolant to mainstream density ratio.
- Mainstream turbulence.

The blowing ratio was estimated using the relation:

$$BR = (\rho_c U_c) / (\rho_m U_m) \quad (1.10)$$

The mainstream mass flux ($\rho_m U_m$) was estimated from the measured mainstream velocity and the estimated mainstream density based on the static pressure and total temperature measured in the test section. The coolant jet velocity (U_c) is estimated from the plenum total pressure, the test section static pressure and the coolant density (ρ_c) is estimated from the coolant temperature.

Density ratio is the ratio between coolant density to mainstream density.

$$DR = \frac{\rho_c}{\rho_g} \quad (1.11)$$

where, ρ_c is coolant density in kg/m^3 and ρ_g is mainstream density in kg/m^3 .

1.6 Introduction to Computational Fluid Dynamics

Computational Fluid Dynamics (CFD) is an analysis of numerical problems based on fluid flow and heat transfer phenomena related to the computer-based simulation of chemical reactions. It covers both the industrial and non-industrial applications. Some of them are mentioned below.

- Aerodynamic analysis in aircraft engineering.
- Prediction of drag coefficient in automobiles and improving air ingestion in engines.
- Hydrodynamic performance of crafts (ships).
- IC engine combustion and gas turbine flows.
- Chip cooling purpose in electrical and electronic engineering.
- Analysis of chemical reaction, mixing and separation type problems.
- Blood flow in non-natural hearts, air flow in breathing in biomedical engineering.

From the past 60 years, CFD is introduced in the design, research, and developmental activities of production and aircraft industries. In recent times, computational methods are used in the IC engine, gas turbine combustion chamber, and boilers design. Also, nowadays the automobile industry is predicting the drag forces with the help of CFD. CFD is well believed as a research and a design tool.

In CFD, numerical based algorithm structural codes are used to solve the fluid flow problems. All the commercial packages provide the normal classy user interfaces to input problematic limits and to examine the output results. So the user can use the commercial package with little training. Therefore, all the CFD codes have three main elements:

- Preprocessor
- Solver
- Post processor

1.6.1 Pre Processor

The input conditions present in the flow problems is given by using pre-processor in CFD programs. Following stages are involved in Pre-processing:

- Geometry creation/modelling and explanation of the flow domain.
- Generation of the grids – The grids are formed in the flow domain with a number of small cells with quadratic, triangular cell structures. Thus the geometry and the flow domain are fully meshed with non-overlapping subdomains.
- Defining the proper physics and chemical phenomenon to the model domain.
- Fluid and material properties to be specified.
- Defining appropriate boundary conditions to the domain such as inlet, outlet conditions, and boundary wall conditions.

The significance of the flow problem is given at each nodes of the cell. For example, velocity, pressure, temperature, etc. The accuracy of the solution depends on the grid size, i.e., the number of cells in the grid. Also, the mesh should be fine where larger

variation occurs from point to point, and coarser where little change in the fluid properties occurs. Normally, if the number of cells is high, then the results will be accurate. But the computational time will increase. In order to optimize the grid size and reduce the time for solving, grid independence test should be performed for the model. Convergence and grid independence are the two main features that describe an effective CFD solution.

1.6.2 Solver

The numerical solution to algebraic equations is found by two methods: Direct Methods and Iterative Methods. Direct methods include Gaussian Elimination Technique, Cramer's Rule, and the Thomas Algorithm. Iterative methods are based on repeated applications of an algorithm; in this method, the initial guess values are very important. Without initial guess values, this method was not possible to solve the problems. Mostly used algorithm for the iterative method is the Jacobi and Gauss-Siedel methods. The variation of the governing equations is carried out by three different methods:

- Finite difference method (FDM)
- Finite element method (FEM)
- Finite volume method (FVM)

These three methods perform the following activities.

- Evaluate the flow variables using simple equations.
- Discretization in exchange for the guesses into the governing flow equations and subsequent mathematical operations
- To find the solution of algebraic equations.

Finite Difference Method: The principle of finite difference methods is mainly based on the numerical schemes used to solve ordinary differential equations. It consists of approximating the differential term by substituting the derivatives in the equation by means of differential quotients. The domain is divided into space and time, and the solution approximations are computed at space or time points. The inaccuracy between the numerical and the exact solution is determined by the error from a differential term

to a difference term. This is called the discretization or truncation error and replicates that a finite part of a Taylor series which is used in the approximation.

Finite Element Method: The formulation of the problem using finite element method results in a system of algebraic equations. The method approximates the unknown function over the domain. The problem is solved by subdividing a large system into smaller and simpler parts which are called finite elements. The simple equations that model these finite elements are then assembled into a larger system of equations that models the entire problem. FEM then uses variational methods from the calculus of variations to approximate a solution by minimizing an associated error function.

The Finite Volume Method: The main advantage of this method is less computational time for solution convergence and less memory usage. FVM is also giving the best accurate solutions in less time compared to all other methods. This method has the following steps:

- Proper incorporation of the fluid flow governing equations on all the finite control volumes of the solution domain.
- Discretization contains the replacement of finite-difference-type approximations in the integrated equation terms which represent the flow processes like convection, diffusion, etc. This converts the integral equations into a scheme of algebraic equations.
- Using an iterative method, the algebraic equations are solved to get the correct solution.

1.6.3 Post Processor

Post processing is nothing but a graphical representation of the results. Present days, the CFD is prepared with multipurpose data representation tools. These tools contain the following features :

- The domain of the geometry and demonstrating the grid.
- Vector (velocity and streamline) plots, 2-D and 3-D surface plots, contour plots of temperature, pressure, etc.

Animation display is one of the advantages of post-processing. Finally, we can get the results at each and every node points in Microsoft excel sheet format.

1.6.4 Equations Governing Fluid Flow and Heat Transfer

The governing equations for fluid flow and heat transfer characterize the conservation laws of physics. The basic laws for the formation of the governing equations are:

- The fluid mass is conserved.
- The rate of change of momentum should equal to the sum of the forces on a fluid particle. (Second law of Newton).
- The rate of change of energy is the same as the sum of the rate of heat addition on a fluid particle and the rate of work done on a fluid particle (first law of thermodynamics).

1.6.4.1 Three Dimensional Mass Conservation Equation

The mass conservation equation states that the rate of increase of mass in the element is equal to the net rate of flow of mass into the element across its faces.

The rate of increase of mass in a fluid element = The net rate of flow of mass into the fluid element

The resulting mass balance equation is divided by the elemental volume ($\partial x \partial y \partial z$), and then the equation becomes,

$$\frac{\partial \rho}{\partial t} + \frac{\partial(\rho u)}{\partial x} + \frac{\partial(\rho v)}{\partial y} + \frac{\partial(\rho w)}{\partial z} = 0 \quad (1.12)$$

or in more compact vector notation

$$\frac{\partial \rho}{\partial t} + \text{div}(\rho U) = 0 \quad (1.13)$$

This is the Continuity equation which is having two terms on the left-hand side. The first term is the rate of change of density with respect to time. The second term is called

a convective term which defines the net mass flow out of the element through its boundaries.

The density is constant for an incompressible fluid, so the equation becomes

$$\text{div}(\rho U) = 0 \quad (1.14)$$

or in longhand representation

$$\frac{\partial u}{\partial x} + \frac{\partial v}{\partial y} + \frac{\partial w}{\partial z} = 0 \quad (1.15)$$

1.6.4.2 Momentum Equation in Three Dimensions

Newton's second law states that the rate of change of momentum of a fluid particle equals the sum of the forces on the particle.

The rate of increase in momentum of a fluid particle = Sum of forces on the fluid particle

Two types of forces are exhibited by the fluid particles. One is the surface force, and another one is body force. Surface force includes pressure and viscous forces. Body force contains gravity, centrifugal, Coriolis and electromagnetic forces.

x Momentum sources

$$\rho \frac{Du}{Dt} = \frac{\partial(-p + \tau_{xx})}{\partial x} + \frac{\partial \tau_{yx}}{\partial y} + \frac{\partial \tau_{zx}}{\partial z} + S_{Mx} \quad (1.16)$$

y component

$$\rho \frac{Dv}{Dt} = \frac{\partial \tau_{xy}}{\partial x} + \frac{\partial(-p + \tau_{yy})}{\partial y} + \frac{\partial \tau_{zy}}{\partial z} + S_{My} \quad (1.17)$$

z component

$$\rho \frac{Dw}{Dt} = \frac{\partial \tau_{xz}}{\partial x} + \frac{\partial \tau_{yz}}{\partial y} + \frac{\partial(-p + \tau_{zz})}{\partial z} + S_{Mz} \quad (1.18)$$

1.6.4.3 Three Dimensional Energy Equation

The energy equation states that the rate of variation of energy on a fluid particle is equal to the summation of the net rate of heat added to the fluid particle and the net rate of work done on the particle.

$$\begin{array}{l} \text{The rate of increase of} \\ \text{energy on the fluid particle} \end{array} = \begin{array}{l} \text{The net rate of heat added to the fluid particle} \\ + \\ \text{The net rate of work done on the fluid particle} \end{array}$$

The energy equation is expressed as:

$$\begin{aligned} \rho \frac{DE}{Dt} = & -div(\rho U) + \left[\frac{\partial(u\tau_{xx})}{\partial x} + \frac{\partial(u\tau_{yx})}{\partial y} + \frac{\partial(u\tau_{zx})}{\partial z} + \frac{\partial(v\tau_{xy})}{\partial x} \right. \\ & + \frac{\partial(v\tau_{yy})}{\partial y} + \frac{\partial(v\tau_{zy})}{\partial z} + \frac{\partial(w\tau_{xz})}{\partial x} + \frac{\partial(w\tau_{yz})}{\partial y} + \left. \frac{\partial(w\tau_{zz})}{\partial z} \right] \\ & + div(k grad T) + S_E \end{aligned} \quad (1.19)$$

1.6.4.4 Navier- Stokes Equations for a Newtonian Fluid

The governing equations have some more unknowns in the form of viscous stress components. By incorporating an appropriate model for the viscous stresses, the conservation equations for fluid flows are obtained. For all the fluid flows, the viscous stresses can be stated as functions of the local deformation rate. In 3-D flows, the local rate of deformation is having both the linear and the volumetric deformation rate.

$$\rho \frac{Du}{Dt} = -\frac{\partial p}{\partial x} + div(\mu grad u) + S_{Mx} \quad (1.20)$$

$$\rho \frac{Dv}{Dt} = -\frac{\partial p}{\partial y} + div(\mu grad v) + S_{My} \quad (1.21)$$

$$\rho \frac{Dw}{Dt} = -\frac{\partial p}{\partial z} + div(\mu grad w) + S_{Mz} \quad (1.22)$$

1.6.5 Turbulence Models

Turbulent flows are described by velocity fluctuations in the flow. These fluctuations can cause transported quantities such as momentum, energy, and species concentration to fluctuate. Subsequently, these fluctuations are in the order of high frequency and small-scale in nature; it is expensive to solve these problems computationally. For this reason, the instantaneous governing equations can be modified into a set of equations based on time-averaged, ensemble-averaged which results that are computationally cheap to solve. But, the modified equations hold additional unknown variables, and turbulence models have the capacity to know the quantities of these variables. The number of additional unknown variables is more than the number of available governing equations and hence leads to the closure problem. The closure problem is resolved by implementing turbulence models. Many turbulence models are available in CFD to solve the problem, but the literature shows that the previous researchers mainly used K- ϵ models for film/effusion cooling problems.

1.6.5.1 Selecting a Suitable Turbulence Model

For all classes of problems, there is no universally accepted single turbulence model is available. The selection of turbulence model depends on the flow physics, the recognized method for a particular problem, the level of accuracy needed, the existing computational facilities, and the total time required for solving the problem. To select the best suitable model for our problem, it is necessary to realize the abilities and limits of the several turbulence models.

1.6.5.2 Realizable k- ϵ Model

The meaning for the word “realizable” describes that the model fulfills some of the mathematical limitations on the Reynolds stresses, consistent with the turbulent flow physics. Both the standard k- ϵ and the RNG k- ϵ models are not realizable. The realizable model displays a considerable amount of developments over the standard k- ϵ and the RNG k- ϵ models, where the flow behaviour which contains rotation, vortices, and streamlines.

Since the realizable k- ϵ model is somewhat fresh, it is not understandable in which cases this model regularly beats the RNG model. But the literature review

indicates that the realizable model is the best among all the k-ε models for numerous validations of flows with separations and secondary vortices. Particularly this model resolves the round-jet irregularity; i.e., it forecasts the rate of spreading for planar and axisymmetric jets.

This model varies from the standard k-ε model in two ways:

- The realizable k-ε model covers a different formulation for the turbulent viscosity.
- The transport equation is modified for the rate of dissipation, ε, has been obtained from a mean-square vorticity fluctuation transport equation.

1.6.5.3 Transport Equations for the Realizable k- ε Model

$$\frac{\partial}{\partial t}(\rho\kappa) + \frac{\partial}{\partial x_j}(\rho\kappa u_j) = \frac{\partial}{\partial x_j} \left[\left(\mu + \frac{\mu_t}{\sigma_\kappa} \right) \frac{\partial \kappa}{\partial x_j} \right] + G_\kappa + G_b - \rho\epsilon - Y_M + S_\kappa \quad (1.23)$$

$$\begin{aligned} \frac{\partial}{\partial t}(\rho\epsilon) + \frac{\partial}{\partial x_j}(\rho\epsilon u_j) \\ = \frac{\partial}{\partial x_j} \left[\left(\mu + \frac{\mu_t}{\sigma_\epsilon} \right) \frac{\partial \epsilon}{\partial x_j} \right] + \rho f_1 S_\epsilon - \rho f_2 \frac{\epsilon^2}{k + \sqrt{\nu\epsilon}} \\ + f_{1\epsilon} \frac{\epsilon}{k} f_{3\epsilon} G_b + S_\epsilon \end{aligned} \quad (1.24)$$

Where G denotes the turbulence kinetic energy. The subscript k and b denotes the mean velocity gradients and buoyancy. Y_M characterizes the momentum contribution. f_1 , f_2 and f_3 are constants. σ_κ and σ_ϵ denotes the respective κ and ε turbulent Prandtl numbers. The user-defined source terms are represented by S_κ and S_ϵ .

1.7 Organization of the Thesis

This thesis contains six chapters. Chapter 1 covers the introduction to the gas turbine engine, combustor zones, need and types of liner cooling arrangements, heat transfer mechanisms across the cooled liner and, along with the basics of CFD. The importance of heat transfer coefficients, adiabatic film cooling effectiveness measurements, NHFR calculations over the film cooled surface and the geometrical and flow parameters involved in the film cooling technology is also explained in this chapter. Chapter 2 provides a detailed literature survey for the different cooling techniques used in the combustor liner. The improvement of surface temperature measurement techniques to get the liner surface temperatures accurately during the experiments and the best turbulence model for the numerical analysis of film cooling is also briefly provided in this chapter based on the previous work of various researchers in this field. At the end of this chapter the research gap, the present study, and objectives of the present work are explained.

In Chapter 3, the experimental rig setup, test plate details, and its fabrication, instrumentation details, experimental procedure and the error estimate of experimental data is presented. Chapter 4 presents the CFD methodology which includes modelling, mesh details, selection of the turbulence model, CFD boundary conditions and grid independence study.

In Chapter 5, the experimental and numerical results along with detailed discussions on the results and trends are presented. Initially, the results of adiabatic film cooling effectiveness, heat transfer coefficient and NHFR values for machined ring 1 & 2 geometries, effusion cooling geometry and combined effusion cooling with machined ring 1 & 2 geometries are presented. Next, the results of overall cooling effectiveness measurements taken in the SS test plates are presented for effusion cooling with and without machined ring geometries, and effusion cooling with impingement geometry is explained. Finally, a comparison study between effusion cooling with impingement and effusion cooling with machined ring geometries is done to find out which combined cooling technique is beneficial for the combustor liner cooling. Chapter 6 gives the conclusions of the present study and the recommendations for future work.

CHAPTER 2

LITERATURE REVIEW

AND

OBJECTIVES OF THE WORK

2 LITERATURE REVIEW

Several numerical and experimental studies were carried out previously to achieve higher convective heat transfer coefficient on the coolant side of the liner. Further, the film-cooling and effusion cooling airflow have been considered on the hot gas side thereby reducing the convective heat transfer coefficient from the hot gas to the liner wall. The basic heat transfer equations to a film-cooled surface are described by Goldstein (1971). Sen et al. (1996) explained the importance of net heat flux reduction (NHFR) which tells the reduction of the heat transfer with and without film-cooling. NHFR combines both the effects of adiabatic film cooling and heat transfer coefficients. This is enlightened by Sen et al. (1996) and Schmidt et al. (1996) for heat transfer coefficients and adiabatic cooling effectiveness respectively. It is important to find out both adiabatic film cooling and heat transfer coefficients to get the overall cooling effectiveness.

2.1 Slot Cooling

In earlier gas turbine combustor, the liner is cooled only by slot cooling. Correlations for film cooling effectiveness in near slot region were described by Lefebvre and Ballal (2010). He explained how the convective heat transfer from the hot combustion gas side varies for the liner with and without film cooling. The coolant jet coming out from the slot changes the temperature and velocity of the hot gases near the liner wall and thereby reduces the convective heat transfer from the hot combustion gases to the liner surface. Yang et al. (2012) investigated one-row, two-row (staggered and aligned arrangement) and three-row parallel-inlet film holes arrangement to find the film cooling characteristics. Their results show that an increase in blowing ratio the heat transfer coefficient decreases and the film cooling effectiveness increases. Park et al. (2009) conducted an experimental study by using a thermochromic liquid crystal method to study the effect of film cooling effectiveness by changing the first slot angle under recirculation flow and the influence of wiggle strip within a slot. Their results show that the film cooling effectiveness decreases significantly in the first slot position, because of the effects of recirculation flow. Inanli et al. (2009) have studied the effect of slot film cooling and effusion cooling on a plexiglass test plate. Flat and angled leap

geometries are tested for three different slot heights of 7.5, 10 and 12.5 mm. They found that the flat leap produces more film cooling effectiveness than the angled one at all blowing ratios. Among the slot height variation leap height of 12.5 mm gives higher effectiveness than the other two. In effusion cooling, they varied the angle of effusion holes (30° and 75°) and found that the cooling effectiveness is reduced for 75° hole angle. This is due to jet penetration into the mainstream and thus reduces the generation of the insulation layer.

2.2 Effusion Cooling

Modern gas turbine combustor liners have effusion cooling holes. Several researchers varied the geometrical parameters of the effusion cooling holes and found the cooling performance. Natsui et al. (2017) investigated four different effusion cooling arrays to find the effect of local and laterally averaged effectiveness, at a blowing ratio ranging from 0.3 to 1.2. They used CO_2 as a coolant to achieve a density ratio of 1.5. They found at lower blowing ratio of 0.3, the film jets are still attached to the test surface, but at blowing ratio of 0.5, jet lift-off takes place and then impinge back after some distance onto the test surface. At higher blowing ratio, the jets reattach much more downstream, distributing the coolant further along the test surface. Natsui et al. (2016) tested full coverage effusion staggered hole arrays by varying the inclination angles, 30° and 45° , and the spacing of the holes as 14.5 and 19.8 times the diameter. Their results show that for these large spacing of holes, after several rows only the coolant merge and begin to interact with lateral holes. At low blowing ratio, throughout the array, each individual jet remains discrete. At higher blowing rates, due to the jet spreading the profile is more uniform as they reattach with the wall.

Cerri et al. (2007) varied both the diameter and distribution of the holes (pitch) and found that a very effective cooling system can be obtained with minimum cooling air consumption by changing the geometrical parameters. The injection hole spacing, the inclination angle of the holes are varied, and the temperature distribution on effusion cooled plates was studied by Gustafsson, and Johansson (2001) using infrared thermography for different temperature ratios, velocity ratios of the two air streams. They tested three different hole angles of 15° , 20° and 30° and found that lower angles are giving better film cooling effectiveness. They varied the streamwise pitch to the

diameter ratio (S_x/D) of 3, 6 and 12 and found that the cooling effectiveness is higher for the closer holes. Legar et al. (2003) have studied the geometrical parameters such as hole diameter, hole angle inclination, and hole pitches to determine the optimal multi-holed plate geometry, by means of infrared thermography and found that the wall cooling effectiveness increases with the hole diameter and decreases with the increase in hole angle. The hole length to diameter ratio (l/D) was varied for a fixed geometry of S_x/D and S_y/D spacing of effusion cooling holes by Arcangeli et al. (2008) and found that the smaller diameter always implies better performance in terms of overall effectiveness. They also developed a correlation for overall effectiveness in terms of l/D ratios based on their results. The velocity profiles for an effusion cooling combustor liner test plate with laser Doppler velocimetry to measure the flow characteristics of the cooling layer is described by Scrittore et al. (2007). Their results indicate that a fully-developed velocity profile was obtained at a location of 15 film-cooling hole rows. Hasan et al. (2013) investigated computationally the effectiveness of effusion film cooling for a split region of full coverage film holes into two zones of cooling rows and their results show that the two zones of cooling holes gave reasonably similar cooling effectiveness compared with the continuous array of holes. The advantage of split cooling holes is that the same cooling effectiveness is achieved with the minimum amount of coolant flow.

Murray et al. (2018) analyzed the cooling performance of effusion holes by experimentally and computationally. They tried to develop a superposition method of a two-dimensional film effectiveness distribution that can give data quickly for an effusion cooling array of holes. Their results show at higher pitches of effusion holes, the superposition method gives satisfactory results, but at lower pitches due to high levels of jet interactions the superposition method was not able to predict the cooling effectiveness accurately.

2.3 Surface Temperature Measurements Techniques

In earlier days the film cooled surface temperature measurements were taken by using thermocouples. Thermocouples will not give a detailed picture of cooling performance and the film cooling flow physics were affected if a large number of thermocouples were used on the test surface. Nowadays researchers are using modern

non-contact type surface temperature measurement techniques. Infrared (IR) imaging technique was used by Zhang et al. (2009) for investigating the overall cooling effectiveness of three effusion cooling test plates. Pressure Sensitive Paint and Thermochromic Liquid Crystal based techniques to measure the adiabatic effectiveness of a multi-perforated plate were used by Caciolli et al. (2013) and found that the adiabatic effectiveness results achieved by the two techniques show decent agreement in terms of average values. Ekkad et al. (2004) describes the procedure for transient infrared thermography for simultaneous measurements of heat transfer coefficient and film cooling effectiveness from a single test. In the same paper, he mentioned the advantages of infrared thermography over the liquid crystal thermographic method. Infrared thermography requires a uniform high emissivity surface, and this will be prepared by coating the measurement surface by black paint easily. Due to the quick preparation of the test surface and the limitations of the liquid crystals, nowadays most of the researchers are using only infrared thermography for film cooling measurements.

Accurate calibration of infrared thermography is essential if it is used for the surface temperature measurements during tests on film/effusion cooling. In situ calibration for quantitative infrared thermography is explained by Martiny et al. (1996). He developed a method to correct temperatures obtained by infrared thermography using thermocouples as a reference temperature. The correction procedure is based on temperature values recorded by the thermocouple, and a corresponding thermal image captured simultaneously under steady-state test conditions. These thermocouple temperature data are used as reference values for the calibration. Also, he mentioned the importance of placing the thermocouples on the surface in such a way that it covers the entire temperature range of interest. Ochs et al. (2009) followed the same procedure of calibration of Martiny et al. (1996) and developed a calibration technique which allows for extrapolation for higher temperature ranges with higher accuracy as compared to existing in situ calibration techniques.

Another important aim in the combustor liner cooling is to get maximum cooling performance with a minimum amount of cooling air flow. So it is necessary to find the mass flow rate and coefficient of discharge through the film cooling holes. The discharge coefficients for the fluid flow through discrete-hole and inclined multihole

double wall for combustor liner were presented by Xu et al. (2000) over a range of Reynolds numbers from 5,000 to 40,000. They found that the discharge coefficients are in the range of 0.7. Also, the discharge coefficient increases upto pressure parameter of 20, and then it shows constant. A numerical study on the effusion cooling system of an aero-engine combustor liner was performed by Andreini et al. (2011), and they found a correlation to predict the discharge coefficient of effusion cooling holes. They developed the correlation for the coefficient of discharge as a function of the ratio between the hole and the annulus Reynolds number, the inlet flow function and the velocity head ratio of the hole. Guo et al. (2011) found out the effect of turbulence intensity on the discharge coefficient of the film cooling hole. Their results show that the discharge coefficients decrease when the turbulence level increases due to the increased mixing losses at both ends of the film cooling hole. The coefficient of discharge value reduced by more than 30% for both subsonic and supersonic flows with high turbulence intensity.

2.4 Numerical Models

In CFD, different turbulence models are available. Many researchers used different turbulence models in their study and tried to find out which turbulence model is best for film/effusion cooling heat transfer studies. Harrison and Bogard (2008) did a comparative study to find out the film cooling effectiveness and heat transfer coefficient using realizable k - ϵ , standard k - ω , and RSM turbulence models. Their results show that the realizable k - ϵ model gives better centerline effectiveness results. Similarly, Silieti et al. (2009) compared three turbulence models and told realizable k - ϵ model provides the best results in comparison with experimental results. El-jumamah (2014) mentioned in his thesis that the standard k - ϵ turbulence model with standard wall function having y^+ values in the range 30 to 45 showed better agreement with the experimentally measured data. But even with the enhanced wall treatment having y^+ values from 1 to 5, shows no significant improvement in the predictions when compared with the standard wall function approach.

2.5 Slot/Effusion Combined Cooling

As the combustor operating temperature has increased, more effective cooling methods are required. Recently researchers are concentrating on a combination of film cooling methods. Combustor liner having a slot injection and an effusion array with a central dilution hole was tried by Andreini et al. (2013) to study the effects of coolant to mainstream density ratio. Their results pointed out that for the effect of density ratio, heat transfer phenomenon is mainly driven by velocity ratio and at the higher blowing/velocity ratios, the adiabatic effectiveness is less sensitive to the cooling flow parameters. Tarchi et al. (2012) used slot injection and an effusion array with a central large dilution hole along with a backward facing step upstream of the slot which generates a large recirculation area to simulate the real combustor flow path. They found that the presence of the step leads to a reduction in effectiveness and does not have effects on the heat transfer coefficient.

2.6 Impingement/Effusion Combined Cooling

Three-dimensional numerical simulation of flow and heat transfer characteristics of impingement/effusion cooling systems were carried out by Jingzhou et al. (2009). Their results show that the cooling effectiveness increases as the spacing between the adjacent holes decreases or the blowing ratio increases. Rhee et al. (2004) investigated the effect of rib arrangements on an impingement/effusion cooling system with crossflow effects. Impingement and effusion holes are arranged in a staggered manner, and they analyzed the effect of cross flow between the injection and effusion plates. For the blowing ratio greater than 1.0, overall heat transfer is increased due to the ribs on the effusion surface, and higher values are obtained with a lesser pitch between the ribs. But the adverse effects on heat/mass transfer was seen due to the prevention of wall jets spreading at lower blowing ratio of 0.5. Wei-hua et al. (2011) studied the impingement with effusion cooling behavior in a curved effusion wall of the combustion chamber, and their results show with decreasing effusion hole angle and effusion hole to hole spacing, the cooling effectiveness is enhanced. Hong et al. (2007) investigated the impingement with effusion cooling system with cross flow and found out that the flow and heat/mass transfer characteristics are changed significantly due to the installation of fins, and also a higher heat/mass transfer coefficient is obtained

due to the flow disturbance and acceleration by the fin in the effusion hole region. Cho et al. (2008) found that due to secondary vortices formed between two adjacent impinging jets, high transfer rate is induced. Due to that in the midway region, the heat transfer coefficient is as high as stagnation heat transfer coefficient. They determined that the staggered hole arrangement shows better performance than the in-line and shifted arrangement.

2.7 Summary of the Literature Survey

The summary of the literature survey shows that the cooling of the combustor liner mainly depends on the geometrical and flow parameters of the cooling holes. The geometrical parameters such as the diameter of the hole, pitch between holes and the film hole angle will be varied in such a way to achieve maximum film cooling effectiveness with a minimum amount of cooling air requirements. Also, the film cooling performance depends upon various flow parameters such as hot gas side Reynolds number, blowing ratio, the density ratio of the coolant to hot gas, the turbulence created by the combustion gases, etc. For a new cooling hole arrangement, experimental or numerical studies to be carried out freshly to find out the cooling effectiveness and heat transfer coefficient distribution downstream of the holes. Effusion cooling gives maximum cooling performance in comparison with slot, machined ring film cooling. Combination of cooling techniques will provide better cooling effectiveness than the individual cooling schemes.

2.8 Research Gap and Need for the Study

In addition to the individual cooling schemes, the literature indicates that there is a requirement for further investigation of a combination of different cooling schemes to achieve better cooling effectiveness. The data available in the literature indicates effusion cooling is the latest and efficient technology which provides more cooling effectiveness. In literature, very limited data are available for the combined cooling techniques, and there is no such previous work was carried out with the combination of the machined ring with effusion hole geometry downstream. CFD data is also not available for the combined machined ring and effusion cooling geometry. So there is a

need to study the adiabatic film cooling and convective heat transfer coefficients over the combined machined ring and effusion cooling geometries.

2.9 Scope of the Present Study

The scope of the present study consists of three parts.

1. The first part consists of adiabatic film cooling effectiveness and heat transfer coefficient measurements for a multirow film cooling configuration with and without machined ring geometries.
2. The second part describes the overall film cooling effectiveness measurements for an effusion cooling geometry with and without machined ring geometries. Effect of the pitch for two effusion cooling geometries is also analyzed.
3. The third part involves the study of overall film cooling effectiveness measurements on an impingement with effusion cooling.

The aim of the first part is to generate adiabatic film cooling effectiveness and heat transfer coefficients for a multirow film cooling configuration with and without machined ring geometries. In this first part, there are three tasks. The first task is to generate film cooling performance data for the machined ring geometries alone. The next task is to generate the film cooling performance data for effusion cooled liner without a machined ring. The third task is to generate film cooling performance data for effusion cooled liner configuration with machined ring upstream. Geometrical parameters of the effusion cooling test plate consist of a hole diameter of 1 mm, hole angle of 27° and 7.2D pitch in both streamwise and spanwise directions. Effusion holes are placed in a staggered manner with 9 holes per row, and there are 13 rows in total. For these adiabatic cooling effectiveness and heat transfer coefficient measurements, the effusion cooled geometry is scaled up by three times. The geometrical parameters of machined ring 1 (MR1) consist of one row of holes with hole diameter(d) of 2.5 mm and a pitch(x) of 10.8 mm. In machined ring 2 (MR2), where the holes are arranged in a staggered manner and are of same hole diameter, same pitch as of MR1. But the two rows of holes are separated by a distance(y) of 2.5 mm. Detailed experiments are carried out to obtain the heat transfer coefficient and adiabatic film cooling effectiveness distribution data in the blowing ratio range of 0.5 to 2.5 and at a mainstream velocity

of 20 m/s. The heat transfer coefficient investigations are carried out using a constant heat flux surface with the coolant and mainstream at the same temperature. The adiabatic film cooling effectiveness measurements are normally carried out with mainstream and coolant at different temperatures, and the effectiveness is derived from the temperature distribution in the flow direction over an adiabatic wall. In this study, the mainstream was at room temperature, and the coolant was at a temperature around -42°C . This simulates the density ratio of 1.3 between the coolant and the mainstream. Uncertainty analysis is carried out for the temperature, pressure, the mass flow rate through the orifice and consequently the maximum relative error referred to the heat transfer coefficient, effectiveness calculation is established. In order to keep uncertainties as low as possible, great attention is paid to Infrared Camera calibration, which is the main source of uncertainty in evaluating surface/wall temperature (T_w). The above investigation is supported by CFD analysis.

The aim of the second part is to find out the overall film cooling effectiveness measurements for effusion cooling geometry with and without machined ring upstream. The effusion test plate is prepared in stainless steel 304 which has a thermal conductivity of 16.2 W/mK at 100°C and having a thickness of 2 mm. Angled holes of 1 mm diameter with an inclination angle of 27° and 7.2D pitch in both streamwise and spanwise directions are drilled through the test plates by the electric discharge machining process. The machined rings which are used in adiabatic cooling measurements is geometrically scaled down by 3 times and used in this overall cooling effectiveness measurements. One more effusion cooling geometry is prepared to find out the effect of pitch between the holes. The second test plate is having a streamwise, and spanwise pitch of 5.4 mm and other geometrical parameters remain the same as that of the first test plate.

The third part consists of overall film cooling effectiveness measurements on impingement with effusion cooling. The effusion plate which is having 5.4 mm pitch in both the spanwise and streamwise directions is selected for this study. An impingement plate made out of 3 mm thick hylam sheet is kept backside of the effusion plate at a distance of 6 mm. The holes in the impingement plate are also arranged in a staggered manner such that each effusion hole is surrounded by four impingement

holes. The impingement holes are of 0.9 mm in diameter and are normal to the plate surface.

In the initial proposal, only the first part is mentioned as the scope of work. But during the course, the second part is added, because the literature suggests the importance of overall cooling effectiveness measurements in effusion cooling. The third part is an additional work of an entirely different combination of cooling technique (Impingement with effusion). This third part study is done just to compare both the combined cooling techniques, and to find out which combination gives better cooling effectiveness.

2.10 Objectives of the Work

- To find the adiabatic film cooling effectiveness and heat transfer coefficients experimentally over the effusion cooled liner surface with and without machined ring geometries at different blowing ratios.
- CFD modeling and studies to find the adiabatic film cooling effectiveness and heat transfer coefficients to support the experimental investigation.
- Overall cooling effectiveness measurements over the effusion cooled liner surface with and without machined ring geometries at different blowing ratios.
- Overall film cooling effectiveness measurements for two effusion cooling geometries of different hole pitch.
- Overall film cooling effectiveness measurements on impingement with effusion cooling are studied for a particular geometry.
- A comparison study between effusion with impingement cooling and effusion with machined ring geometries.

CHAPTER 3

EXPERIMENTAL SETUP

AND

METHODOLOGY

3 EXPERIMENTAL SETUP AND METHODOLOGY

3.1 Experimental Setup

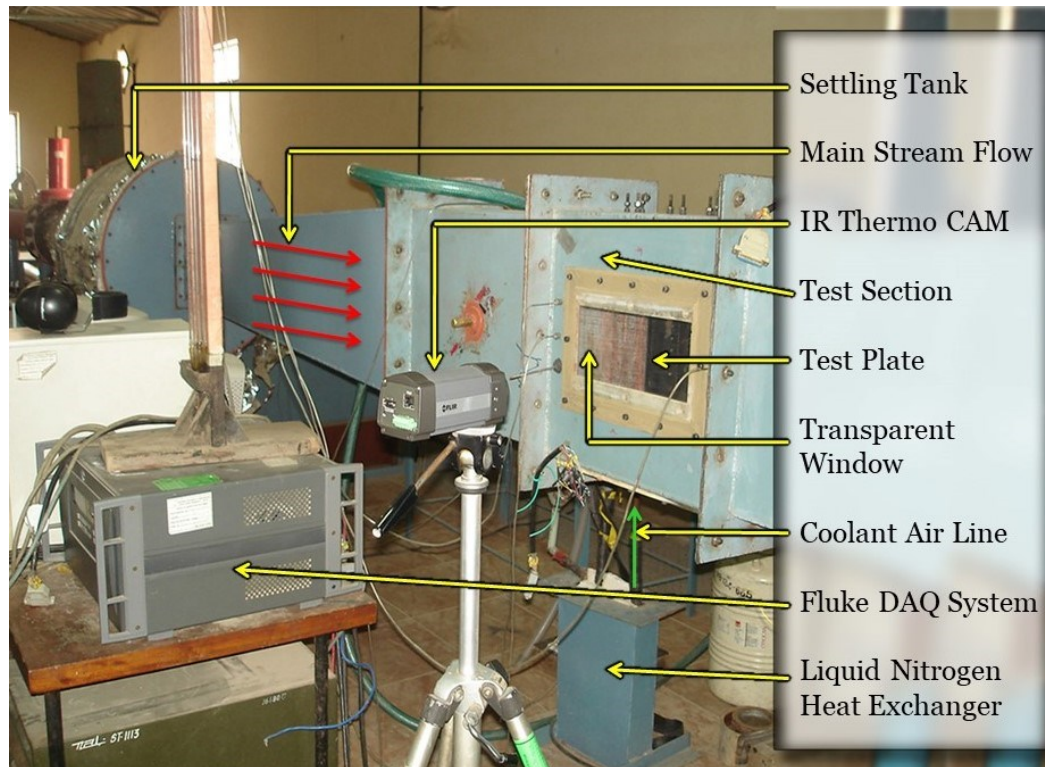


Fig. 3.1 Photograph of the film/effusion cooling test setup

The experimental activities are carried out at CSIR-National Aerospace Laboratories, Bangalore. The Film cooling test rig available at Heat Transfer Lab of Propulsion Division is used for this study. Fig. 3.1 shows the photograph of the film cooling test setup. Experiments are carried out in a 2-D blowdown tunnel. The mainstream air is drawn from the centralized compressed air reservoir. The tunnel consists of a flow control valve, heater, settling chamber and test section. Through the flow control valve, the flow is controlled in the mainstream tunnel. A 150 kW electrical heater with a PID (Proportional Integral Derivative) controller is used to heat the mainstream air. The settling chamber is provided with screens to reduce the turbulence level in the mainstream. The size of the rectangular test section is 395 mm x 175 mm. The test section is provided with two openings on the opposite sides, one for mounting the test plate with the coolant supply system and the other for fixing a transparent window for viewing the test plate. The transparent window is so selected that it allows the infrared radiation in the spectral band of the IR camera. A secondary flow line is

established for supplying the film cooling flow to the test plate which is also drawn air from the same reservoir from which the mainstream is drawn. This coolant flow is supplied through a regulator, mass flow meter and a liquid nitrogen heat exchanger to the coolant chamber. In the liquid nitrogen heat exchanger, air is passed through the copper coils which is surrounded by liquid nitrogen. According to the requirement of coolant temperature, the level of liquid nitrogen is varied in the heat exchanger. The test plate with the cooling hole arrangement is fixed to the coolant chamber which provides the cooling air for flowing through the machined ring and effusion holes. Fig. 3.2 shows the schematic layout of the film/effusion cooling test rig.

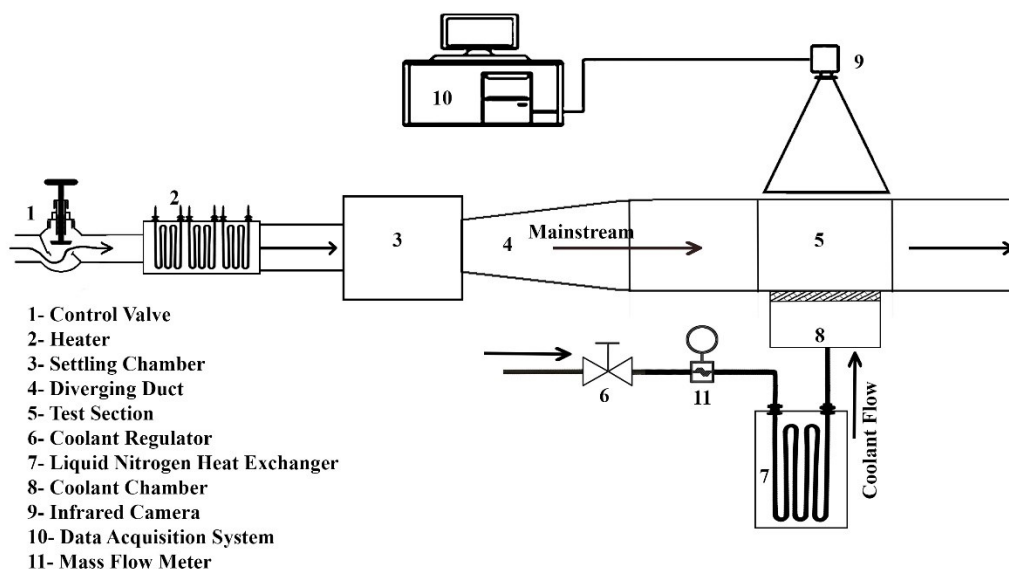


Fig. 3.2 Schematic layout of the film/effusion cooling test rig

Two static pressure taps at different locations are provided on the coolant chamber wall to measure the coolant static pressure. As the velocity of flow in the coolant chamber is small, the measured static pressure is taken as the total pressure of the coolant. Two thermocouples are inserted into the coolant chamber to measure the coolant temperature. Two pitot tubes for mainstream wall static pressure measurement and two thermocouples to measure the mainstream total temperature are located upstream of the test plate in the mainstream duct. At the same location, total pressure taps are provided for estimating flow velocity. Each static, total pressure tap and thermocouple are placed on the opposite sides of the mainstream duct wall, but at the same sectional plane. Always at two locations, measurements are taken, and the average

is used for further calculations. The velocity upstream of the test model is estimated from the measured total pressure of the pitot tube, the wall static pressure and the required flow velocity is set by controlling the inlet flow control valve.

3.2 Test Plate Details

3.2.1 Geometric Details of Machined Ring

A number of parameters influence the behavior of machined ring geometries. The main parameters among them are, the distance between the machined ring and effusion cooling geometry, machined ring geometry height, the hole arrangement, the hole diameter and the velocity of the jet through the machined ring holes. Fig. 3.3 shows the geometric details of the two machined ring arrangements. These geometries have similarities with the geometries of parallel inlet holes described by Yang et al. (2012). They studied one row, two rows with the aligned and staggered arrangement and three rows of film cooling holes. They varied the film hole diameter in the range of 2 mm to 7 mm, the pitch between holes as 5 mm to 10 mm and the distance between the rows as 5 mm for a double row, 2.5 mm for three rows. But in the present study, the following geometrical parameters are considered for the machined rings. Machined ring 1 (MR1) having one row of holes, consists of hole diameter(d) 2.5 mm and a pitch(x) of 10.8 mm. In machined ring 2 (MR2), where the holes are arranged in a staggered manner having the same hole diameter, with the same pitch as of MR1. But the two rows of holes are separated by a distance(y) of 2.5 mm. These machined ring geometries are prepared on the hylam material.

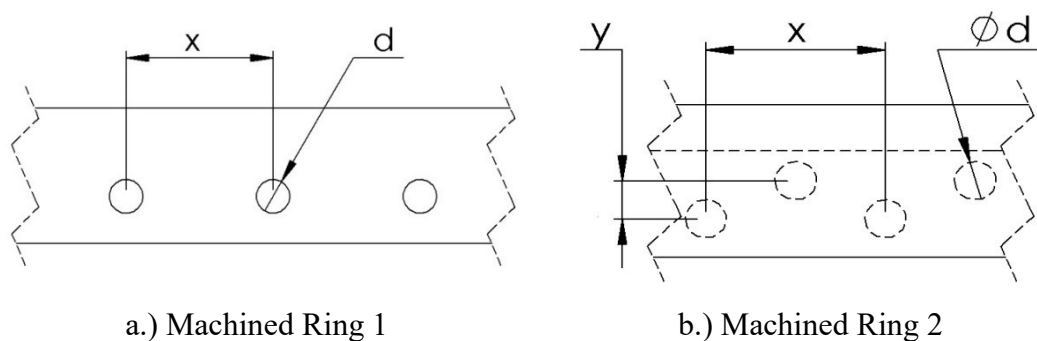


Fig. 3.3 Schematic of machined ring geometries

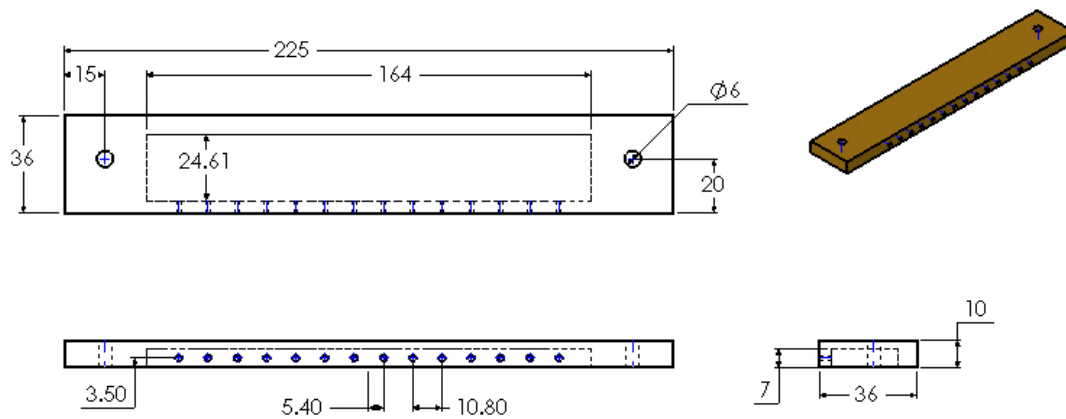


Fig. 3.4 Schematic of the machined ring with one row of holes

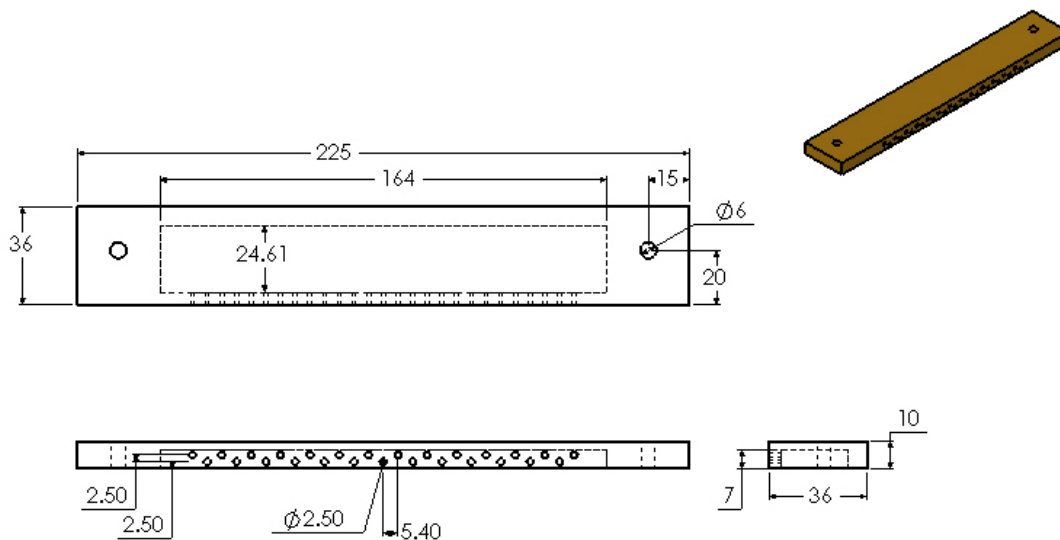


Fig. 3.5 Schematic of the machined ring with two rows of holes

Fig. 3.4 and Fig. 3.5 show the geometric details of the machined ring arrangements. For the measurements of adiabatic film cooling effectiveness and heat transfer coefficients with machined ring geometries, a test plate made out of hard polyurethane foam material is attached downstream of the machined ring geometries. The thickness(t) of the hard foam is 15 mm with a thermal conductivity of 0.02 W/mK. Thin stainless steel sheet of 0.2 mm thickness is fixed over the hard foam and adhered using adhesive Araldite. Before fixing the stainless steel sheet to the base substrate, fourteen thermocouples are fixed to the sheet, covering the plate length in the flow direction to measure the surface temperature for use as the reference temperature for evaluating background correction in infrared temperature measurement. As the thermocouples are fixed on the bottom side of the stainless steel sheet, markers are

provided on the top side to identify their locations when viewing the test plate through an infrared camera. The model is painted using high emissivity black paint to ensure uniform emissivity for the viewed surface. The test plate so fabricated is assembled onto the top flange (made out of hylam) of the plenum, through which the coolant flow is fed to the film cooling holes. In the top flange, provision is made to install the machined ring geometries. The schematic of the machined ring test plate assembly is shown in Fig. 3.6.

For heat transfer coefficient measurements, copper bus-bars are attached at the two ends of the stainless steel sheet through which electrical power is supplied to heat the sheet. Thus the test plate is prepared in such a way that both film cooling effectiveness and heat transfer coefficient can be acquired using the same model.

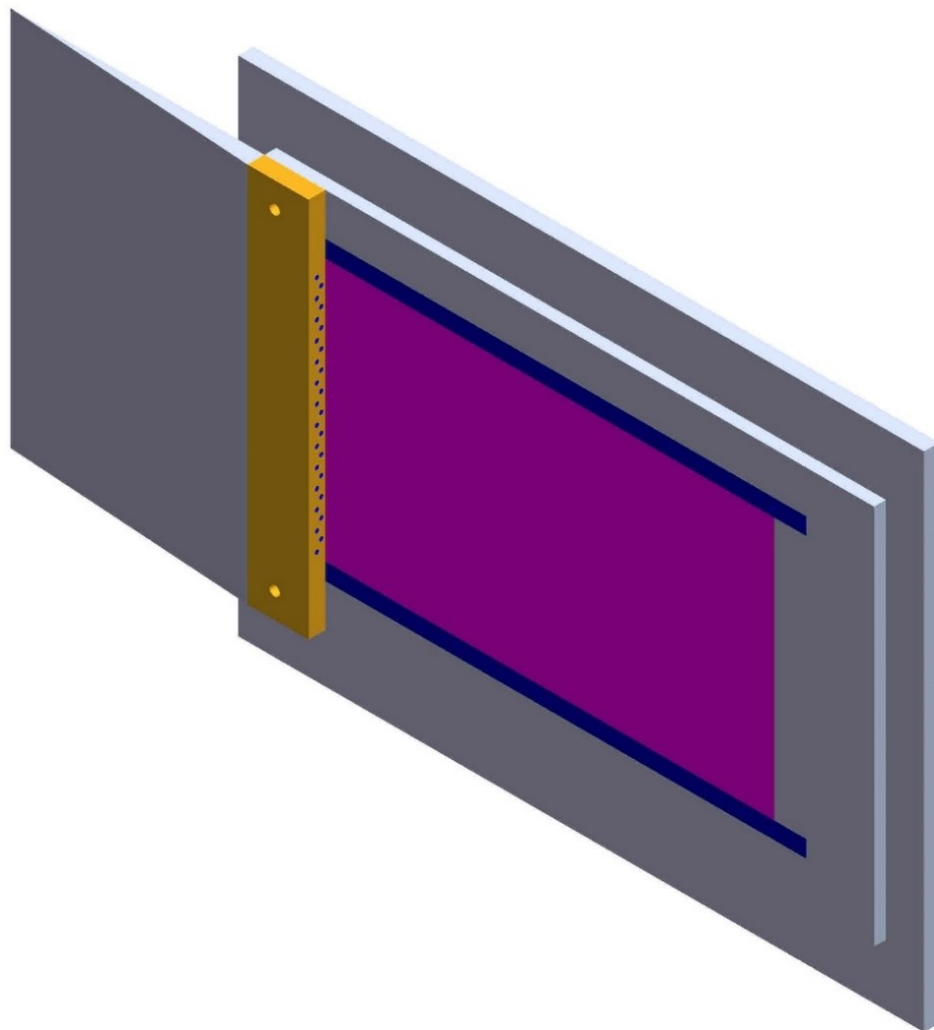


Fig. 3.6 Schematic of the machined ring test plate assembly

3.2.2 Geometric Details of Effusion Test Plate

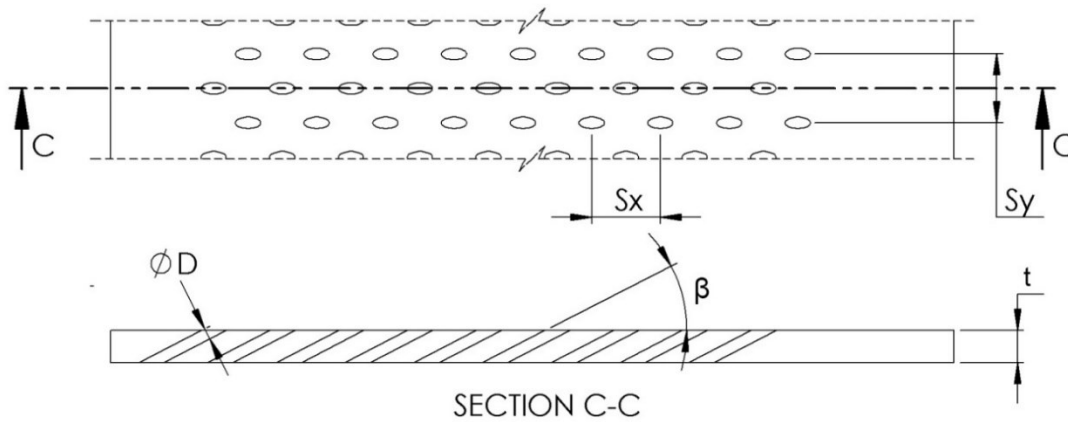


Fig. 3.7 Geometric details of the effusion test plate

For adiabatic film cooling effectiveness measurements, the test plate for the multirow effusion cooling was prepared in a low thermal conductivity substrate (hard polyurethane foam), and the holes are drilled in that. The geometric detail of the effusion test plate is shown in Fig. 3.7 and it is scaled up 3 times when compared to the original geometry that is used in the metal liner plates. The thickness (t) of the hard foam is 15 mm with a thermal conductivity of 0.02 W/mK. The effusion cooling holes are drilled at 27° hole angle (β), 3.0 mm hole diameter (D) with 9 holes in a row having a streamwise pitch (S_x) of $7.2D$. There are 13 rows of cooling holes with $7.2D$ spanwise spacing (S_y) between rows arranged in a staggered manner. The geometrical parameter of this effusion cooling holes is designed in such a way that it would not replicate the previously available literature survey and also it has to give the best cooling effectiveness in terms of performance. Gustafsson and Johansson (2001) tested three different hole angles of 15° , 20° and 30° and found that lower angles are giving better film cooling effectiveness. Similarly, Legar et al. (2003) made a study on 20° , 30° and 90° and their results show that the wall cooling effectiveness decreases with the increase in hole angle. In other research papers also, researchers used a hole angle of 30° for their studies. So, in comparison with the earlier researcher's results, it is decided to have hole angle of 27° in this present study for better performance.

For adiabatic cooling effectiveness tests generally scaled up models have been tested by researchers. Gustafsson and Gunnar Johansson (2001) used 5 mm diameter effusion holes, whereas Zhang et al. (2009) and used 5.7 mm diameter in their adiabatic

film cooling effectiveness studies. So, in this study, it is decided to have an effusion cooling hole diameter of 3 mm for the adiabatic model. To find out the overall cooling effectiveness metal liner plates are used. For metallic liner test plates, the same geometric parameters that are used in the real engine are considered for testing. Legar et al. (2003) studied the effect of hole diameter varied from 0.3 mm to 0.7 mm and found that the hole diameter increases cooling effectiveness also increases due to the increase in mass flow through the holes. Jingzhou et al. (2009) used 1 mm diameter effusion cooling holes in his studies. Generally, the hole diameter of 0.3 to 1.2 mm was suggested by the researchers. So, for overall cooling effectiveness study, effusion cooling hole diameter of 1 mm is selected and used in the stainless-steel metallic liner test plate.

The pitch between the holes is another important parameter while selecting/designing effusion hole arrangements. Gustafsson and Johansson (2001) varied the streamwise pitch to the diameter ratio (S_x/D) of 3, 6 and 12. Jingzhou et al. (2009) varied the streamwise pitch to the diameter ratio (S_x/D) of 1.5, 2 and 2.5 and spanwise pitch to the diameter ratio (S_y/D) of 3, 4 and 5. The results of both the papers show that the cooling effectiveness is higher for the closer holes. In the present study, the 7.2D pitch is used in both the streamwise and spanwise direction.

Thin stainless steel sheet of 0.2 mm thickness with the required effusion cooling hole geometry, machined by water jet cutting, is fixed over the hard foam and adhered using adhesive Araldite. Before fixing the stainless steel sheet to the base substrate, eight thermocouples are fixed to the sheet, covering the plate length in the flow direction to measure the surface temperature for use as the reference temperature for evaluating background correction in infrared temperature measurement. As the thermocouples are fixed on the bottom side of the stainless steel sheet, markers are provided on the top side to identify their locations when viewing the test plate through an infrared camera. The model is painted using high emissivity black paint to ensure uniform emissivity for the viewed surface. The test plate so fabricated is assembled onto the top flange (made out of hylam) of the plenum, through which the coolant flow is fed to the film cooling holes. In the top flange, provision is made to install the machined ring geometries upstream of the multirow hole arrangement. The schematic

of the effusion test plate assembly and effusion test plate with a machined ring assembly is shown in Fig. 3.8 and Fig. 3.9.

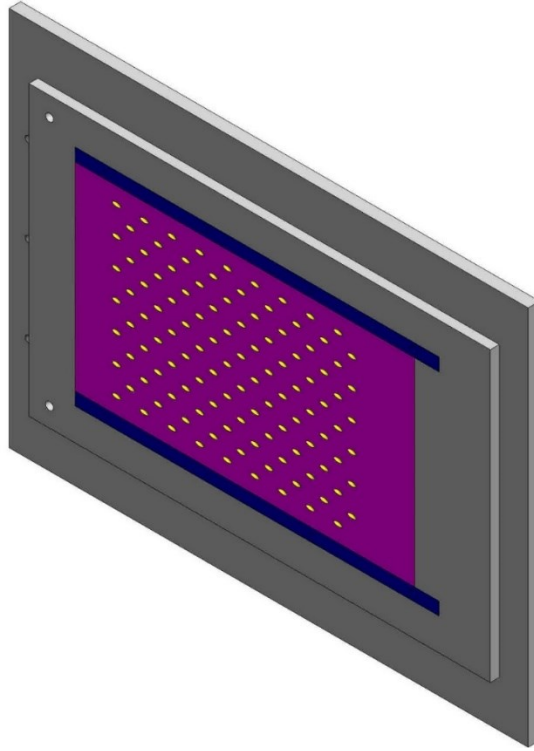


Fig. 3.8 Schematic of the effusion test plate assembly

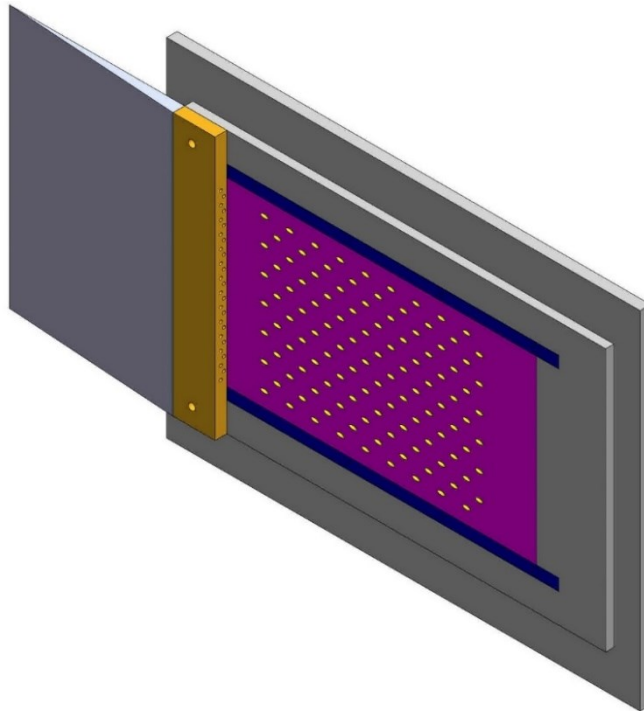


Fig. 3.9 Schematic of the effusion test plate with the machined ring assembly

For overall cooling effectiveness measurements, this same effusion cooling geometry is retained but scaled down by 3 times. This test plate is prepared in stainless steel and having a thickness of 2 mm. Angled holes of 1 mm diameter with an inclination angle of 27° are drilled through the test plate by electric discharge machining (EDM) process. Effusion holes are placed in a staggered manner with 9 holes per row, and there are 13 rows in total. The number of holes are 117. The streamwise and spanwise pitch distance is $7.2D$. The geometry has a hole density of 28.54 holes/in^2 . Fig. 3.10 shows the geometrical details of the test plate. Photograph of the test plate for overall cooling effectiveness measurements is shown in Fig. 3.11. Apart from this, another test plate is fabricated with the same geometrical parameters of the effusion holes except the hole pitch. For the second plate hole pitch of $5.4D$ is chosen which is less than the first geometry. This analysis will give the effect of hole pitch on effusion cooling geometry.

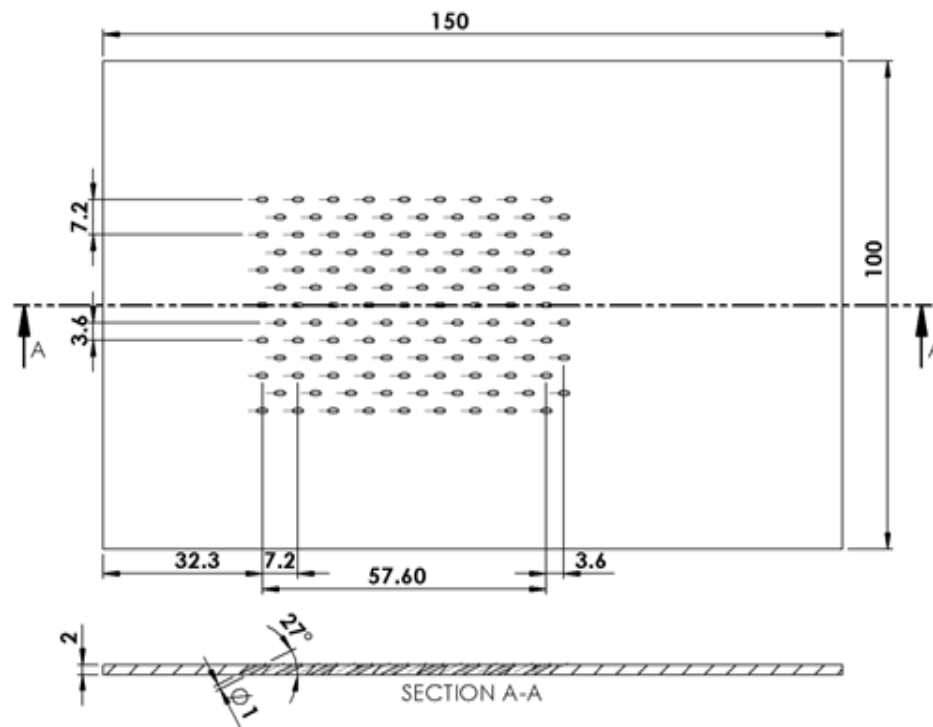


Fig. 3.10 Geometrical details of the test plate for overall cooling effectiveness

The stainless-steel test plate contains three regions namely the upstream region before the start of cooling holes, the multi-holed region, and the region downstream of the cooling holes. In the upstream region, heat transfer takes place by conduction

through the plate, convection on both sides of the plate and also by radiation on both sides of the plate. In the multi-holed region, the heat transfer occurs by radiation, convection, conduction through holes, and by the film cooling effect. After the multi-holed region, the film cooling effect is developed and achieved in the downstream region. In the actual liner, radiation effects are considered on both sides of the liner. However, in our experiments, the effect due to radiation is minimum and are neglected.

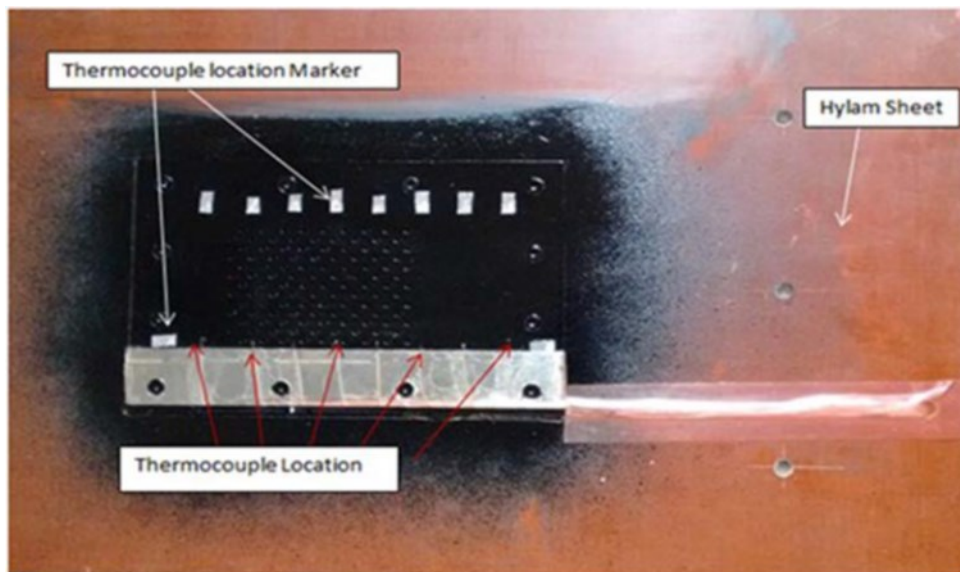


Fig. 3.11 Photograph of the test plate for overall cooling effectiveness

The schematic of the mainstream and the coolant flow through the effusion, and machined ring geometry holes are shown in Fig. 3.12. The effusion cooling geometry is positioned at a distance of 32 mm from the machined ring exit. Both the machined rings have a wedge shape arrangement at the inlet with gradual taper up to the machined ring height, in order to ensure a smooth mainstream flow over the machined ring geometries in the streamwise direction of the flow. The machined ring communicates with the coolant chamber through the slot provided in the top flange. For the tests with effusion holes alone, the machined ring geometry was removed, and the coolant flow slot area for the machined ring was blocked. Test plate length along the streamwise direction is shown in terms of X/D . The test plate starts at $X/D=0$ and ends at $X/D=80$. Similarly, the effusion cooling holes are starting at $X/D=10.6$ and ends at $X/D=70$.

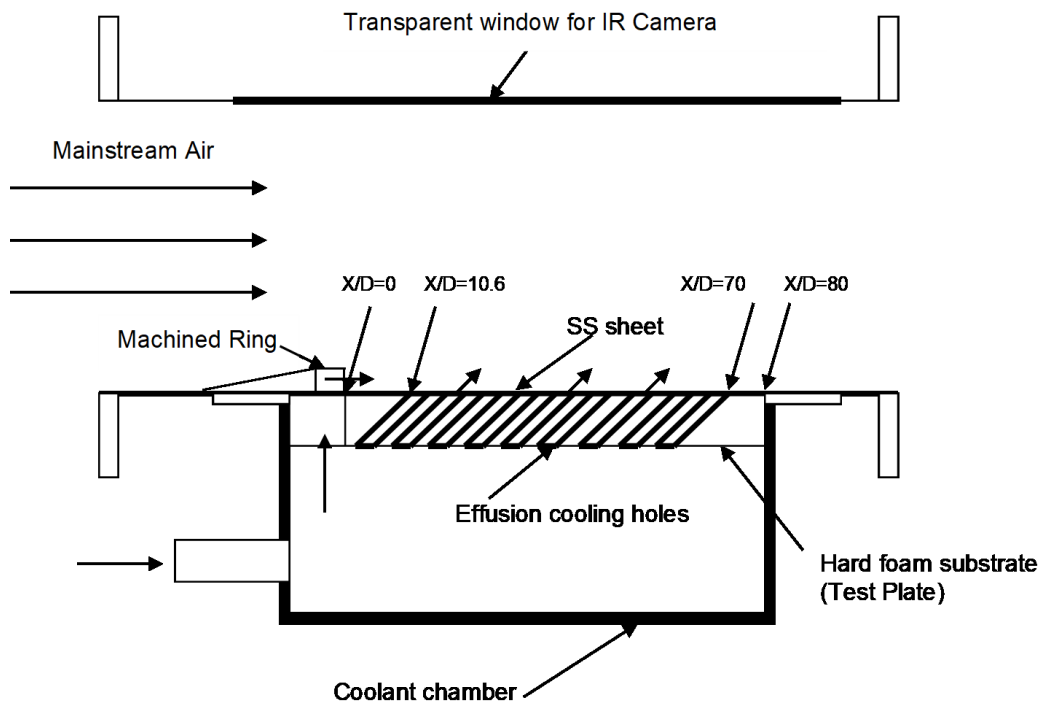


Fig. 3.12 Schematic of effusion cooling with machined ring cooling flow along with the mainstream flow

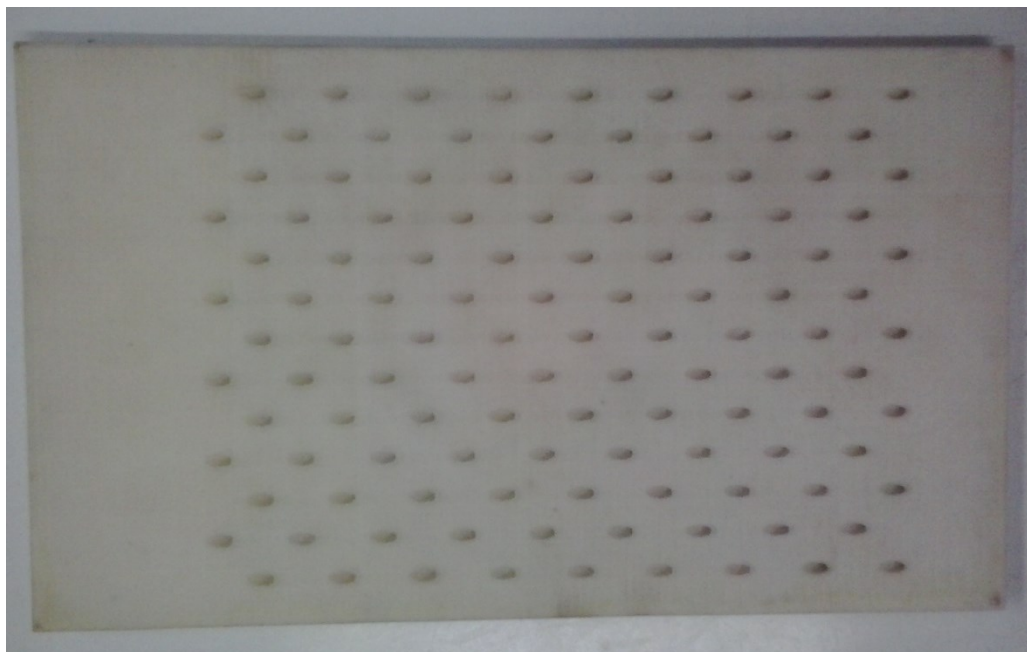


Fig. 3.13 Photograph of the fabricated adiabatic effusion test plate

Fabricated models of adiabatic effusion test plate and machined ring geometries are shown in Fig. 3.13 to Fig. 3.15.



Fig. 3.14 Photograph of fabricated machined Ring 1 with one row of holes



Fig. 3.15 Photograph of fabricated machined Ring 2 with two rows of holes

3.3 Instrumentation Systems

3.3.1 Thermocouples

Mainstream and coolant air temperature measurements are carried out by using Omega make K-type thermocouples which are connected to a Fluke temperature data acquisition system. Four thermocouples are used to measure the fluid temperatures: two for mainstream air and other two for coolant air temperature measurements. Apart from these, eight thermocouples are fixed in the test plate to measure the surface temperature for use as the reference temperature for evaluating background correction in infrared temperature measurement. These thermocouples are calibrated with reference to a standard calibrated thermocouple and the measurements taken by these thermocouples are having an accuracy of $\pm 1^{\circ}\text{C}$.

3.3.1.1 Thermocouple Calibration

In order to achieve accurate readings from a thermocouple, it is essential to calibrate each and every thermocouple used in the experiments. A thermal bath, which gives control and stable constant temperature, is used for the calibration purpose. It gives uniform temperature and covers a large enough area so that a standard reference thermocouple can adequately be inserted into it. A measuring instrument, such as Fluke calibrator is used to measure reference thermocouple output. Initially, the thermal bath is set to a particular temperature and one junction of the thermocouple, which is to be calibrated, is then placed into the thermal bath. The other junction is connected to the

Fluke, and the temperature readings of this thermocouple and the standard reference thermocouple are recorded. By increasing the temperature at different increments based on our temperature range, i.e., between the upper and lower limits, this process is repeated. The error between this thermocouple and the standard reference thermocouple is calculated for all the measurements.

3.3.2 Infrared Camera

Test plate surface temperature measurement is taken by FLIR SC 325 infrared camera having a resolution of 320 x 240 pixels and an accuracy of $\pm 1.5^{\circ}\text{C}$. IR camera is having a manufacturer's calibration curve, which converts the raw radiation value to temperature. However, the manufacturer's calibration was made against a black body. In our experiments, the test plate image is a grey body because it depends upon various factors like radiation emitted from the test surface, radiation reflected from the tunnel walls, the transmissivity of the window material, the radiation reflected from the window material and the background atmospheric radiation. Therefore, a separate calibration was made according to our temperature range.

3.3.2.1 Infrared Camera Calibration

Infrared camera calibration is carried out based on the procedure explained by Martiny et al. (1996). The test plate is heated from room temperature to 80°C with an interval of 2°C . For each interval, the IR image raw count value and the thermocouple value in Celsius are recorded. From each image, the location of the thermocouple is identified by the marker, and that particular raw count values are taken and plotted against the thermocouple values for the series of points. Similarly, the test plate was cooled to a lower temperature below atmosphere up to -20°C at an interval of 2°C . The temperature against raw count calibration from -20°C to 80°C and the raw count against temperature calibration are shown in Fig. 3.16 and Fig. 3.17 respectively. Thus, the IR camera is calibrated in the required temperature range, and the calibration equations are generated from the plots. In our experimental study, the IR image is captured in raw radiation values and then converted into temperature values using these calibration equations.

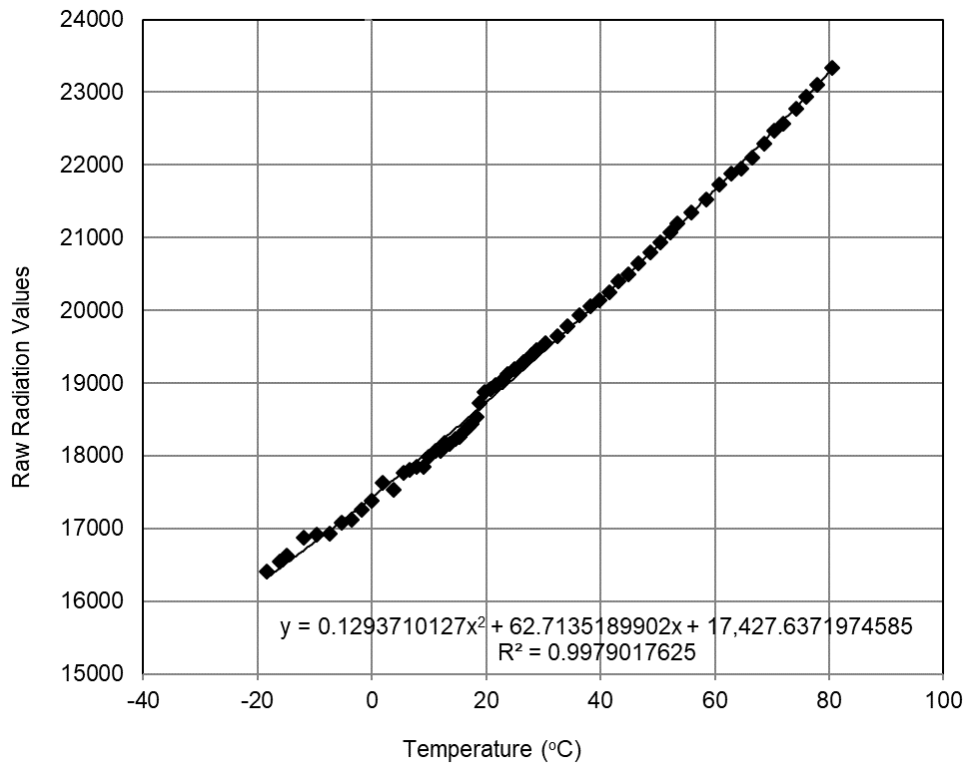


Fig. 3.16 Variation of raw radiation values with respect to temperature

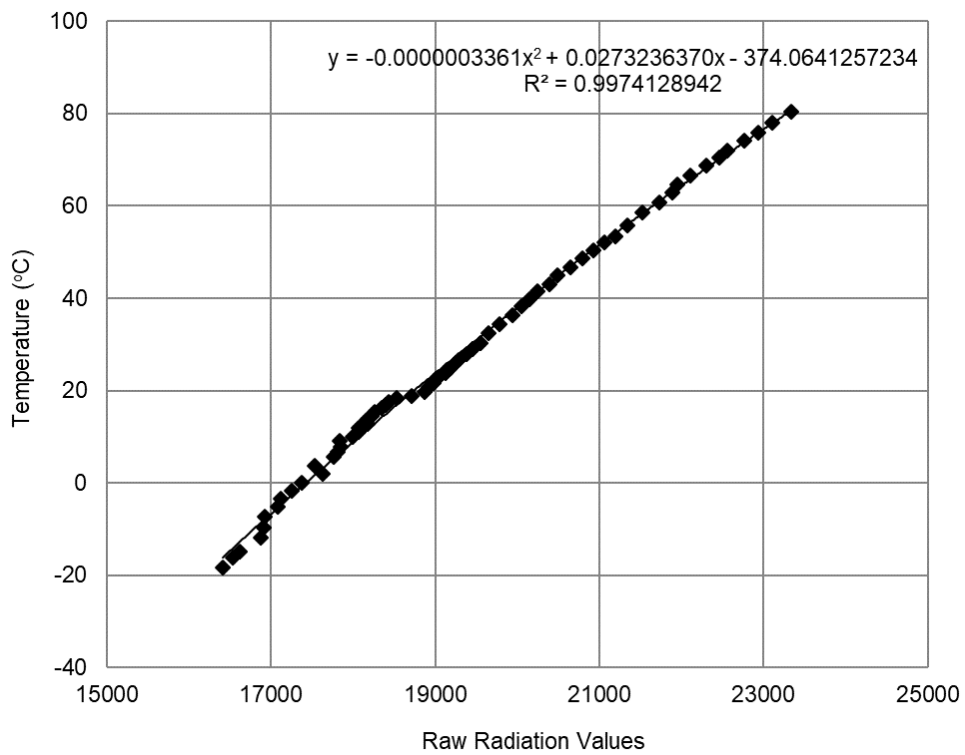


Fig. 3.17 Variation of temperature with respect to raw radiation values

In the present study, during tests, the background radiation varies from day to day due to the atmospheric temperature variation. An in-situ calibration was carried out for each and every acquired data to solve this problem, during the tests. The image acquired by the camera is in raw radiation values. The thermocouple data in Celsius is converted into raw radiation value using the equation mentioned in Fig. 3.16. From the image, the thermocouple locations are identified, and the raw radiation values for each thermocouple is extracted. The difference between the image raw radiation value and the thermocouple converted radiation value is estimated and called as a correction factor for the particular day background radiation. This correction factor is added to all the pixel values in the image. Thus the correction factor applied image is converted to temperature using the equation mentioned in Fig. 3.17 and this temperature is used to calculate the adiabatic film cooling effectiveness and heat transfer coefficients.

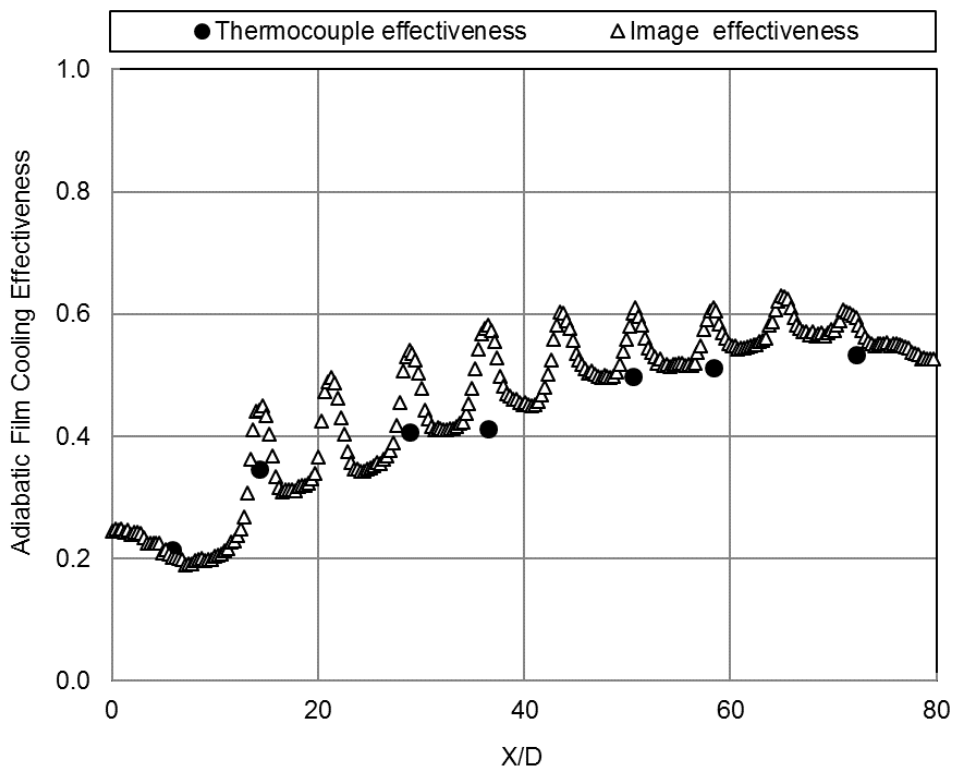


Fig. 3.18 Comparison of thermocouple effectiveness and image effectiveness values

In order to ensure the camera calibration procedure is correct, the result of adiabatic film cooling effectiveness for effusion cooled test plate at blowing ratio of 2.5 test run is plotted in Fig. 3.18. This plot shows the effectiveness result which is

calculated from the thermocouple temperature values and also from the thermographic image values. From this plot, the results show that the thermocouple temperature effectiveness values and the thermographic image effectiveness values are matching. So the in-situ calibration of the thermographic image with reference to the thermocouple is satisfied.

3.3.3 Pressure Net Scanner

Total and static pitot tubes are fixed in the coolant chamber and in the mainstream duct to measure the coolant chamber pressure and the mainstream total and static pressures. These pressures are measured by a pressure net scanner (Model 9116 Pneumatic Intelligent Pressure Scanner).

The mainstream mass flux ($\rho_m U_{ms}$) was calculated from the mainstream velocity and the mainstream density. The mainstream density is calculated based on the static pressure and total temperature measured in the test section.

$$U_{ms}^2 = 2 * \left(\frac{P_t - P_s}{\rho_{ms}} \right) \quad (3.1)$$

The mainstream density (ρ_m) is estimated from the mainstream temperature and the mainstream pressure.

The average coolant jet velocity through all the holes (U_c) is estimated from the coolant chamber/plenum total pressure, the test section/mainstream static pressure and the coolant density (ρ_c). The coolant density (ρ_c) is estimated from the coolant temperature and the coolant chamber pressure.

$$U_c^2 = 2 * \left(\frac{P_{cc} - P_s}{\rho_c} \right) \quad (3.2)$$

3.3.4 Orifice Plate

An orifice plate is used in the coolant line to estimate the coolant mass flow rate through the film cooling holes. The orifice hole diameter of 20.13 mm is used, and the upstream, downstream static pressure ports to the orifice plate are made at D_p , $D_p/2$ locations respectively as per the BIS standards. The mass flow is calculated based on

the equations given in the BIS standard. Orifice upstream and downstream pressures are also measured by the pressure net scanner. The mass flow measurements and the coefficient of discharge through the machined ring holes and effusion cooling holes are given in Appendix-I.

3.4 Experimental Procedure

3.4.1 Adiabatic Film Cooling Effectiveness Measurement

The cooling effectiveness measurements are carried out with hot mainstream and the coolant at a lower temperature. For adiabatic film cooling effectiveness measurement, the mainstream air at an atmospheric temperature of 30°C is allowed to pass over the test section at the required flow velocity of 20 m/s. Generally, at the combustor primary and secondary zones, the hot gas mainstream velocities are less. So in this study, the mainstream air velocity of 20 m/s is set by measuring the static and total pressures in the mainstream duct. The flow velocity is estimated from the total and static pressure measurements in the mainstream duct. The Reynolds number at this velocity and based on the hydraulic diameter of the duct is 3×10^5 . The secondary air is set to the required pressure based on the blowing ratio in the coolant plenum through a pressure regulator and cooled to -42°C while passing through the liquid nitrogen heat exchanger. The blowing ratio considered in this study is the global blowing ratio through the effusion cooling holes in the test plate. The coolant total pressure inside the coolant chamber is kept constant both in the streamwise and spanwise direction of the cooling holes. The temperature of the film cooling air is measured inside the plenum at two locations. Once both the air streams are set to the required blowing ratio, the following things are recorded. Test model surface temperature measurement was taken by FLIR SC 325 infrared camera with in-situ calibration with respect to the thermocouples fixed on the test plate. Mainstream and coolant air temperature measurement are recorded by Omega make K-Type thermocouples which are connected to a Fluke temperature data acquisition system. The static and total pressure measurements of mainstream and the coolant pressure by the pressure net scanner and finally the coolant mass flow measurement was estimated by orifice plate pressure taps readings. This procedure is repeated for the other blowing ratios.

3.4.2 Convective Heat Transfer Coefficient Measurement

For convective heat transfer coefficient measurements, constant heat flux at the surface can be provided with a thin stainless steel foil. Thin metal foils are more suitable due to the uniform resistance of the membrane, which is important in providing constant heat flux. Otherwise, power distribution is difficult to calculate. The constant heat flux boundary condition is generated by heating the stainless steel sheet attached over the surface by low voltage high current AC power. The high current low voltage AC electrical power is supplied to the stainless steel sheet fixed onto the model through an autotransformer and a step-down transformer with the step-down ratio of 230:4. A current transformer located on one of the input leads to the model is used for current measuring. The current transformer has a step-down ratio of 1000:1. The current transformer output, being current, is passed through a standard 9.4 Ohm resistor and the voltage drop is measured by the data logger. The heat supplied is estimated from the relation:

$$Q_e = \frac{V * I}{W * L} \quad (3.3)$$

Where W is the width of the sheet, L is the length over which voltage drop V is measured, and I is the current supplied. A relation between V and I is obtained by measuring the voltage drop over length L as a function of current:

$$V = c * I \quad (3.4)$$

Fig. 3.19 shows a typical V versus I curve for the thin stainless steel sheet which was used for the machined ring geometries. This sheet doesn't have the effusion holes. Fig. 3.20 shows typical V versus I curve for the thin stainless steel sheet which was used for the effusion cooling. In this thin stainless steel foil, effusion-cooling holes are made using water jet cutting.

Hence, the heat supplied can be estimated from the relation:

$$Q_e = \frac{c * I * I}{W * L} \quad (3.5)$$

Because of the finite thermal conductivity of the substrate, part of the power supplied is transferred to the substrate. To estimate this conduction loss, the model outer surface is covered with thermal wool of low thermal conductivity to eliminate all losses from the exposed surface of the model. Power is supplied to the model, and the model temperature is recorded after attaining steady condition. This is a measure of the conduction loss for the measured surface temperature. As the model inner surface is at room temperature, the difference between the model temperature and room temperature was used to characterize the heat loss Q_L .

Fig. 3.21 and Fig. 3.22 shows typical heat loss power variation with the difference in test plate and room temperature for the substrate used on machined ring geometries and effusion cooling respectively. As the heat loss through radiation was small and negligible, the net power supplied is estimated from the relation:

$$C_1 = Q_{net} = Q_e - Q_L \quad (3.6)$$

The heat transfer coefficient is calculated from the relation:

$$h_f = \frac{C_1}{T_{aw} - T_m} \quad (3.7)$$

where T_{aw} is the local wall temperature estimated from thermogram and T_m is the measured mainstream temperature.

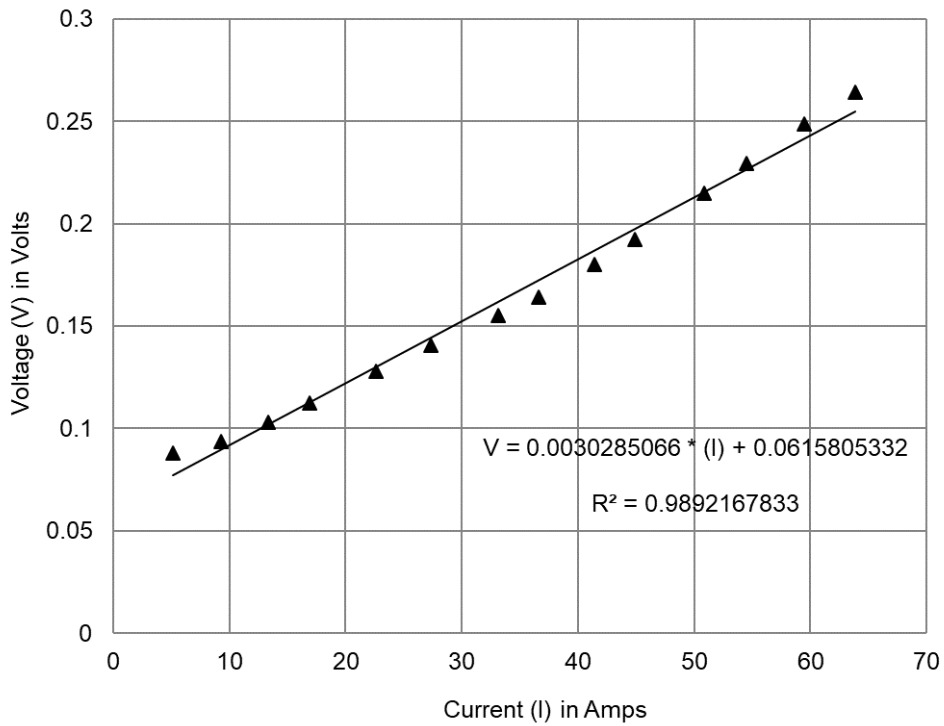


Fig. 3.19 Variation of voltage with respect to the current supplied for thin stainless steel sheet for machined ring geometries

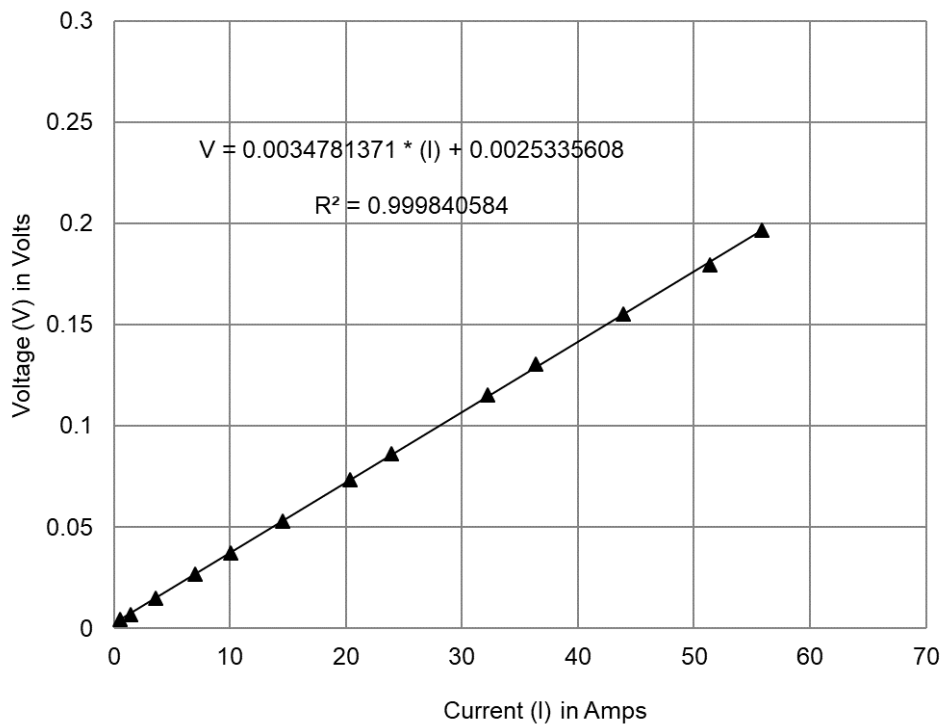


Fig. 3.20 Variation of voltage with respect to the current supplied for thin stainless steel sheet with effusion cooling holes

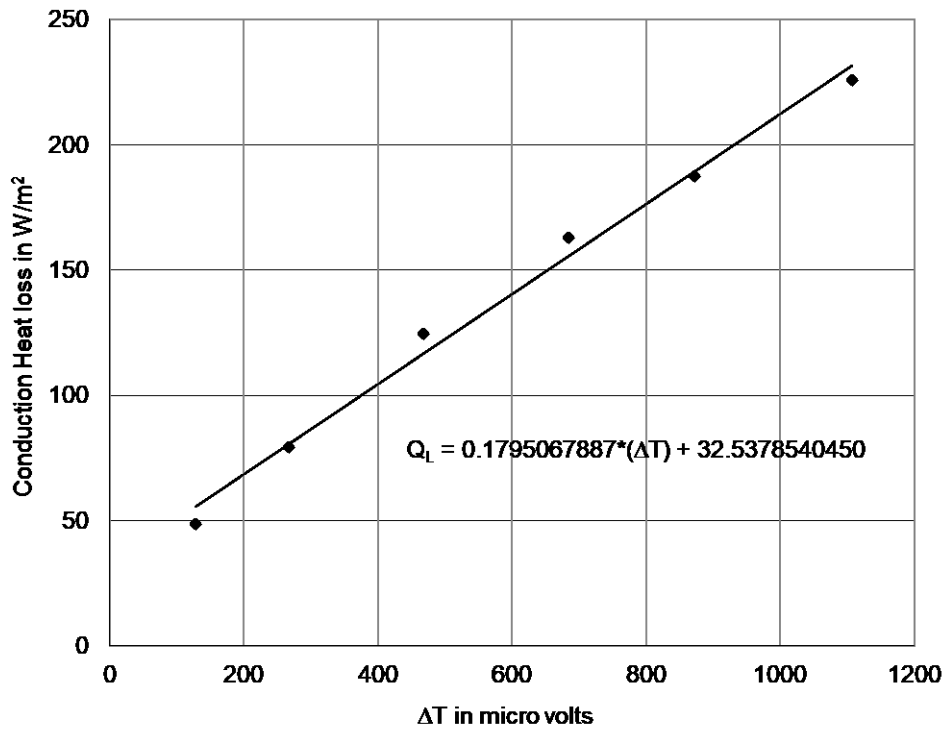


Fig. 3.21 Conduction heat loss with respect to the temperature difference across the substrate used for machined ring geometry

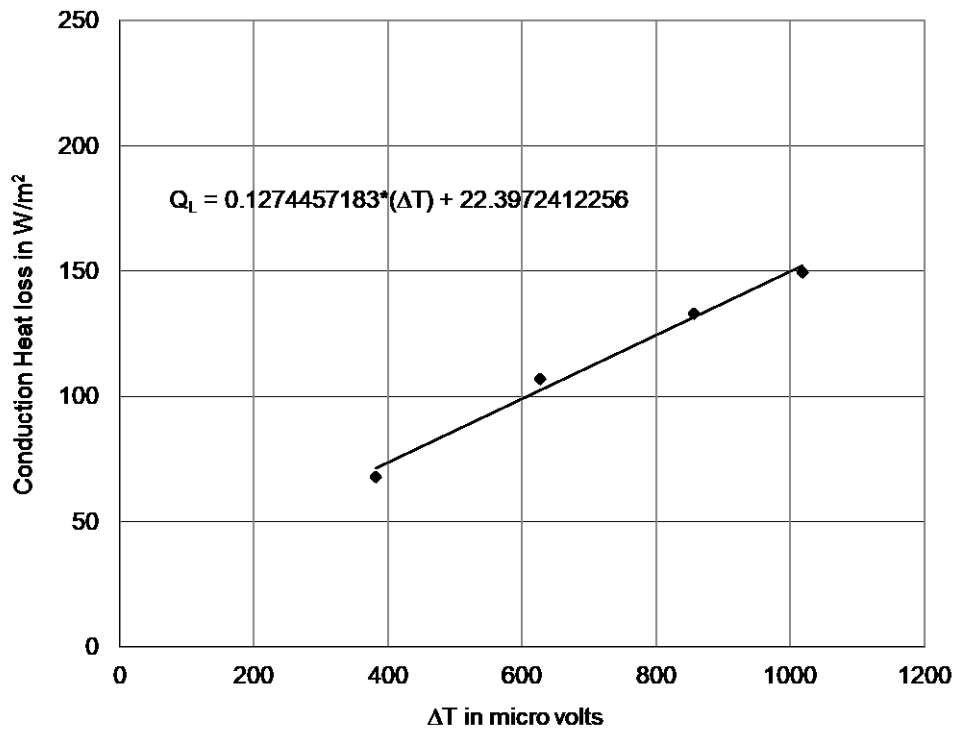


Fig. 3.22 Conduction heat loss with respect to the temperature difference across the substrate used for effusion cooling holes

For the heat transfer coefficient measurements, the mainstream and the coolant air is set at the same temperature. The required blowing ratio is set, and subsequently, the electrical power was supplied to the stainless steel sheet. The surface temperatures were monitored in a data logger. The power was adjusted in such a way that the maximum temperature measured did not exceed air temperature by more than 25° C. Sufficient time was allowed to reach steady condition. The temperatures and the current supplied to the sheet were recorded in the data logger over a period of 30 seconds, and the average value was taken for calculation of heat transfer coefficient. At the same time, two thermal images were recorded by using the IR camera. The pressure readings were noted down. The local heat transfer coefficient was calculated by dividing the net heat flux supplied to the stainless steel sheet to the difference between the measured wall and free stream temperature.

3.5 Error Estimate

The error estimate/uncertainty is calculated based on the procedure explained by Holman (1994). The mainstream and the coolant temperatures are measured with an accuracy of $\pm 1^\circ\text{C}$ by K-type thermocouples. The test plate temperature is estimated from the FLIR infrared thermographic system output with an accuracy of $\pm 1.5^\circ\text{C}$. With the above temperature measurement accuracy, the uncertainty in the cooling effectiveness is calculated at the mainstream temperature of 30°C and coolant temperature of -42°C for two levels of cooling effectiveness 0.6 and 0.3. The error in the estimated cooling effectiveness amounts to $\pm 3.85\%$ at $\eta = 0.6$ and $\pm 7.79\%$ at $\eta = 0.3$. Pictorial representation of error band of adiabatic film cooling effectiveness for effusion cooling holes at a blowing ratio 2.0 is shown in Fig. 3.23. The long dash lines show the upper and lower limit of the error band and the continuous line is the actual cooling effectiveness. The repeatability of data is also verified by two different test runs for the same conditions, and the results show that the cooling effectiveness is identical for both the test runs.

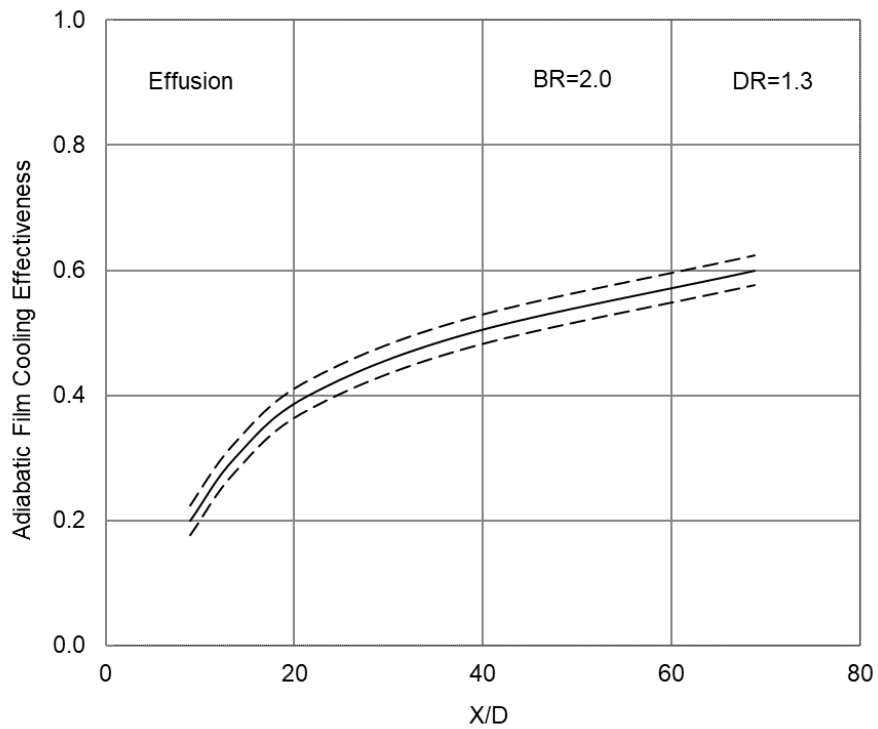


Fig. 3.23 Pictorial representation of error band for adiabatic film cooling effectiveness of effusion cooling holes

Pressure net scanner is having an accuracy of $\pm 0.05\%$ of measured pressure. An uncertainty analysis performed based on the pressure and temperature readings indicates that the uncertainty in the calculated blowing ratio is $\pm 0.4\%$ for BR=2.5 and $\pm 1.9\%$ for BR=0.5. Error in the heat transfer coefficient is estimated for two values of lower and higher heat transfer coefficients. The uncertainty is $\pm 11.48\%$ for $87 \text{ W/m}^2\text{K}$ and $\pm 8.74\%$ for $120 \text{ W/m}^2\text{K}$. Detailed uncertainty calculation and procedure for the parameters are attached in Appendix-II.

CHAPTER 4

COMPUTATIONAL METHODOLOGY

4 COMPUTATIONAL METHODOLOGY

4.1 Modeling

The numerical analysis is done using ANSYS workbench. The test plate is modeled in solid works design software, and the domain is created using the design modeler of ANSYS. It consists of the solid plate, flow domain inside the holes and the mainstream domain above the plate. For adiabatic cooling effectiveness and convective heat transfer coefficient measurements, computations are performed only to find out the effect of convection heat transfer on the top plate surface. The conduction heat transfer within the solid plate is not considered, and hence solid plate is subtracted from the computation domain using 'Boolean' operation.

The mainstream domain has the dimensions of 901mm×180mm×350mm. These dimensions are taken from the actual test section dimensions used in the experiments. For adiabatic cooling effectiveness and convective heat transfer coefficient measurements, the presence of coolant chamber domain does not make any difference in the final results. Hence to simplify CFD analysis coolant flow injection was directly given into the test plate cooling holes.

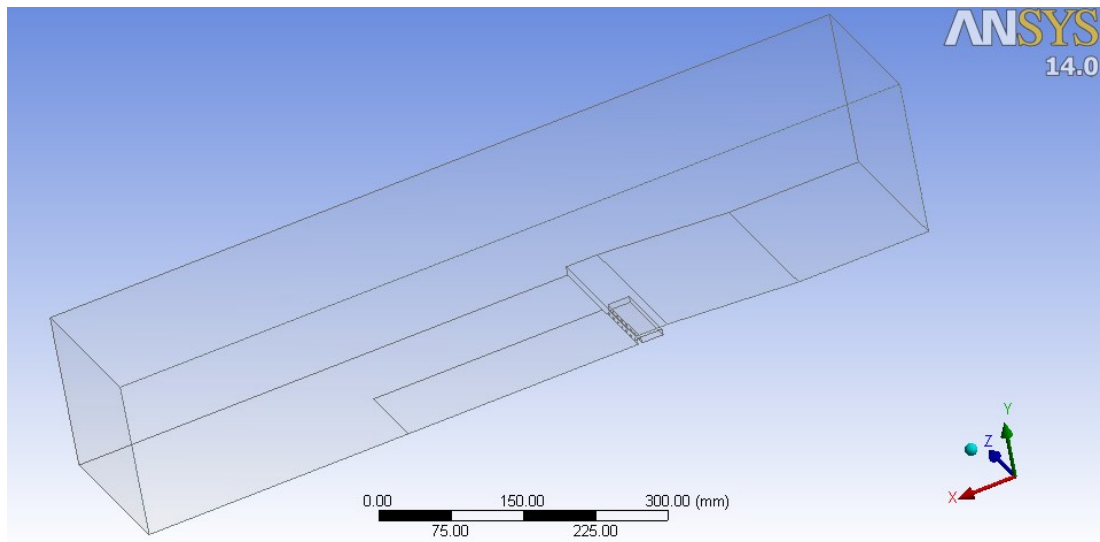


Fig. 4.1 Modeling of machined ring 1

The cut section of the domain along with the test geometry for the adiabatic models of machined ring 1, machined ring 2, effusion cooling, effusion with machined ring 1 and effusion with machined ring 2 are shown in Fig. 4.1 to Fig. 4.5.

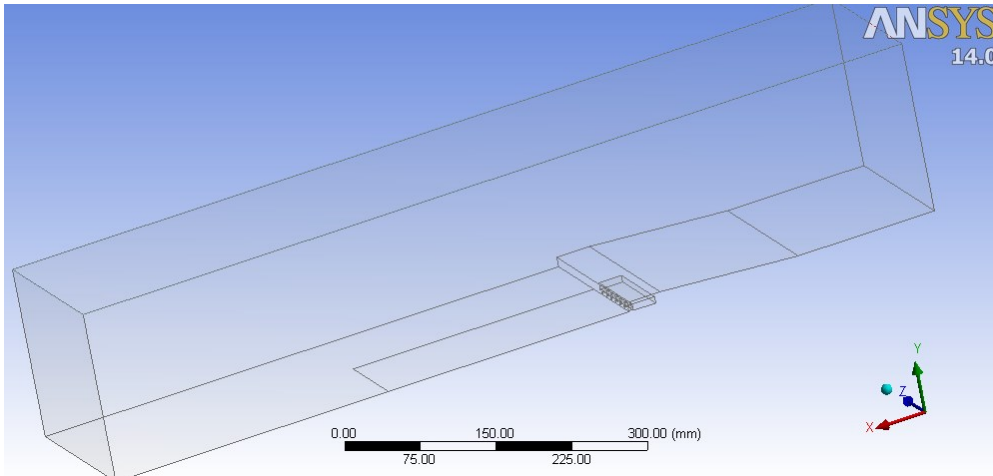


Fig. 4.2 Modeling of machined ring 2

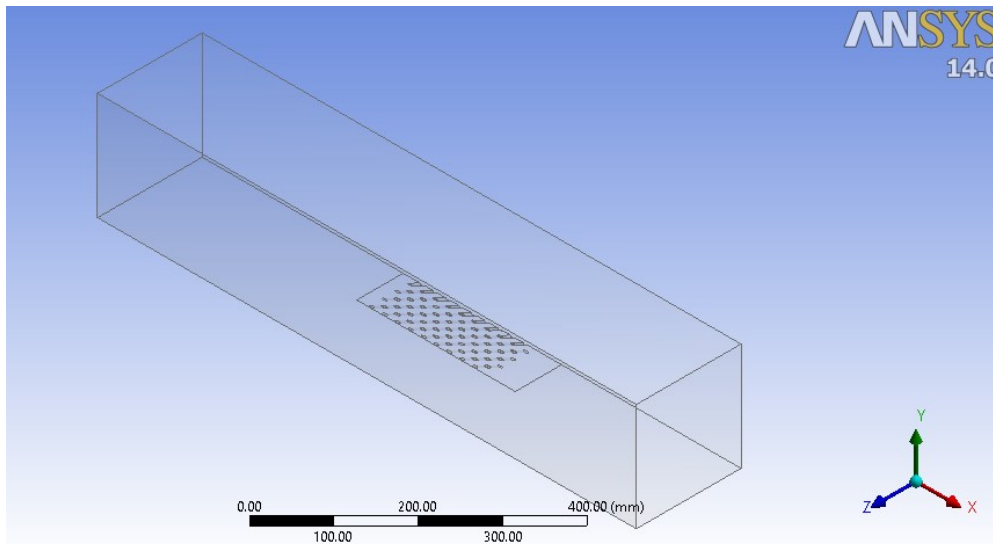


Fig. 4.3 Modeling of effusion cooling holes

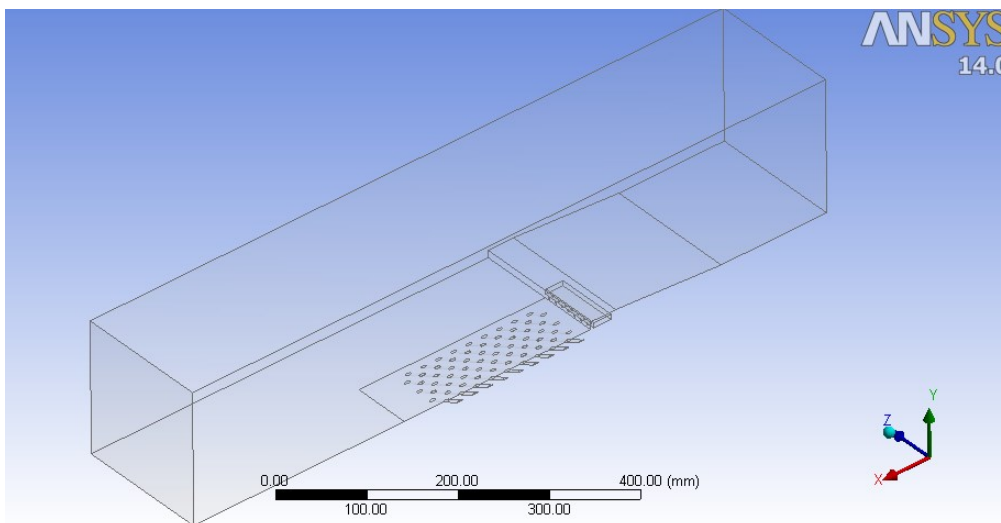


Fig. 4.4 Modeling of effusion holes with machined ring 1

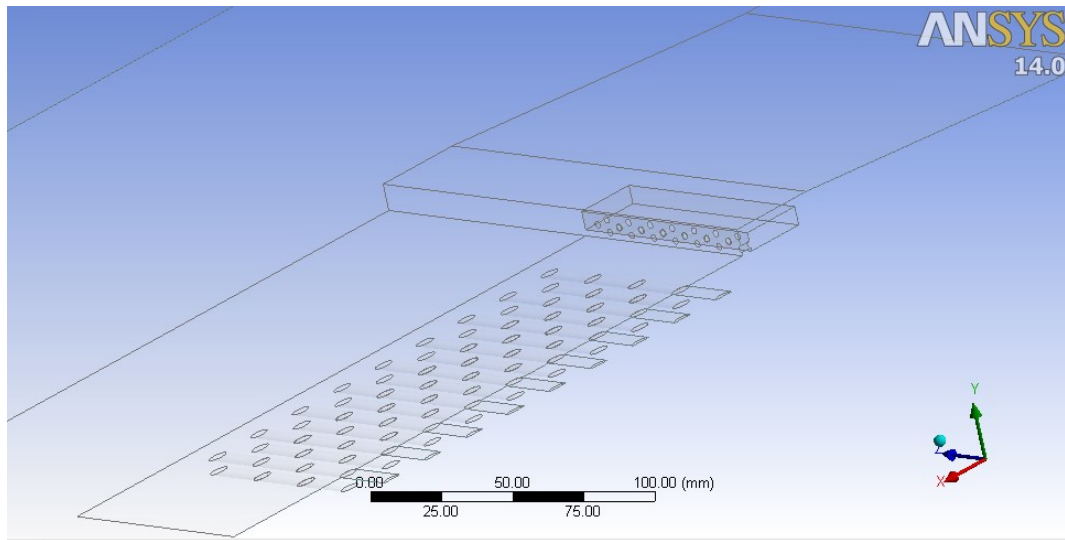


Fig. 4.5 Modeling of effusion holes with machined ring 2

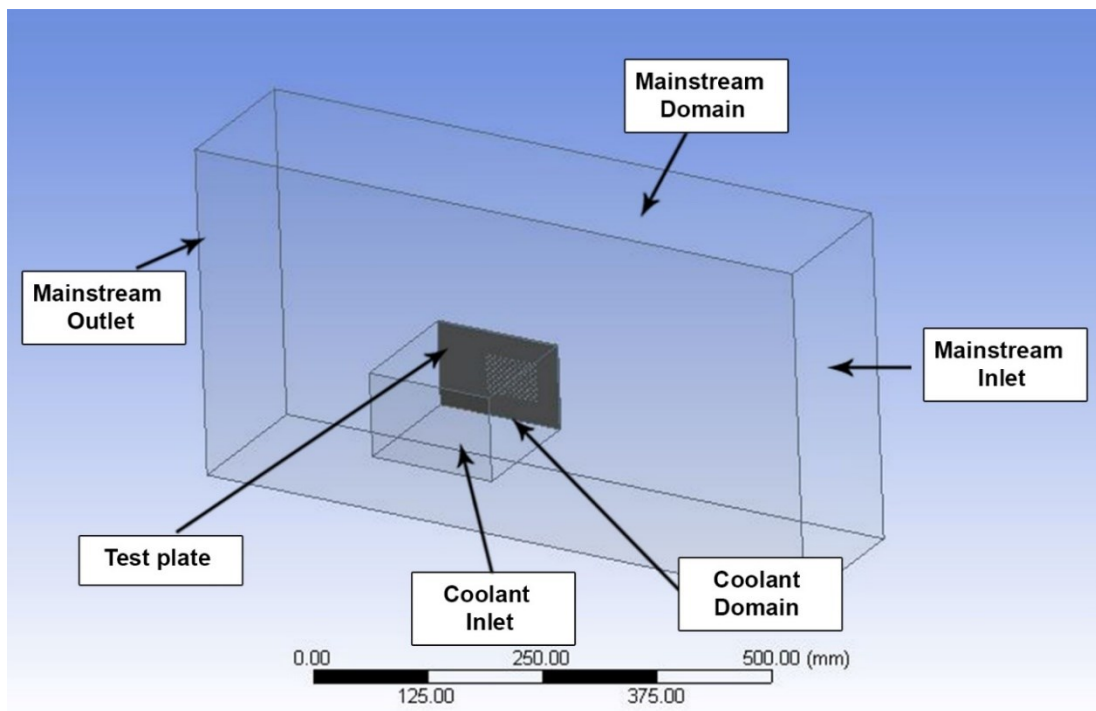


Fig. 4.6 Computational domain for conjugate analysis of effusion cooling with boundary conditions

The conjugate analysis is carried out to find out the overall cooling effectiveness measurements on the effusion test plate. For this conjugate analysis, the mainstream domain has dimensions of 750 mm * 175 mm * 390 mm. In order to capture the convective heat transfer at the coolant entry side to the test plate, coolant chamber is provided at the back of the test plate which is having the dimensions of 150 mm * 150

mm * 100 mm. Conduction within the effusion test plate thickness is considered. Computation domain for conjugate analysis of effusion cooling along with the boundary conditions is shown in Fig. 4.6.

4.2 Mesh Generation

The whole domain is then meshed using ANSYS workbench meshing tool to generate an unstructured mesh of relevance zero. Fine meshing is made in the hole regions in such a way that each coolant holes are having at least 5 layers of meshing. In order to get the accurate resolution of the coolant and mainstream flow mixing near the test plate wall, local refinement in terms of inflation layers are created. Final average orthogonal quality of mesh is 0.80, and the average skewness is 0.3. The meshing of the adiabatic models is shown in Fig. 4.7 to Fig. 4.9.

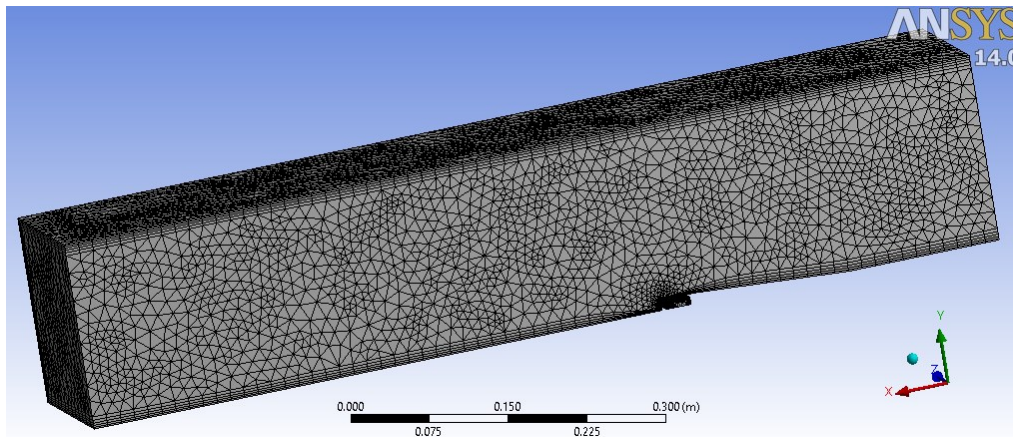


Fig. 4.7 Meshing details for machined ring 1

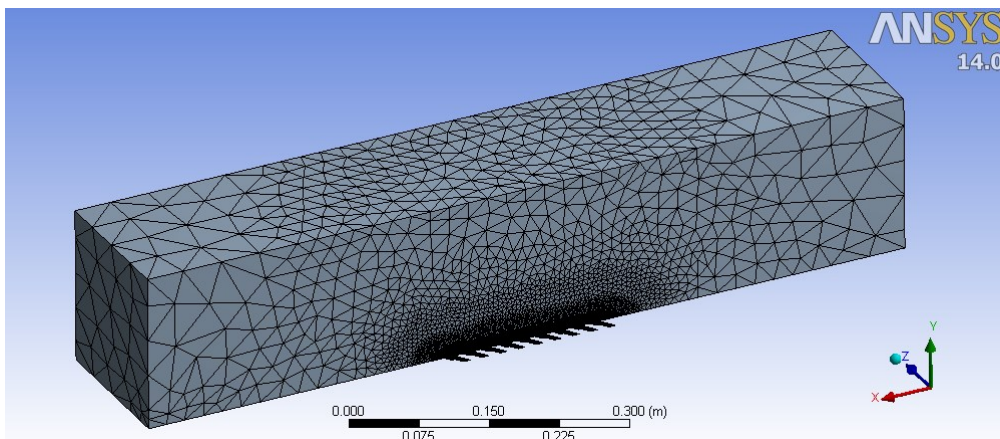


Fig. 4.8 Meshing details for effusion cooling

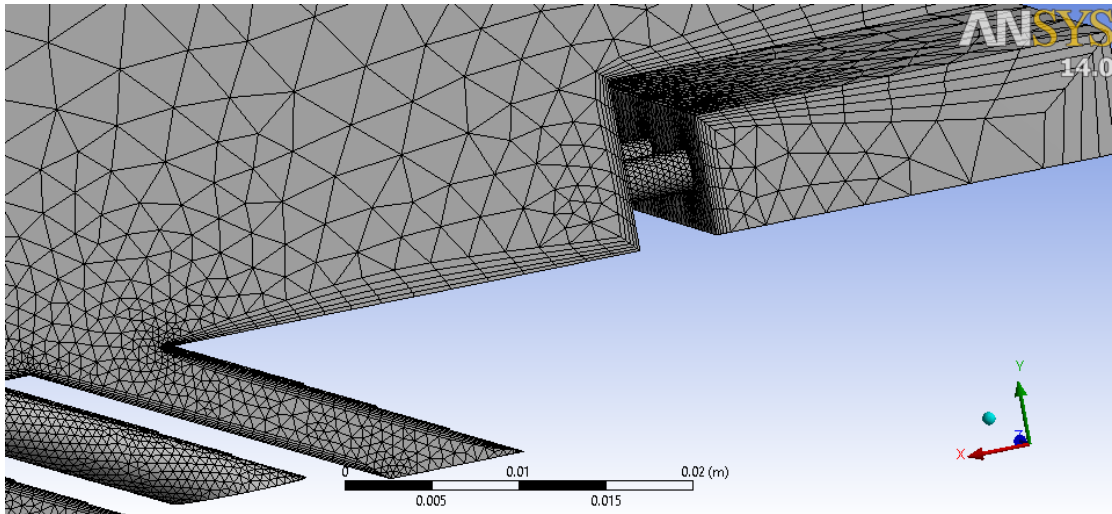


Fig. 4.9 Meshing details for effusion cooling with machined ring 1

4.3 Boundary Conditions

The boundary conditions for CFD are mentioned in Table 4.1. Mainstream inlet side is given a velocity inlet as the boundary condition, with the mainstream outlet as pressure outlet. The coolant inlet was given as a pressure inlet condition, for which the different coolant pressures at different blowing ratios are established. For all the test cases the mainstream velocity is given as 20 m/s. Table 4.2 gives the test matrix for the heat transfer coefficient and adiabatic film cooling effectiveness measurements.

Table 4.1 CFD boundary conditions

Named selection	Type of condition
Mainstream Inlet	Velocity Inlet
Mainstream Outlet	Pressure Outlet
Coolant Inlet	Pressure Inlet
Duct Surface	Wall

Table 4.2 Test matrix for heat transfer coefficient and adiabatic film cooling effectiveness measurements

Heat Transfer Coefficient										
Main Stream Conditions (27 deg)						Coolant conditions (27 deg)				
BR	Temp	Density	Velocity	M S (Del P)		Temp	Density	Velocity	Chamber Pressure	
<i>Const</i>	<i>Kelvin</i>	<i>Kg/m3</i>	<i>m/sec</i>	<i>N/m2</i>	<i>mm of H2O</i>	<i>Kelvin</i>	<i>Kg/m3</i>	<i>m/sec</i>	<i>N/m2</i>	<i>mm of H2O</i>
0.50	300	1.172	20	234.4	23.90	300	1.172	10.00	58.60	5.98
1.00	300	1.172	20	234.4	23.90	300	1.172	20.00	234.40	23.90
1.50	300	1.172	20	234.4	23.90	300	1.172	30.00	527.40	53.78
2.00	300	1.172	20	234.4	23.90	300	1.172	40.00	937.60	95.61
2.50	300	1.172	20	234.4	23.90	300	1.172	50.00	1465.00	149.39

Adiabatic Film Cooling Effectiveness										
DR 1.3										
Main Stream Conditions (27 deg)						Coolant Conditions (-42 deg)				
BR	Temp	Density	velocity	M S (Del P)		Temp	Density	Velocity	Chamber Pressure	
<i>const</i>	<i>kelvin</i>	<i>Kg/m3</i>	<i>m/sec</i>	<i>N/m2</i>	<i>mm of H2O</i>	<i>Kelvin</i>	<i>Kg/m3</i>	<i>m/sec</i>	<i>N/m2</i>	<i>mm of H2O</i>
0.50	300	1.172	20	234.4	23.90	231	1.522	7.67	44.77	4.57
1.00	300	1.172	20	234.4	23.90	231	1.522	15.34	179.08	18.26
1.50	300	1.172	20	234.4	23.90	231	1.522	23.01	402.94	41.09
2.00	300	1.172	20	234.4	23.90	231	1.522	30.68	716.33	73.05
2.50	300	1.172	20	234.4	23.90	231	1.522	38.35	1119.27	114.13

Note: Density of Air at 27Deg C = 1.172 Kg/m³ and at -42 Deg C = 1.522 Kg/m³

For heat transfer coefficients, experimental values of heat flux are given to the test plate surface and the coolant, mainstream temperatures are given as 300 K. For the adiabatic film cooling effectiveness, coolant and mainstream pressure, temperature conditions are maintained at the values given in the test matrix.

4.4 Turbulence Model Selection

CFD analysis is carried out on Fluent and steady state pressure based solver is used for the analysis. Turbulence model k-ε realizable with standard wall functions chosen to perform the simulation. This is considered based on the previous research work done by Harrison and Bogard (2008) and Silieti et al. (2009), who have got convincing results using k-ε realizable model. For this analysis, residuals for the energy equation in the order 10⁻⁸ and for continuity, momentum equation residuals in the order of 10⁻³ are considered. Second order upwind scheme is used for discretization, and coupled scheme of algorithm is used for the analysis.

4.5 Grid Independence Study

The grid independence study was performed for different mesh sizes on all the geometries, and the optimum grid size is chosen for further analysis. The grid independence study for the conjugate effusion cooling test plate which has 7.2D pitch is explained as follows. The mesh sizes of 0.43, 0.85 and 1.15 million elements were generated with ANSYS meshing tool as shown in Fig. 4.10. The numerical simulation is performed for all the three different mesh sizes of the domain, and the effectiveness results are plotted in Fig. 4.11. The middle line effectiveness results of CFD for all mesh sizes are matching with the experimental middle line effectiveness. To reduce the computational time, the domain with the least mesh size is chosen for further analysis of all the test run conditions. Hence domain with a grid size of 0.43 million elements is considered as the optimum grid size in this particular conjugate analysis.

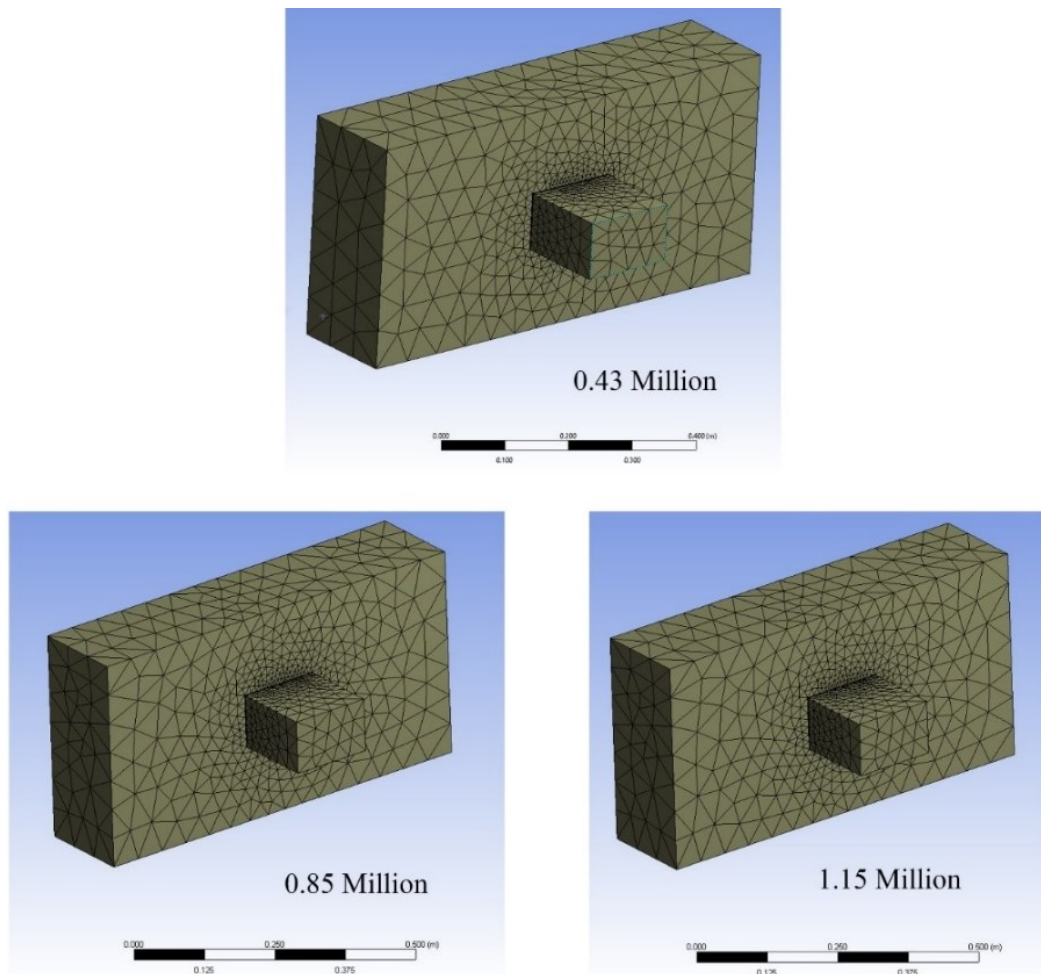


Fig. 4.10 Different mesh sizes for grid independence study

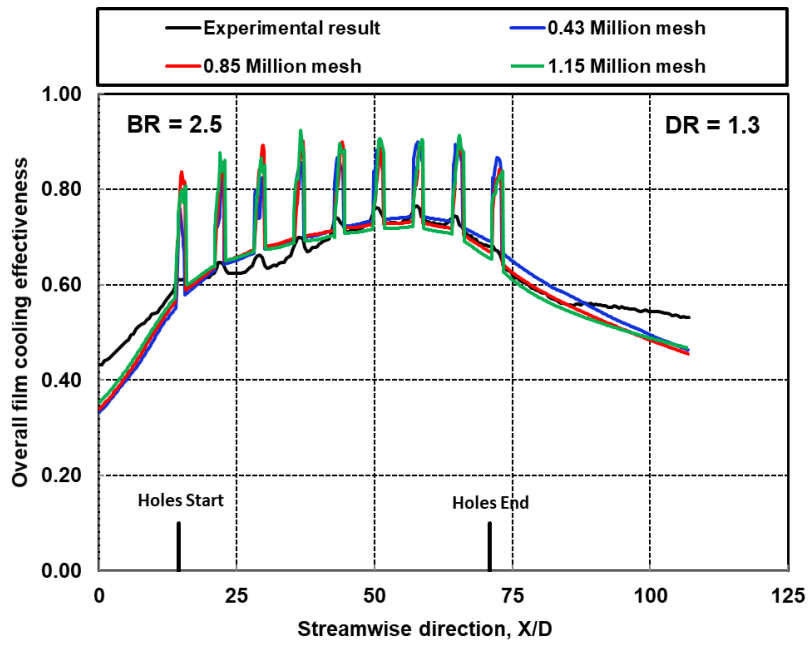


Fig. 4.11 CFD overall film cooling effectiveness results at different mesh sizes in comparison with the experimental result

CHAPTER-5

RESULTS AND DISCUSSION

5 RESULTS AND DISCUSSION

5.1 Machined Ring 1

5.1.1 Adiabatic Film Cooling Effectiveness

For adiabatic film cooling effectiveness measurement, the secondary air and the mainstream air are maintained at different temperatures. The recorded thermographic image of the test plate by IR camera during a machined ring test run is shown in Fig. 5.1. This image clearly shows the markers for identifying the thermocouple locations. There are 14 thermocouples fixed to the test plate. Seven are at the top, and the remaining seven are at the bottom. The region in-between the top and bottom thermocouples are identified, and those pixels values are averaged in the spanwise direction, and the average effectiveness values are calculated. The legend bar shows the raw radiation values which are converted into temperature values by using the calibration equations as mentioned earlier.

Fig. 5.2 shows the experimental adiabatic film cooling effectiveness distribution in streamwise direction for machined ring 1. Blowing ratio is varied from 0.5 to 2.5. Results show that the adiabatic effectiveness is increased with increase in blowing ratio. These results are averaged over a two-pitch region of holes in the spanwise direction. More cooling effectiveness is found near the machined ring cooling holes and decreases as the distance increases due to the mixing of coolant with the hot mainstream. Immediate downstream of holes 0.6 effectiveness values are found, and it gradually reduces as the X/D increases. The gradual reduction also depends upon the blowing ratio, i.e., the velocity of the coolant jet coming out of these holes.

Fig. 5.3 shows the CFD adiabatic film cooling effectiveness distribution in streamwise direction for machined ring 1. Blowing ratio is varied from 0.5 to 2.5. Results show that the adiabatic effectiveness is increased with increase in blowing ratio. More cooling effectiveness is found near the machined ring cooling holes and decreases as the distance increases due to the mixing of coolant with the hot mainstream.

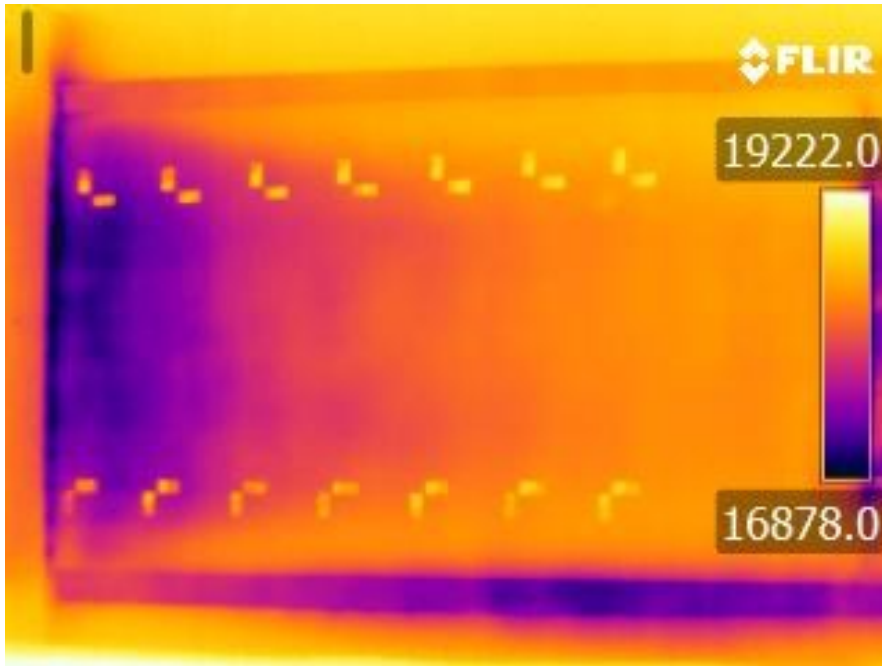


Fig. 5.1 Thermographic image of test plate during a machined ring test run

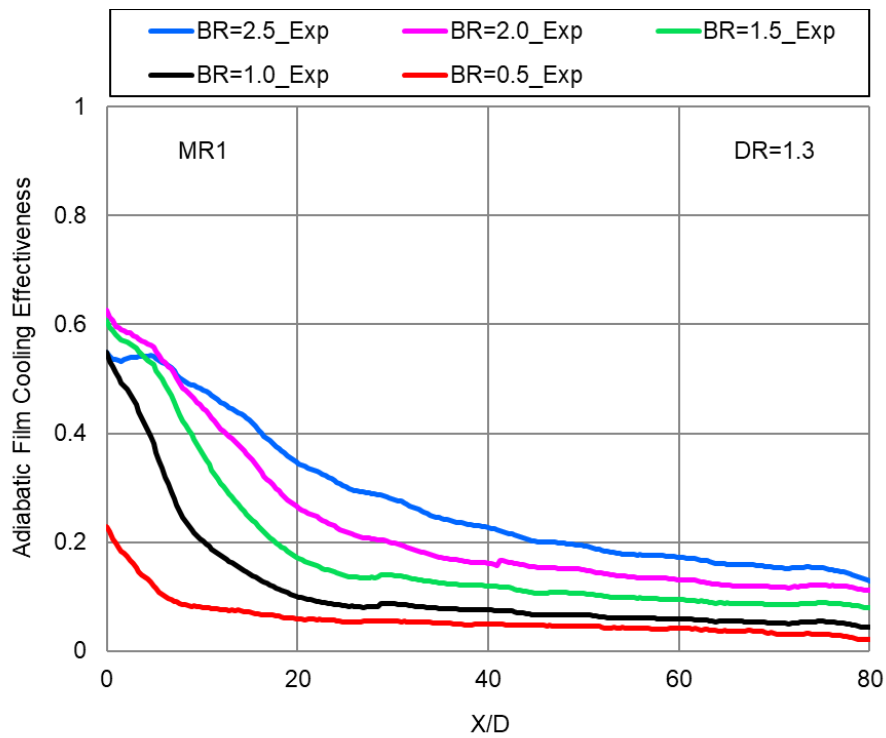


Fig. 5.2 Experimental adiabatic film cooling effectiveness distribution for machined ring 1

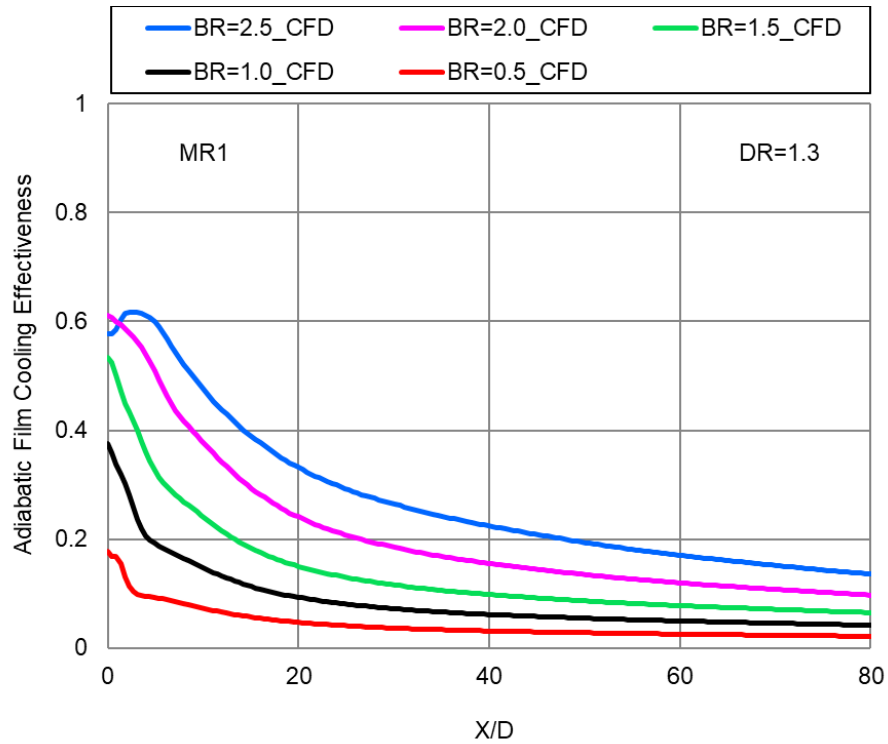
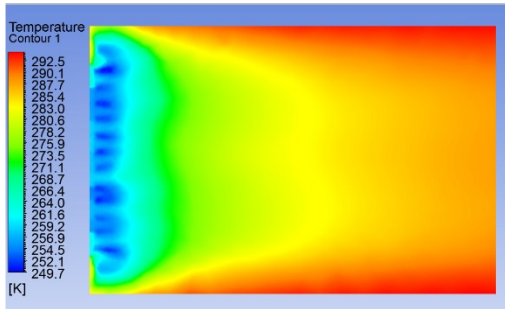


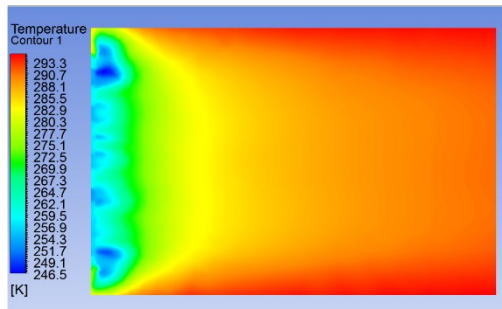
Fig. 5.3 CFD adiabatic film cooling effectiveness distribution for machined ring 1

Fig. 5.4 shows the CFD adiabatic test plate temperature contours for machined ring 1 at different blowing ratios. From the contours, it is seen that as the blowing ratio increases the film formation or coverage increases along the length of the test plate in the streamwise direction. Due to this, the effectiveness increases as the blowing ratio increases. For each and every blowing ratio at the exit of the machined ring holes, the temperature is less, and it increases along the length of the test plate in the streamwise direction. In Fig. 5.5, the flow field temperature contours shows the mixing behavior of mainstream and the coolant ejecting out of the machined ring holes. Near the machined ring holes, the film temperature is less and as the X/D increases film temperature gradually increases due to the mixing between the coolant and the mainstream.

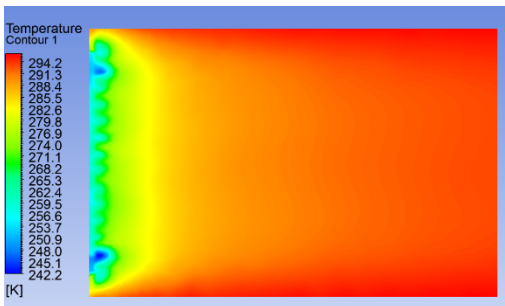
Fig. 5.6 shows the experimental and CFD comparison results for the machined ring 1 geometry at different blowing ratios. The CFD cooling effectiveness results are matching with the experimental results after X/D of 20 for lower blowing ratios. However, near the film cooling holes upto X/D of 20, CFD is not capturing the mixing behavior of coolant and mainstream, and thus effectiveness variation of $\pm 10\%$ is found. For higher blowing ratios of 2.0 and 2.5, both the results are more or less the same.



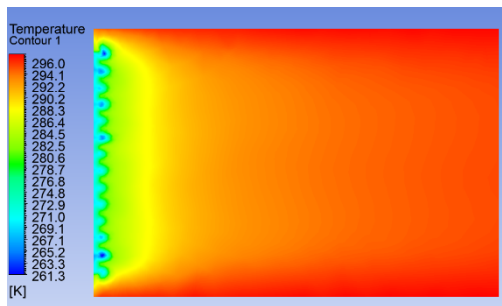
BR=2.5



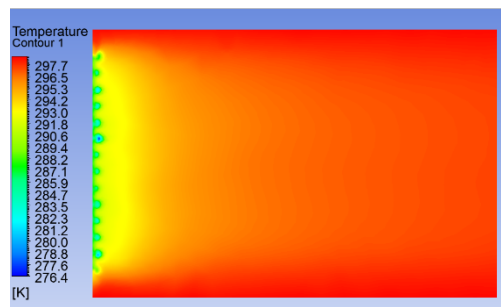
BR=2.0



BR=1.5

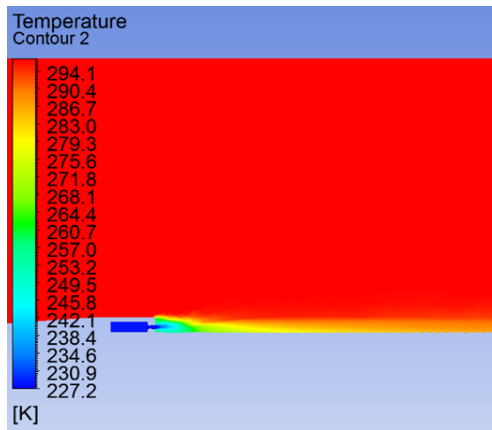


BR=1.0

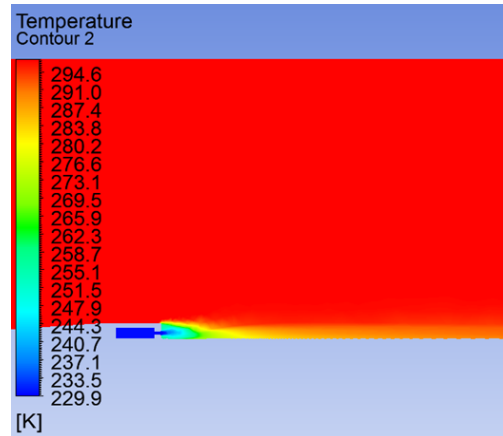


BR=0.5

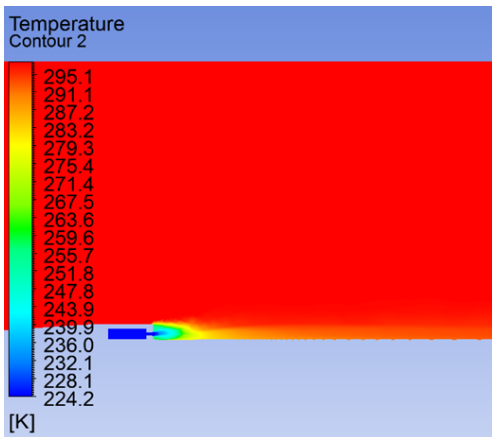
Fig. 5.4 CFD adiabatic test plate temperature contours for machined ring 1 at different blowing ratios



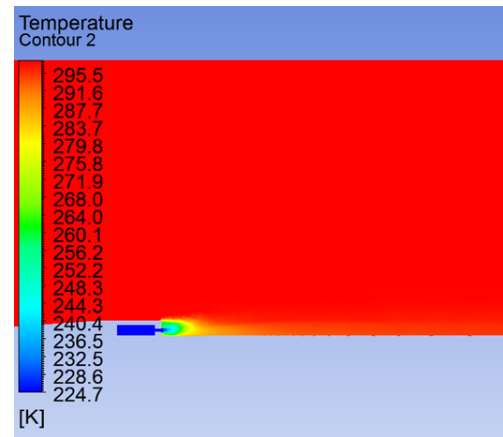
BR=2.5



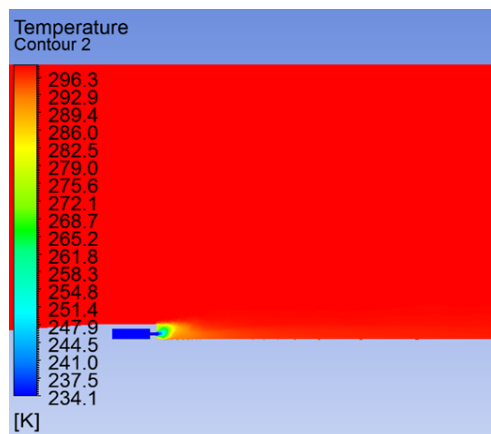
BR=2.0



BR=1.5

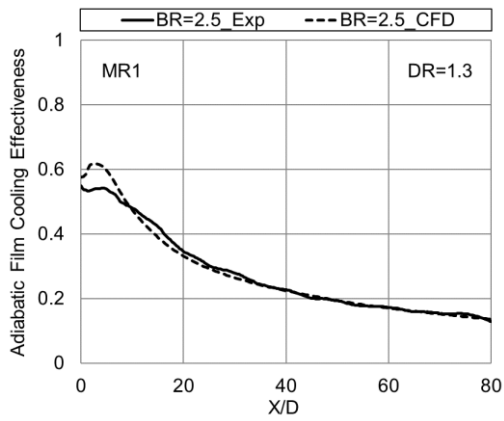


BR=1.0

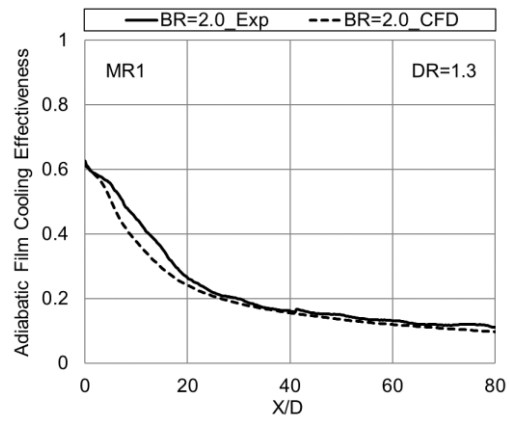


BR=0.5

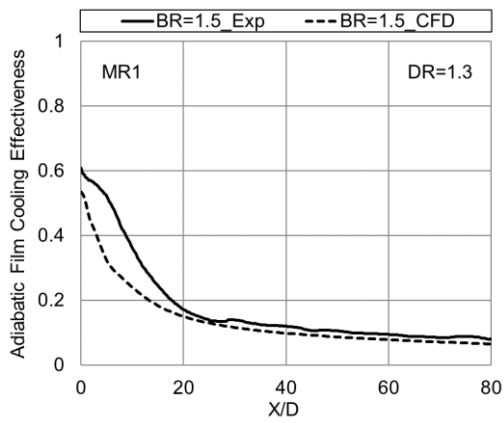
Fig. 5.5 CFD flow field temperature contours for machined ring 1 at different blowing ratios



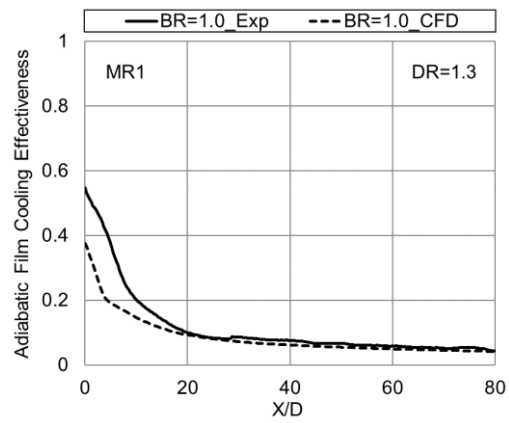
BR=2.5



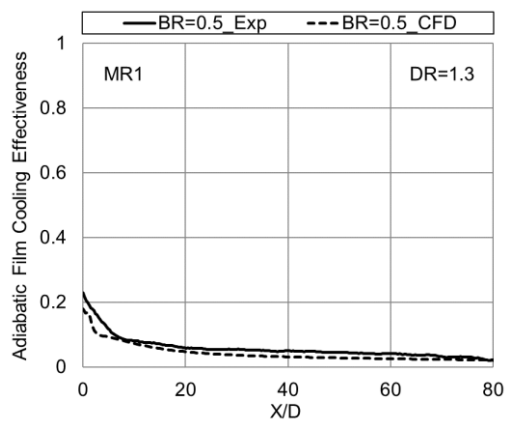
BR=2.0



BR=1.5



BR=1.0



BR=0.5

Fig. 5.6 Comparison of experimental and CFD adiabatic film cooling effectiveness for machined ring 1 at different blowing ratios

5.1.2 Heat Transfer Coefficients

For the heat transfer coefficient measurements, the mainstream and the coolant air is set at the same temperature. The required blowing ratio is set, and subsequently, the electrical power was supplied to the stainless steel sheet. The surface temperatures were monitored in a data logger. The power was adjusted in such a way that the maximum surface temperature measured did not exceed more than 55°C. Sufficient time was allowed to reach steady condition, and the temperatures, current supplied to the sheet were recorded in the data logger over a period of 30 seconds, and the average value was taken for calculation of heat transfer coefficient. At the same time, two thermal images were recorded by using the IR camera. The pressure readings were noted down. The local heat transfer coefficient was calculated by dividing the net heat flux supplied to the stainless steel sheet to the difference between the measured wall and free stream temperature.

Initially, to find out the heat transfer coefficient for the zero blowing ratio case, the coolant supply through the machined ring cooling holes are blocked, and the thin SS sheet is heated by means of electrical power. Only mainstream flow is allowed to flow over the SS sheet at the particular flow velocity, and the mainstream heat transfer coefficient is calculated. Fig. 5.7 shows the mainstream heat transfer coefficient distribution over the test surface. Due to the presence of wedge upto the height of the machined ring, the mainstream flow smoothly flows over the machined ring and touches the test plate surface after X/D of 20. So the mainstream heat transfer coefficient is constant after X/D of 20 and is 86 W/m²K for that particular Reynolds number of the mainstream. But before X/D of 20, there is no flow of mainstream, and the heat transfer coefficient gradually increases.

Fig. 5.8 shows the film heat transfer coefficient in the streamwise direction for machined ring 1 at different blowing ratios. The results show that the heat transfer coefficient increases with an increase in blowing ratio upto X/D of 20. Near the holes the heat transfer variation is significant, and above X/D of 20, there is not much variation with respect to blowing ratio.

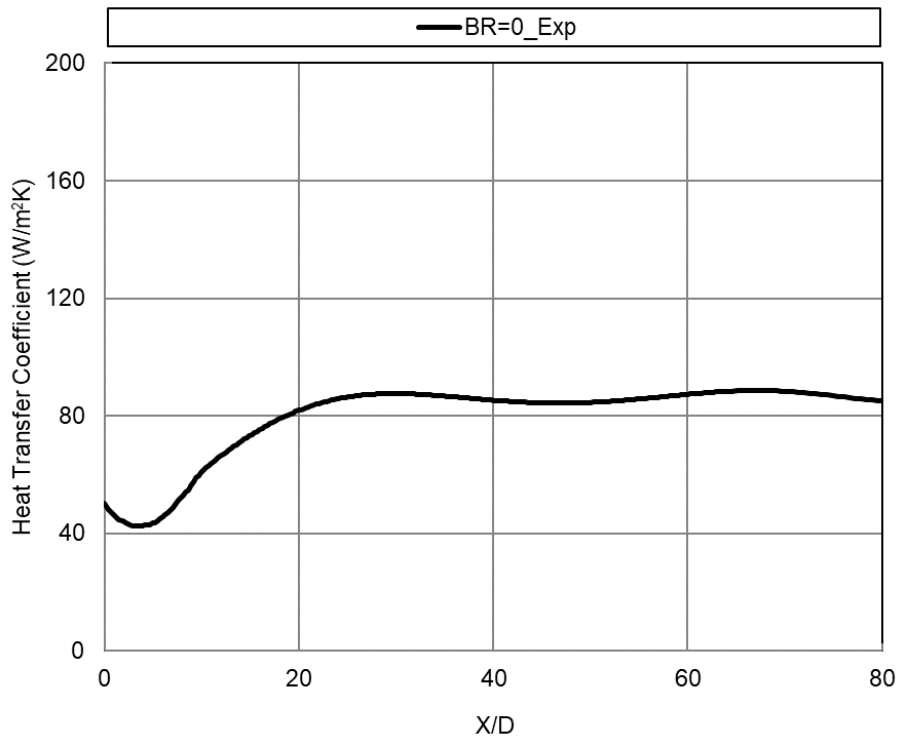


Fig. 5.7 Mainstream heat transfer coefficient in the streamwise direction

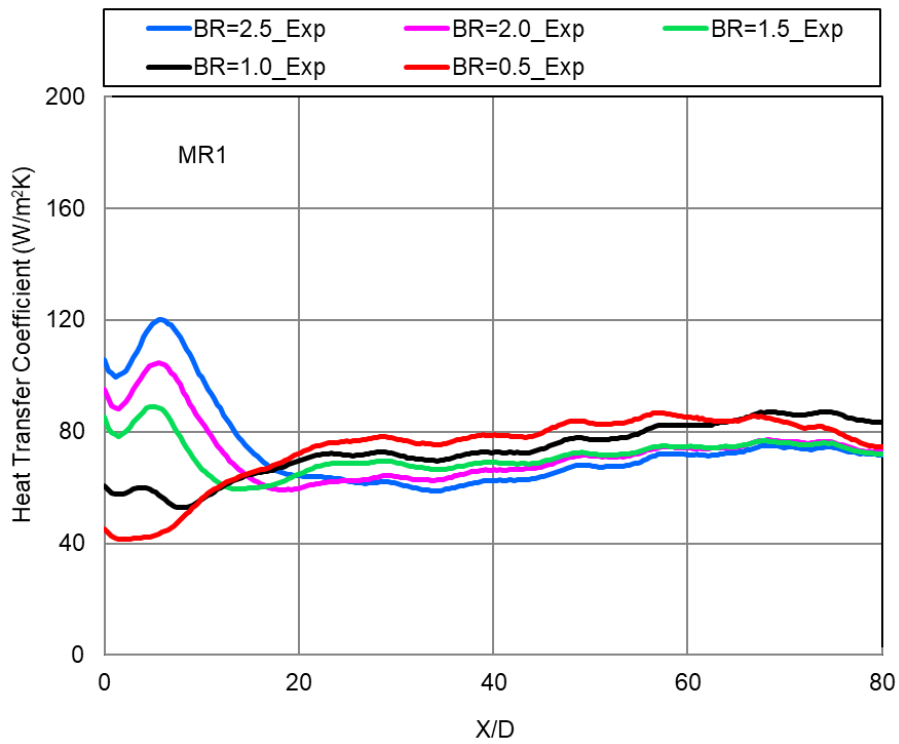


Fig. 5.8 Experimental film heat transfer coefficient for machined ring 1

Fig. 5.9 shows the heat transfer coefficient ratio in streamwise direction for machined ring 1. Heat transfer coefficient ratio is the ratio between the film heat transfer coefficient and the heat transfer coefficient without film. The results show that the heat transfer coefficient ratio increases with an increase in blowing ratio upto X/D of 20. There is not much variation with respect to blowing ratio above X/D of 20 and it shows more or less the values equal to the mainstream heat transfer coefficient only.

Fig. 5.10 shows the CFD film heat transfer coefficient in streamwise direction for machined ring 1. The results show that the heat transfer coefficient increases with an increase in blowing ratio upto X/D of 25. Afterward, it decreases as the blowing ratio increases, but the variation in heat transfer values are minimum. $BR=0.5$ shows nearly equal values as of mainstream heat transfer coefficient, i.e., without the coolant film. For other blowing ratios the film heat transfer coefficient increases upto X/D of 25, then it decreases less than the mainstream heat transfer coefficient.

Fig. 5.11 shows the comparison between experimental and CFD film heat transfer coefficient for all the blowing ratios. The spanwise averaged CFD values and their trends are almost matching with experimental values. But the CFD values are little bit above the experimental values at all the blowing ratios.

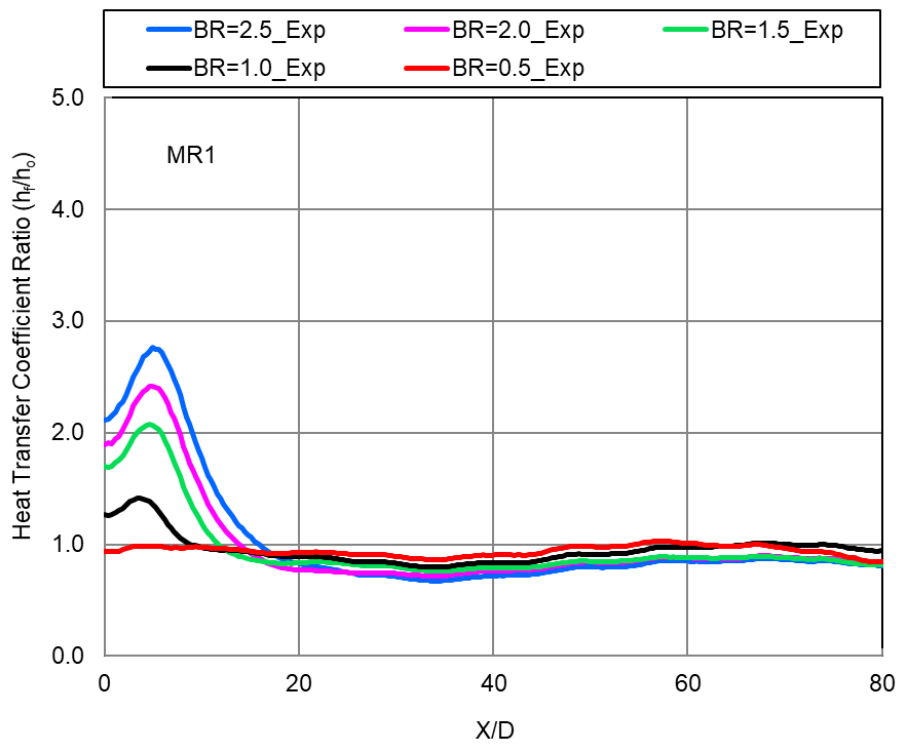


Fig. 5.9 Experimental heat transfer coefficient ratio for machined ring 1

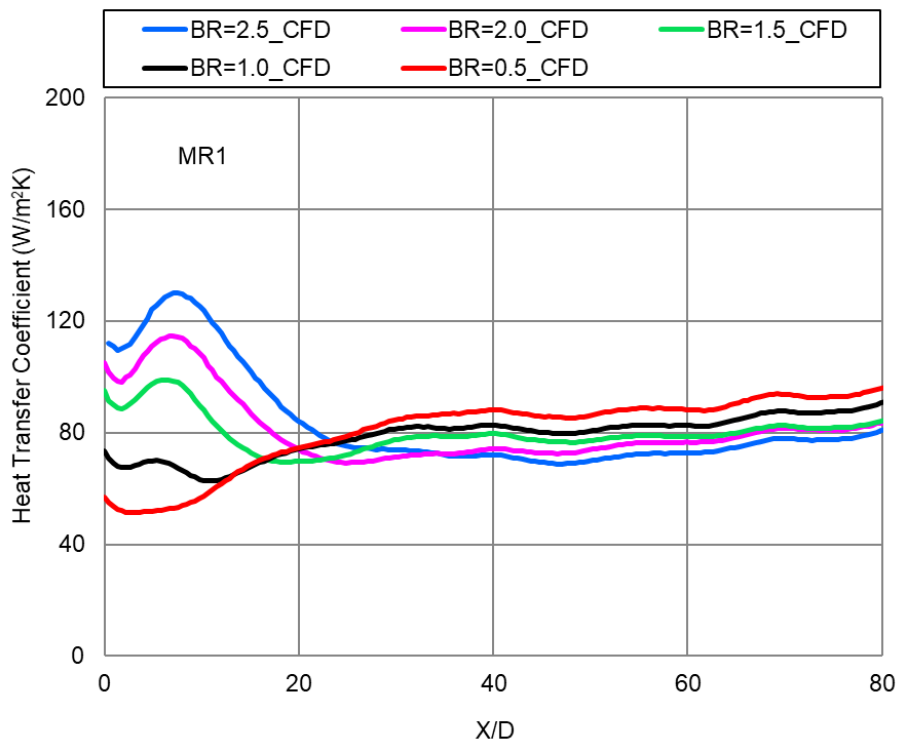


Fig. 5.10 CFD film heat transfer coefficient for machined ring 1

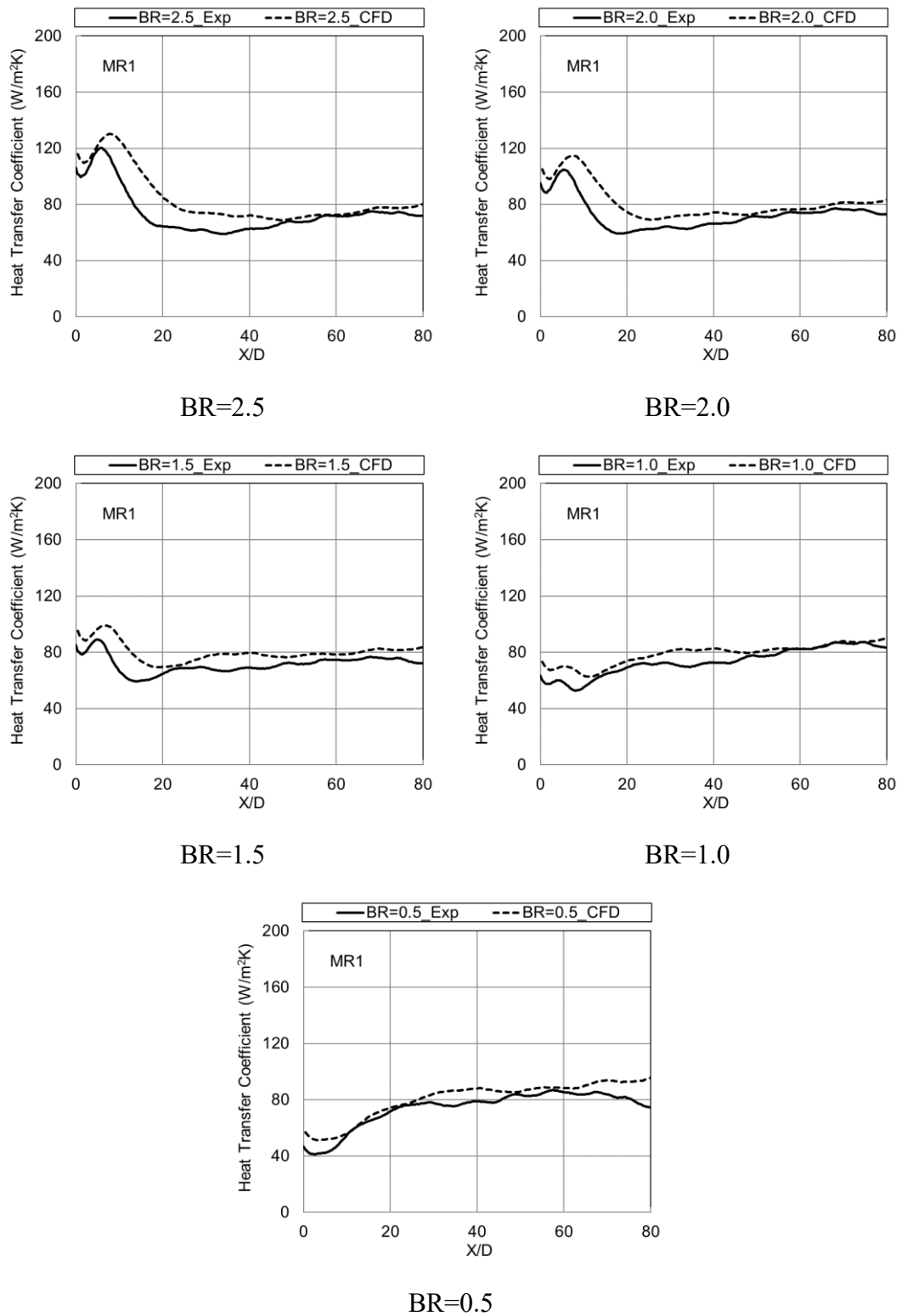


Fig. 5.11 Comparison of experimental and CFD film heat transfer coefficient for machined ring 1 at different blowing ratios

5.1.3 Net Heat Flux Reduction

Net Heat Flux Reduction (NHFR) is a commonly used parameter to evaluate the reduction of heat flux across a cooled surface. It tells how much reduction in the heat flux happens due to the film cooling. NHFR values are calculated based on the equation 1.8 explained in chapter 1. But the θ value in equation 1.9 is assumed based on the following literature papers. Sen et al. (1996) described that the calculation of NHFR requires a value for θ which is to be assumed since the actual value of θ is dependent on the real turbine blade conditions. Hence they used a value of $\theta = 1.6$, which is typical of film cooled turbine blade operation, for these calculations. Christophel et al. (2005) explained that, in the equation of NHFR, all variables had been measured experimentally except θ . So, a constant value of $\theta=1.6$, which corresponds to the cooling effectiveness of 62.5% was used for their calculation. Also, they explained that the NHFR could become negative when high heat transfer augmentation is not accompanied by high film cooling. The negative values of NHFR show that the cooling mechanism is causing an increased heat load to the surface. The negative NHFR is due to the localized high heat transfer with low effectiveness. Dittmar et al. (2004) used a θ value of 1.5 in their calculations to find out the NHFR values downstream of shaped film cooling holes on the turbine vane. Similarly, Abdala and Elwekeel (2016) did CFD simulations of film cooling effectiveness, heat transfer for annular film hole and found the NHFR values. They applied a typical θ value of 1.5 which is generally used for gas turbine blade applications for the NHFR values calculations. The literature shows two values of θ (1.5 and 1.6) were used in the calculation of NHFR. But, in this report θ value of 1.6 is used in the calculation of NHFR which corresponds to cooling effectiveness of 62.6% (inverse of 1.6).

Fig. 5.12 shows the effect of blowing ratio on NHFR distribution for machined ring 1. The results show that the NHFR increases with an increase in blowing ratio. Higher NHFR values are found immediately downstream of machined ring holes and as the X/D increases the values gradually reduces upto X/D of 35. Thereafter the values are constant for the particular blowing ratio. The negative values of NHFR for low blowing ratio cases shows that the localized high heat transfer with low effectiveness in those particular regions.

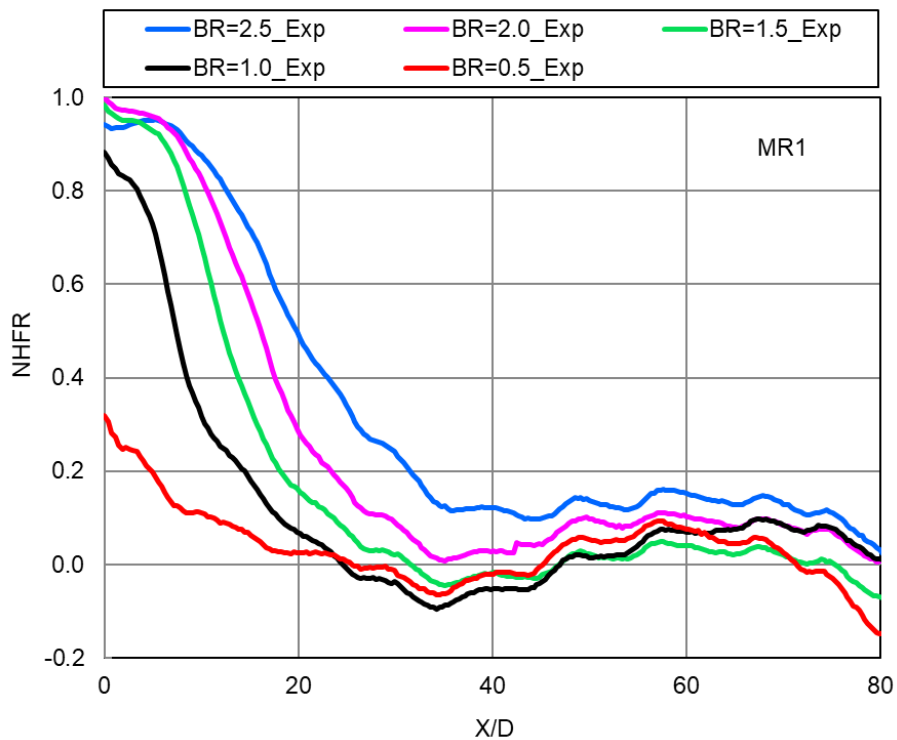


Fig. 5.12 Effect of blowing ratio on NHFR distribution for machined ring 1

5.2 Machined Ring 2

5.2.1 Adiabatic Film Cooling Effectiveness

Fig. 5.13 shows the experimental adiabatic film cooling effectiveness distribution in streamwise direction for machined ring 2. Blowing ratio is varied from 0.5 to 2.5. Results show that the adiabatic effectiveness is increased with increase in blowing ratio. Similar to the machined ring geometry 1, in this case also more cooling effectiveness is found near the machined ring cooling holes and decreases as the distance increases due to the mixing of coolant with the hot mainstream. The highest effectiveness value of 0.85 to 0.9 is seen near the hole region at higher blowing ratios.

Fig. 5.14 shows the CFD adiabatic film cooling effectiveness distribution in streamwise direction for machined ring 2. Blowing ratio is varied from 0.5 to 2.5. As seen in the experimental results, the CFD results also show that the adiabatic effectiveness is increased with increase in blowing ratio. More cooling effectiveness is found near the machined ring cooling holes and decreases as the distance increases due to the mixing of coolant with the hot mainstream.

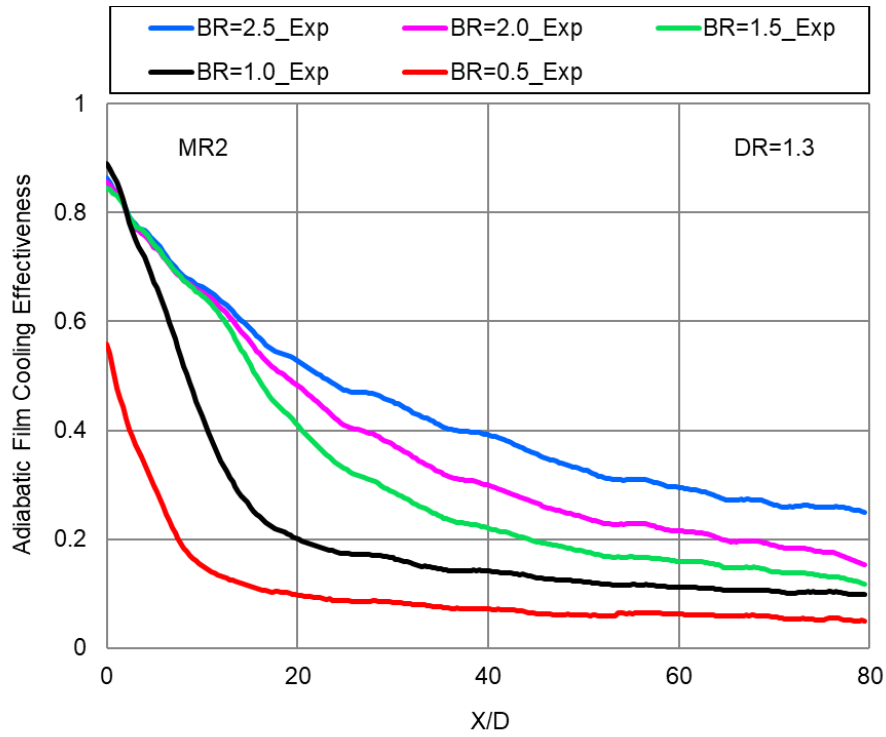


Fig. 5.13 Experimental adiabatic film cooling effectiveness distribution for machined ring 2

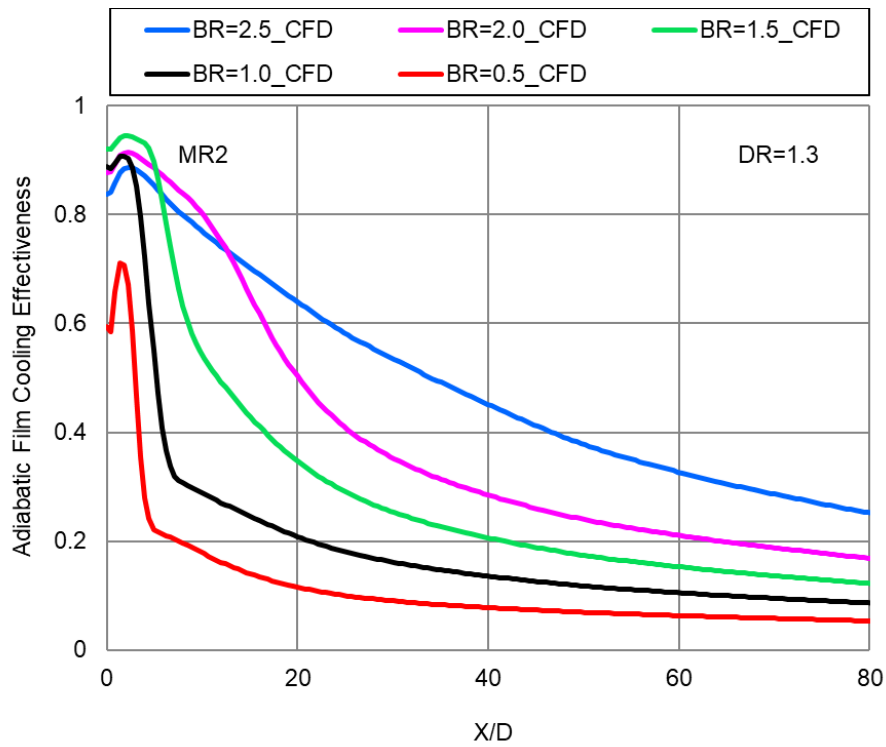
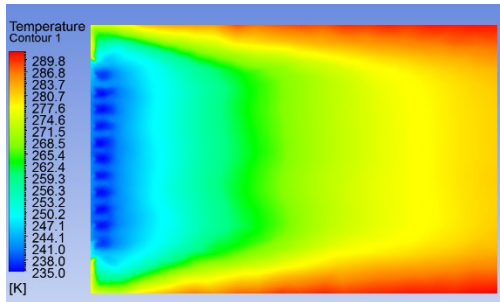


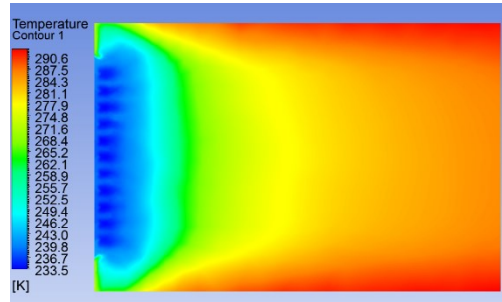
Fig. 5.14 CFD adiabatic film cooling effectiveness distribution for machined ring 2

Fig. 5.15 shows the CFD adiabatic test plate temperature contours for machined ring 2 at different blowing ratios. From the contours, it is seen that as the blowing ratio increases the film formation or coverage increases along the length of the test plate in the streamwise direction. Due to this, the effectiveness increases as the blowing ratio increases. But the film formation is more when compared to the MR1 due to the more number of holes in MR2. The coolant mass flow is higher than the MR1. For each and every blowing ratio at the exit of the machined ring holes, the temperature is less, and it increases along the length of the test plate in the streamwise direction.

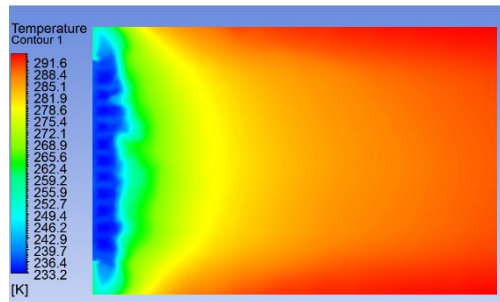
Fig. 5.16 shows the experimental and CFD comparison results for the machined ring 2 geometry at different blowing ratios. The CFD cooling effectiveness results are matching with the experimental results all the blowing ratios after X/D of 20. However, near the film cooling holes upto X/D of 20, CFD is not capturing the mixing behavior of coolant and mainstream, and thus effectiveness variation of $\pm 10\%$ is found.



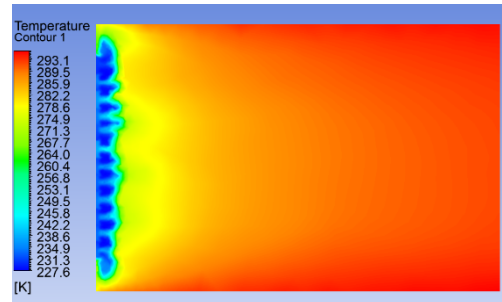
BR=2.5



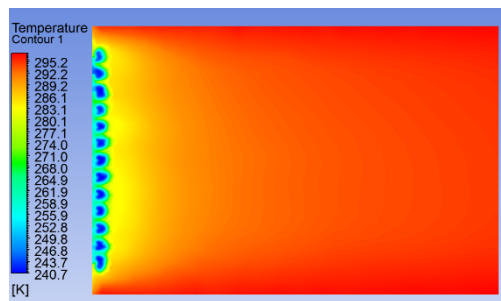
BR=2.0



BR=1.5



BR=1.0



BR=0.5

Fig. 5.15 CFD adiabatic test plate temperature contours for machined ring 2 at different blowing ratios

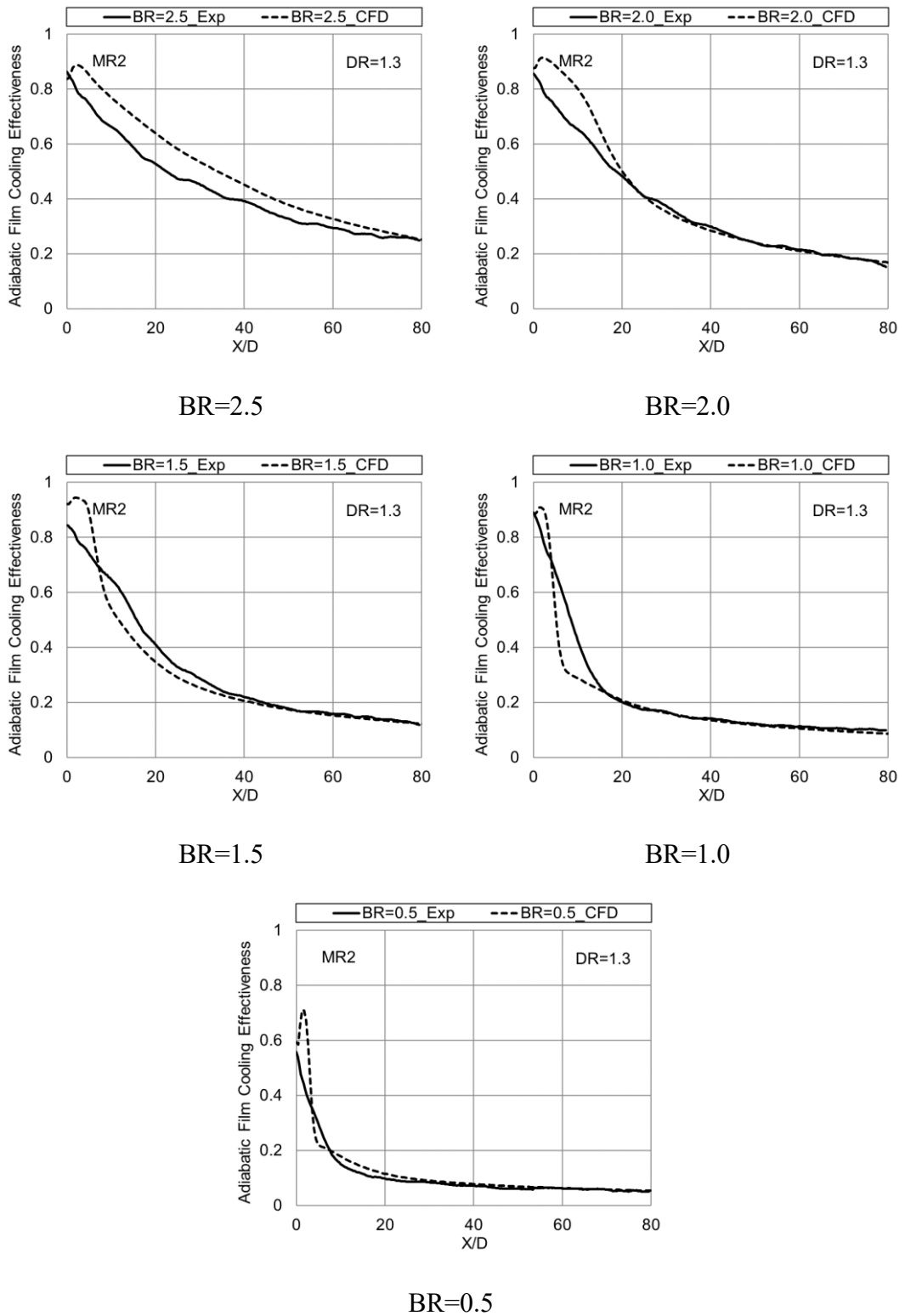


Fig. 5.16 Comparison of experimental and CFD adiabatic film cooling effectiveness for machined ring 2 at different blowing ratios

5.2.2 Heat Transfer Coefficients

Fig. 5.17 shows the film heat transfer coefficient in streamwise direction for machined ring 2. The results show that the heat transfer coefficient increases with an increase in blowing ratio upto X/D of 20. Except for $BR=0.5$, for other blowing ratios the heat transfer coefficient increases and attains peak value at X/D of 5 and decreases continuously upto X/D of 20. There is not much variation with respect to blowing ratio above X/D of 20.

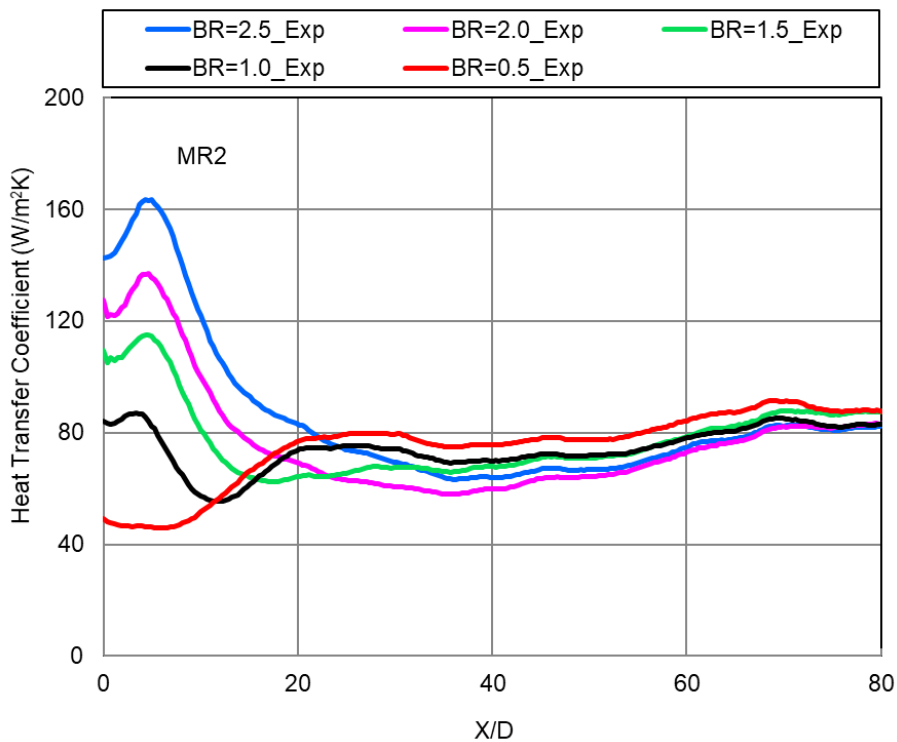


Fig. 5.17 Experimental film heat transfer coefficient for machined ring 2

Fig. 5.18 shows the heat transfer coefficient ratio in streamwise direction for machined ring 2. The results show that the heat transfer coefficient ratio increases with an increase in blowing ratio upto X/D of 20. There is not much variation with respect to blowing ratio above X/D of 20 and it shows the mainstream heat transfer coefficient only. Fig. 5.19 shows the CFD film heat transfer coefficient in streamwise direction for machined ring 2. The results show that the heat transfer coefficient increases with an increase in blowing ratio upto X/D of 25. For all the blowing ratios the heat transfer coefficient trends are matching with experimental results, but the values are little bit above than the experimental values. This comparison is shown in Fig. 5.20. After X/D

of 40 and above, the heat transfer coefficients show equal values as of heat transfer coefficient without film. This shows that the effect of heat transfer coefficient variation due to the coolant film is only upto X/D of 40.

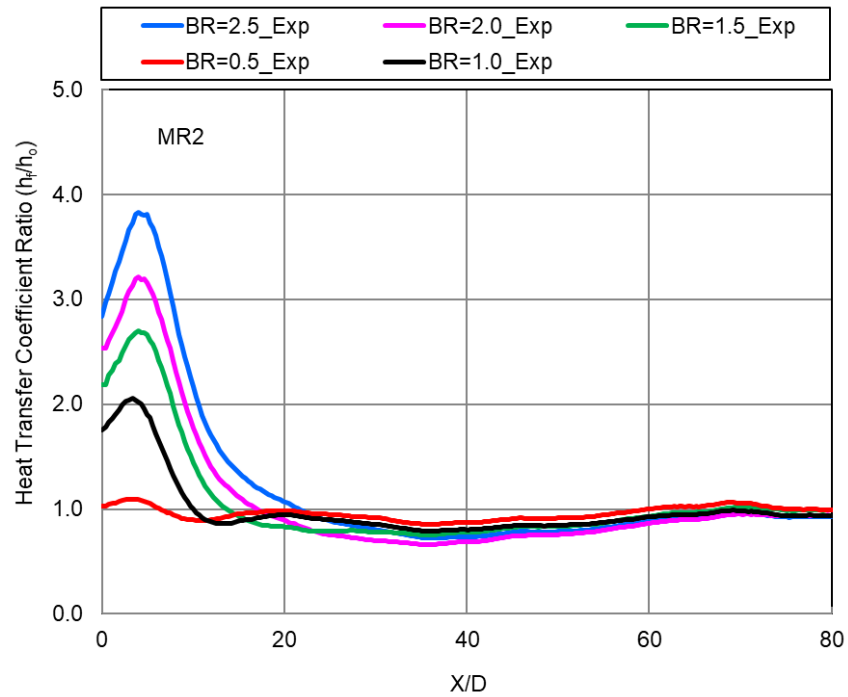


Fig. 5.18 Experimental heat transfer coefficient ratio for machined ring 2

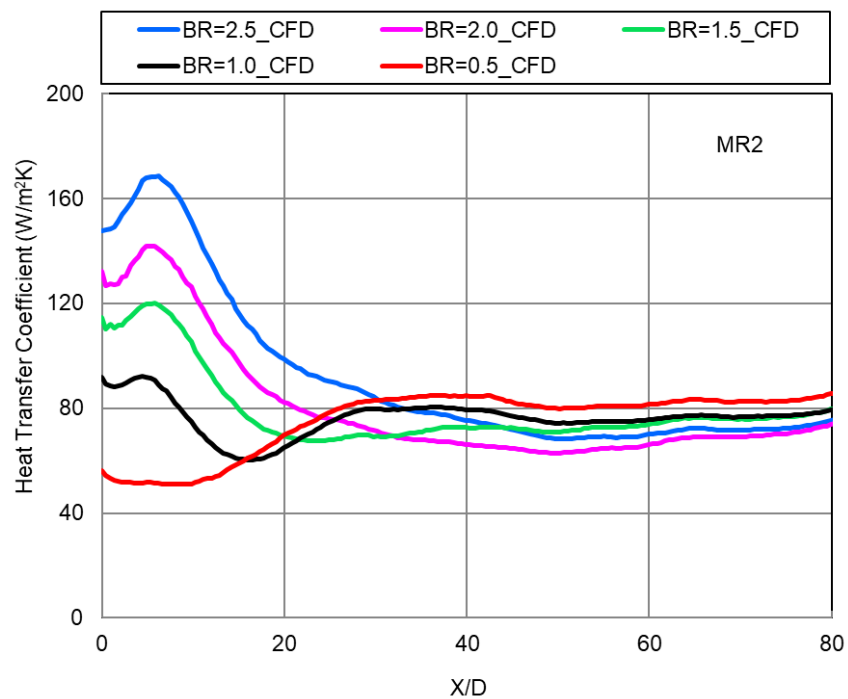
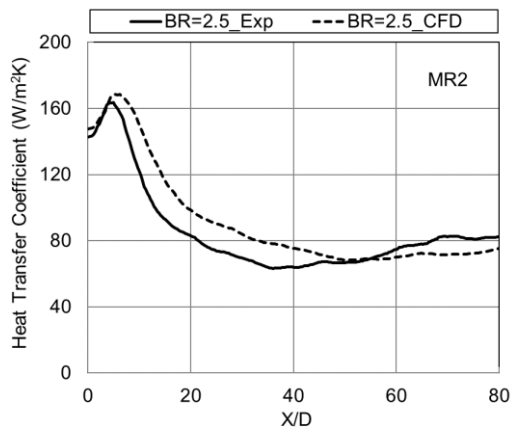
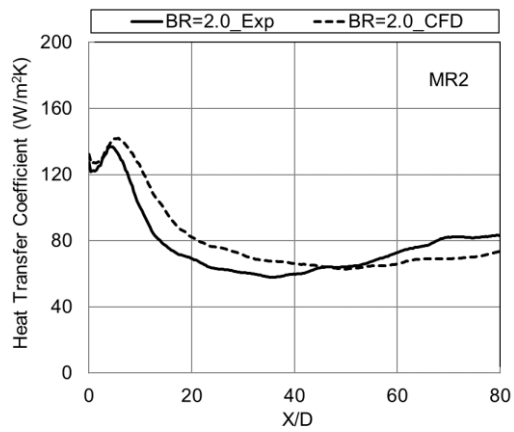


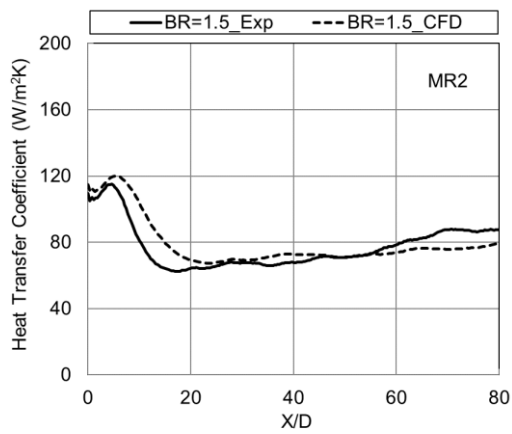
Fig. 5.19 CFD film heat transfer coefficient for machined ring 2



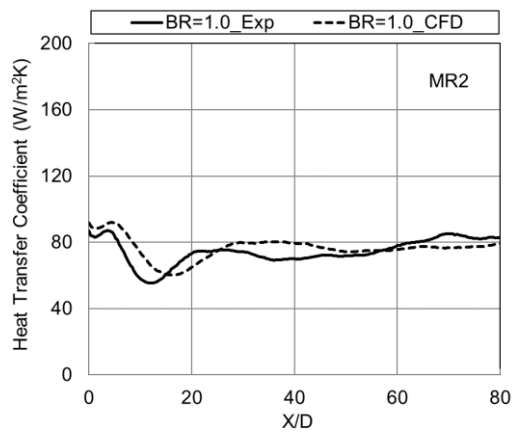
BR=2.5



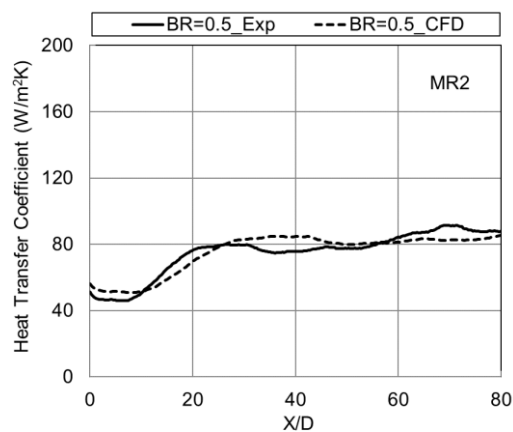
BR=2.0



BR=1.5



BR=1.0



BR=0.5

Fig. 5.20 Comparison of experimental and CFD film heat transfer coefficients for machined ring 2 at different blowing ratios

5.2.3 Net Heat Flux Reduction

Fig. 5.21 shows the effect of blowing ratio on NHFR distribution for machined ring 2. The results show that the NHFR increases with an increase in blowing ratio. Higher NHFR values are found immediately downstream of machined ring holes and as the X/D increases the values gradually reduces upto X/D of 55. Thereafter the values are constant for the particular blowing ratio. The negative values of NHFR for blowing ratio 0.5 shows that the localized high heat transfer with low effectiveness in those particular regions.

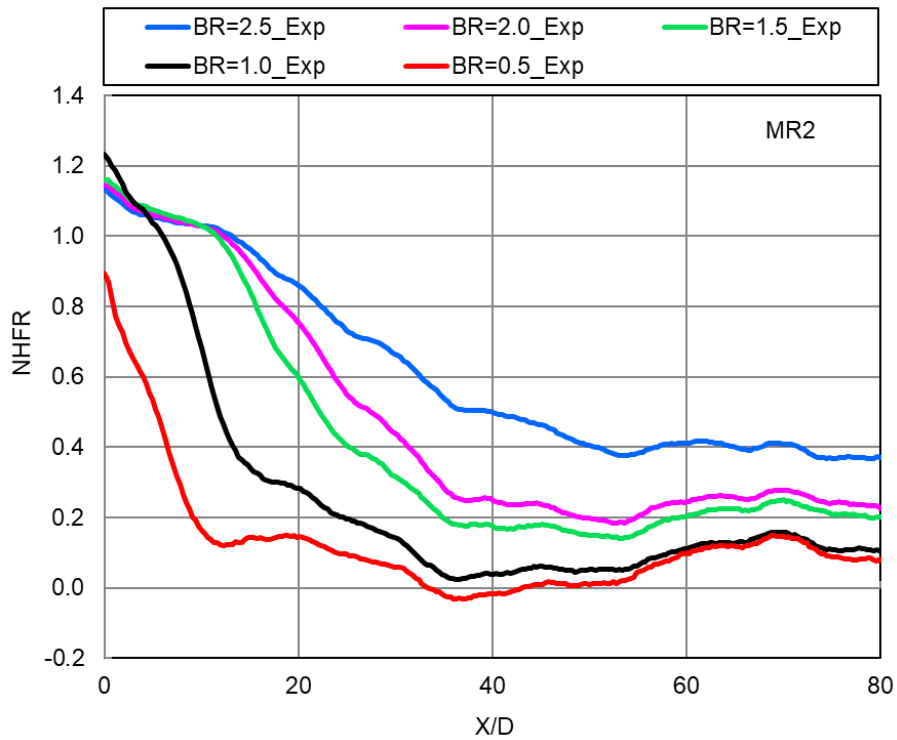


Fig. 5.21 Effect of blowing ratio on NHFR distribution for machined ring 2

5.3 Comparison Between Two Machined Ring Geometries

Fig. 5.22 shows the comparison of adiabatic cooling effectiveness experimental results for the two machined ring geometries at different blowing ratios. The results show that the cooling effectiveness is higher for machined ring 2 than machined ring 1 at all the blowing ratios. This is because, machined ring 2 has more cooling holes with two rows of holes arranged in a staggered manner, whereas the machined ring 1 is having one row of holes. In addition, more coolant mass flow is flowing through the cooling holes for machined ring 2 and the film formed has more coverage in the downstream distance.

Fig. 5.23 shows the comparison of the heat transfer coefficient experimental results for the two machined ring geometries at different blowing ratios. The results show that the heat transfer coefficient is higher for machined ring 2 than machined ring 1 upto X/D of 40 at blowing ratio of 2.5 and upto X/D of 20 at blowing ratio ranging from 2.0 to 1.0. At $BR=0.5$ there is no variation in the heat transfer coefficient distribution.

Fig. 5.24 shows the comparison of net heat flux reduction for the two machined ring geometries at different blowing ratios. The results show that the NHFR is higher for machined ring 2 than machined ring 1 at all the blowing ratios. This is because of the machined ring 2 which has more cooling holes than machined ring 1. The coolant flow through machined ring 2 holes produces more film coverage than machined ring 1 and thus reduces the heat flux from the hot mainstream to the wall surface. Higher values of NHFR shows higher adiabatic cooling effectiveness and lower heat transfer from the hot mainstream gases.

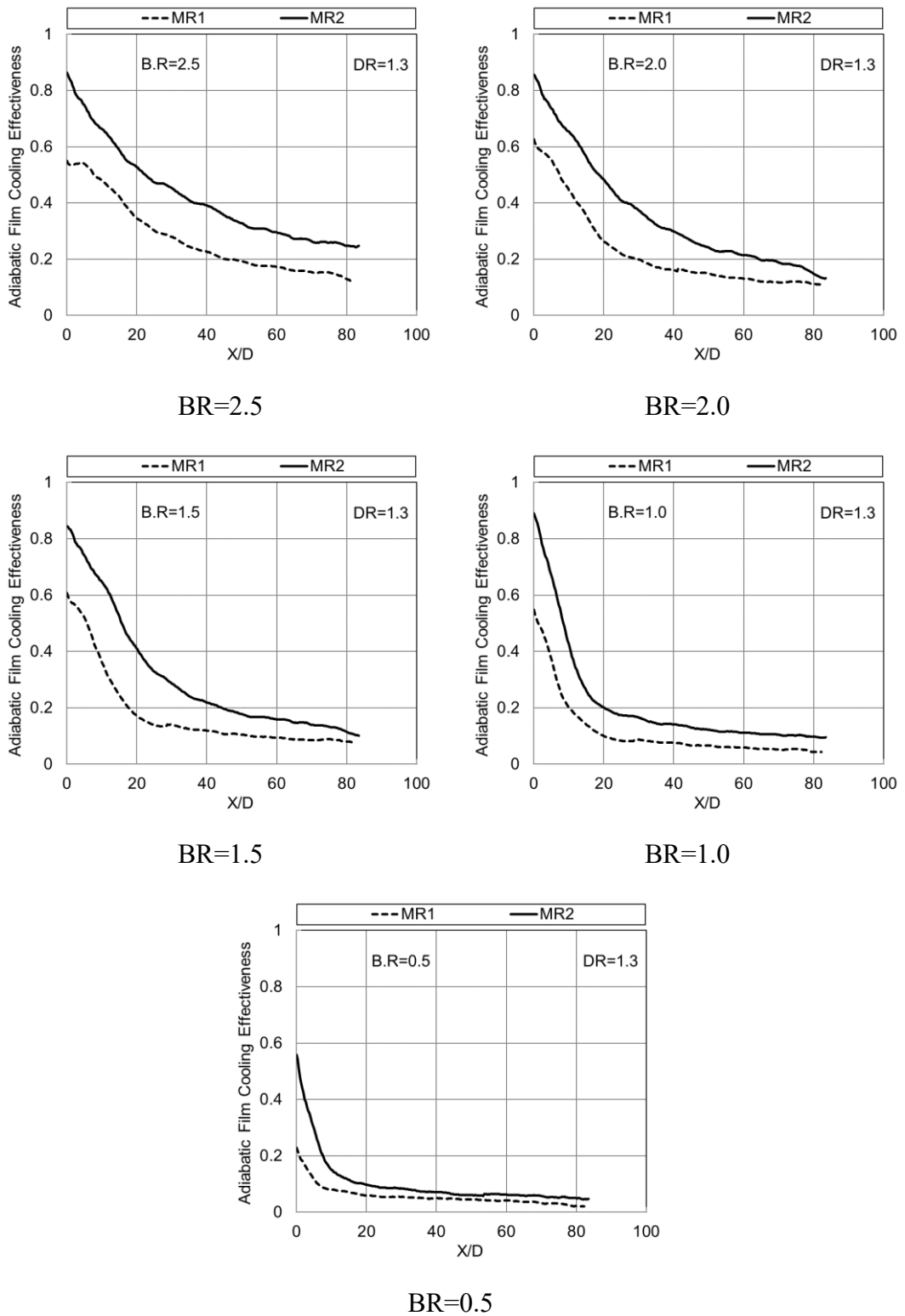
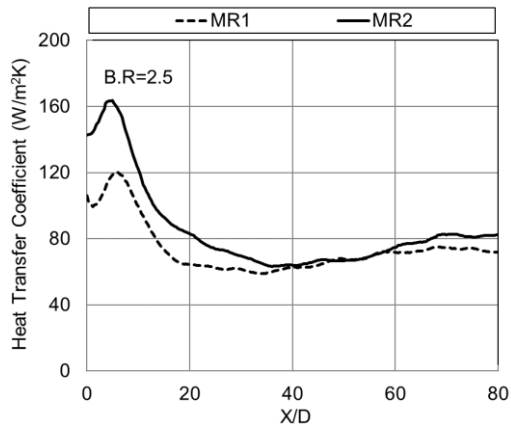
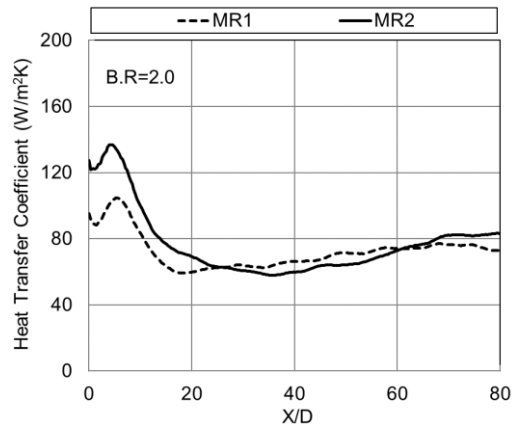


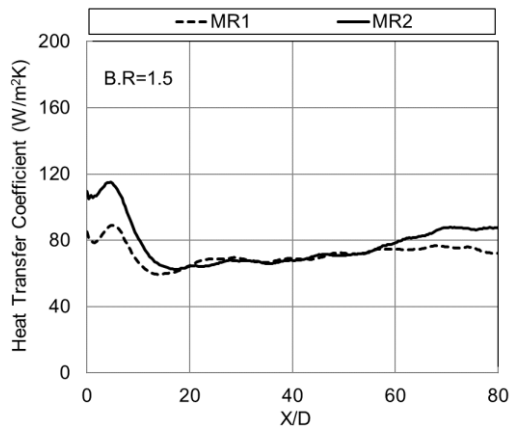
Fig. 5.22 Comparison of adiabatic film cooling effectiveness for machined ring 1 & 2 at different blowing ratios



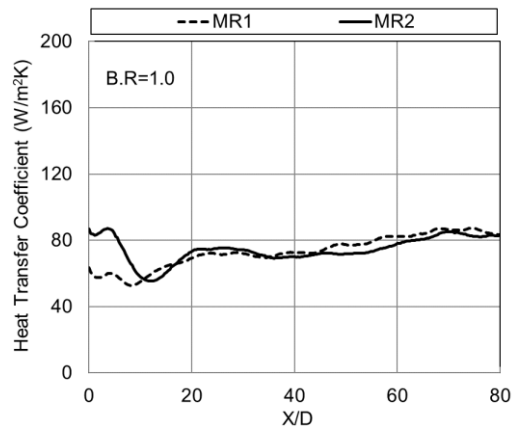
BR=2.5



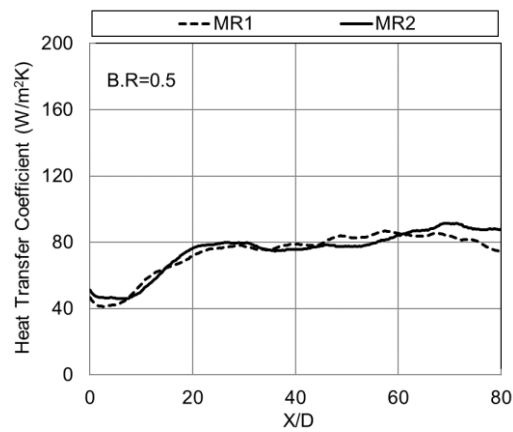
BR=2.0



BR=1.5



BR=1.0



BR=0.5

Fig. 5.23 Comparison of film heat transfer coefficient for machined ring 1 & 2 at different blowing ratios

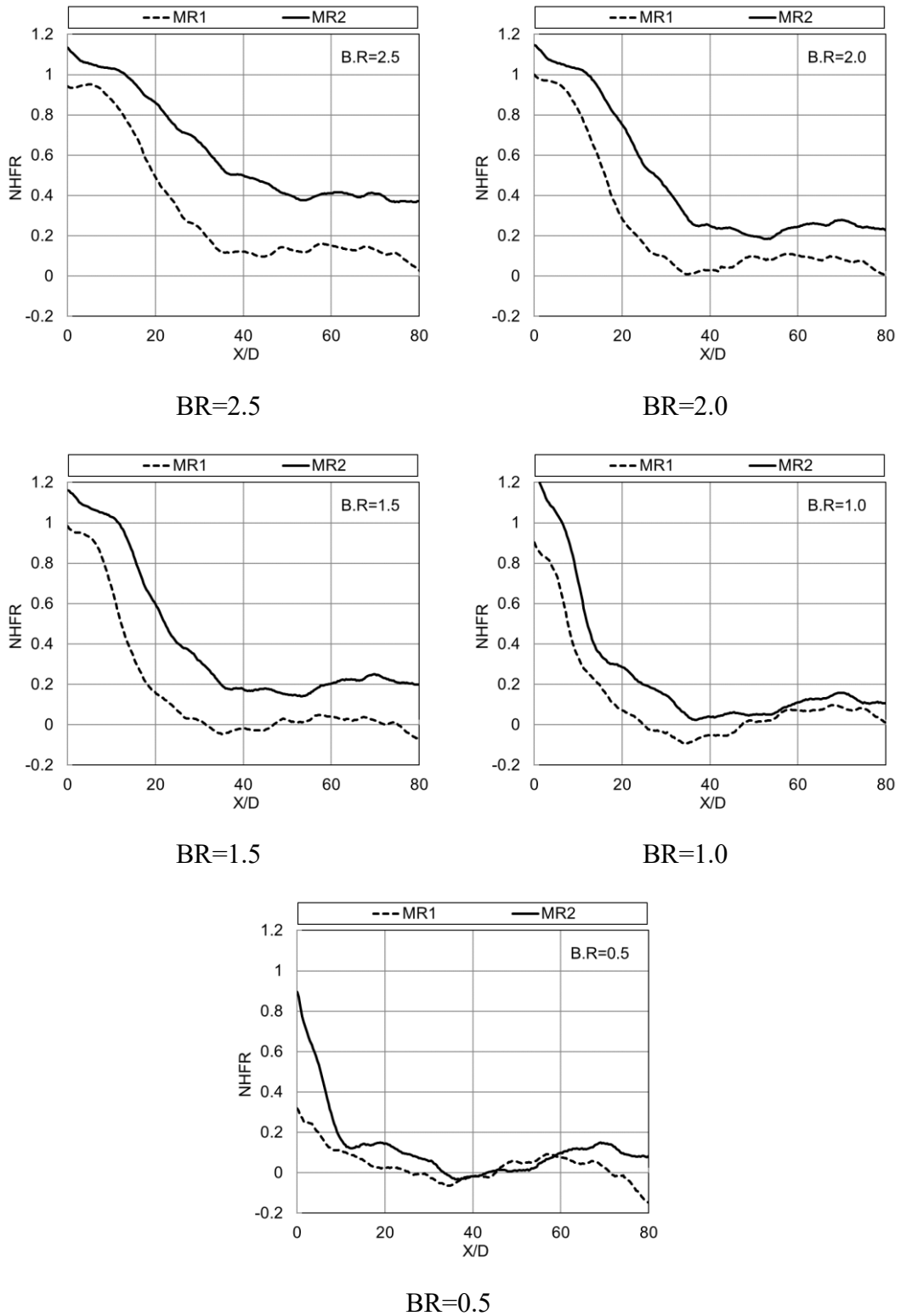


Fig. 5.24 Comparison of net heat flux reduction for machined ring 1 & 2 at different blowing ratios

5.4 Effusion Cooling

5.4.1 Adiabatic Film Cooling Effectiveness

For adiabatic film cooling effectiveness measurement, the secondary air is set to the required pressure in the coolant plenum through a pressure regulator and cooled to -42°C while passing through the liquid nitrogen heat exchanger and the mainstream air is kept at room temperature. The temperature of the film cooling air is measured inside the plenum at two locations. Thermographic image of effusion cooled test plate during the test run of 2.5 blowing ratio is shown in Fig. 5.25.

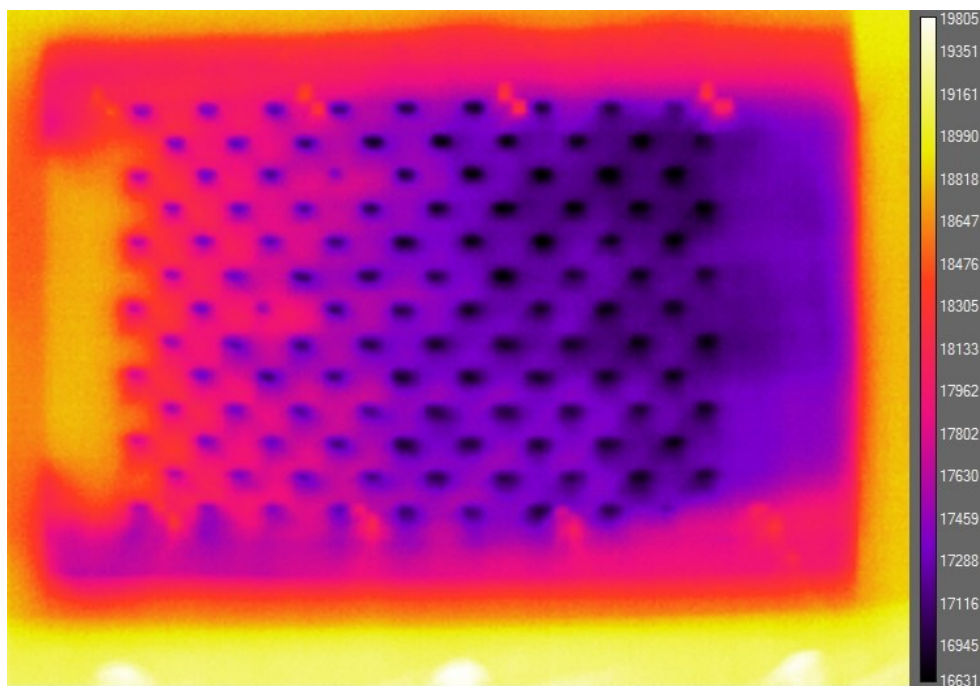


Fig. 5.25 Thermographic image of effusion cooled test plate at 2.5 blowing ratio

Fig. 5.26 shows the experimental adiabatic film cooling effectiveness distribution in streamwise direction for effusion cooling holes. Blowing ratio is varied from 0.5 to 2.5. Results show that the adiabatic effectiveness is increased with increase in blowing ratio. For a particular blowing ratio, cooling effectiveness continuously increases from the starting of the holes to the end region of holes. The cooling effectiveness decreases after the end region of holes.

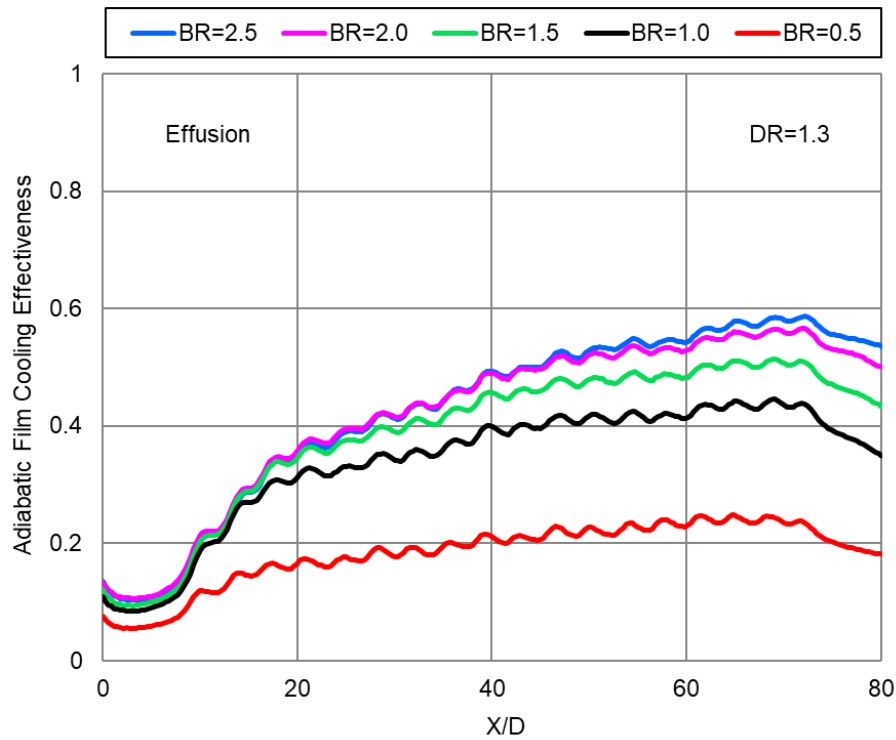


Fig. 5.26 Experimental adiabatic film cooling effectiveness distribution for effusion cooling holes

The CFD adiabatic film cooling effectiveness in streamwise direction for effusion cooling holes is shown in Fig. 5.27 for blowing ratios of 0.5 to 2.5. For two pitch region of holes, spanwise averaged values are taken. From this result, it is observed that the adiabatic effectiveness is increased with increase in blowing ratio at the end of the effusion holes. Effusion cooling holes are starting at an X/D of 10 and ends at X/D of around 70. For a specific blowing ratio, cooling effectiveness continuously increases from the starting of the holes upto the end of holes. This phenomenon is due to the additive nature of film formed by the coolant flow coming out from the consecutive holes in the row. This occurrence was found at all blowing ratios.

The CFD temperature contours in streamwise direction for effusion cooling holes is shown in Fig. 5.28 for blowing ratios of 0.5 to 2.5. The mainstream and coolant flow is from left to right. From the contours, it is seen that the starting region of the test plate shows the mainstream temperature (red colour) prior to the effusion holes. The film is formed due to the coolant flow through the effusion holes, and it is gradually

spreading due to the additive nature of film formation from the consecutive holes. Thus the temperature of the test plate is reduced as the X/D increases. Also, it is observed that at low blowing ratios, the coolant is attached to the surface from the starting of holes onwards. At higher blowing ratios of 2.5, the coolant jet lift-off takes place, and it attaches after some distance, then the coolant flow merges with other rows of effusion cooling holes.

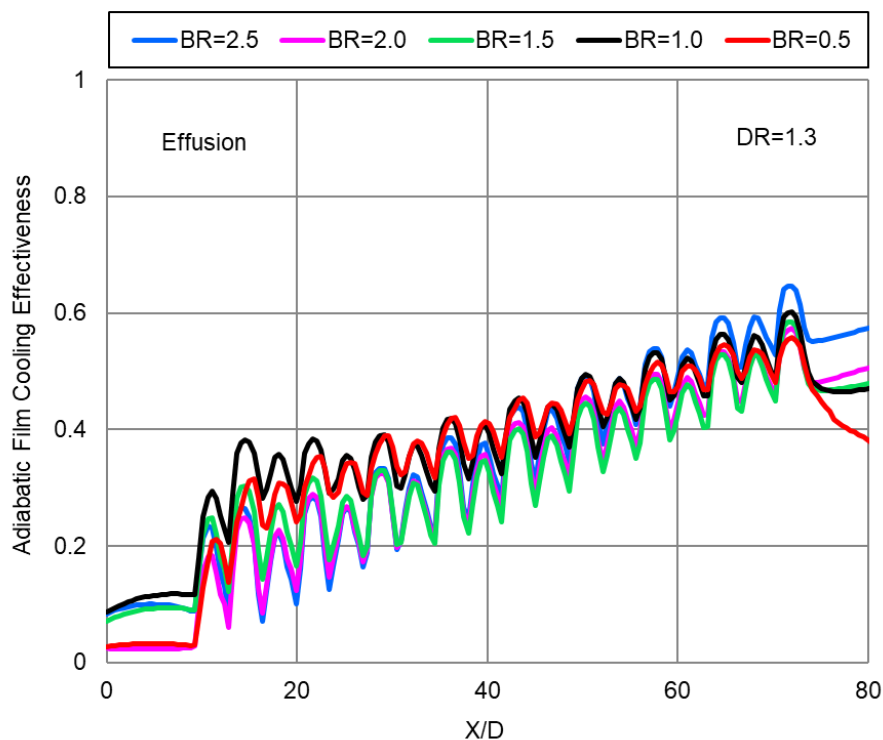
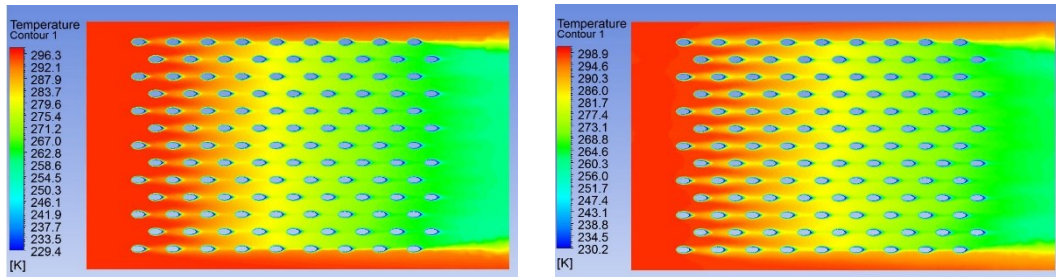


Fig. 5.27 CFD adiabatic film cooling effectiveness distribution for effusion cooling holes

The CFD flow field contours in streamwise direction for effusion cooling holes is shown in Fig. 5.29 for blowing ratios of 0.5 to 2.5. The film boundary layer formed is shown in this contours. Red colour shows the mainstream temperature, and the blue refers to the coolant temperature. For blowing ratio of 0.5, the coolant boundary layer is having less thickness and attached to the surface from the starting of holes onwards. As the blowing ratio increases, the boundary layer thickness increases due to the coolant jet lift-off.

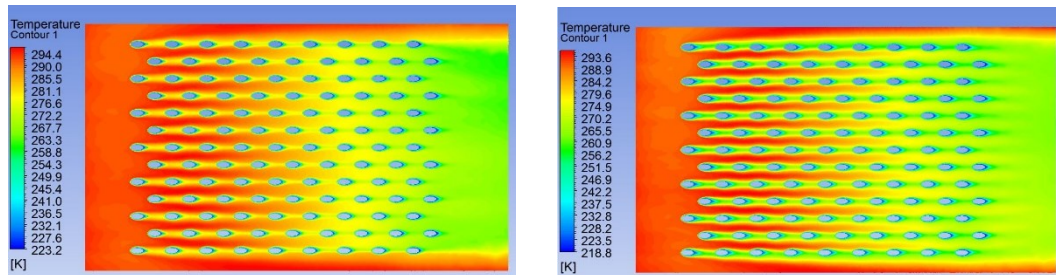
The experimental and CFD comparison of adiabatic film cooling effectiveness in streamwise direction is shown in Fig. 5.30 for all the blowing ratios. From this result,

it is observed that the CFD adiabatic effectiveness trends are matching with the experimental results. But CFD is showing less effectiveness values for BR=2.5, 2.0 and 1.5 than experimental results. At BR=1.0 it is matching, and at BR=0.5 it is higher than experimental results.



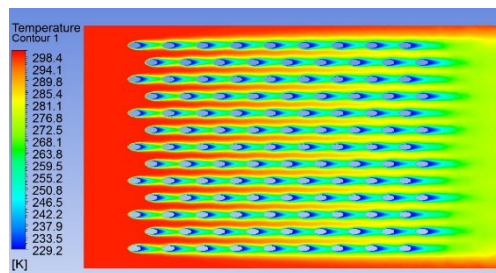
BR=2.5

BR=2.0



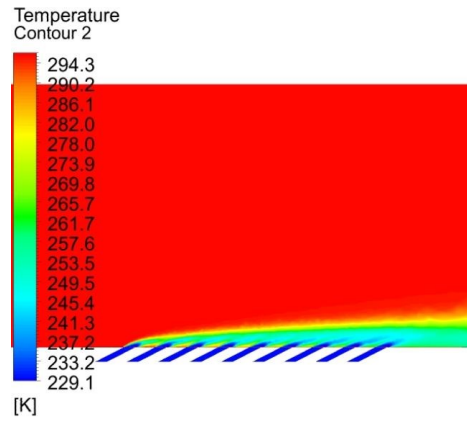
BR=1.5

BR=1.0

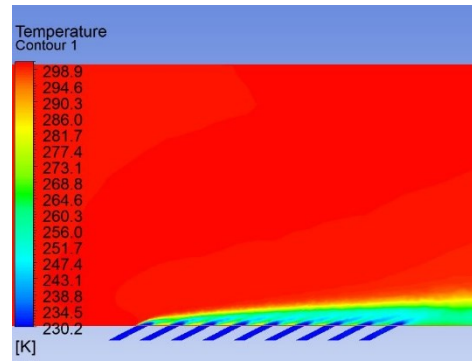


BR=0.5

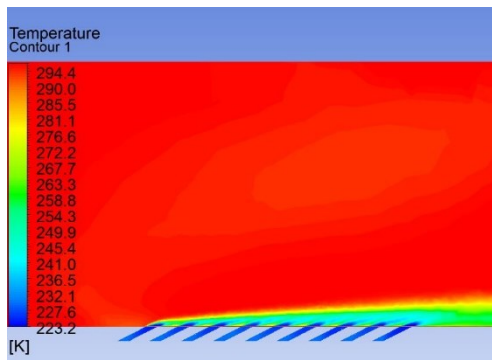
Fig. 5.28 CFD temperature contours for adiabatic effusion cooling holes



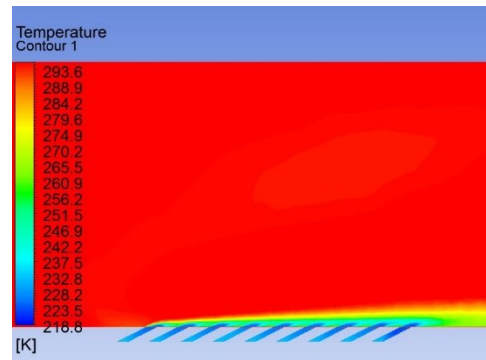
BR=2.5



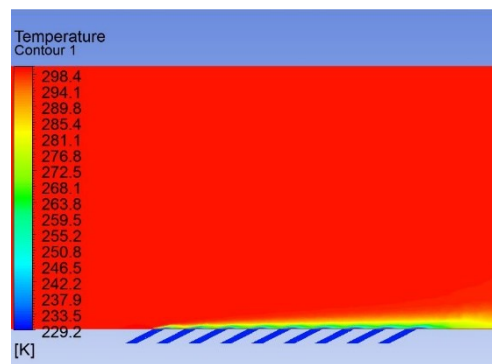
BR=2.0



BR=1.5



BR=1.0



BR=0.5

Fig. 5.29 CFD flow field contours for adiabatic effusion cooling holes

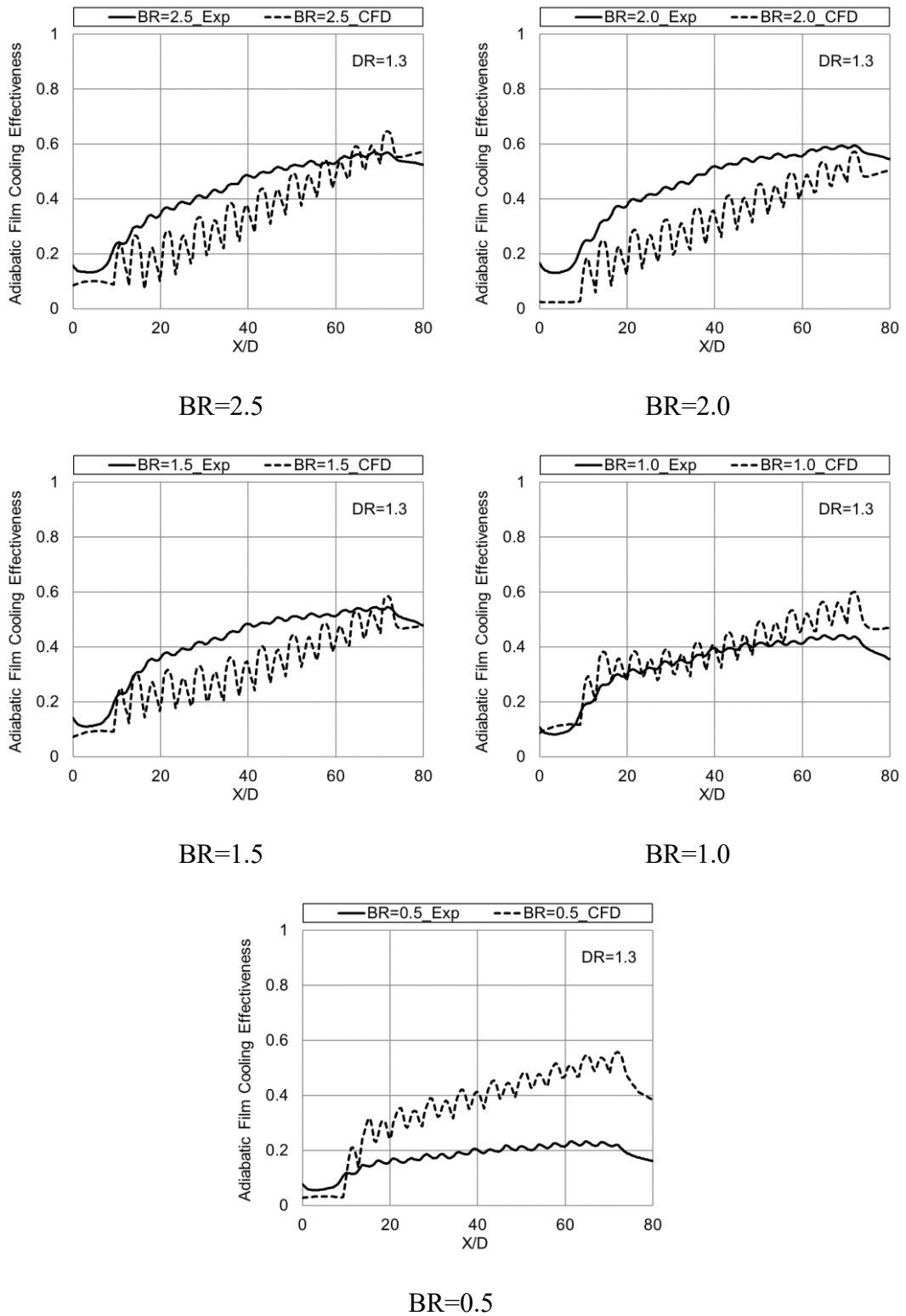


Fig. 5.30 Comparison of experimental and CFD adiabatic film cooling effectiveness for effusion cooling holes

5.4.2 Heat Transfer Coefficients

Fig. 5.31 shows the experimental film heat transfer coefficient in streamwise direction for effusion cooling holes. The results show that the heat transfer coefficient increases with an increase in blowing ratio. The peaks show the location of holes, but the heat transfer coefficient has a constant value from the start to the end of the effusion holes for each and every blowing ratio.

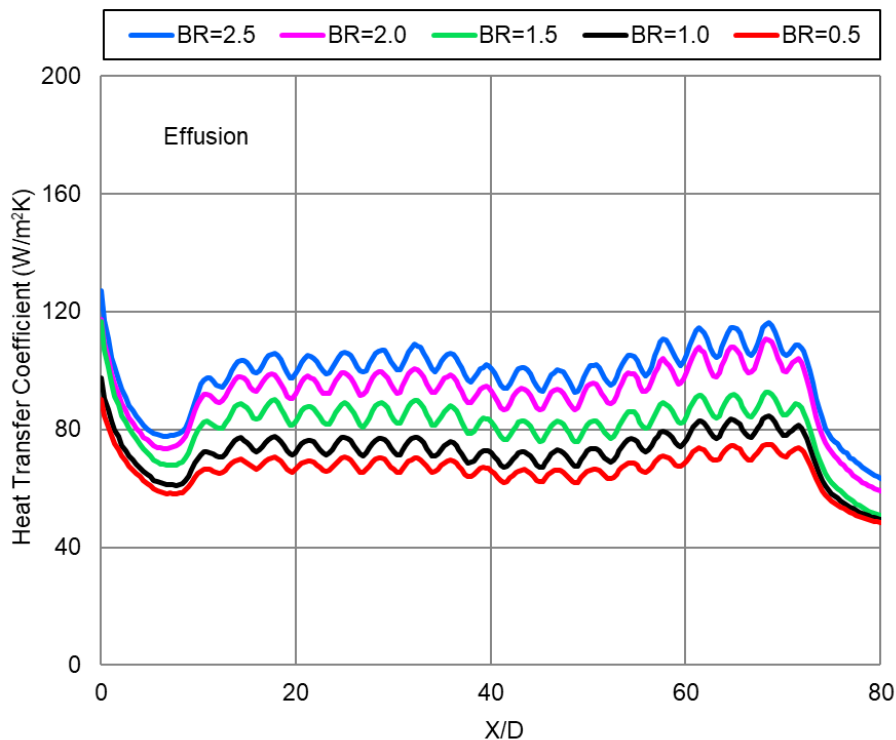


Fig. 5.31 Experimental film heat transfer coefficient for effusion cooling holes

Fig. 5.32 shows the heat transfer coefficient ratio in streamwise direction for effusion cooling holes. The experimental heat transfer coefficient results obtained for each blowing ratio is divided by the baseline (BR=0) heat transfer coefficient for effusion holes. The results show that the heat transfer coefficient ratio increases with an increase in blowing ratio. Fig. 5.33 shows the CFD film heat transfer coefficient in streamwise direction for effusion cooling holes. The results show that the film heat transfer coefficient increases with an increase in blowing ratio. Due to the film coverage is more at higher blowing ratios, the heat is taken away from the surface by the coolant film. But in the actual engine case, the coolant film reduces the heat transfer from the hot combustion gases to the liner surface. The peaks show the location of holes, but the

heat transfer coefficient has a constant value from the start to the end of the effusion holes for each and every blowing ratio.

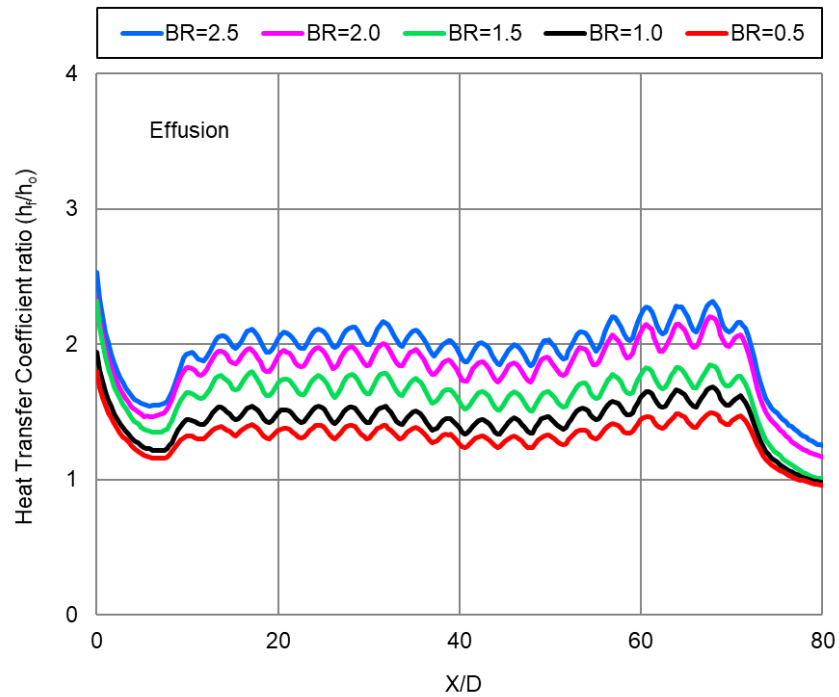


Fig. 5.32 Heat transfer coefficient ratio for effusion cooling holes

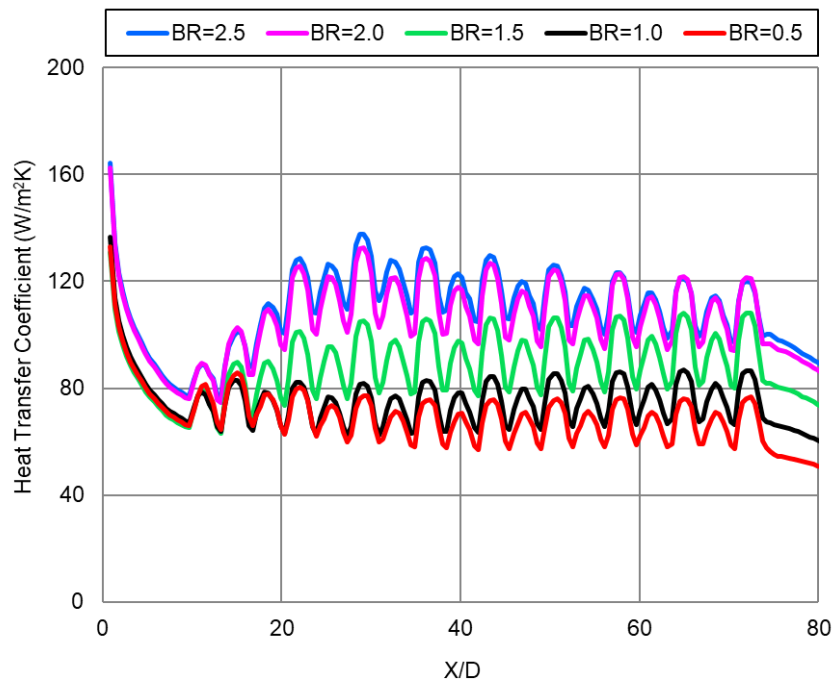


Fig. 5.33 CFD film heat transfer coefficient for effusion cooling holes

The comparison of the film heat transfer coefficient for experimental and CFD are shown in Fig. 5.34 for all the blowing ratios. From this result, both the CFD and experimental trends have a closer agreement, but the CFD values are little above the experimental values. In the hole locations, heat transfer coefficient values are higher and decrease after the holes. The experimental results show less heat transfer coefficient values at the start and end of the test plate than the CFD values. This is because at the edges, uniform heat flux cannot be obtained during experiments. Similarly, at the hole locations also, there would be non-uniform heat flux near the edges of each and every hole. That's the reason the values are less than CFD in the effusion hole region.

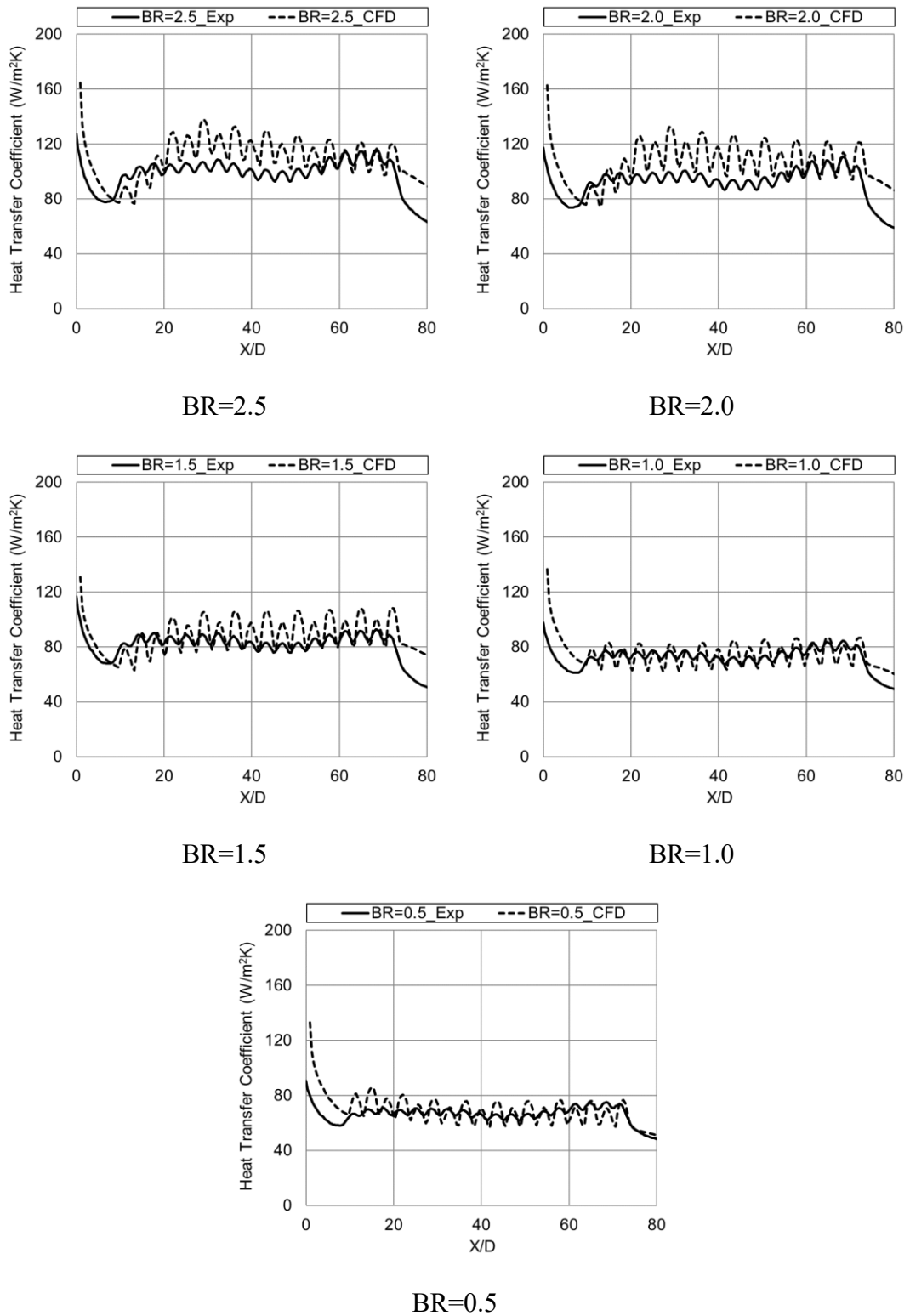


Fig. 5.34 Comparison of experimental and CFD film heat transfer coefficient for effusion cooling holes

5.4.3 Net Heat Flux Reduction

Fig. 5.35 shows the effect of blowing ratio on NHFR distribution for effusion cooling holes. The results show that the NHFR increases with an increase in blowing ratio. For blowing ratio 1.0 and above, NHFR values continuously increase from the starting of the effusion holes to till the end of holes due to a continuous increase in effectiveness values. Thereafter it suddenly decreases. For blowing ratio of 0.5, the values of NHFR are low in the middle region of holes, and negative values are seen at the end of the hole region.

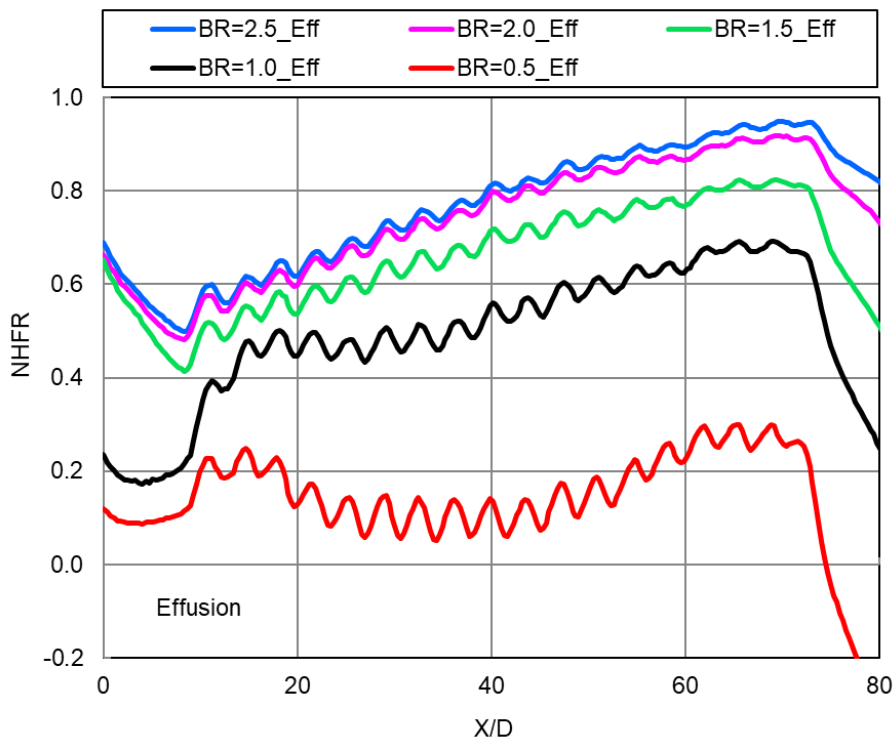


Fig. 5.35 Effect of blowing ratio on NHFR distribution for effusion cooling holes

5.5 Effusion Cooling with MR1

5.5.1 Adiabatic Film Cooling Effectiveness

Fig. 5.36 shows the thermographic image of effusion cooled test plate with machined ring geometry 1 during the test run of 2.5 blowing ratio. The blue colour in the starting region of the test plate prior to the effusion holes indicates the flow of coolant through the machined ring holes. The label shows the radiation values captured by the IR camera during the test run.

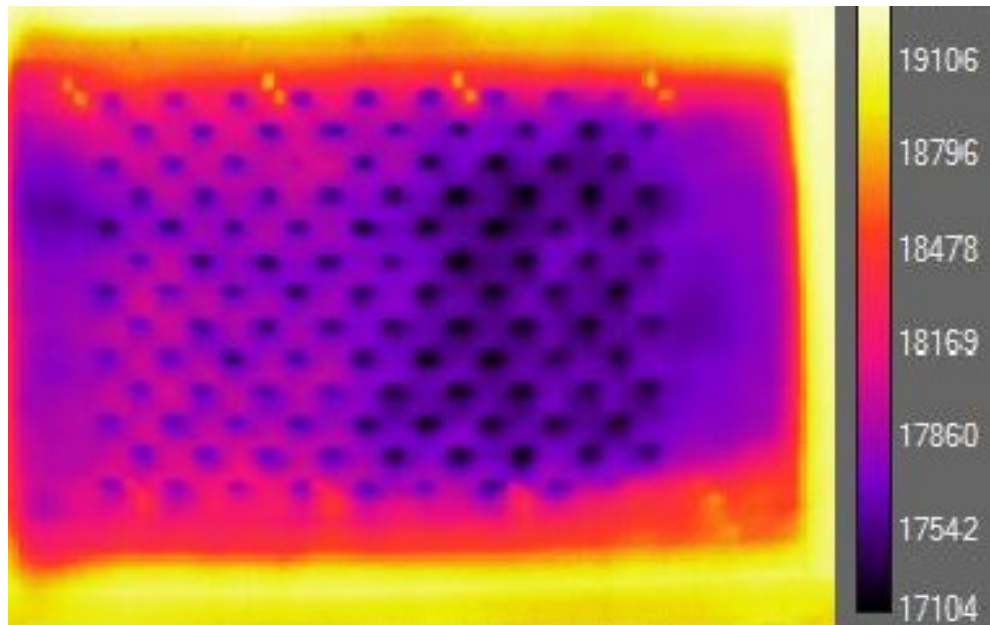


Fig. 5.36 Typical thermographic image of effusion cooling with MR1 at BR 2.5

Fig. 5.37 and Fig. 5.38 shows the experimental and CFD adiabatic film cooling effectiveness distribution in streamwise direction for effusion cooling holes with machined ring geometry 1. Blowing ratio is varied from 0.5 to 2.5. Results show that the adiabatic effectiveness is increased with increase in blowing ratio. Effusion cooling holes are starting at an X/D of 10 and ends at X/D of around 70. For all the blowing ratios, cooling effectiveness before the effusion holes are more due to the cooling provided by the machined ring geometry holes. The machined ring effect was seen upto X/D of 20. From the starting region to mid-region of the effusion holes, the cumulative cooling effect of both the machined ring and effusion holes are observed. At the end region of effusion holes, the cooling effectiveness produced only by effusion cooling holes is seen. From this figure for blowing ratios 2 and 2.5, it is observed that the cooling effectiveness is higher at the start of the test plate and maintained the same effect upto the end of the test plate due to the combined effect of both the machined ring and effusion holes.

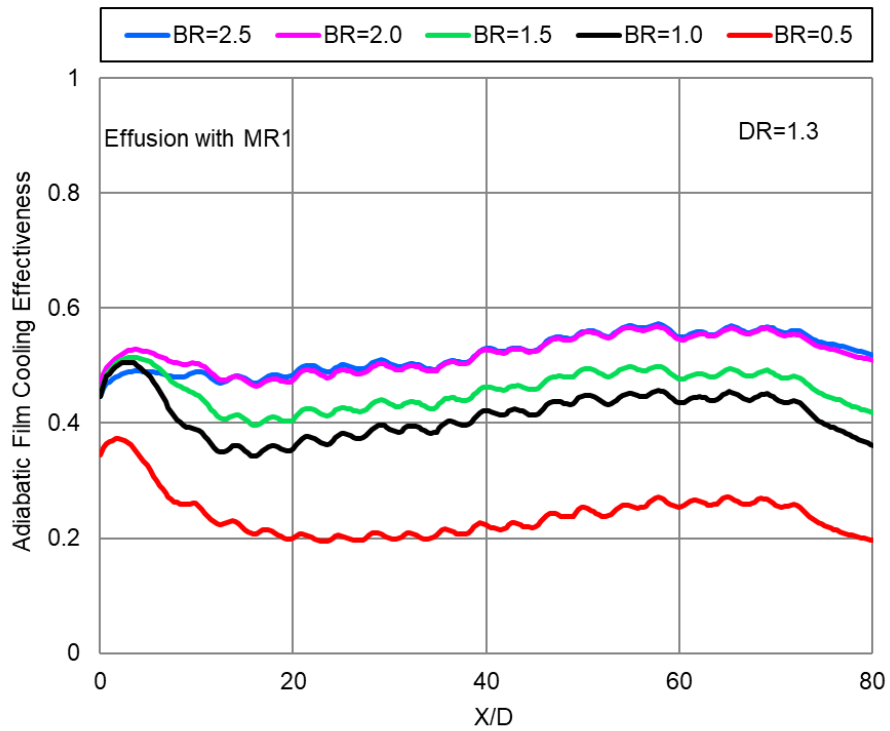


Fig. 5.37 Experimental adiabatic film cooling effectiveness distribution for effusion cooling holes with machined ring geometry 1

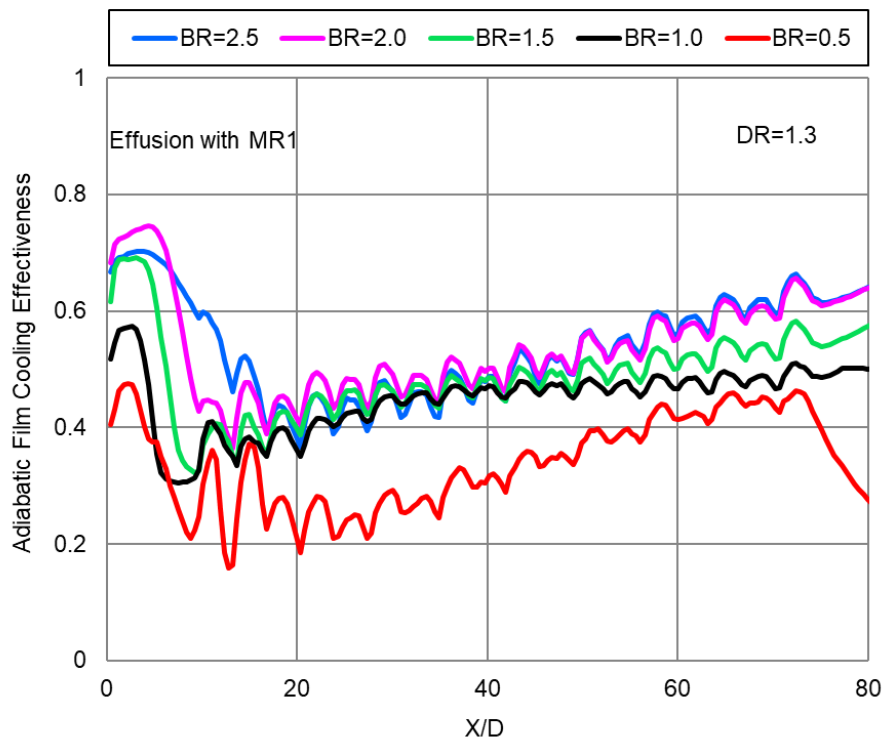
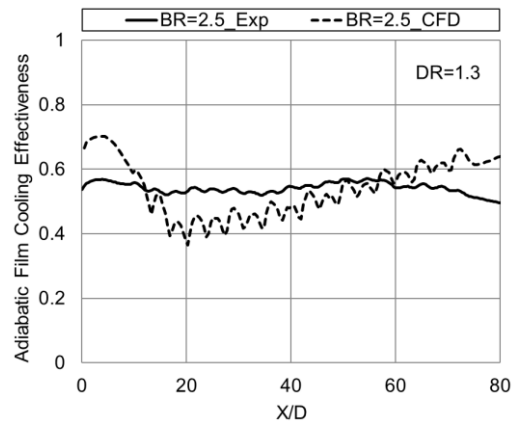
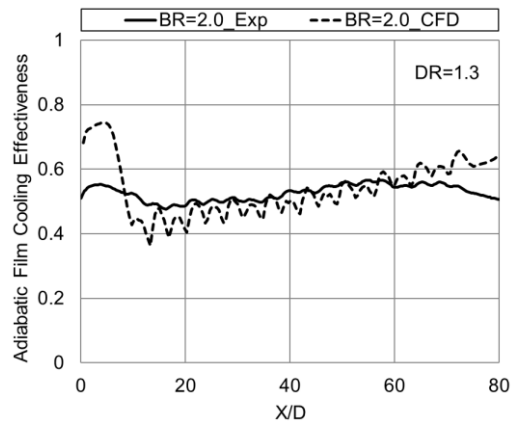


Fig. 5.38 CFD adiabatic film cooling effectiveness for effusion cooling holes with machined ring geometry 1

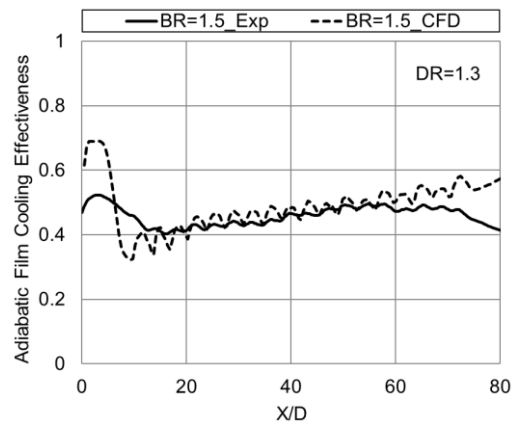
The experimental and CFD comparison of adiabatic film cooling effectiveness in streamwise direction for effusion with machined ring 1 is shown in Fig. 5.39 for all the blowing ratios. From this result, it is observed that the CFD adiabatic effectiveness trends are matching with the experimental results. But for higher blowing ratios, little deviation of effectiveness values is seen because CFD is not predicting the mixing phenomenon of mainstream and coolant properly. For lower blowing ratios of 0.5 and 1.0, the deviation is more.



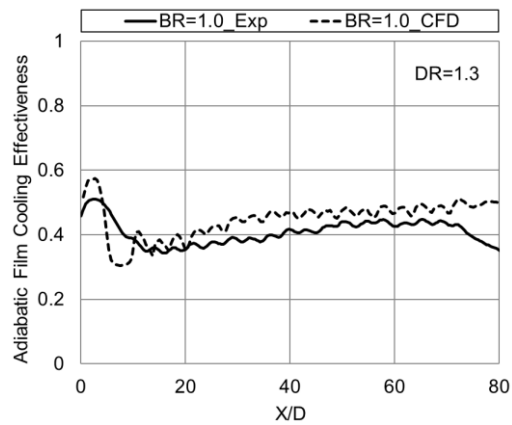
BR=2.5



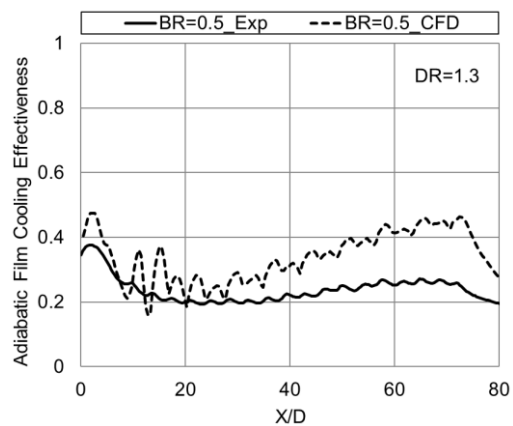
BR=2.0



BR=1.5



BR=1.0



BR=0.5

Fig. 5.39 Comparison of experimental and CFD film cooling effectiveness for effusion cooling holes with machined ring geometry 1

5.5.2 Heat Transfer Coefficients

Fig. 5.40 and Fig. 5.41 shows the experimental and CFD film heat transfer coefficient in streamwise direction for effusion cooling holes with machined ring 1 respectively. The results show that the heat transfer coefficient increases with an increase in blowing ratio. Due to machined ring 1 geometry, there is an increase in heat transfer coefficient prior to the effusion holes for all the blowing ratios.

Fig. 5.42 shows the heat transfer coefficient ratio in streamwise direction for effusion cooling holes with machined ring geometry 1. The experimental heat transfer coefficient results obtained for each blowing ratio is divided by the baseline (BR=0) heat transfer coefficient for effusion holes with machined ring geometry. The results show that the heat transfer coefficient ratio increases with an increase in blowing ratio.

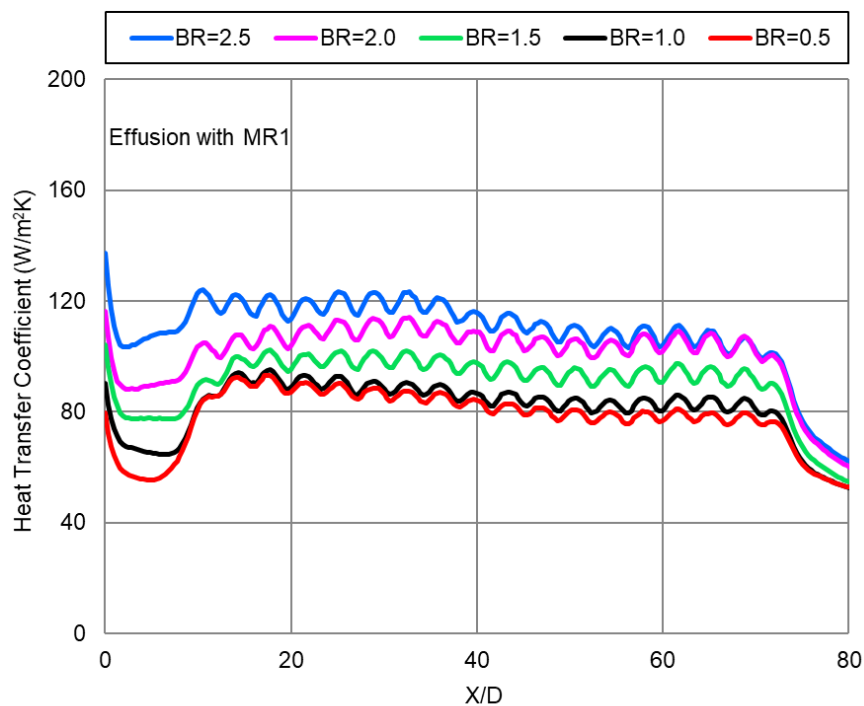


Fig. 5.40 Experimental film heat transfer coefficient for effusion cooling holes with machined ring geometry 1

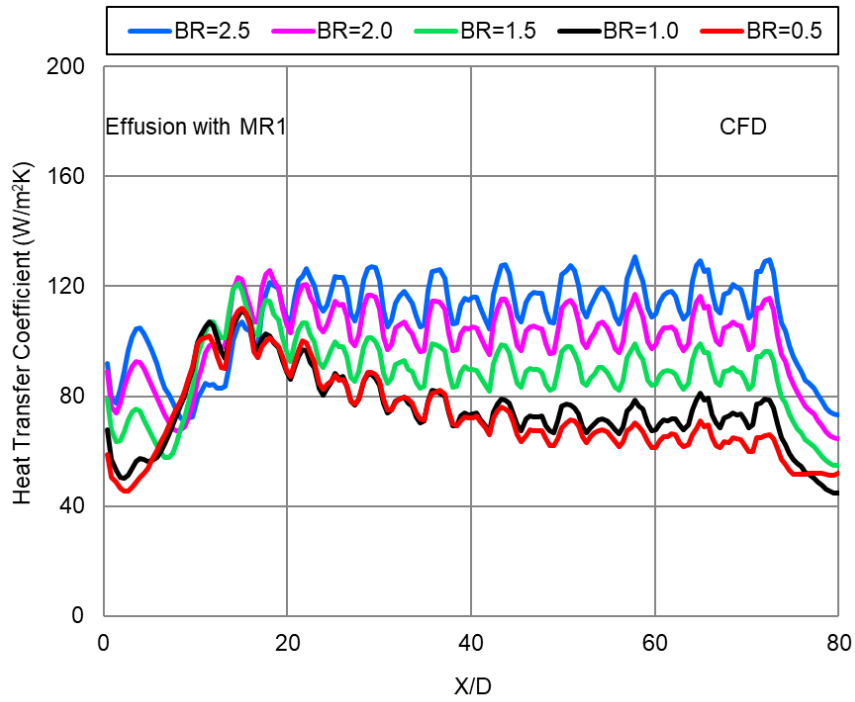


Fig. 5.41 CFD film heat transfer coefficient for effusion cooling holes with machined ring geometry 1

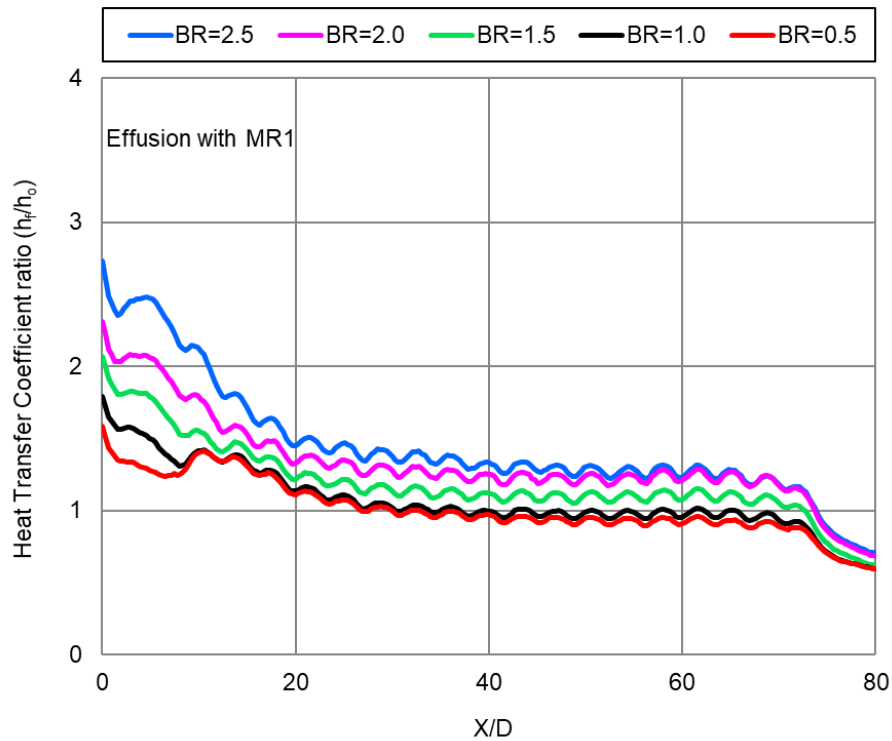
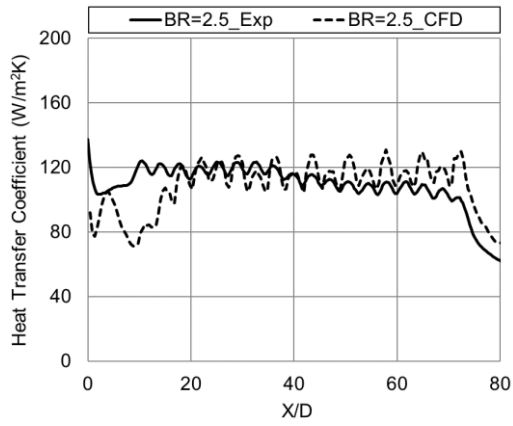
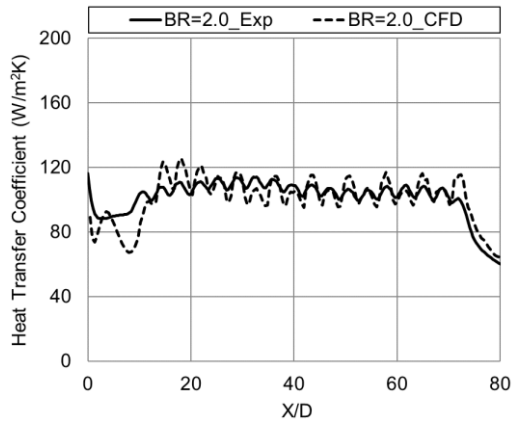


Fig. 5.42 Heat transfer coefficient ratio for effusion cooling holes with machined ring geometry 1

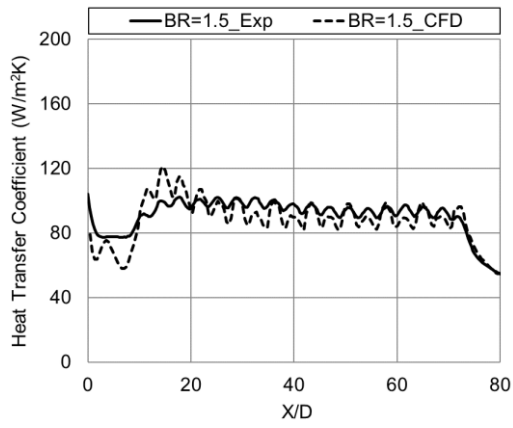
The experimental and CFD comparison of film heat transfer coefficient in streamwise direction for effusion with machined ring 1 is shown in Fig. 5.43 for all the blowing ratios. From this result, it is observed that the CFD film heat transfer coefficient trends are matching with the experimental results. But little deviation of effectiveness values is seen at the mixing region ($X/D < 20$) of the machined ring, effusion, and mainstream flow because CFD is not predicting the mixing phenomenon of mainstream and coolant properly. After $X/D > 20$ both the results are matching together.



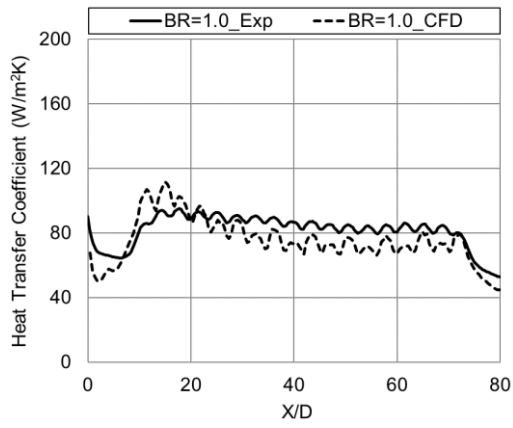
BR=2.5



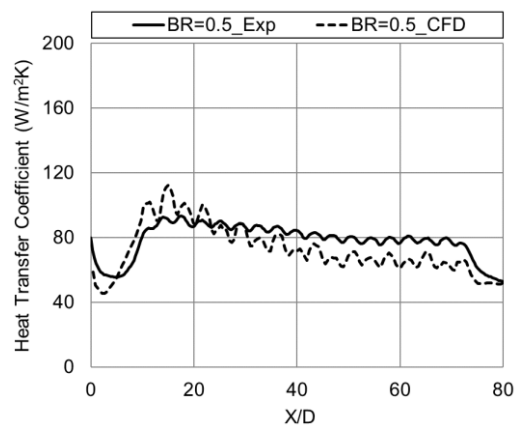
BR=2.0



BR=1.5



BR=1.0



BR=0.5

Fig. 5.43 Comparison of experimental and CFD film heat transfer coefficient for effusion cooling holes with machined ring geometry 1

5.5.3 Net Heat Flux Reduction

Fig. 5.44 shows the effect of blowing ratio on NHFR distribution for effusion cooling with machined ring 1 holes. The results show that the NHFR increases with an increase in blowing ratio. For blowing ratio 2.5 and 2.0, NHFR values are constant from the downstream of machined ring holes to till the end of effusion cooling holes due to constant effectiveness values. But for blowing ratio 1.5 and 1.0, NHFR values are higher in the downstream of machined ring holes, and it shows constant values in the effusion cooling hole region. For blowing ratio of 0.5, the values of NHFR continuously decreases till the mid-region of effusion holes and thereafter it is constant up to the end of the effusion hole region.

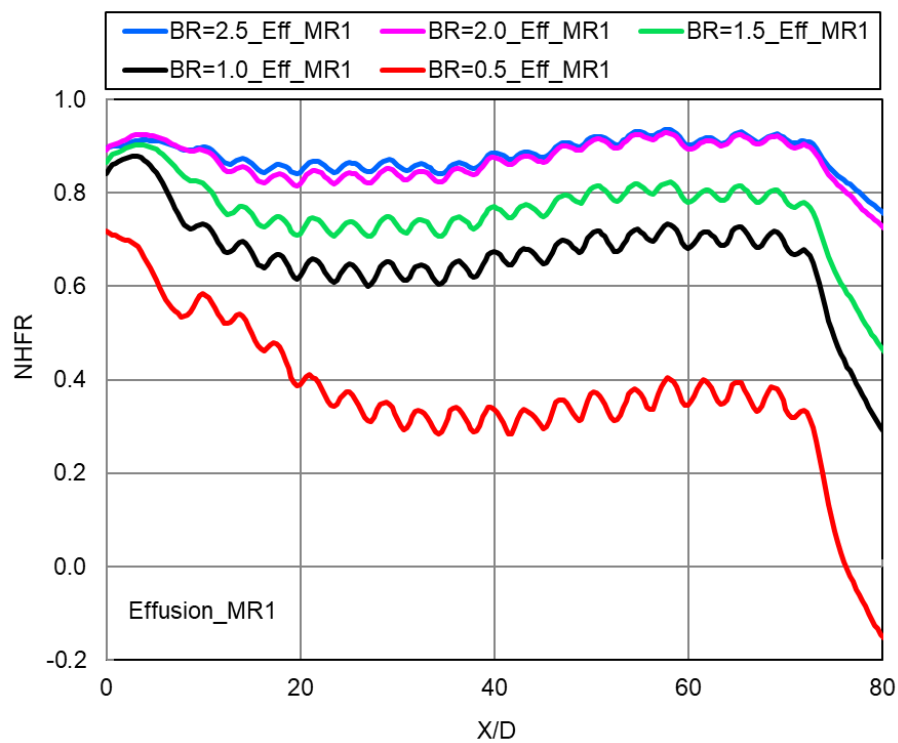


Fig. 5.44 Effect of blowing ratio on NHFR distribution for effusion cooling holes with machined ring geometry 1

5.6 Effusion Cooling with MR2

5.6.1 Adiabatic Film Cooling Effectiveness

Fig. 5.45 and Fig. 5.46 shows the experimental and CFD adiabatic film cooling effectiveness distribution in streamwise direction for effusion cooling holes with machined ring geometry 2 respectively. Blowing ratio is varied from 0.5 to 2.5. Results show that the adiabatic effectiveness is increased with increase in blowing ratio. For all the blowing ratios, cooling effectiveness before the effusion holes are more due to the cooling provided by the machined ring geometry holes. From the start of the test plate to the end, cooling effectiveness is constant for a blowing ratio of 2.5 and 2.0. For the remaining blowing ratios, starting region shows more cooling effect due to machined ring geometry and further downstream effusion holes cooling effect is observed.

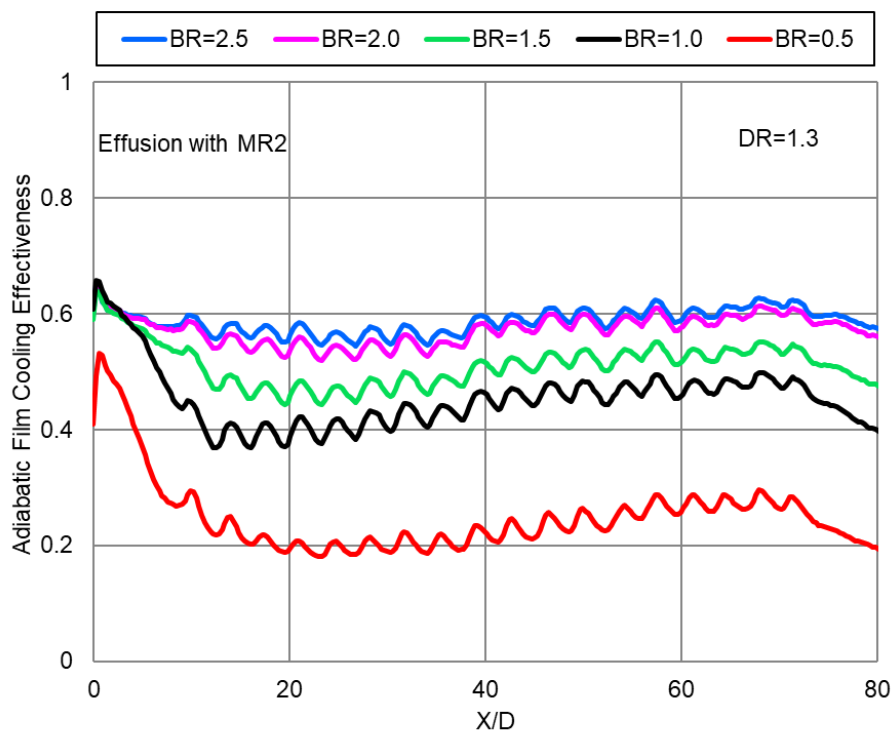


Fig. 5.45 Experimental adiabatic film cooling effectiveness distribution for effusion cooling holes with machined ring geometry 2

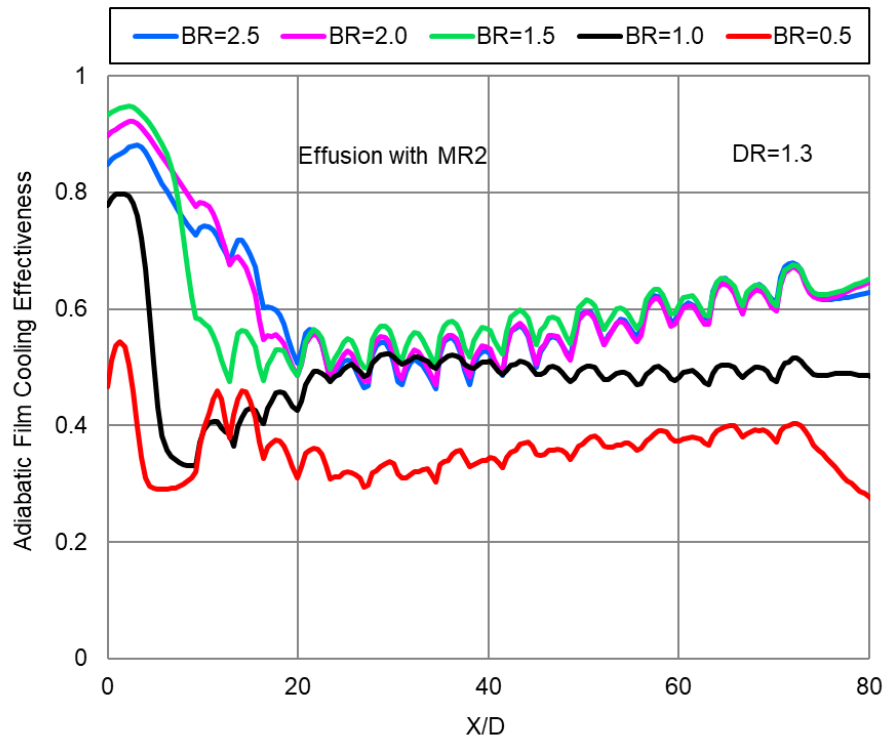


Fig. 5.46 CFD film cooling effectiveness for effusion cooling holes with machined ring geometry 2

Fig. 5.47 shows the CFD temperature contour at a blowing ratio of 2.5 for effusion cooling holes with machined ring geometry 2. In the colour bar, blue colour (229.6 K) shows the coolant temperature, and the red colour (294.6) shows the mainstream temperature. From the contour, the mainstream and the coolant flow is from left to right. The coolant flow through the machined ring holes cools the starting region of the test plate, i.e., prior to the effusion holes which can be seen as blue colour. At the first few effusion holes, the temperatures are less due to the effect of combined coolant flow from the machined ring and effusion holes. Afterward, the temperature slightly increased at the middle holes and then it decreased towards the end region of holes.

Fig. 5.48 shows the CFD flow field contour at a blowing ratio of 2.5 for effusion cooling holes with machined ring geometry 2. It is clearly seen that the flow from the machined ring holes forms the coolant film at the starting of the test plate. Then at the first and second effusion holes both the coolant flow from the machined ring and effusion mix together and forms the film boundary layer. The boundary layer of the

film gradually increases throughout the length of the test plate in the streamwise direction. This film protects the heat transfer from the hot mainstream to the liner surface.

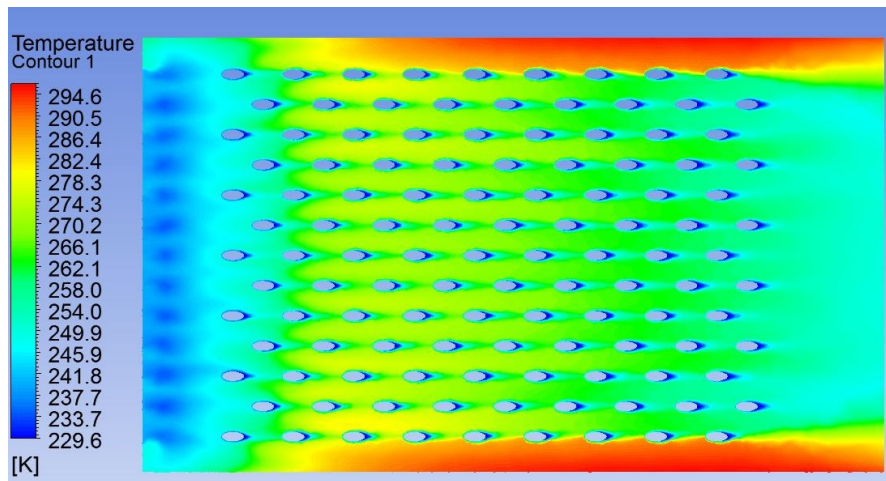


Fig. 5.47 CFD temperature contour at blowing ratio of 2.5 for effusion cooling holes with machined ring geometry 2

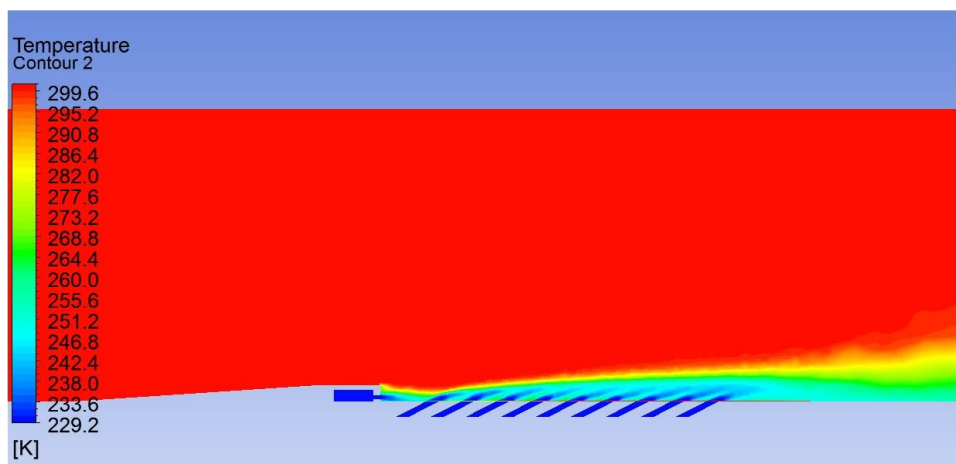


Fig. 5.48 CFD flow field contour at blowing ratio of 2.5 for effusion cooling holes with machined ring geometry 2

Fig. 5.49 shows the comparison between experimental and CFD adiabatic film cooling effectiveness at all blowing ratios. Both the experimental and CFD adiabatic film cooling effectiveness trends are almost same, but CFD shows higher values than experimental. The region before effusion holes, CFD shows higher values for all the blowing ratios. But in the effusion hole region, the CFD and experimental values are almost the same for higher blowing ratios of 2.5 to 1.5. For lower blowing ratio cases of 1.0 and 0.5, the difference is significant.

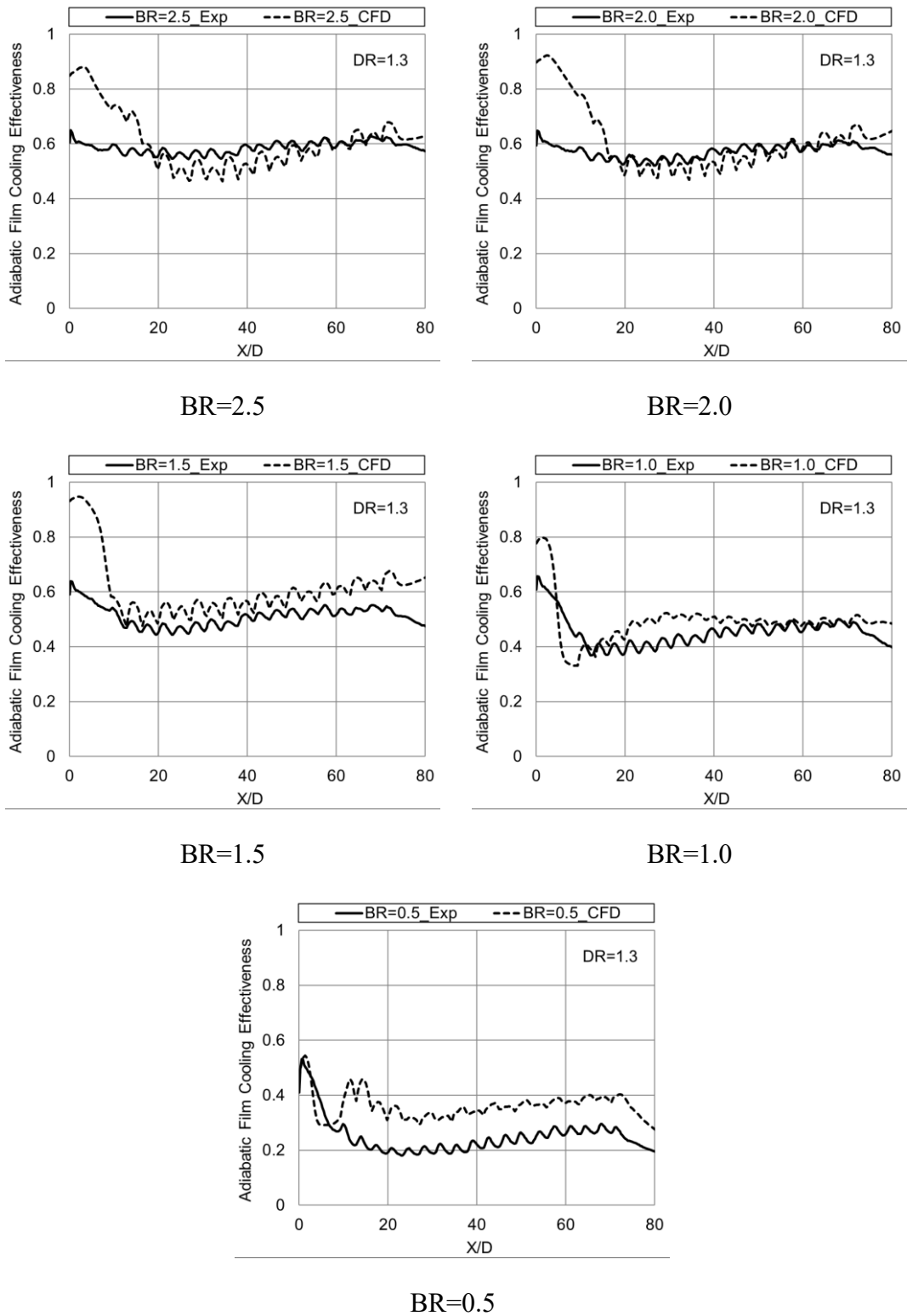


Fig. 5.49 Comparison of experimental and CFD film cooling effectiveness for effusion cooling holes with machined ring geometry 2

5.6.2 Heat Transfer Coefficients

Fig. 5.50 and Fig. 5.51 shows the experimental and CFD film heat transfer coefficient respectively in the streamwise direction for effusion cooling holes with machined ring 2. The results show that the heat transfer coefficient increases with an increase in blowing ratio. Due to machined ring 2 geometry, there is an increase in heat transfer coefficient prior to the effusion holes for all the blowing ratios. The increase in heat transfer coefficient is seen throughout the length of the test plate in the flow direction.

Fig. 5.52 shows the heat transfer coefficient ratio in streamwise direction for effusion cooling holes with machined ring geometry 2. The experimental heat transfer coefficient results obtained for each blowing ratio is divided by the baseline (BR=0) heat transfer coefficient for effusion holes with machined ring geometry. The results show that the heat transfer coefficient ratio increases with an increase in blowing ratio. But at the starting due to the higher heat transfer coefficient of machined ring flow, higher heat transfer ratio is seen upto X/D of 10. From X/D 10 to around 35 both the combined effects of the machined ring and effusion flow is observed.

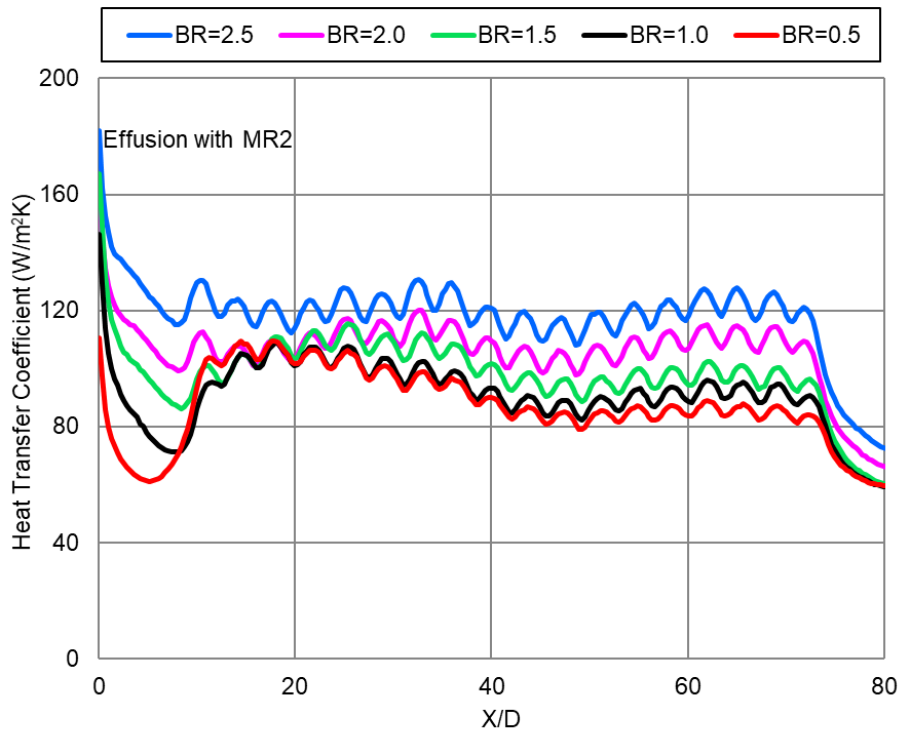


Fig. 5.50 Experimental film heat transfer coefficient for effusion cooling holes with machined ring geometry 2

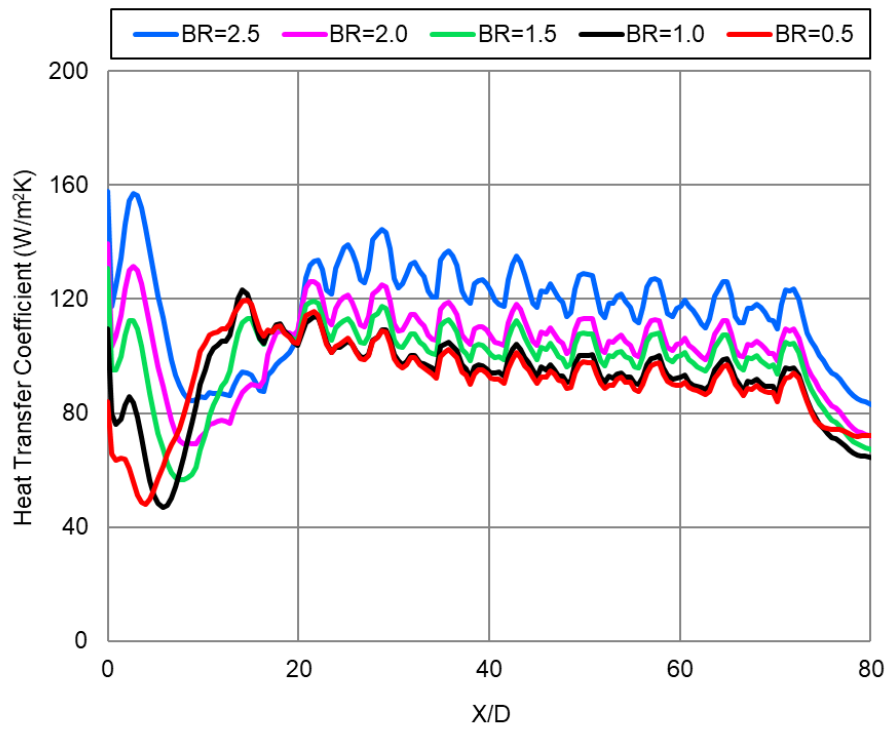


Fig. 5.51 CFD film heat transfer coefficient for effusion cooling holes with machined ring geometry 2

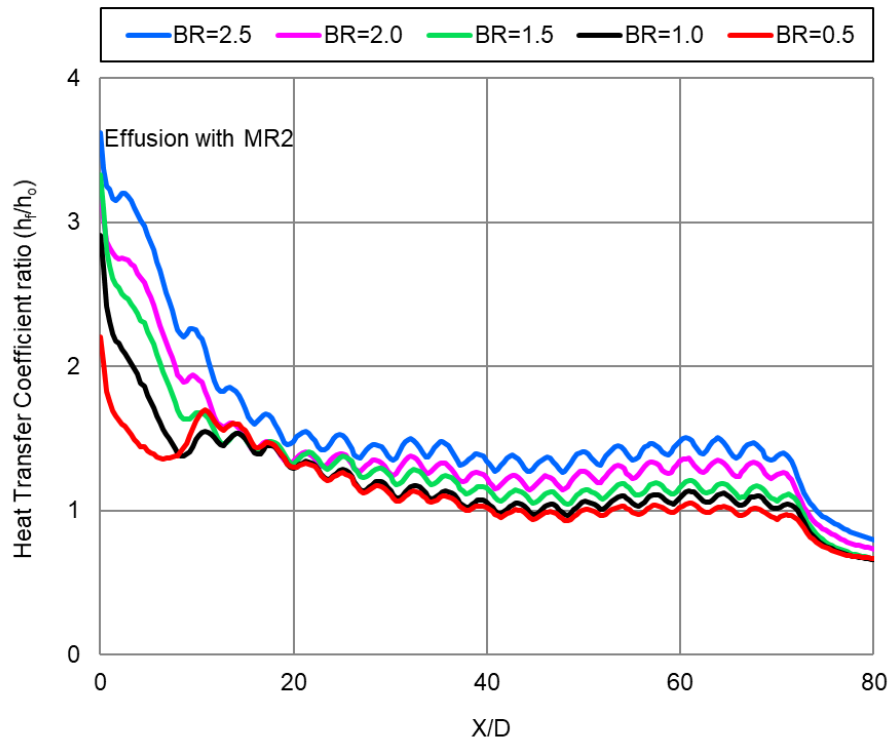
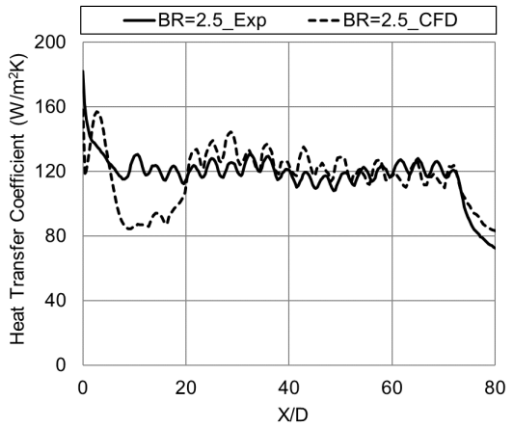
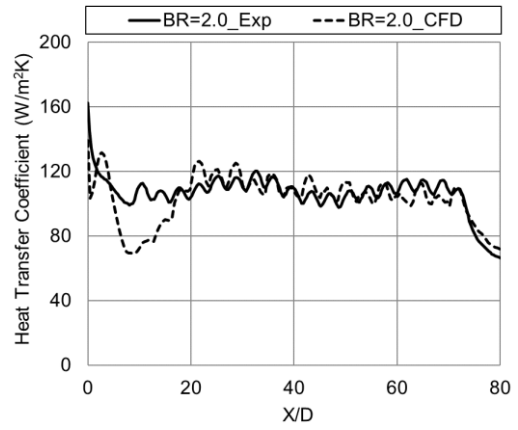


Fig. 5.52 Heat transfer coefficient ratio for effusion cooling holes with machined ring geometry 2

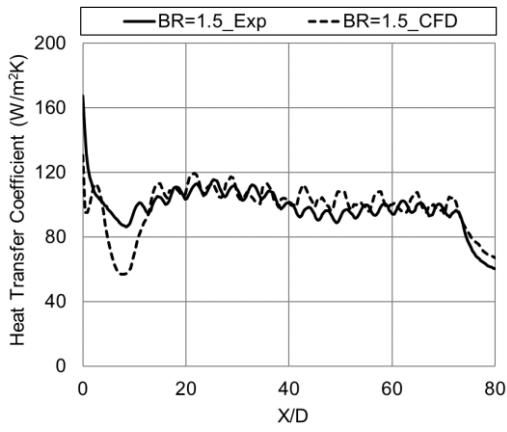
Fig. 5.53 shows the comparison between experimental and CFD film heat transfer coefficients at all blowing ratios. Both the experimental and CFD values are matching in most of the region, but it only varies at the flow region where the machined ring flow, effusion flow, and the mainstream flow mixing all together. The reason behind this is that the CFD is not able to capture the mixing phenomenon accurately.



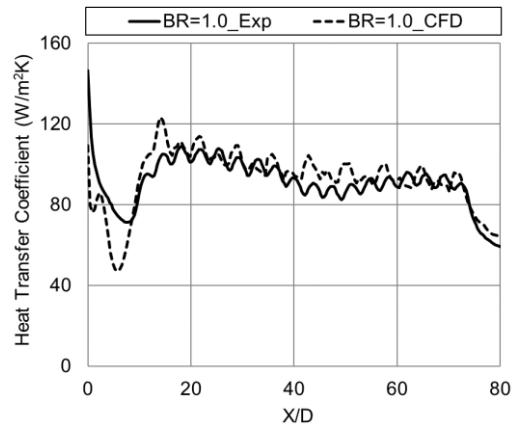
BR=2.5



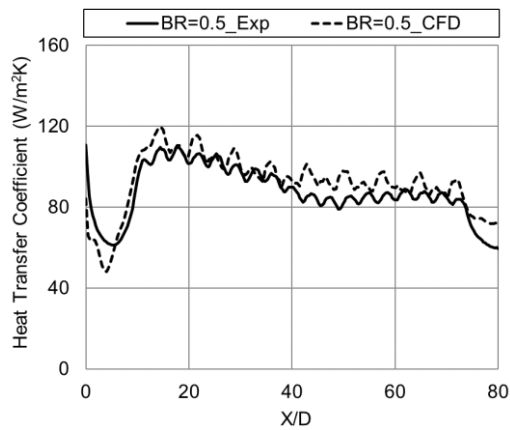
BR=2.0



BR=1.5



BR=1.0



BR=0.5

Fig. 5.53 Comparison of experimental and CFD film heat transfer coefficient for effusion cooling holes with machined ring geometry 2

5.6.3 Net Heat Flux Reduction

Fig. 5.54 shows the effect of blowing ratio on NHFR distribution for effusion cooling with machined ring 2 holes. The results show that the NHFR increases with an increase in blowing ratio. For blowing ratio 2.5 and 2.0, NHFR values are constant from the downstream of machined ring holes to till the end of effusion cooling holes due to constant effectiveness values. But for blowing ratio 1.5 and 1.0, NHFR values are higher in the downstream of machined ring holes, and it shows constant values in the effusion cooling hole region. For blowing ratio of 0.5, the values of NHFR continuously decreases till the mid-region of effusion holes and thereafter it is constant up to the end of the effusion hole region.

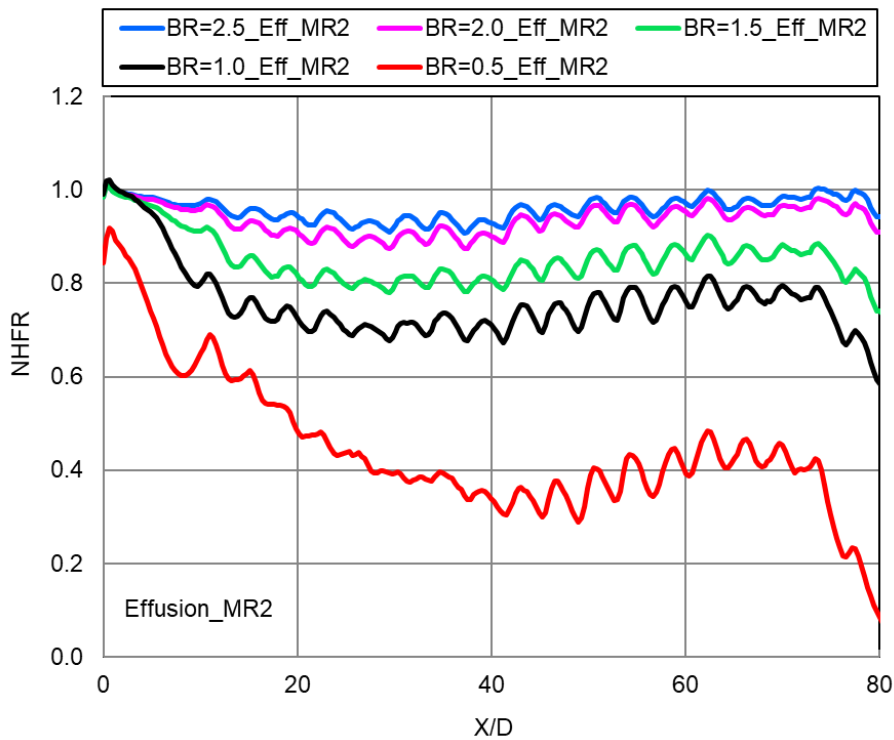


Fig. 5.54 Effect of blowing ratio on NHFR distribution for effusion cooling holes with machined ring geometry 2

5.7 Comparison Between Effusion Cooling with and Without Machined Ring Geometries

Fig. 5.55 shows the comparison of adiabatic cooling effectiveness results for the effusion holes with and without machined ring geometries upstream at all the blowing ratios. The results show that the cooling effectiveness is higher for effusion holes with machined ring geometries. Machined ring geometries are giving higher effectiveness than effusion holes because the film formed from the machined ring cooling holes increases the effectiveness in the starting region prior to the effusion holes. The same phenomenon was seen in other blowing ratios also. In the effusion cooling case, the effectiveness increases gradually from the starting to end region of the holes. But in effusion cooling with machined ring geometries case, from $X/D=0$ onwards shows higher effectiveness due to the coolant flow through the machined ring holes. For the blowing ratio of 2.5 and 2.0, the effectiveness tends to merge with effusion cooling effectiveness at X/D of 60. At blowing ratio of 1.5 and 1.0, it merges with effusion cooling effectiveness at X/D of 40. But in lower blowing ratio of 0.5, it merges even before at X/D of 30.

Fig. 5.56 shows the comparison of heat transfer coefficient results for the effusion holes with and without machined ring geometries upstream at different blowing ratios. The results show that the heat transfer coefficient is higher for effusion holes with machined ring geometries at all the blowing ratios. At each blowing ratio case, effusion holes with machined ring geometry 1 & 2 give more film heat transfer coefficient compared to the effusion cooling holes alone. The machined ring flow combines with the flow through the effusion holes and gives higher film heat transfer coefficient upto the end of the test plate. At higher blowing ratios, the starting region, i.e., the region between the exit of the machined ring holes ($X/D=0$) to the start of the effusion holes ($X/D=10.67$) also shows higher heat transfer coefficient. Machined ring geometry 2 gives higher heat transfer coefficient than machined ring geometry 1 because it has more cooling holes with less hole pitch than the machined ring 1. In addition, more coolant mass flow is flowing through the cooling holes for machined ring 2 and the film formed has more coverage in the downstream distance.

Fig. 5.57 shows the comparison of net heat flux reduction results for the effusion holes with and without machined ring geometries at different blowing ratios. The results show that the NHFR is higher for effusion holes with machined ring geometries at all the blowing ratios. At each blowing ratio case, effusion holes with machined ring geometry 1 & 2 give more NHFR compared to the effusion cooling holes alone. The machined ring flow combines with the flow through the effusion holes and gives higher NHFR upto the end of the test plate. At higher blowing ratios, the starting region, i.e., the region between the exit of the machined ring holes ($X/D=0$) to the start of the effusion holes ($X/D=10.67$) also shows higher NHFR. The effusion hole along with machined ring geometry 2 is giving higher NHFR than the other two cases. This is due to the more amount of coolant flow through the cooling holes for machined ring 2 and the film formed has more coverage in the downstream distance.

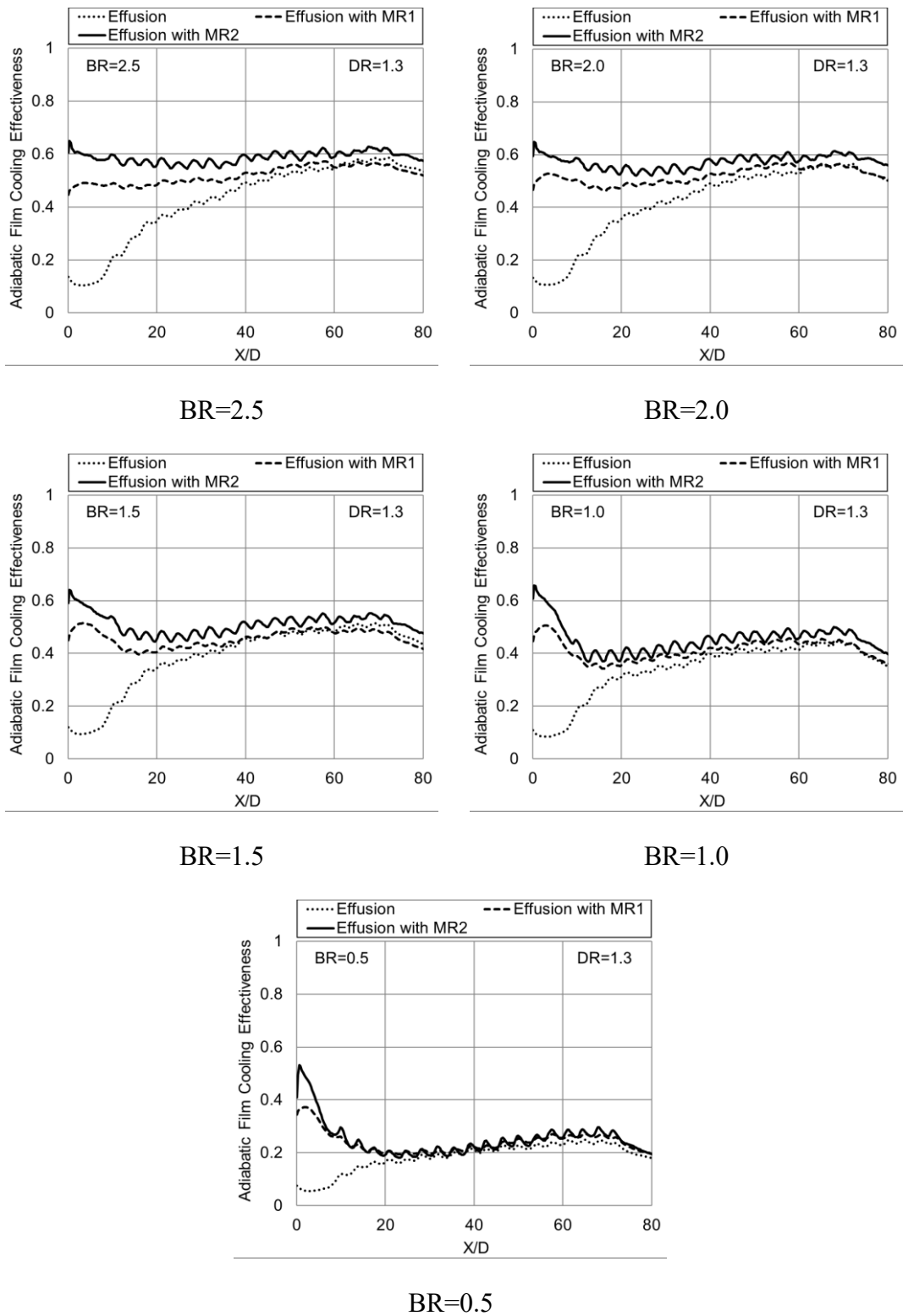
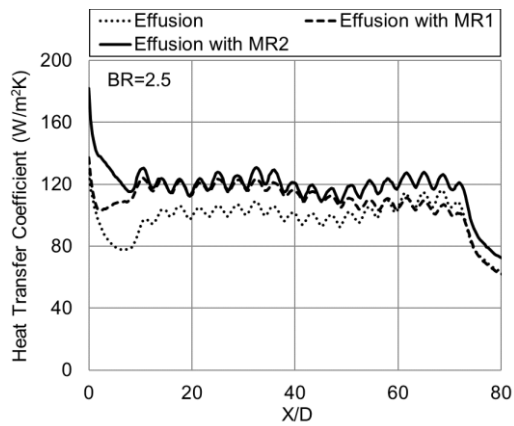
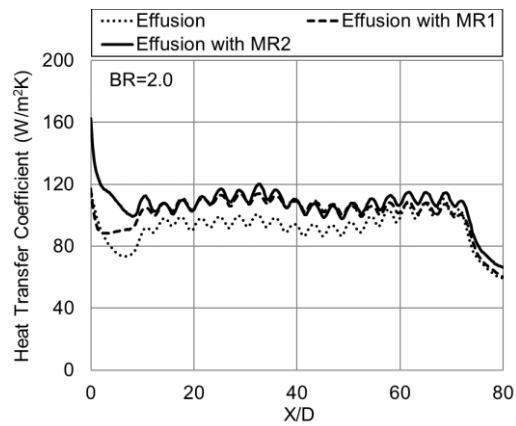


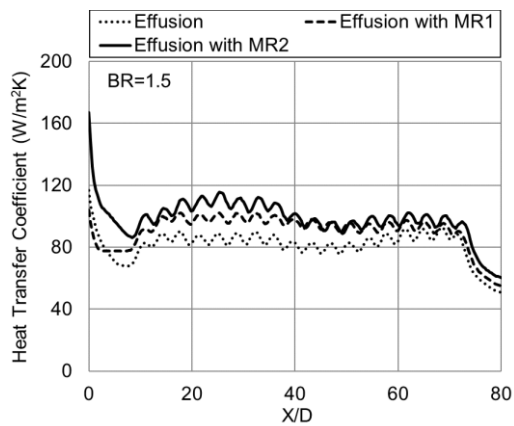
Fig. 5.55 Comparison of adiabatic film cooling effectiveness for effusion holes with and without machined ring geometries at different blowing ratios



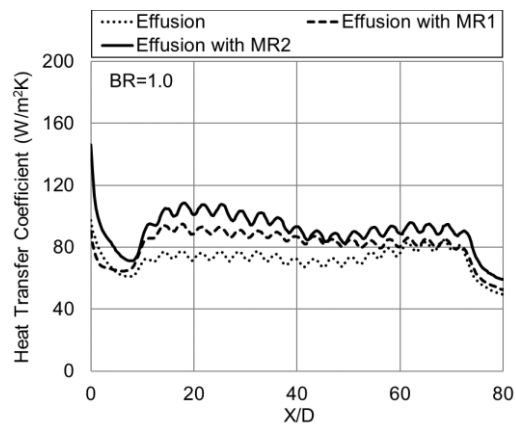
BR=2.5



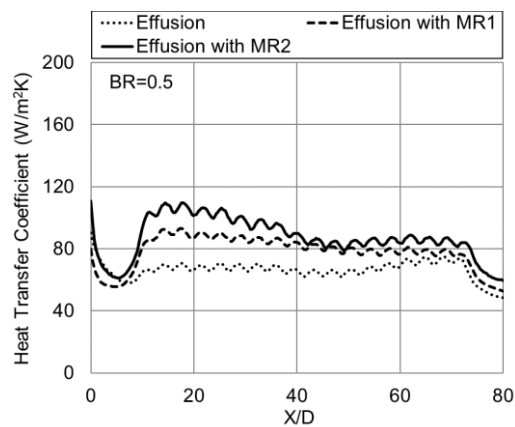
BR=2.0



BR=1.5



BR=1.0



BR=0.5

Fig. 5.56 Comparison of film heat transfer coefficient for effusion holes with and without machined ring geometries at different blowing ratios

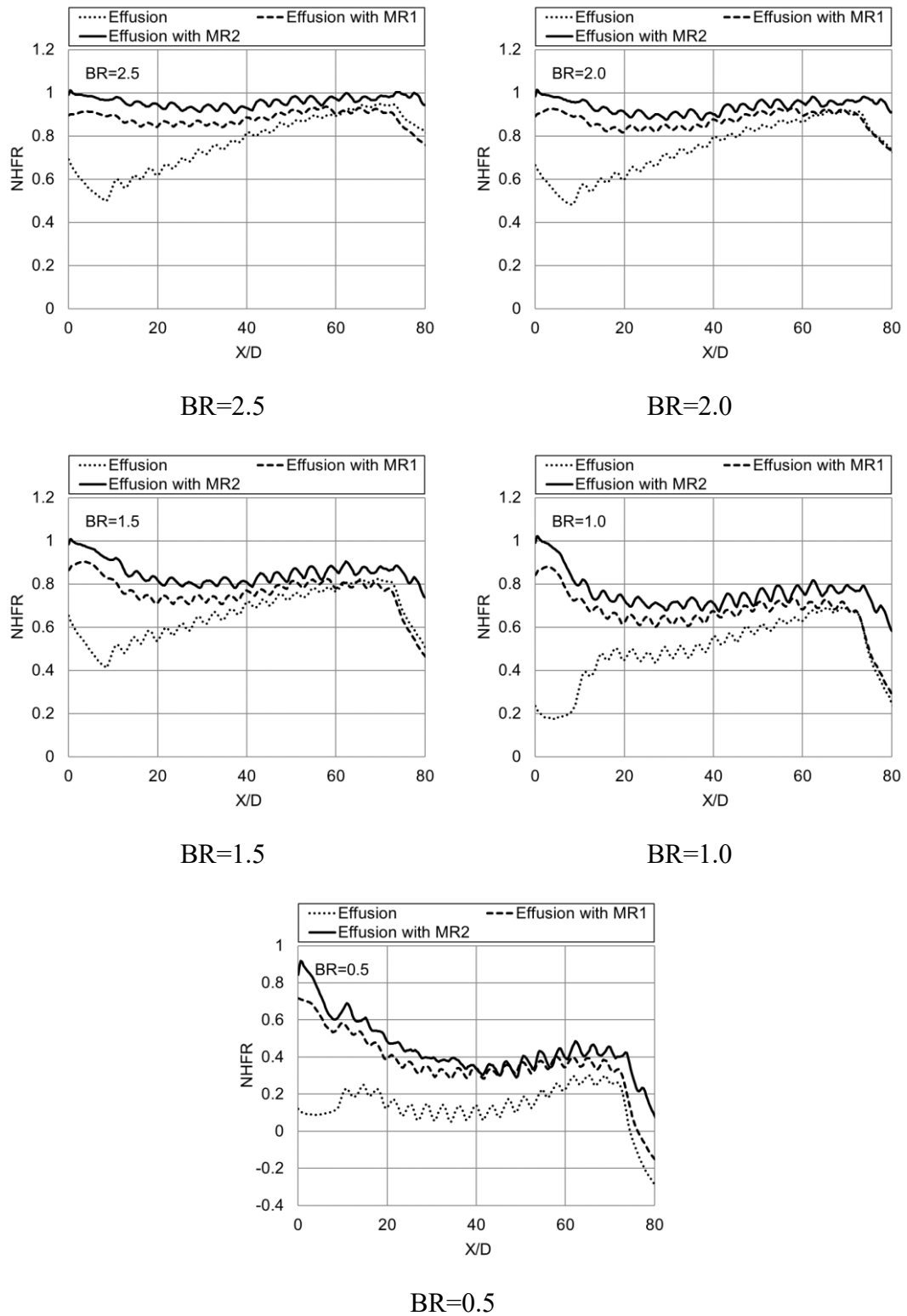


Fig. 5.57 Comparison of net heat flux reduction for effusion holes with and without machined ring geometries at different blowing ratios

5.8 Overall Cooling Effectiveness for Effusion Holes

In the previous sections, the importance of net heat flux reduction is described. But the NHFR tells only the effect of heat flux reduction with and without film cooling. For the slot cooling or film cooling with larger pitch holes, NHFR values are sufficient to find out the metal liner surface temperatures. But in the case of effusion cooling, the effusion holes are closely packed together and the effect of heat transfer takes place inside the holes is significant when the coolant passes through the holes. This overall cooling effectiveness includes the combined effect of convective heat transfer coefficient from the hot mainstream to the effusion plate, the adiabatic film cooling effectiveness, the convective heat transfer coefficient of cold air when it flows through the cooling holes, conduction through the liner thickness and the convective heat transfer coefficient at the backside of the effusion plate to the coolant air in the coolant chamber. Thus the overall cooling effectiveness measurements through the metallic liner test plates is important for effusion holes which resemble the real engine conditions.

The overall cooling effectiveness measurements are carried out with hot mainstream and the coolant at a lower temperature. The mainstream air velocity of 20 m/s is set by measuring the static and total pressures in the mainstream duct. The Reynolds number at this velocity and based on the hydraulic diameter of the duct is 3×10^5 . After setting the flow, the heater coils are energized. Approximately 20 minutes is required to heat the mainstream air to reach the required temperature of 80°C. After establishing the steady-state condition of the mainstream air, the coolant flow is set using the coolant chamber total pressure for a particular blowing ratio. The temperature of the coolant air passing through the liquid nitrogen heat exchanger is continuously monitored, and the level of liquid nitrogen in the heat exchanger is adjusted in such a way that the coolant temperature maintains at 0°C. Thus, the density ratio between coolant to mainstream is maintained at 1.3 for overall cooling effectiveness. The reference thermocouples fixed to the test plate is connected to a temperature indicator, and the test plate temperature is continuously monitored. The test plate is assumed to attain steady condition when the change in measured temperature of the test plate over

a period of 1 minute is less than $\pm 1^\circ\text{C}$ and the thermogram of the test plate are recorded by the infrared camera. At the same time, the mainstream temperature (T_m) and coolant temperature (T_c) are also recorded. The approximate Biot numbers expected inside the cooling holes and on the gas side in actual engine conditions are maintained during the tests. Once the readings are recorded for a particular blowing ratio, then the coolant chamber pressure is adjusted for the next blowing ratio, and the same procedure is repeated.

5.8.1 Test plate with 7.2D Pitch

Overall film cooling effectiveness is calculated for the test plate having a hole diameter of 1 mm, 27° hole angle and a hole pitch of 7.2D in both streamwise and spanwise direction. Experimental and numerical analyses are carried out for the flow through effusion holes. The results from the numerical solution for a spanwise averaged two pitch region are extracted along the streamwise direction and compared with the experimental results for the same spanwise averaged two pitch region. The overall effectiveness distribution results of spanwise averaged two pitch region for density ratio of 1.3 at different blowing ratios obtained experimentally are plotted along streamwise direction X/D as shown in Fig. 5.58. The effusion holes start at 12.5 X/D from the starting edge of the plate and end at 79 X/D . The overall effectiveness is observed to increase with an increase in blowing ratio from 0.5 to 2.5, along with the downstream direction of the hole region. For all blowing ratios as the X/D increases the effectiveness increases upto the end of the holes due to the cumulative film effects from the previous holes. At the end of the hole region, the effectiveness drops.

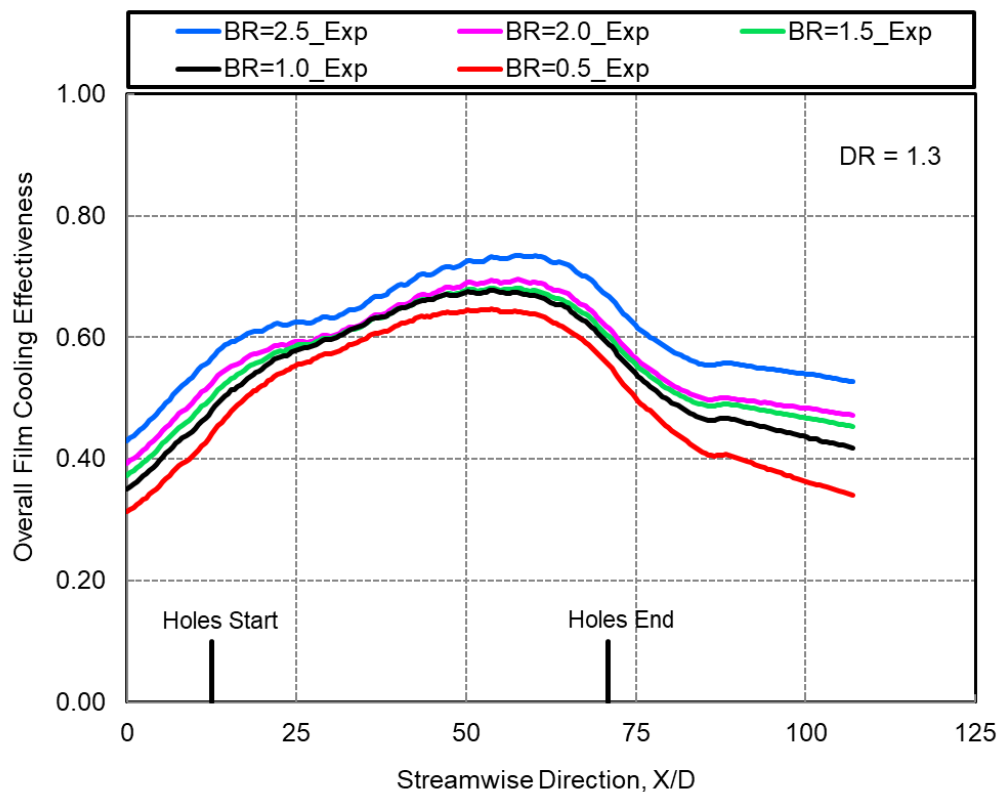


Fig. 5.58 Effect of blowing ratio on experimental overall cooling effectiveness for 7.2D pitch effusion holes

The overall effectiveness results for the two pitch region from CFD are plotted for the density ratio of 1.3 as shown in Fig. 5.59. The results show that the effectiveness increases with increase in blowing ratio from 0.5 to 2.5. The maximum value of effectiveness in Fig. 5.59 is 0.72 at X/D of 62, for a blowing ratio of 2.5. The start and the end region of holes are also marked by separate lines on the graph. The effectiveness before the effusion hole region is purely due to convection cooling by the coolant present at the backside of the test plate.

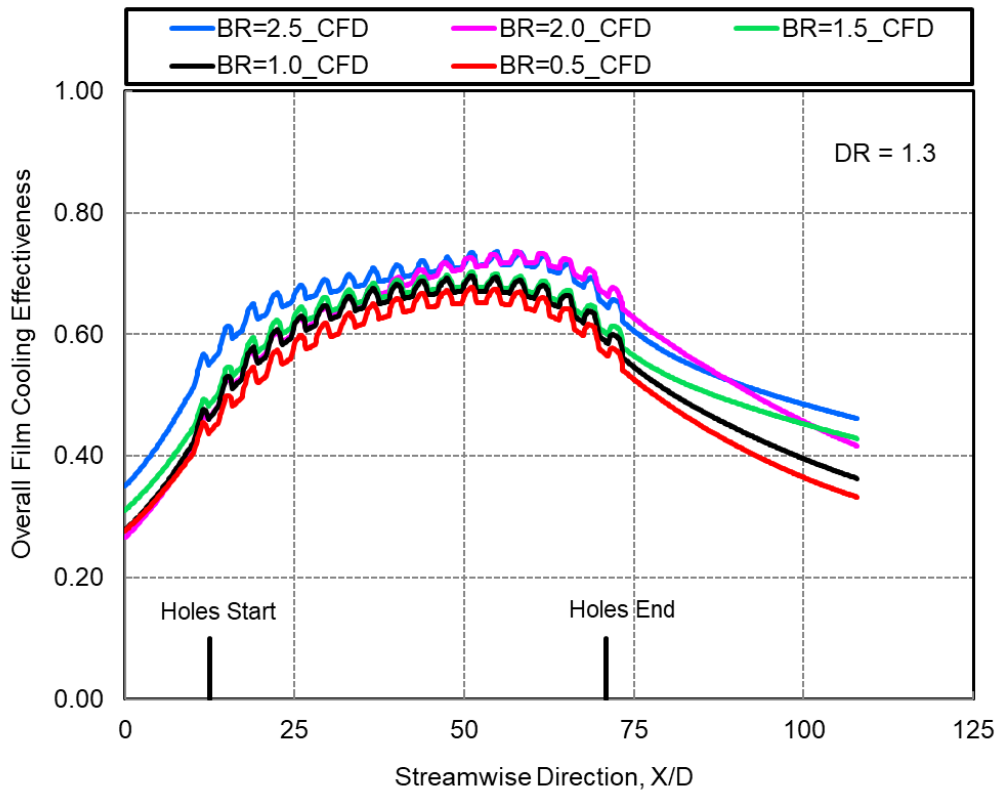


Fig. 5.59 Effect of blowing ratio on CFD overall cooling effectiveness for 7.2D pitch effusion holes

The comparison of overall effectiveness results from experiment and CFD are plotted for all blowing ratios in Fig. 5.60. From the results, it is observed that the experimental and CFD results are matching at the hole region. The CFD results are showing the coolant temperature which is coming out from the effusion holes, and thus the spanwise averaged two pitch region results shows some peaks in the effectiveness values. As mentioned earlier, there are 9 holes in a cooling row and the immediate next row is arranged in a staggered manner. Due to this, the spanwise averaged CFD results are showing eighteen peaks from the hole start to end region. But in the experiments, the test plate temperature is taken by the IR image, which is reading the surface temperature in each and every hole. Due to this, the experimental averaged results are not showing the peaks at the holes because the surface temperature is lower than the coolant temperature.

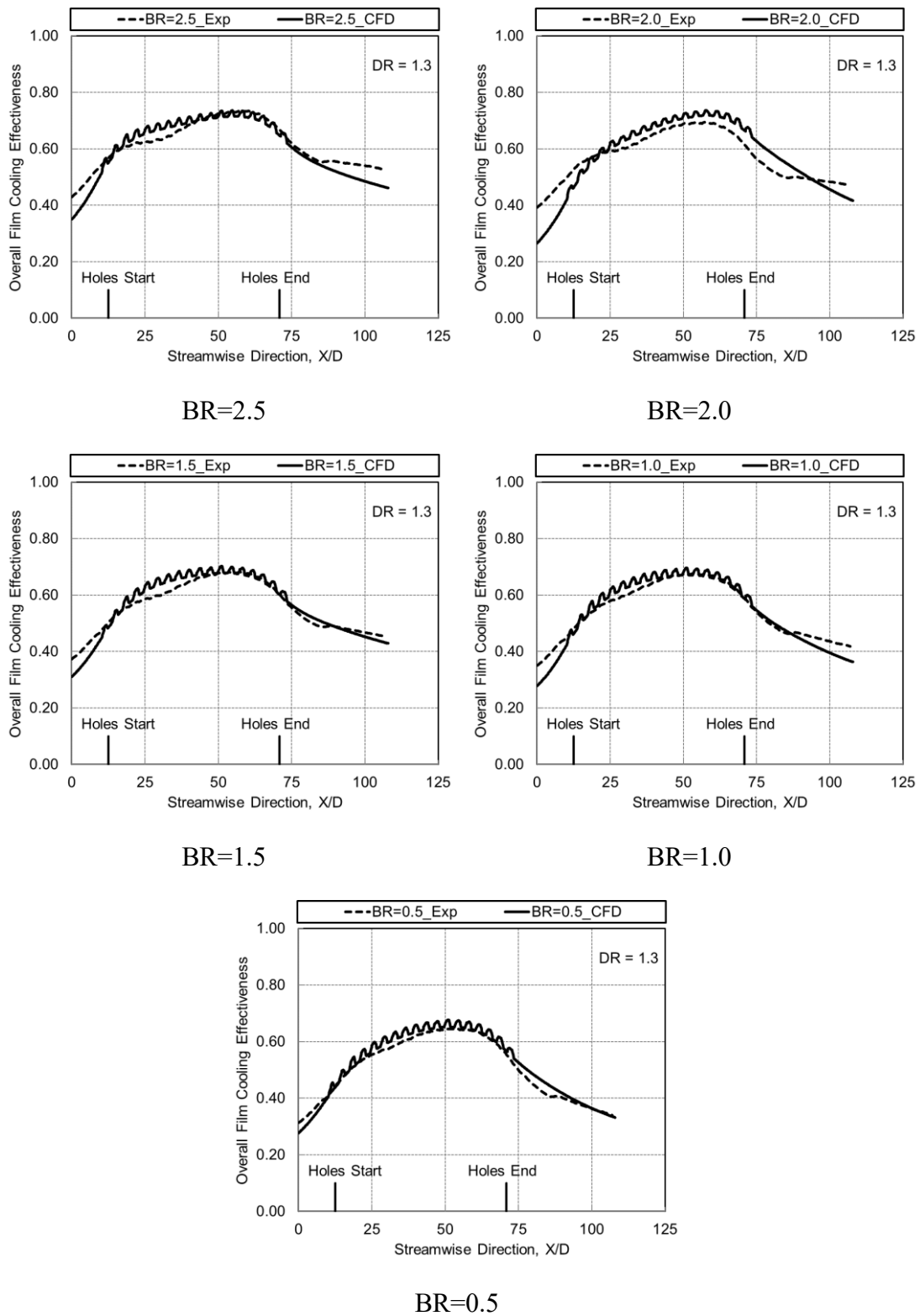


Fig. 5.60 Comparison of experimental and CFD overall film cooling effectiveness at different blowing ratios

The thermographic image obtained from an IR camera is compared with the temperature contours obtained from CFD simulation. The comparison of experimental and CFD temperature contours for a blowing ratio of 2.0 is shown in Fig. 5.61. The contours show the cumulative cooling effect from all the holes in the streamwise direction. The experimental IR image temperature legend bar shows the raw radiation values captured by the camera. But in CFD the legend bar shows the temperature in Kelvin.

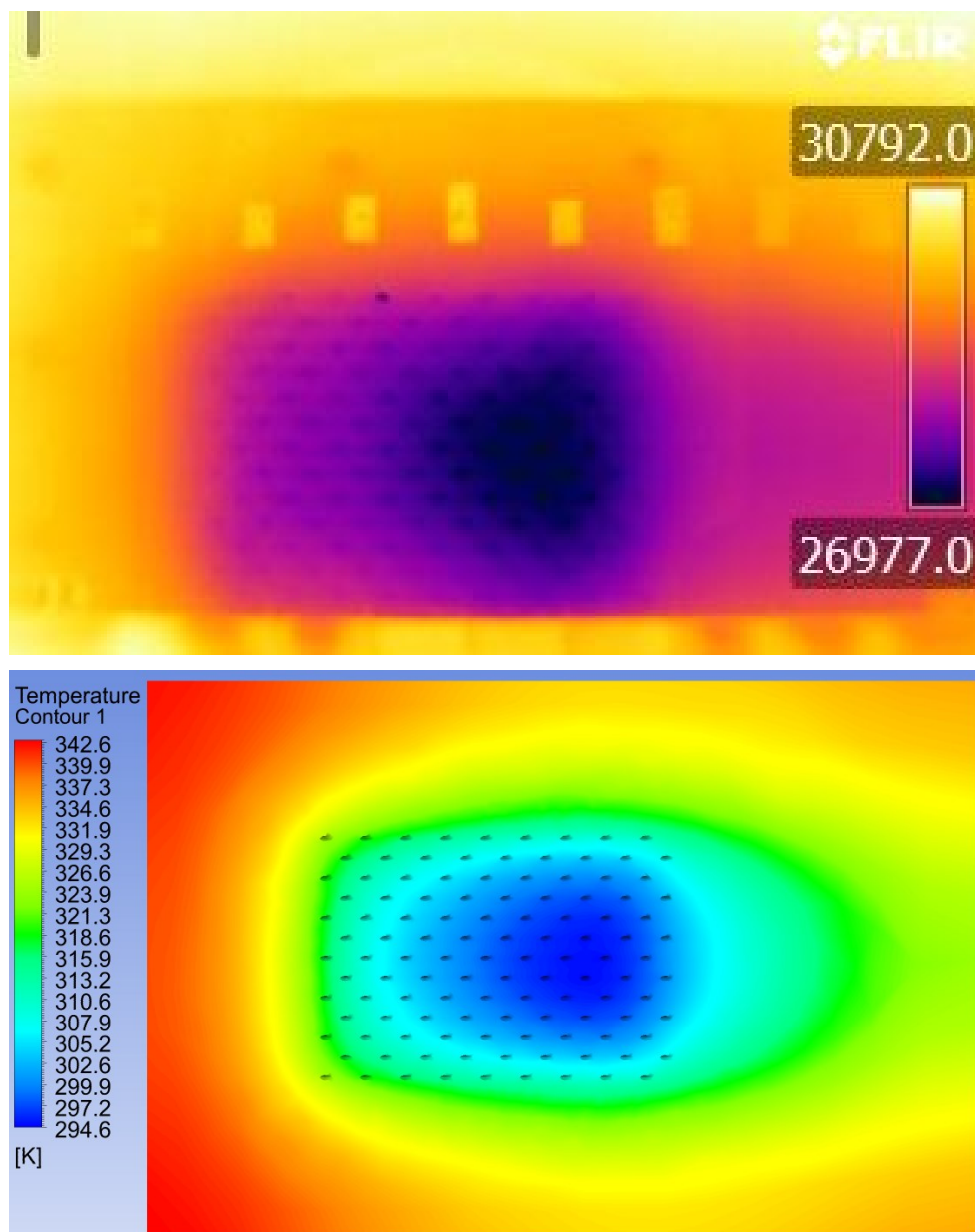


Fig. 5.61 Experimental and CFD overall film cooling temperature contours for 7.2D pitch effusion holes at a blowing ratio of 2.0

Effectiveness contours are obtained by running the MATLAB program for each and every pixel locations of the thermographic image. The effectiveness contours of spanwise two pitch region at all blowing ratios are shown in Fig. 5.62 for experimental data and for CFD data, it is shown in Fig. 5.63. The contours show the increase in effectiveness from blowing ratios of 0.5 to 2.5, for both experimentally and CFD. The colour red in the legend bar represents the higher experimental effectiveness in the range of 0.7 to 0.75. From the start of holes to end of the holes, effectiveness increases in the streamwise direction. As the increase in blowing ratio, the contours show an increase in cooling effectiveness.

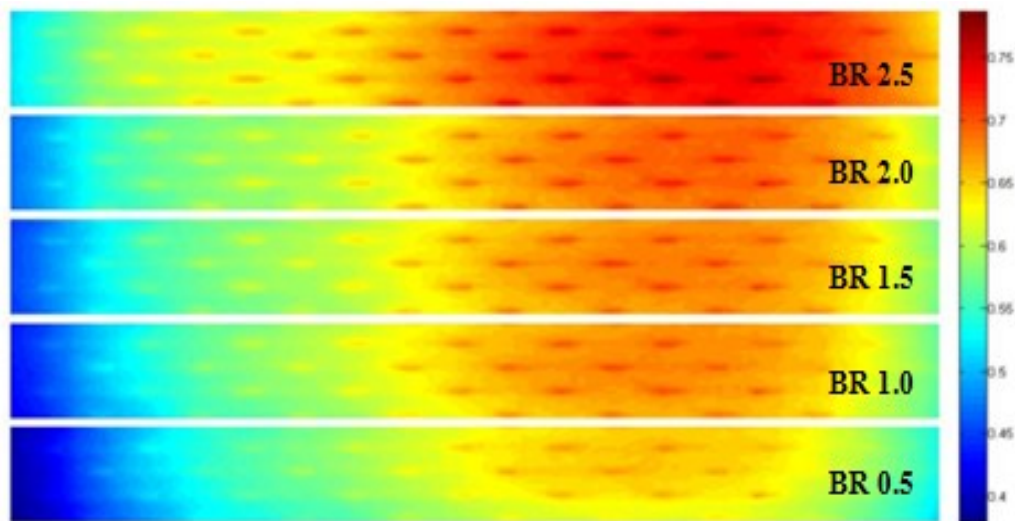


Fig. 5.62 Experimental overall cooling effectiveness contours at different blowing ratios for 7.2D pitch effusion holes

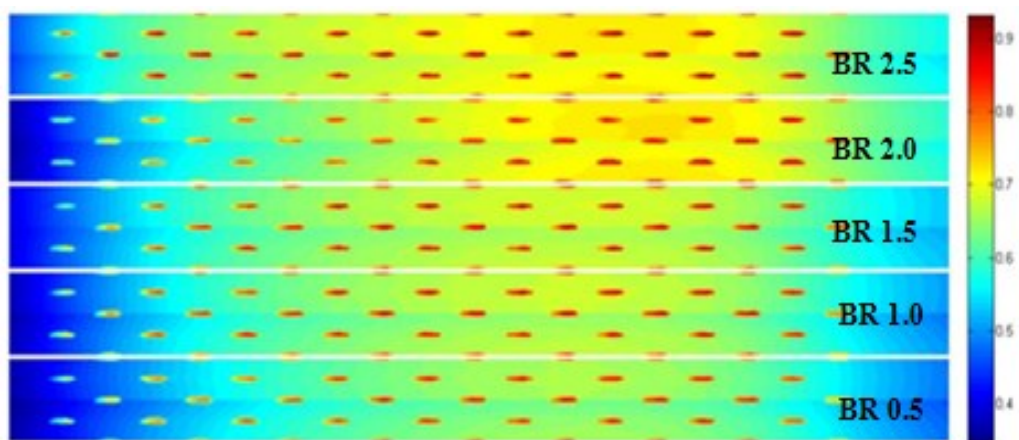


Fig. 5.63 CFD overall cooling effectiveness contours at different blowing ratios for 7.2D pitch effusion holes

5.8.2 Test Plate with 5.4D Pitch

Another test plate is prepared with the same geometrical parameters of the previous test plate, but only the pitch is varied as 5.4D in both the streamwise and spanwise directions. So the pitch between the holes is less compared to the previous test plate. Since the previous results show not much variation between the experimental and CFD results, only experimental overall film cooling effectiveness is generated for this test plate. The overall effectiveness distribution results of spanwise averaged two pitch region for density ratio of 1.3 at different blowing ratios obtained experimentally are plotted along streamwise direction X/D as shown in Fig. 5.64. The effusion holes start at 11.3 X/D from the starting edge of the plate and end at 52.6 X/D . The overall effectiveness is observed to increase with an increase in blowing ratio from 0.5 to 2.5, along with the downstream direction of the hole region. For all blowing ratios as the X/D increases the effectiveness increases upto the end of the holes due to the cumulative film effects from the previous holes. At the end of the hole region, the effectiveness drops.

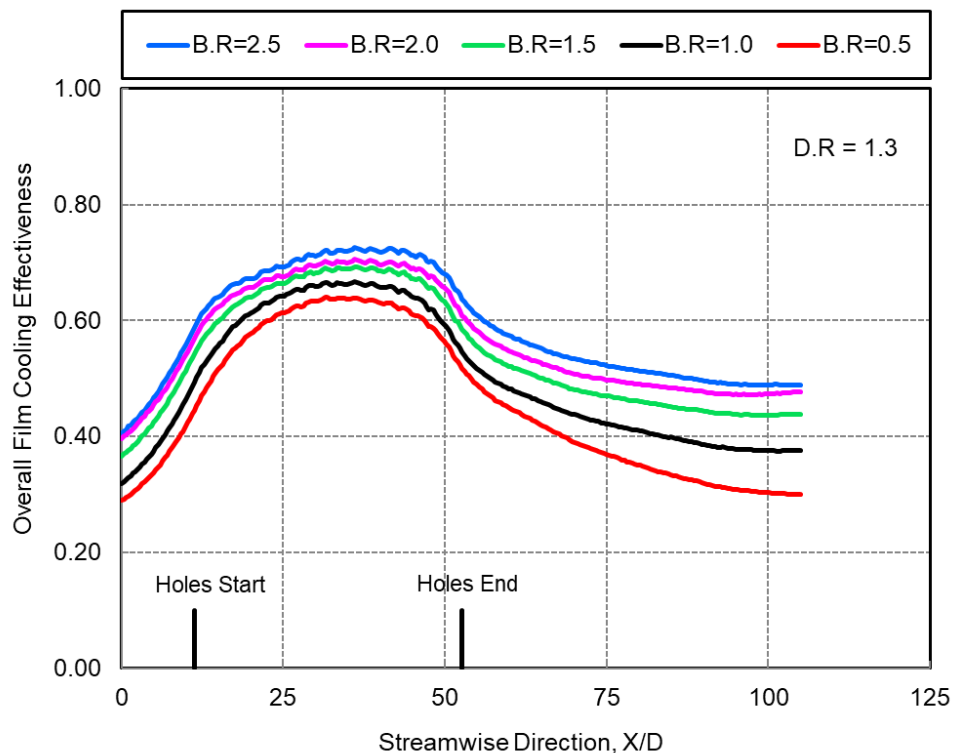


Fig. 5.64 Effect of blowing ratio on the experimental overall cooling effectiveness for 5.4D pitch effusion holes

Fig. 5.65 shows a typical thermal image of 5.4D pitch effusion plate for a blowing ratio of 2.5. The thermographic image covers the upstream region before the start of cooling holes, the multiholed region, and the region downstream of the cooling holes. In the upstream region, heat transfer takes place by conduction through the plate and also by convection on both sides of the plate. In the multiholed region the heat transfer occurs by convection & conduction through holes, and by the film cooling effect. After the multiholed region, the film cooling effect is developed and achieved in the downstream region. In the actual liner, radiation effects will be considered on both sides of the liner. However, in the present experimental study, the effect due to radiation is minimum and hence neglected.

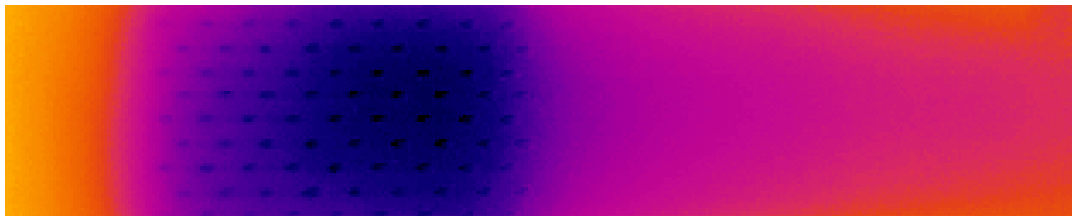


Fig. 5.65 Typical thermal image of overall cooling effectiveness effusion plate at a blowing ratio of 2.5

Fig. 5.66 shows the effectiveness contours at blowing ratios of 0.5 to 2.5 for effusion holes having a 5.4D pitch. The contours are plotted around spanwise two pitch region and from the start of the first hole in a row to end of the last hole. At all blowing ratios, the starting region of holes shows less effectiveness because the film formation just started from the first column of holes. As the X increases, the effectiveness increases due to the additive nature of film formed by the coolant flow coming out from the consecutive holes in the row. At the end region of holes, effectiveness value decreases as there are no further holes downstream. But the film formed by the end region holes has cooling effect upto the end of the test plate as seen from the thermal image, Fig. 5.65.

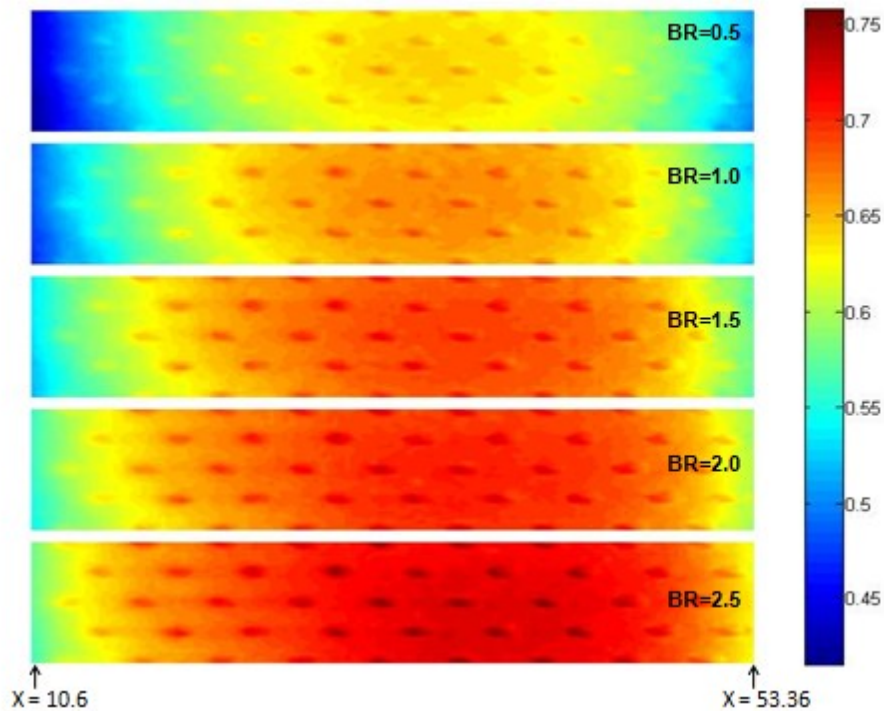


Fig. 5.66 Experimental overall cooling effectiveness contours for 5.4D pitch effusion holes at different blowing ratios

5.8.3 Effect of Pitch for effusion holes

The test plates having 7.2D and the 5.4D pitch between effusion holes are compared, and the results are shown in Fig. 5.67. The number of holes per row is maintained at 9 holes for both the test plates. So, the holes are starts at 11.3 X/D from the starting edge of the test plate and end at 52.6 X/D for 5.4D pitch, and the effusion holes for 7.2D pitch test plate starts at 12.5 X/D from the starting edge of the plate and ends at 79 X/D. The holes start, and holes end are mentioned with the same data series line style at each and every comparison plots. The comparison results for all the blowing ratios show that the overall cooling effectiveness variation is not much as the pitch decreases. This is observed from the plots that the peak or highest effectiveness value at each blowing ratio for both the test plates are more or less the same. The increasing trend of effectiveness from the start of the holes and the decreasing trend of effectiveness at the end of holes are similar at each blowing ratios. From the results, the higher pitch of 7.2D will be useful because it covers more area for cooling with the same number of holes and with the same coolant mass flow.

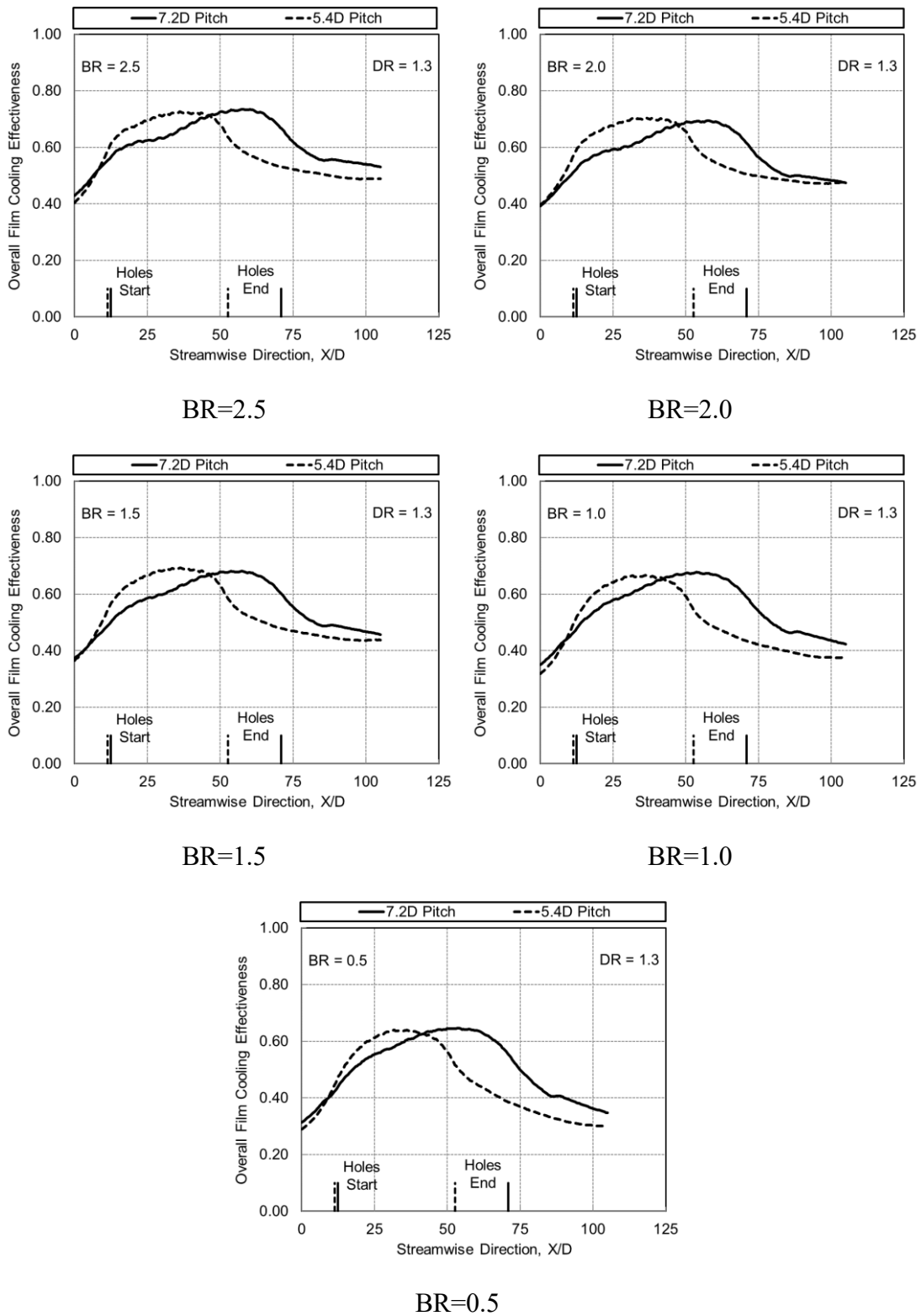


Fig. 5.67 Comparison of overall film cooling effectiveness for 7.2D and 5.4D pitch effusion holes at different blowing ratios

5.9 Overall Cooling Effectiveness for Effusion Holes with Machined Ring Geometries

Conjugate CFD analysis is carried out to find the overall cooling effectiveness for effusion holes with machined ring geometries. The effusion plate having a hole diameter of 1 mm, 27° hole angle and a hole pitch of 7.2D in both streamwise and spanwise direction is used for this analysis. Since the validation of CFD and experimental results are already carried out in the effusion cooling holes geometry, here experimental tests were not performed, and only conjugate CFD analysis was done. The geometrical parameters of both the machined ring geometries which are used in the adiabatic analysis are scaled down 3 times in this conjugate analysis. The geometries are modelled in the solid works design software, meshing and the analysis are carried out in Ansys workbench.

The CFD overall effectiveness distribution results of spanwise averaged two pitch region for effusion holes with machined ring geometry 1 at different blowing ratios are plotted along streamwise direction X/D as shown in Fig. 5.68. The effusion holes start at 10.6 X/D from the starting edge of the plate and end at 77 X/D . The X/D between the exit of machined ring holes and the start of the effusion holes is maintained the same as in the adiabatic effusion model with the machined ring placed upstream. The overall effectiveness is observed to increase with an increase in blowing ratio from 0.5 to 2.5. The increase in effectiveness due to the effect of machined ring flow is clearly seen upto X/D of 20. Afterward, for BR 1.5 to 2.5, the combined effect of machined ring 1 and effusion flow is not much varied. For all blowing ratios the effectiveness increases upto the X/D of 60 due to the cumulative film effects from the previous holes, and then it decreases.

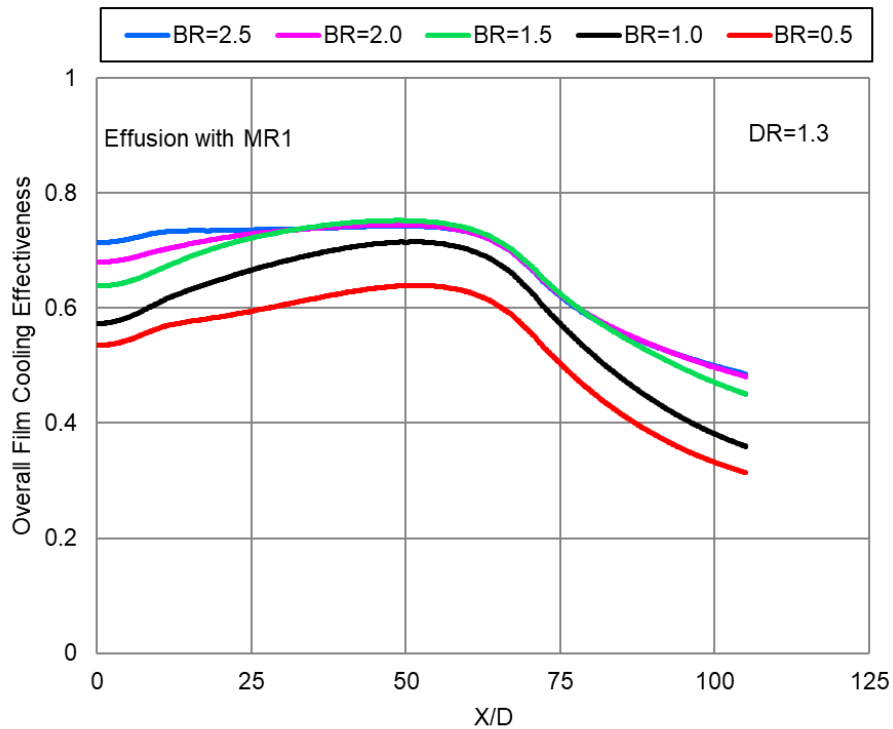
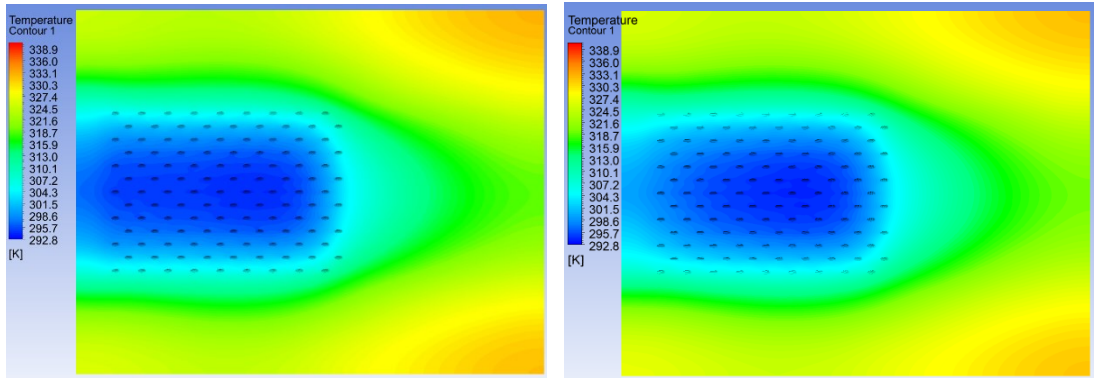


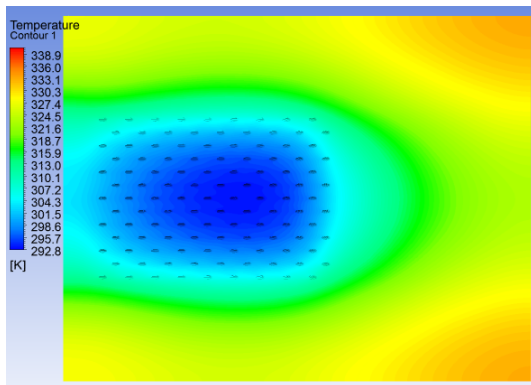
Fig. 5.68 Effect of blowing ratio on the overall cooling effectiveness for effusion holes with machined ring geometry 1

Fig. 5.69 shows the CFD conjugate test plate temperature contours for effusion with machined ring 1 at different blowing ratios. Mainstream temperature is set at 357 K, and coolant temperature at 273 K. The test plate temperature legend bar shows that the test plate is cooled upto 292.8 K near the holes and the maximum temperature of 338.9 K is achieved at the end of the test plate. For a blowing ratio of 0.5, the variation in the temperature distribution is maximum and is reduced as the blowing ratios increased. The temperature contour shows that the starting region of the test plate is cooled by the coolant flow through the machined ring holes. In the effusion hole region, the test plate is cooled not only by the combined film formation of a machined ring, effusion flow and also gets cooled when the coolant flows through each and every hole of effusion. In this conjugate analysis conduction also plays a vital role as the temperature at both sides of the test plate is different.

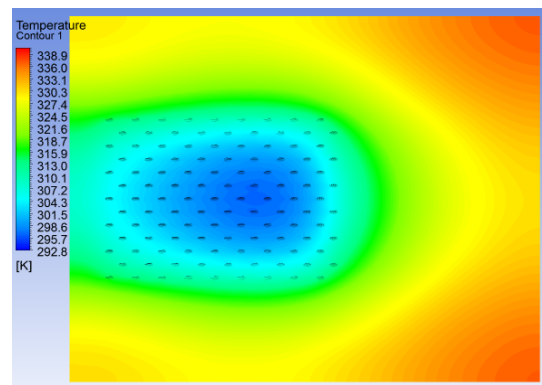


BR=2.5

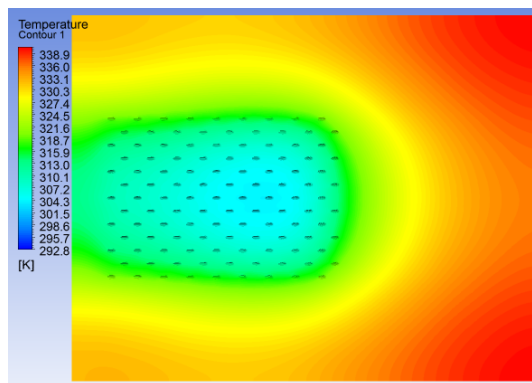
BR=2.0



BR=1.5



BR=1.0



BR=0.5

Fig. 5.69 CFD conjugate test plate temperature contours for effusion with machined ring 1 at different blowing ratios

The CFD overall effectiveness distribution results of spanwise averaged two pitch region for effusion holes with machined ring geometry 2 at different blowing ratios are plotted along streamwise direction X/D as shown in Fig. 5.70. The increase in effectiveness due to the effect of machined ring flow is clearly seen upto X/D of 20. Afterward, for BR 1.5 to 2.5, the combined effect of machined ring 2 and effusion flow is not much varied. For BR=2.5, the maximum effectiveness achieved in the starting region of the machined ring flow is 0.8 which is high when compared to the machined ring 1 flow. For all blowing ratios, the effectiveness increases upto the X/D of 60 due to the cumulative film effects from the previous holes, and then it decreases.

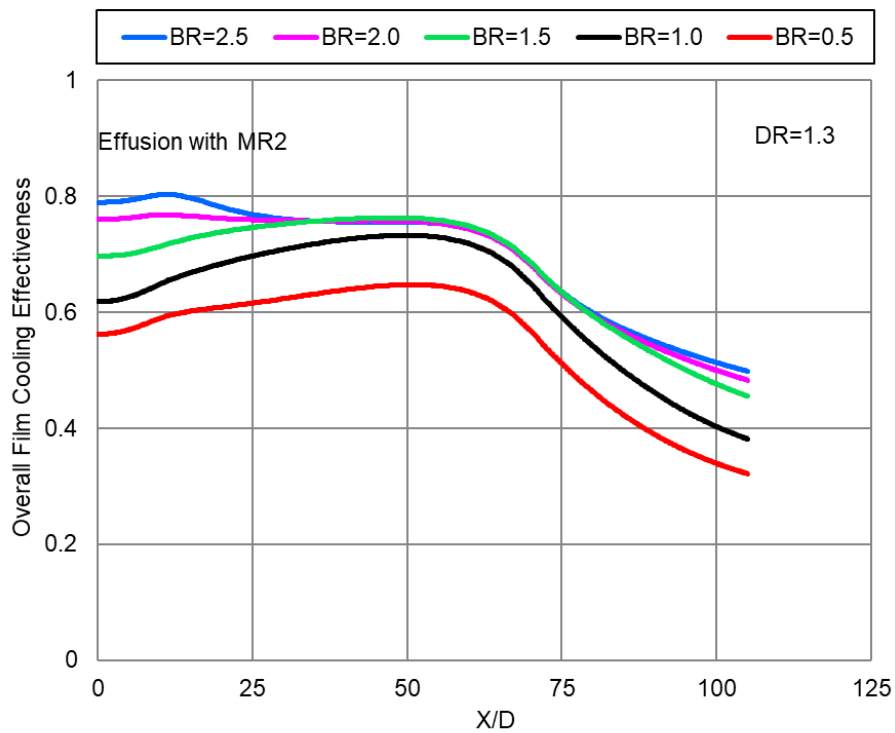


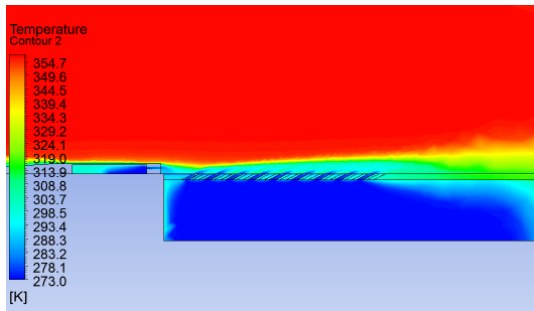
Fig. 5.70 Effect of blowing ratio on the overall cooling effectiveness for machined ring geometry 2

Fig. 5.71 shows the CFD flow field temperature contours for effusion with machined ring 2 at different blowing ratios. From these contours, the boundary layers created by the film formation due to the effusion, machined ring flows are clearly visible. The highest temperature in the legend bar shows the mainstream flow temperature, and the lowest shows the coolant temperature. The boundary layer of the film increases as the blowing ratio increases. As the thickness of the test plate is 2 mm,

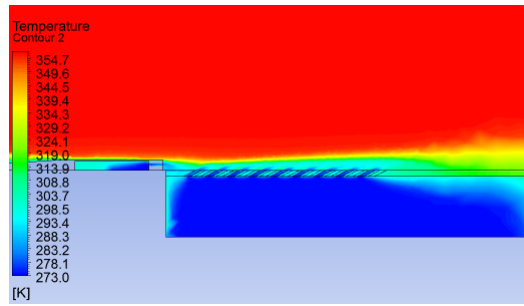
and across the thickness the temperature variation is minimum. In the coolant chamber at the effusion hole region, the coolant temperature is equal to 273 K. But at the end of the test plate in the coolant chamber due to the conduction effects, the coolant gets heated up which is shown by these contours.

Fig. 5.72 shows the CFD conjugate test plate temperature contours for effusion with machined ring 2 at different blowing ratios. Mainstream temperature is set at 357 K, and coolant temperature at 273 K. The test plate temperature legend bar shows that the test plate is cooled upto 288.8 K near the holes and the maximum temperature of 335.8 K is achieved at the end of the test plate. The difference between the maximum and minimum temperatures are less when compared to the effusion flow with machined ring 1 test plate, which shows that the test plate is cooled further due to coolant flow effect of machined ring 2. For a blowing ratio of 0.5, the variation in the test plate temperature distribution is maximum and is reduced as the blowing ratios increased. The temperature contour shows that the starting region of the test plate is cooled by the coolant flow through the machined ring holes. In the effusion hole region, the test plate is cooled not only by the combined film formation of a machined ring, effusion flow and also gets cooled when the coolant flows through each and every hole of effusion. In this conjugate analysis conduction also plays a vital role as the temperature at both sides of the test plate is different.

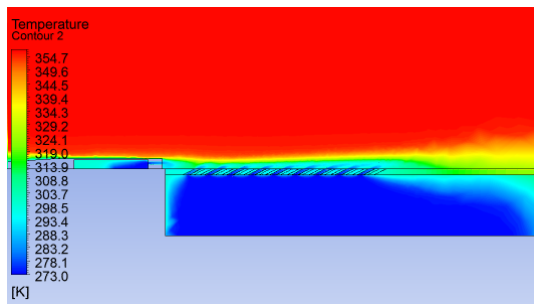
Fig. 5.73 shows the comparison of overall film cooling effectiveness for effusion holes with and without machined ring geometries at different blowing ratios. The effusion with machined ring geometries shows higher effectiveness than the effusion flow alone. Both the machined rings give higher overall cooling effectiveness than the effusion flow alone. The effect is maximum at the starting region of the test plate. The combined machined ring and effusion flow effect are visible upto X/D of 60 for higher blowing ratios. For $BR=0.5$, the effect is only upto X/D of 40.



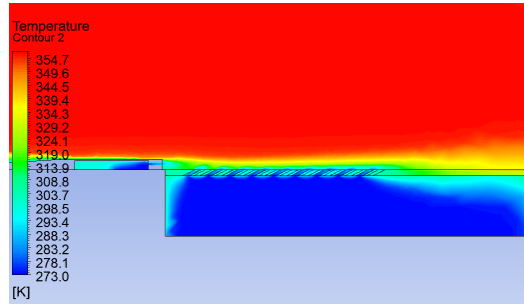
BR=2.5



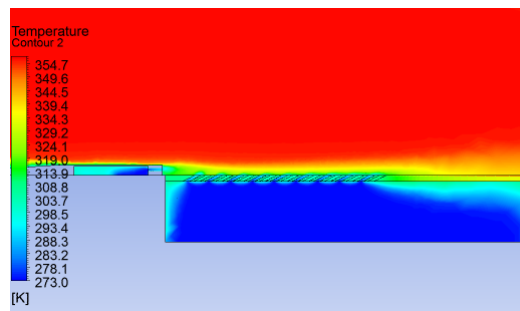
BR=2.0



BR=1.5

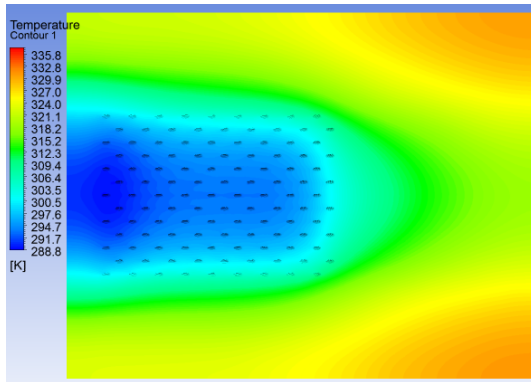


BR=1.0

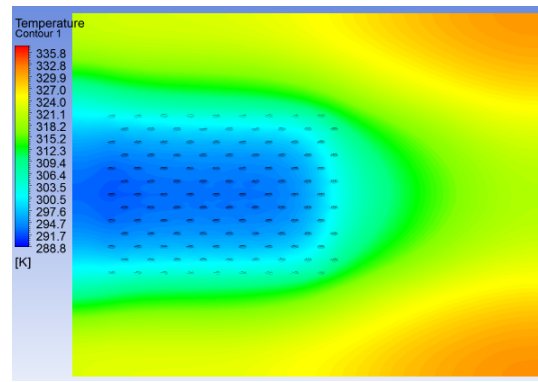


BR=0.5

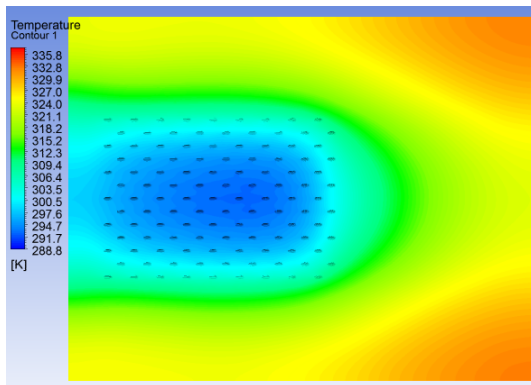
Fig. 5.71 CFD conjugate streamwise temperature contours for effusion with machined ring 2 at different blowing ratios



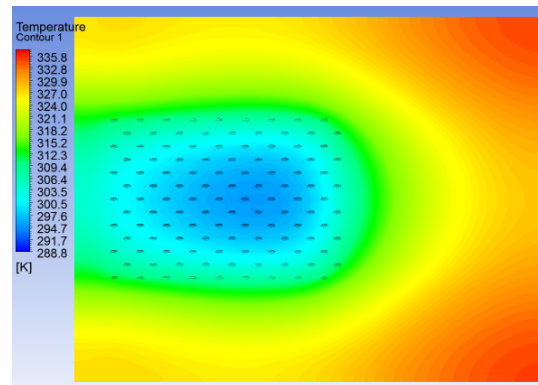
BR=2.5



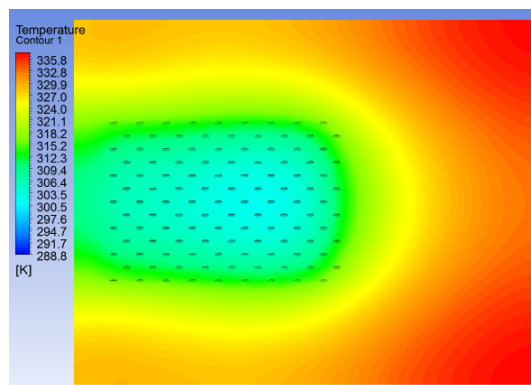
BR=2.0



BR=1.5



BR=1.0



BR=0.5

Fig. 5.72 CFD conjugate test plate temperature contours for effusion with machined ring 2 at different blowing ratios

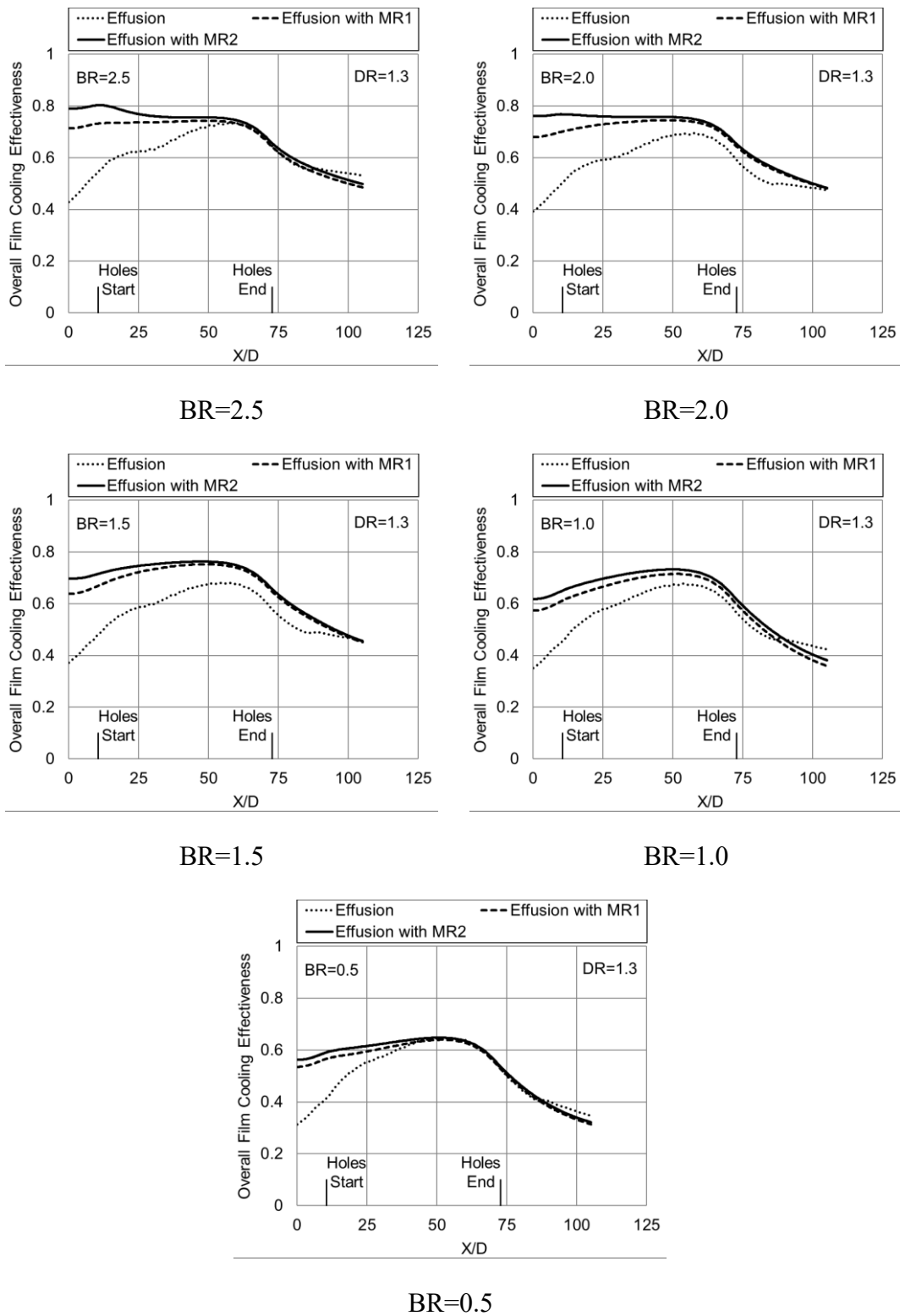


Fig. 5.73 Comparison of overall film cooling effectiveness for effusion holes with and without machined ring geometries at different blowing ratios

5.10 Overall Cooling Effectiveness for Effusion with Impingement Holes

Another combination of cooling study, i.e., effusion cooling with impingement holes at backside is carried out. Fig. 5.74 shows the schematic of the effusion cooling test rig with the impingement test plate. The test plate which is having effusion holes of $5.4D$ pitch in spanwise and streamwise directions is used to find out the effect of impingement on effusion cooling. An impingement plate made out of 3 mm thick hylam sheet is kept backside of the effusion plate at a distance of 6 mm. The holes in the impingement plate are also arranged in a staggered manner such that each effusion hole is surrounded by four impingement holes. The impingement holes are of 0.9 mm diameter and normal to the plate surface. Fig. 5.75 shows the geometrical details of the impingement plate.

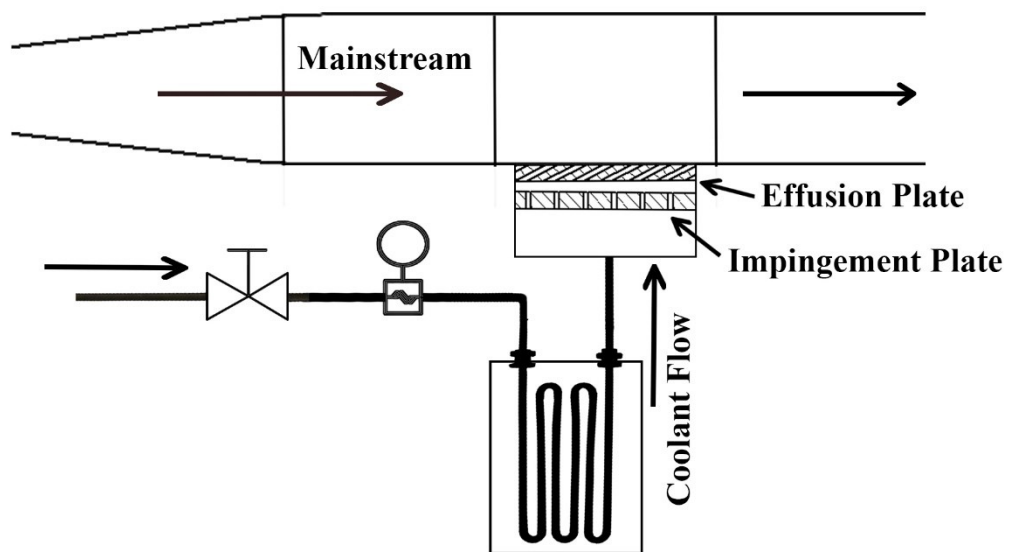


Fig. 5.74 Schematic of the effusion cooling test rig with the impingement test plate

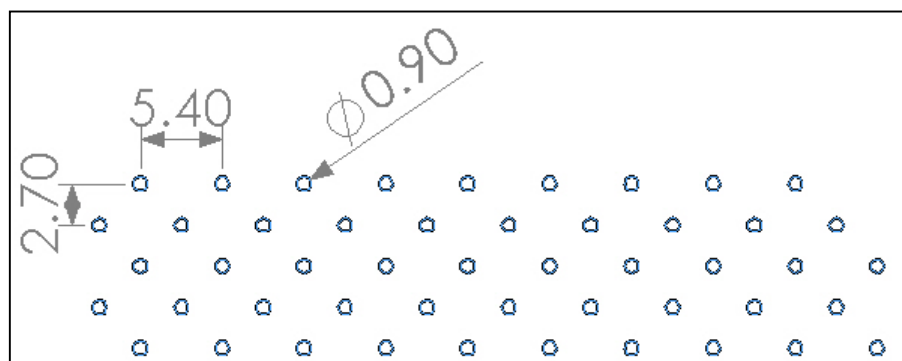


Fig. 5.75 Geometrical details of the impingement plate

Fig. 5.76 shows a thermal image of the effusion plate at a blowing ratio of 2.5 with flow through impingement holes at the backside. In comparison with Fig. 5.65, it is clearly visible that the impingement flow cools the inner side of the effusion plate and gives higher cooling from the starting region of the hole onwards. The impingement jet which is coming out from the impingement holes flows at a higher velocity and hit the targeted effusion test plate. This high jet velocity produces higher convective heat transfer coefficients at the cold side of the effusion plate and thus increases the overall cooling effectiveness.

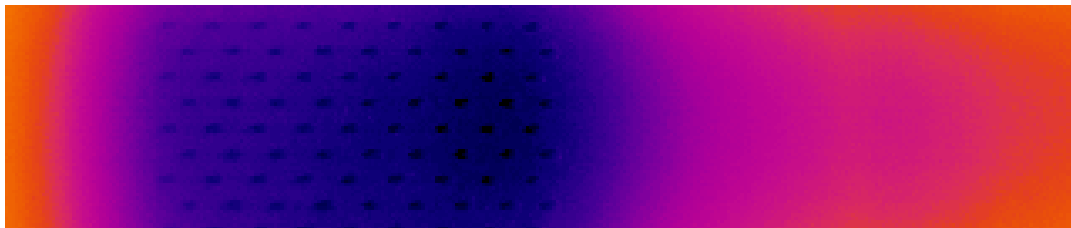


Fig. 5.76 Typical thermal image of effusion plate at a blowing ratio of 2.5 with impingement plate at the backside

Fig. 5.77 shows the effectiveness contours at blowing ratios of 0.5 to 2.5 for effusion holes with impingement flow. The contours are plotted around spanwise two pitch region and from the start of the first hole in a row to end of the last hole. It is clearly seen from the contours, that the effectiveness values are higher from the first to last holes due to the effect of impingement flow which is covering the entire region of effusion holes.

Fig. 5.78 shows the effect of overall film cooling effectiveness of effusion cooling holes with impingement holes at the backside. The cooling effectiveness is lower at a blowing ratio of 0.5 and gradually increases as the blowing ratio increases. The impingement flow hits and cools the inner side of the effusion plate and then comes out from the effusion holes and forms the film over the plate surface. The increase in effectiveness from the starting to end region of holes is marginal, but it is higher when compared with coolant flow through effusion holes alone without impingement.

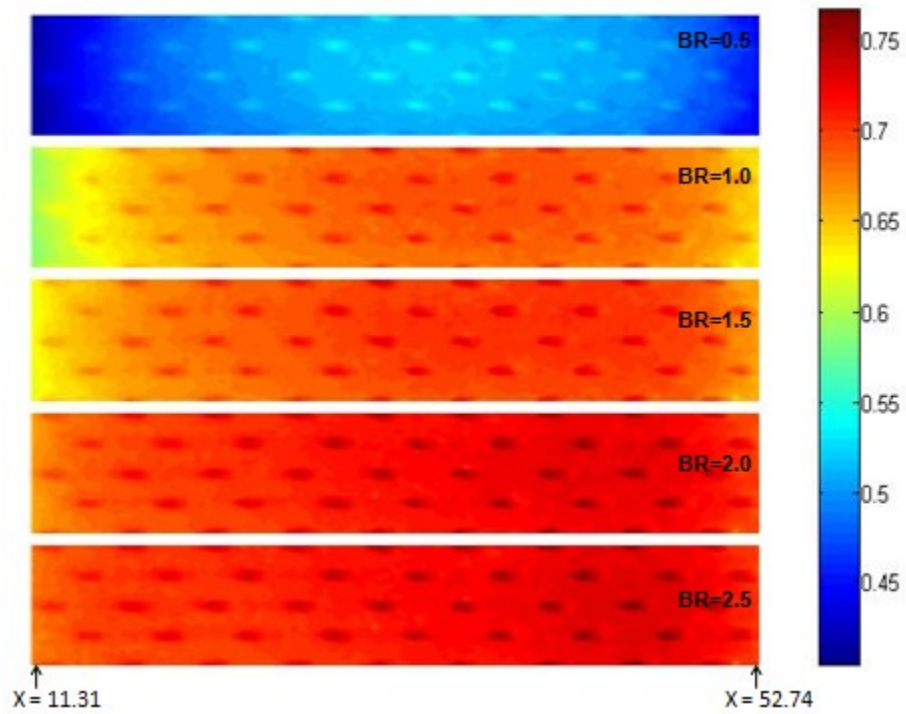


Fig. 5.77 Experimental overall cooling effectiveness contours of effusion holes with impingement flow at different blowing ratios

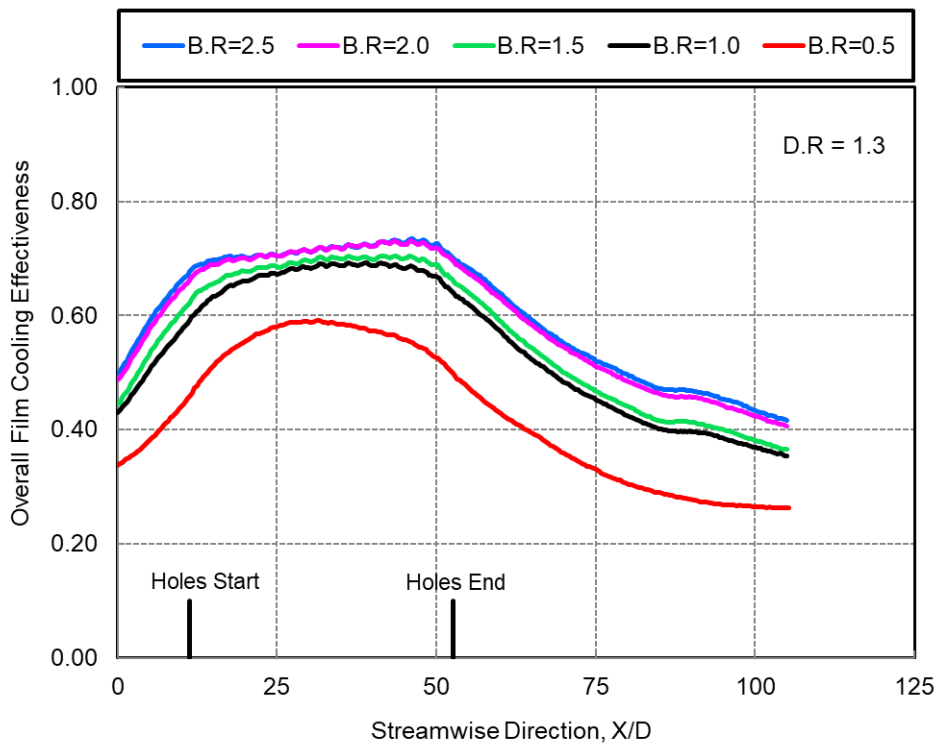


Fig. 5.78 Effect of blowing ratio on the overall cooling effectiveness of effusion holes with impingement holes at the backside

The results for the effusion plate without impingement plate is already explained in Fig. 5.64. Now the experimental results for effusion plate with and without impingement plate are compared at all blowing ratios and plotted in Fig. 5.79. Except blowing ratio of 0.5, all other blowing ratios show higher effectiveness for the effusion plate with impingement holes at the backside. The impinging jets hit at a higher velocity at the inner side of the effusion plate and locally cools the inner surface first and then ejects out through the effusion cooling holes to form a protective film layer. The starting region of the effusion holes are also covered by the impingement holes and thus shows higher effectiveness compared to the effusion plate without impingement. But, at a blowing ratio of 0.5, the impingement case shows less averaged effectiveness. This may be due to the flow phenomenon in-between the impingement plate and the effusion plate at lower velocity jets.

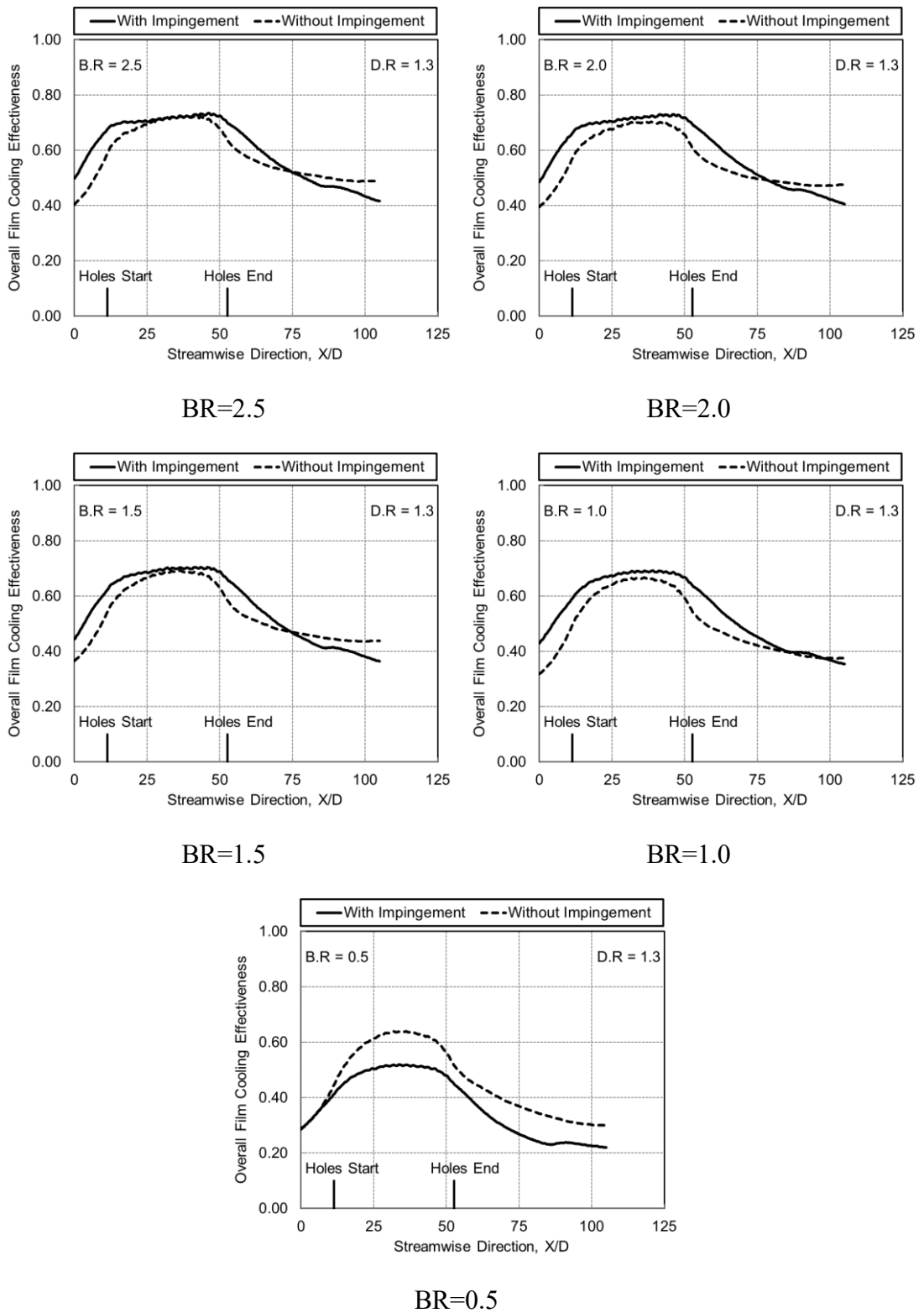


Fig. 5.79 Effect of impingement on effusion cooling at different blowing ratios

Fig. 5.80 shows the effect of impingement on cooling effectiveness at different X locations for a blowing ratio of 2.5. The x-axis shows the spanwise distance covering two pitch region of holes. The dashed lines in the figure indicate the effectiveness values of effusion holes with impingement holes at the backside and the continuous lines indicate the effectiveness values of effusion holes without impingement. The effusion hole region in the test plate starts at X=11.3 and ends at X=52.6. In the starting region of holes at X=11.3, there is a massive increase in effectiveness for impingement cum effusion flow. In the middle region of holes (X=31), there is not much variation between the impingement and without impingement case. But at the end region of holes, the effectiveness values drop for without impingement case. The impinging jets cover the entire region of the effusion holes and produce higher convective heat transfer coefficients at the cold side of the effusion plate which removes the heat from the effusion plate. The cold side convective heat transfer coefficient is higher than the hot side convective heat transfer coefficient for the impingement flow case. But for the effusion flow the hot side convective heat transfer coefficient gradually reduces and the effectiveness increases due to the film formation from the consecutive holes in the row.

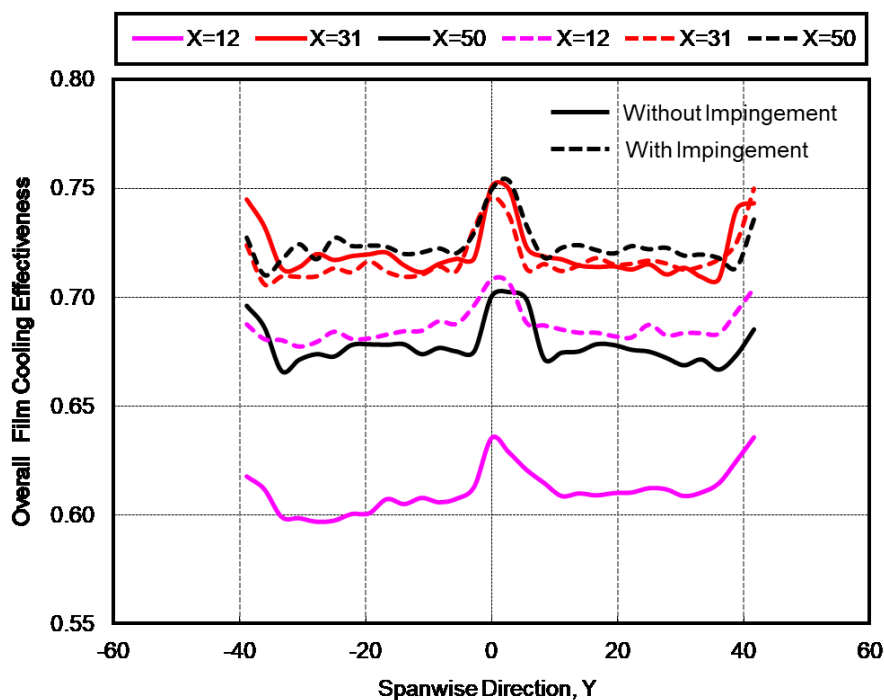
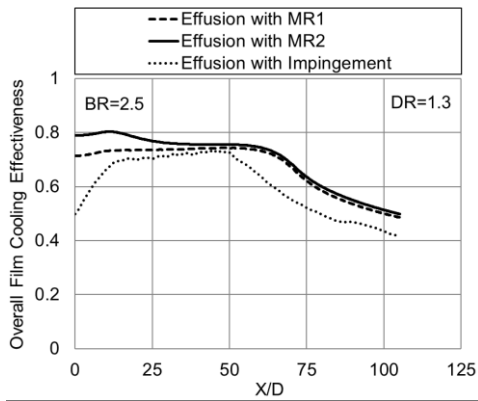


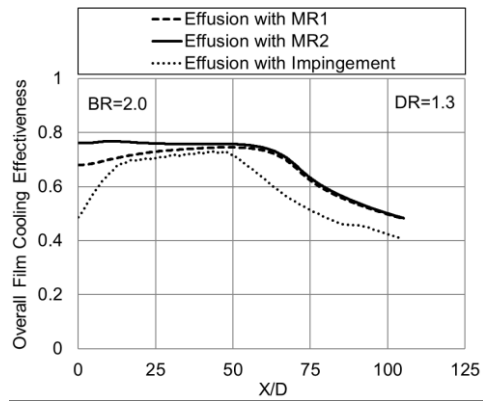
Fig. 5.80 Effect of impingement on overall cooling effectiveness at different x locations for a blowing ratio of 2.5

5.11 Comparison Between Effusion with Impingement and Effusion with Machined Ring Geometries

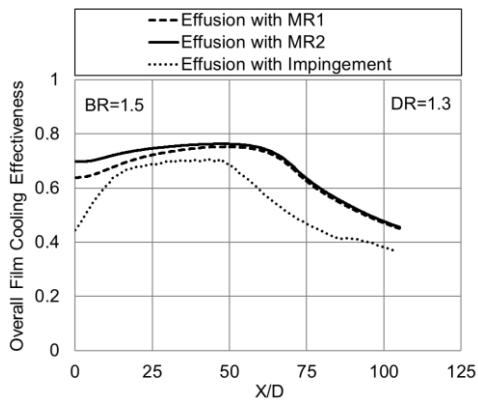
The comparison is made between effusion with impingement and effusion with machined ring geometries and are shown in Fig. 5.81. This comparison is made in order to analyze which combination of geometry is giving better overall cooling effectiveness. From the results, it is seen that the effusion with machined ring geometries shows better cooling effectiveness than the effusion with impingement geometry at all the blowing ratios analyzed in this study. Throughout the test plate length across the streamwise direction, the effusion with machined ring geometries gives higher effectiveness. The effect is higher at the region before effusion holes and also at the downstream of effusion holes. The disadvantage of using an impingement plate with effusion cooling is, it adds extra weight to the combustor. So, it is recommended to put the effusion with machined ring cooling geometry in the real combustor at propulsion division of CSIR-NAL.



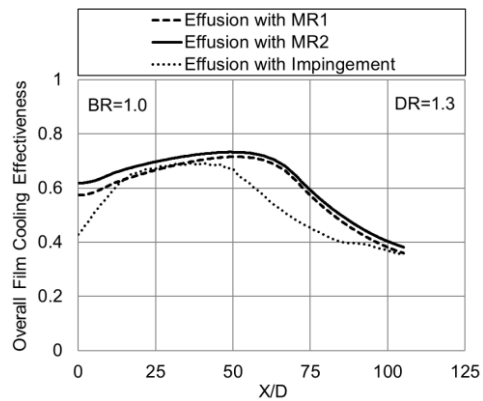
BR=2.5



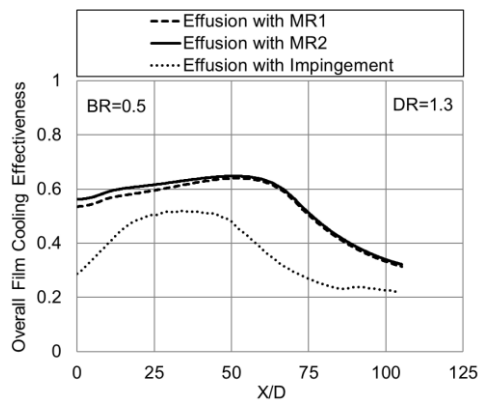
BR=2.0



BR=1.5



BR=1.0



BR=0.5

Fig. 5.81 Overall cooling effectiveness comparison between effusion with impingement and effusion with machined ring geometries at different blowing ratios

CHAPTER 6

CONCLUSIONS

AND

SCOPE FOR FUTURE WORK

6 CONCLUSIONS

- The machined ring geometries which resemble the slot cooling gives the following conclusions in the adiabatic film cooling effectiveness and heat transfer coefficient measurements.
 - Near the machined ring cooling holes, the adiabatic film cooling effectiveness is higher and attains a value of 0.84 and around 0.6 for MR2 and MR1 respectively for $BR \geq 1.0$. Afterwards it decreases continuously as the X/D increases in the streamwise direction due to the mixing of coolant with mainstream.
 - The adiabatic film cooling effectiveness and the heat transfer coefficient increases with respect to increasing in blowing ratio. Machined ring 2 gives 20% higher cooling effectiveness than machined ring 1 at all blowing ratios upto X/D of 20 due to the more amount of coolant flow through the holes. After X/D of 20 and above, the percentage increase in cooling effectiveness reduces to 10% for lower blowing ratio cases.
 - The blowing ratio effect in heat transfer coefficient variation is seen upto X/D of 20 for both the machined ring geometries and then it is constant. At the exit of machined ring cooling holes, the heat transfer coefficient attains a higher value of $160 \text{ W/m}^2\text{K}$ and around $120 \text{ W/m}^2\text{K}$ for MR2 and MR1 respectively at BR of 2.5. This values decreases with decrease in blowing ratio. For BR of 0.5, the heat transfer coefficient values are almost equal for both MR1 and MR2.

- The effusion cooling which is multiple rows of film cooling gives the following conclusions in the adiabatic film cooling effectiveness and heat transfer coefficient measurements.
 - The adiabatic cooling effectiveness continuously increases from the starting of the effusion holes and upto the end of holes. This phenomenon is due to the additive nature of film formed by the coolant flow coming out from the consecutive holes in the row. This occurrence was found at all blowing ratios.
 - The adiabatic film cooling effectiveness and the heat transfer coefficient increases with an increase in blowing ratio. At higher blowing ratio of 2.5, the

heat transfer coefficient reaches a value of around $100 \text{ W/m}^2\text{K}$ at the effusion cooling hole region.

- For BR of 2.5, the adiabatic film cooling effectiveness continuously increases and attains a maximum value of 0.58 at the end of effusion holes. The effectiveness values for BR of 2.5 and 2.0 are almost equal, it is considered that BR=2.0 would be the optimum blowing ratio for this effusion cooling hole design. Further increase in blowing ratio leads to direct coolant jet mixing with the mainstream.
- In order to increase the cooling effectiveness in the starting region of effusion cooling geometry, machined ring geometry was fixed ahead of effusion cooling holes. These machined ring geometries act as wall jet and reduce the hot side heat load by its film cooling performance. The combined effusion cooling and machined ring geometries gave the combined film cooling performance, and the following conclusions are made.
- Spanwise averaged effectiveness shows increase in blowing ratio from 0.5 to 2.5, adiabatic cooling effectiveness increases in the streamwise direction for effusion cooling and effusion cooling with machined ring geometries.
 - Comparison result shows that the effusion cooling with machined ring geometries has higher cooling effectiveness than the effusion cooling geometry alone at all blowing ratios. The coolant coming out from the machined ring holes have significant cooling effect upto X/D of 20 for both the machined ring geometries at B.R 0.5 and upto X/D of 40 for other higher blowing ratios.
 - MR1 with effusion and MR2 with effusion shows an increase in effectiveness of 40% and 50% respectively than the effusion cooling alone at the starting region of the test plate.
 - For blowing ratios 2.0 and above the adiabatic cooling effectiveness is showing higher constant cooling effectiveness value of 0.6 from the start to the end of the test plate for the effusion with machined ring geometries compared to the effusion cooling geometry alone.
 - The convective heat transfer coefficient shows around 20% higher values of film heat transfer coefficient for effusion with machined ring geometries.

- The 2 mm thickness effusion test plate for overall cooling effectiveness measurements is made out of stainless steel consists of three regions: The upstream region before the start of cooling holes, the multiholed/effusion hole region, and the region downstream of the cooling holes. In the upstream region, heat transfer takes place by conduction through the plate and also by convection on both sides of the plate. In the multiholed region the heat transfer occurs by convection, conduction through holes, and by the film cooling effect. After the multiholed region, the film cooling effect is developed and achieved in the downstream region. In the actual combustor liner, radiation effects will be considered on both sides of the liner. However, in the present experimental studies, the effect due to radiation is minimum and neglected. The following conclusions are arrived based on the overall film cooling effectiveness measurements carried out on effusion cooling with and without machined ring geometries.
 - Spanwise averaged overall cooling effectiveness shows an increase in blowing ratio from 0.5 to 2.5, cooling effectiveness increases in the streamwise direction for effusion cooling and effusion cooling with machined ring geometries.
 - As seen in adiabatic film cooling effectiveness measurements, the comparison results of overall cooling effectiveness also show that the effusion cooling with machined ring geometries has 20 to 30% higher cooling effectiveness than the effusion cooling geometry alone at the starting region of the test plate.
 - The machined ring geometries cooling effect has seen upto X/D of 60, and then it merges with effusion cooling geometry effectiveness curve.

- An experimental study is carried out to find out the effect of impingement flow behind a liner plate having effusion holes. The effects are presented for the overall film cooling effectiveness on an effusion plate with and without impingement holes for blowing ratios ranging from 0.5 to 2.5.
 - In the case of effusion cooling with impingement flow, the impinging jets hit the inner side of the effusion plate and then the flow is strongly attracted by the

surrounding effusion holes which increases the cold side convective heat transfer coefficients.

- The comparison result shows that the effusion cooling with impingement flow has better cooling effectiveness than effusion cooling without impingement flow due to the increase in heat removal from the cold side of the effusion plate.
 - Before and after effusion cooling hole region, impingement cooling shows 10% higher cooling effectiveness. At the effusion hole region, the impingement cooling has less effect.
- A comparison is made between effusion cooling with impingement and effusion cooling with machined ring geometries. This comparison is made in order to see which combination of geometry is giving better overall cooling effectiveness.
- From the results, it is understood that the effusion with machined ring geometries shows around 12 to 20% better cooling effectiveness than the effusion with impingement geometry at all the blowing ratios analyzed in this study.
 - Throughout the test plate length across the streamwise direction, the effusion with machined ring geometries gives higher effectiveness. The effect is 20% higher at the region before effusion holes and also 12% higher at the downstream of effusion holes.
 - The disadvantage of using an impingement plate in effusion with impingement cooling is that it adds extra weight to the combustor.

6.1 Scope for Future Work

- The distance between the machined ring and effusion cooling holes starting can be varied and studied.
- Compound angle effusion cooling holes along with machined ring can be studied.
- Any other variations in geometric and flow parameters can be tried to increase the cooling effectiveness.

REFERENCES

- Abdala, A.M.M. and Elwekeel, F.N.M. (2016). “CFD simulations of film cooling effectiveness and heat transfer for annular film hole.” *Arab J. Sci. Eng.*, 41, 4247–4262.
- Andrei, L., Andreini, A., Bianchini, C., Caciolli, G., Facchini, B., Mazzei, L., Picchi, A. and Turrini, F. (2014). “Effusion cooling plates for combustor liners - experimental and numerical investigations on the effect of density ratio.” *J. Energy Procedia*, 45, 1402 – 1411.
- Andreini, A., Bonini, A., Caciolli, G., Facchini, B., and Taddei, S. (2011). “Numerical study of aerodynamic losses of effusion cooling holes in aero-engine combustor liners.” *J. Engineering for Gas Turbines and Power*, 133, 021901-1 - 021901-10.
- Andreini, A., Caciolli, G., Facchini, B. and Tarchi, L. (2013). “Experimental evaluation of the density ratio effects on the cooling performance of a combined slot/effusion combustor cooling system.” *ISRN Aerospace Engineering*, Article ID 423190.
- Andreini, A., Ceccherini, A., Facchini, B., Tarchi, L., and Toni, L. (2009). “Hole spacing effect on adiabatic effectiveness of effusion cooling arrays for turbine endwall application: experimental and numerical results.” *Proc., on eighth European Turbomachinery Conference*, 23 - 27 March, Graz, Austria, 553–567.
- Andrews, G., Asere, A., Gupta, M. and Mkpadi, M. (1985).” Full coverage discrete hole film cooling: the influence of hole size.” *J. Turbo Jet Engines*, 2 (3), 213–225.
- Andrews, G., Gupta M. and Mkpadi, M. (1985).” Full coverage discrete hole film cooling: cooling effectiveness.” *J. Turbo Jet Engines*, 2 (3), 199–212.
- Arcangeli, L., Facchini, B., Surace, M. and Tarchi, L. (2008). “Correlative analysis of effusion cooling systems.” *J. Turbomachinery*, 130, 011016-1 – 011016-7.
- Bohn, D. and Moritz, N. (2000). “Influence of hole shaping of staggered multi-hole configurations on cooling film development.” *J. The American Institute of Aeronautics and Astronautics (AIAA)*, Paper No. 2579.

Caciolli, G., Facchini, B., Picchi, A. and Tarchi, L. (2013). "Comparison between PSP and TLC steady-state techniques for adiabatic effectiveness measurement on a multiperforated plate." *J. Experimental Thermal and Fluid Science*, 48, 122-133.

Cerri, G., Giovannelli, A., Battisti, L. and Fedrizzi, R. (2007). "Advances in effusive cooling techniques of gas turbines." *J. Applied Thermal Engineering*, 27, 692-698.

Cho, H.H., Rhee, D.H. and Goldstein, R.J. (2008). "Effects of hole arrangements on local heat/mass transfer for impingement/effusion cooling with small hole spacing." *J. Turbomachinery*, 130, 041003-1 – 041003-11.

Christophel, J.R., Thole, K.A. and Cunha F.J. (2005). "Cooling the tip of a turbine blade using pressure side holes—Part II: Heat transfer measurements." *J. Turbomachinery*, 127, 278-286.

Dittmar, J., Schulz, A., and Wittig, S. (2004). "Adiabatic effectiveness and heat transfer coefficient of shaped film cooling holes on a scaled guide vane pressure side model." *Int. J. Rotating Machinery*, 10 (5), 345–354.

Ekkad, S.V., Ou, S. and Rivir, R.B. (2004). "A transient infrared thermography method for simultaneous film cooling effectiveness and heat transfer coefficient measurements from a single test." *J. Turbomachinery*, 126, 597-603.

El-jumma A.M. (2014). "Impingement and Impingement/Effusion Cooling of Gas Turbine Components: Conjugate Heat Transfer Predictions." Ph.D Thesis, The Univ. of Leeds, Faculty of Engineering School of Chemical and Process Engineering Energy Research Institute (ERI), Leeds, LS2 9JT, United Kingdom.

Goldstein, R.J. (1971). "Film Cooling,," *Advances in Heat Transfer*, 7, 321-379.

Goodro, M., Ligrani, P., Fox, M. and Moon, H K. (2011). "Full-coverage film cooling: film effectiveness and heat transfer coefficients for dense and sparse hole arrays at different blowing ratios." *Proc., ASME Turbo Expo*, GT2011-45389.

Guo, L., Yan, Y.Y. and Maltson, J.D. (2011). "Numerical study on discharge coefficients of a jet in crossflow.", *Computers & Fluids*, 49, 323–332.

Gustafsson, B.K.M. and Johansson, G.T. (2001). "An experimental study of surface temperature distribution on effusion-cooled plates." *J. Engineering for Gas Turbines and Power*, 123, 308-316.

Han, J.C., Dutta, S. and Ekkad, S.V. (2012). "Gas turbine heat transfer and cooling technology." *CRC Press*, Second Edition, United States.

Harrison, K.L, and Bogard, D.G. (2008). "Comparison of RANS turbulence models for prediction of film cooling performance." *Proceedings of ASME Turbo Expo 2008: Power for Land, Sea and Air*, GT2008-50366, June 9-13, Berlin, Germany.

Hasan, R. and Puthukkudi, A. (2013). "Numerical study of effusion cooling on an adiabatic flat plate." *J. Propulsion and Power Research*, 2(4), 269-275.

Holman, J.P. (1994). "Experimental methods for engineers." *McGraw Hill Inc*, 6th Edition, United States.

Hong, S.K, Rhee, D.H. and Cho, H.H. (2007). "Effects of fin shapes and arrangements on heat transfer for impingement/effusion cooling with crossflow." *J. Heat Transfer*, 129, 1697-1707.

https://commons.wikimedia.org/wiki/File:Jet_engine.svg

https://en.wikipedia.org/wiki/Brayton_cycle

Hu, Y. and Ji, H. (2004). "Numerical study of the effect of blowing angle on cooling effectiveness of an effusion cooling." *Proc., ASME Turbo Expo*, GT2004-54043.

Inanli, S., Yasa, T., and Ulas, A. (2016). "Experimental investigation of effusion and film cooling for gas turbine combustor." *12th International Conference on Heat Transfer, Fluid Mechanics and Thermodynamics*, 11 to 13 July, Spain.

Jingzhou, Z., Hao, X. and Chengfeng, Y. (2009). "Numerical study of flow and heat transfer characteristics of impingement/effusion cooling." *Chinese J. Aeronautics*, 22, 343-348.

Krewinkel, R. (2013). "A review of gas turbine effusion cooling studies." *Int. J. Heat and Mass Transfer*, 66, 706-722.

Lakshminarayana, B. (1996). "Fluid Dynamics and Heat Transfer of Turbomachinery." *Wiley*, New York.

Lefebvre, A.H. and Ballal D.R. (2010). "Gas turbine combustion." *Taylor and Francis*, Third Edition, United States.

Leger, B., Miron, P. and Emidio, J.M. (2003). "Geometric and aero-thermal influences on multiholed plate temperature: application on combustor wall." *Int. J. Heat and Mass Transfer*, 46, 1215-1222.

Martiny, M., Schiele, R., Gritsch, M., Schulz, A. and Wittig, S. (1996). "In situ calibration for quantitative infrared thermography." *QIRT'96 Eurotherm Seminar No.50*. Stuttgart, Germany, Sept. 2-5.

Murray, A.V., Ireland, P.T., Wong, T.H., Tang S.W. and Rawlinson, A.J. (2018). "High resolution experimental and computational methods for modelling multiple row effusion cooling performance." *Int. J. Turbomachinery Propulsion and Power*, 3(1), 4, 1-16.

Natsui, G., Claretti, R., Ricklick, M.A., Kapat, J.S., Crawford, M.E., Brown, G. and Landis, K. (2016). "Experimental evaluation of large spacing compound angle full-coverage film cooling arrays: adiabatic film cooling effectiveness." *J. Turbomachinery*, 138, 071001-1 - 071001-8.

Natsui, G., Little, Z., Kapat, J.S. and Dees J.E. (2017). "Adiabatic film cooling effectiveness measurements throughout multirow film cooling arrays." *J. Turbomachinery*, 139, 101008-1 - 101008-12.

Ochs, M., Horbach, T., Schulz, A., Koch, R. and Bauer, H-J. (2009). "A novel calibration method for an infrared thermography system applied to heat transfer experiments." *Meas. Sci. Technol.*, 20, 075103-075111.

- Park, K.H., Yang, K.M., Lee, K.W., Cho, H.H., Ham, H.C. and Hwang, K.Y. (2009). "Effects of injection type on slot film cooling for a ramjet combustor." *J. Mechanical Science and Technology*, 23, 1852-1857.
- Rhee, D.H., Nam, Y.W., and Cho, H.H. (2004). "Effects of rib turbulator on heat/mass transfer for Impingement/effusion cooling with crossflow." *42nd AIAA Aerospace Sciences Meeting and Exhibit*, 5-8 January, Reno, Nevada, AIAA 2004-499.
- Schmidt, D.L., Sen, B. and Bogard, D.G. (1996). "Film cooling with compound angle holes: adiabatic effectiveness." *ASME J. Turbomachinery*, 118, 807–813
- Scrittore, J. J., Thole, K. A. and Burd, S. W. (2007). "Investigation of velocity profiles for effusion cooling of a combustor liner." *J. Turbomachinery*, 129, 518-526.
- Sen, B., Schmidt, D.L. and Bogard, D.G. (1996). "Film cooling with compound angle holes: heat transfer." *ASME J. Turbomachinery*, 118, 800–806.
- Silieti, M., Kassab, A.J., Divo, E. (2009). "Film cooling effectiveness: comparison of adiabatic and conjugate heat transfer CFD models." *Int J Thermal Science*, 48(12), 2237–2248.
- Tarchi, L., Facchini, B., Maiuolo, F. and Coutandin, D. (2012). "Experimental investigation on the effects of a large recirculating area on the performance of an effusion cooled combustor liner." *J. Engineering for Gas Turbines and Power*, 134, 041505-1 – 041505-9.
- Wei-hua, Y., Jun, C., Rui, S., Xu-Sheng, H. and Shuang-wen, S. (2011). "Experimental investigation on impingement-effusion film-cooling behaviors in curve section.", *Acta Astronautica*, 68, 1782-1789.
- Xu, Q., Lin, Y. and Liu, G. (2000). "The discharge coefficient of the double wall with inclined multihole and discrete-hole for combustor liner." *J. Propulsion Technology*, ISSU 113, 49-52.

Yang, W., Liu, X., Li, G. and Zhang, J. (2012). "Experimental investigation on heat transfer characteristics of film cooling using parallel-inlet holes." *Int. J. Thermal Sciences*, 60, 32-40.

Zhang, C., Song, B., Lin, Y., Xu, Q. and Liu, G. (2009). "Cooling effectiveness of effusion walls with deflection hole angles measured by infrared imaging." *J. Applied Thermal Engineering*, 29, 966-972.

APPENDIX I

I MASS FLOW MEASUREMENTS

In a gas turbine engine, the secondary flow for various cooling applications should be kept minimum. The aim is to achieve the maximum cooling of the hot section components with minimum coolant/secondary air flow. So it is important to measure the coolant mass flow through the film/effusion cooling holes. To measure the actual mass flow rate through the cooling holes, an orifice plate is fixed in the coolant line before the coolant chamber. The upstream and downstream static pressure ports on the orifice plate are made at D_p and $D_p/2$ locations as per the BS 1042 standards for the mass flow measurements.

The theoretical mass flow (\dot{m}_{theo}) is estimated based on the coolant density, coolant hole flow area and coolant flow velocity through the film cooling holes. The theoretical flow velocity through the cooling holes is calculated based on the pressure difference across the cooling holes using Bernoulli's equation. Using this theoretical velocity, the theoretical mass flow rate is calculated. The ratio of actual to theoretical coolant mass flow provides the coefficient of discharge (Cd) of the cooling hole. The coefficient of discharge is found using the relation:

$$Cd = \frac{\dot{m}_{act}}{\dot{m}_{theo}}$$

The actual coolant mass flow is measured based on the upstream and downstream pressures of the orifice. The following equation is arrived based on the BIS standards reference.

$$\text{Mass flow in Kg/hr, } \dot{m}_{act} = 0.121198 * \sqrt{\Delta P * (P_{up} + 680)}$$

Where, ΔP = Differential Pressure across the orifice plate in mm of H₂O
 P_{up} = Orifice upstream pressure in mm of Hg

Here, the coolant line orifice diameter is 20.13 mm, and the 2-inch diameter pipe is used for the coolant line flow.

I.1 Machined Ring Geometries

Fig. I.1 shows the mass flow measurements through the cooling holes for machined ring geometries. As the coolant chamber pressure increases, the mass flow increases through the cooling holes. In other words, as the pressure ratio across the cooling hole increases the mass flow increases. The coefficient of discharge through the cooling hole is plotted against the coolant Reynolds number in Fig. I.2. The machined ring geometry holes are 2.5 mm in diameter, and the coefficient of discharge through these holes are in the order of 0.65. As both the machined ring geometry holes are 2.5 mm hole diameter, the coefficient of discharge through these holes are same. But the mass flow through the machined ring 2 is higher than machined ring 1 due to more number of holes.

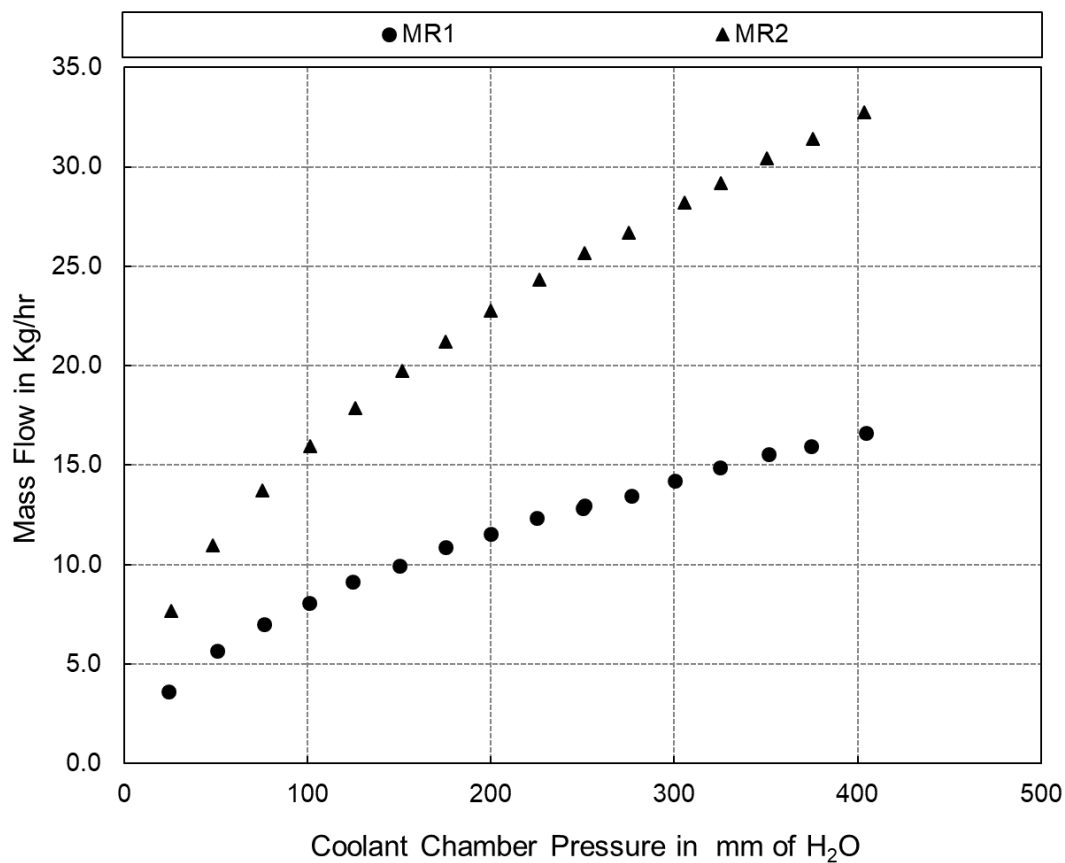


Fig. I.1 Mass flow through the cooling holes for machined ring 1

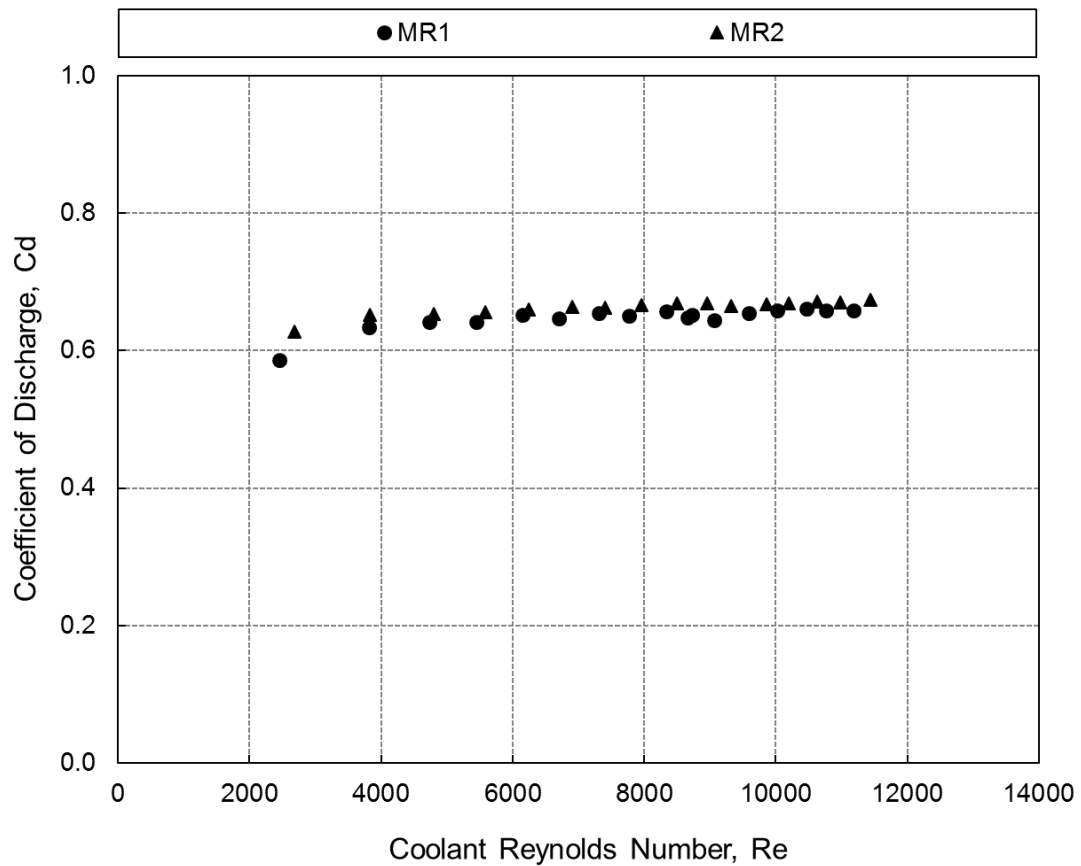


Fig. I.2 Coefficient of discharge through the cooling holes for machined ring 1

I.2 Effusion Cooling – Adiabatic Test Plate

The effusion cooling holes are 3 mm diameter for the adiabatic model. There are 117 holes arranged in a staggered manner. The mass flow through these holes is higher as shown in Fig. I.3. As the coolant chamber pressure increases the mass flow through the holes increases due to the increase in pressure difference across the coolant hole. The coefficient of discharge through the holes are shown in Fig. I.4 and found to be in the order of 0.50.

I.3 Effusion Cooling – SS Test Plate

The effusion cooling holes drilled in the stainless steel test plates are having 1.0 mm diameter. Such type of hole diameter is used in the real combustor liner, and the mass flow through these holes are shown in Fig. I.5. The coefficient of discharge through the holes increases as the coolant Reynolds number increases as shown in Fig. I.6.

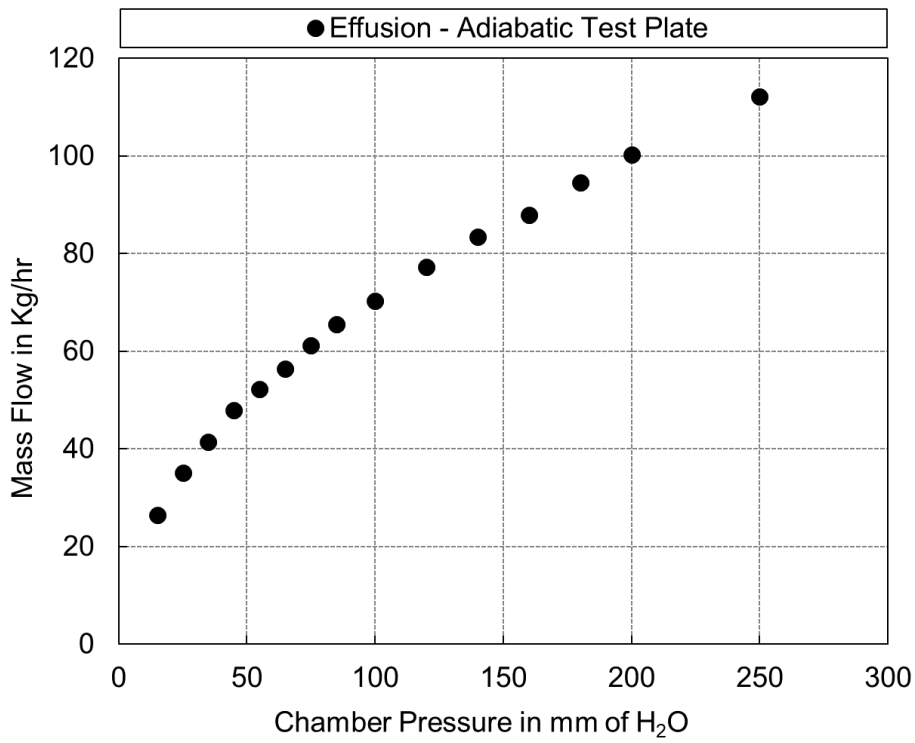


Fig. I.3 Mass flow through the effusion cooling holes for the adiabatic test plate

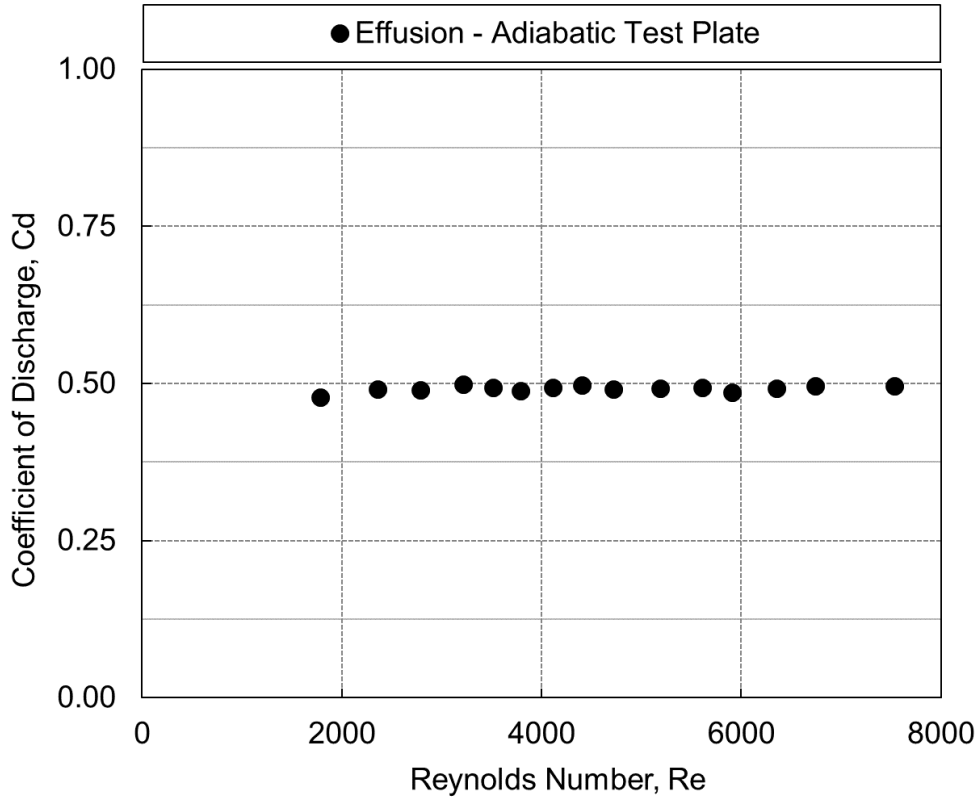


Fig. I.4 Coefficient of discharge through the effusion cooling holes for the adiabatic test plate

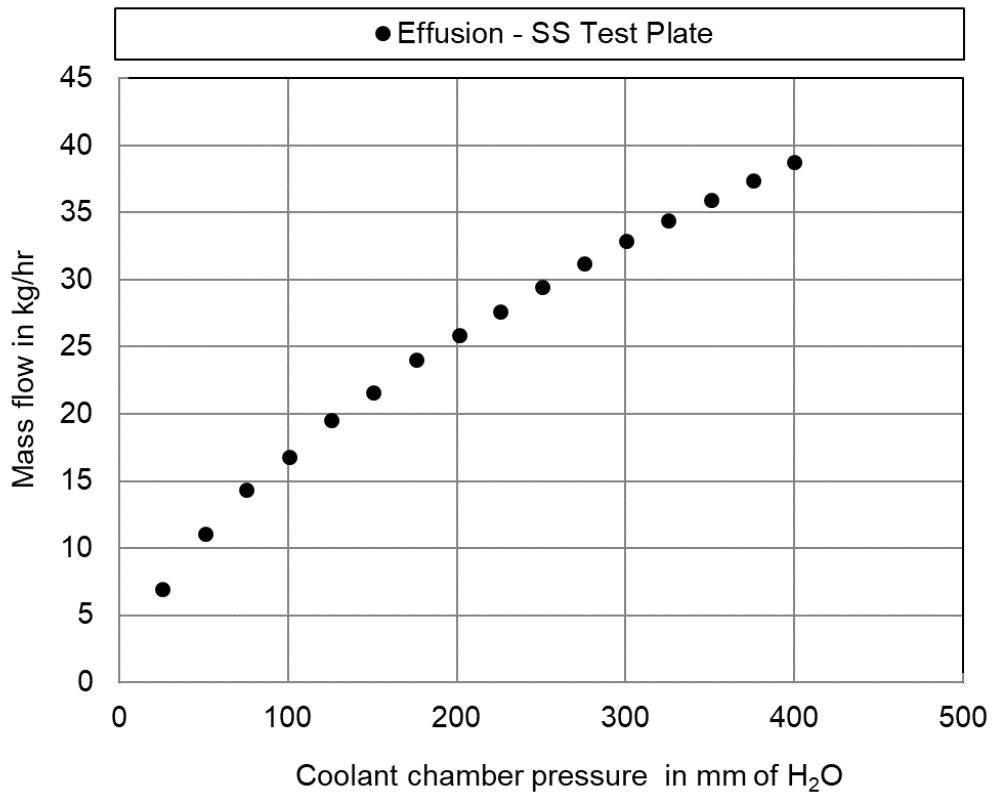


Fig. I.5 Mass flow through the effusion cooling holes for SS test plate

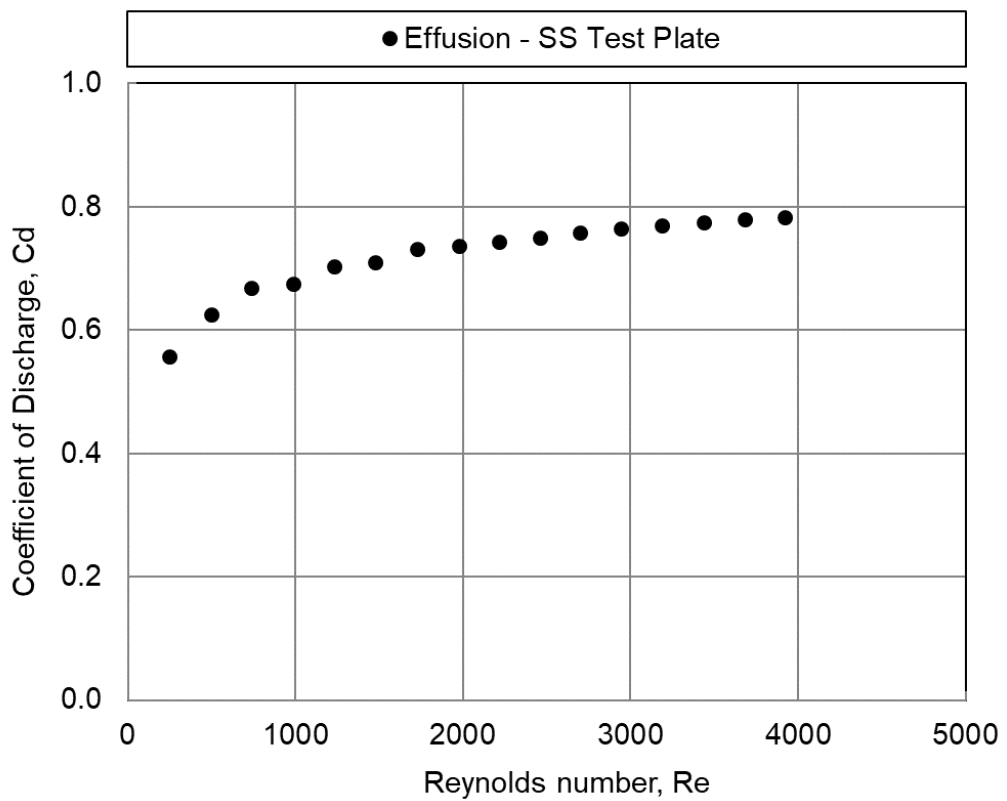


Fig. I.6 Coefficient of discharge through the effusion cooling holes for SS test plate

APPENDIX II

II UNCERTAINTY ANALYSIS

The list of instruments and its specifications used in the experiments for the data acquisition and monitoring of the parameters are shown in Table II.1. Before using these instruments for the experimental studies, the pressure scanner, temperature data acquisition system and the thermocouples are calibrated against standard primary calibrators. IR camera calibration procedure is already mentioned in Chapter 3.

Table II.1 Specifications of the instruments

Sl. No.	Name of Instrument	Specifications	Accuracy
1	K – Type Thermocouples	Omega make, -200 to 1260 °C	Accuracy: $\pm 0.25^{\circ}\text{C}$
2	Fluke Temp. Data Acquisition System (Model: 2680 A)	No. of Channels: 80	Accuracy: $\pm 0.75^{\circ}\text{C}$
3	FLIR Make A325sc Infra-Red Camera	Temperature range: -20 to 120°C and 0 to 350°C	Accuracy: $\pm 1.5^{\circ}\text{C}$
4	Intelligent Pressure Scanner (Model: 9116, Pressure System)	Measurement Range: 10 Inches of Water Column to 10 PSID. No. of Channels: 16 Operating temperature: 0 to 50 °C	Accuracy: $\pm 0.05\%$ of Full Scale

The uncertainty values are estimated using the procedure mentioned by Holman J.P. (1994).

II.1 Blowing Ratio

Blowing Ratio (BR) is defined as,

$$BR = \frac{\rho_c \cdot U_c}{\rho_m \cdot U_m}$$

For higher blowing ratio of 2.5, the following values are given as input for the calculation of uncertainty.

P_t = mainstream total pressure, 101559.4 Pa

P_s = mainstream static pressure, 101335 Pa

P_c = coolant pressure, 102444.3 Pa

T_c = coolant temperature, 231 K

T_m = mainstream temperature, 300 K

Thermocouples are calibrated and having an accuracy of 0.25°C. These thermocouples are connected to a Fluke data acquisition system which is having an accuracy of 0.75°C. So the total uncertainty of the measured thermocouple temperature is $\pm 1^\circ\text{C}$.

ω_{T_m} = uncertainty in mainstream temperature, ± 1 K

ω_{T_c} = uncertainty in coolant temperature, ± 1 K

ω_{P_t} = uncertainty in mainstream total pressure, ± 1 Pa

ω_{P_s} = uncertainty in mainstream static pressure, ± 1 Pa

ω_{P_c} = uncertainty in coolant pressure, ± 1 Pa

$$BR = \left(\sqrt{\frac{P_c \cdot T_m \cdot (P_c - P_s)}{P_t \cdot T_c (P_t - P_s)}} \right)$$

$$\frac{\partial BR}{\partial P_c} = \left(\sqrt{\frac{T_m \cdot (2P_c - P_s)^2}{4(P_c^2 - P_c \cdot P_s)(P_t \cdot T_c (P_t - P_s))}} \right)$$

$$\frac{\partial BR}{\partial T_m} = \left(\sqrt{\frac{P_c (P_c - P_s)}{4T_m P_t \cdot T_c (P_t - P_s)}} \right)$$

$$\frac{\partial BR}{\partial P_s} = \sqrt{\frac{P_c \cdot T_m \cdot (P_c - P_t)^2}{4 \cdot P_t \cdot T_c (P_t - P_s)^3 \cdot (P_c - P_s)}}$$

$$\frac{\partial BR}{\partial P_t} = \sqrt{\frac{P_c \cdot T_m \cdot (-2P_t + P_s)^2 \cdot (P_c - P_s)}{4 \cdot P_t^3 \cdot T_c (P_t - P_s)^3}}$$

$$\frac{\partial BR}{\partial T_c} = \sqrt{\frac{P_c \cdot T_m (P_c - P_s)}{P_t \cdot T_c^3 (P_t - P_s)}}$$

$$\omega BR = \left[\left(\frac{\partial BR}{\partial T_c} \omega T_c \right)^2 + \left(\frac{\partial BR}{\partial p_t} \omega p_t \right)^2 + \left(\frac{\partial BR}{\partial p_s} \omega p_s \right)^2 + \left(\frac{\partial BR}{\partial T_m} \omega T_m \right)^2 + \left(\frac{\partial BR}{\partial p_c} \omega p_c \right)^2 \right]^{\frac{1}{2}}$$

$$\omega BR = \left[\left(\sqrt{\frac{P_c \cdot T_m (P_c - P_s)}{P_t \cdot T_c^3 (P_t - P_s)}} \cdot \omega T_c \right)^2 + \left(\sqrt{\frac{P_c \cdot T_m \cdot (-2P_t + P_s)^2 \cdot (P_c - P_s)}{4 \cdot P_t^3 \cdot T_c (P_t - P_s)^3}} \cdot \omega p_t \right)^2 + \left(\sqrt{\frac{P_c \cdot T_m \cdot (P_c - P_t)^2}{4 \cdot P_t \cdot T_c (P_t - P_s)^3 \cdot (P_c - P_s)}} \cdot \omega p_s \right)^2 + \left(\left(\sqrt{\frac{P_c (P_c - P_s)}{4 T_m P_t \cdot T_c (P_t - P_s)}} \right) \omega T_m \right)^2 + \left(\sqrt{\frac{T_m \cdot (2P_c - P_s)^2}{4 (P_c^2 - P_c \cdot P_s) (P_t \cdot T_c (P_t - P_s))}} \cdot \omega p_c \right)^2 \right]^{\frac{1}{2}}$$

$$\omega BR = 0.010121$$

$$BR = 2.544788$$

$$\frac{\omega BR}{BR} = \frac{0.010121}{2.544788}$$

$$= 0.003977$$

Thus, at the blowing ratio of 2.54, uncertainty is 0.4% i.e. 2.54 ± 0.01 .

Similarly, for the lower blowing ratio of 0.5, uncertainty is calculated based on the procedure explained above.

$$\omega BR = 0.008586$$

$$BR = 0.448167$$

$$\frac{\omega BR}{BR} = \frac{0.008586}{0.448167} = 0.019159$$

Thus, at the blowing ratio of 0.448, the uncertainty is 1.92% i.e. 0.448 ± 0.009 .

II.2 Adiabatic Cooling Effectiveness

Adiabatic cooling effectiveness,

$$\eta = \frac{T_m - T_{aw}}{T_m - T_c}$$

For adiabatic cooling effectiveness, $\eta = 0.6$,

T_m = mainstream temperature, 303 K

T_{aw} = adiabatic wall temperature, 259.8 K

T_c = coolant temperature, 231 K

ωT_m = uncertainty in mainstream temperature, ± 1 K

ωT_c = uncertainty in coolant temperature, ± 1 K

ωT_{aw} = uncertainty in adiabatic wall temperature, ± 1.5 K

$$\frac{\partial \eta}{\partial T_m} = \frac{T_{aw} - T_c}{(T_m - T_c)^2}$$

$$\frac{\partial \eta}{\partial T_{aw}} = \frac{-1}{(T_m - T_c)}$$

$$\frac{\partial \eta}{\partial T_c} = \frac{T_m - T_{aw}}{(T_m - T_c)^2}$$

$$\omega \eta = \left\{ \left(\frac{\partial \eta}{\partial T_m} * \omega T_m \right)^2 + \left(\frac{\partial \eta}{\partial T_{aw}} * \omega T_{aw} \right)^2 + \left(\frac{\partial \eta}{\partial T_c} * \omega T_c \right)^2 \right\}^{0.5}$$

$$\omega \eta = \left\{ \left(\frac{T_{aw} - T_c}{(T_m - T_c)^2} * \omega T_m \right)^2 + \left(\frac{-1}{(T_m - T_c)} * \omega T_{aw} \right)^2 + \left(\frac{T_m - T_{aw}}{(T_m - T_c)^2} * \omega T_c \right)^2 \right\}^{0.5}$$

$$\omega \eta = 0.023116$$

$$\frac{\omega \eta}{\eta} = \frac{0.023116}{0.6}$$

$$= 0.038526$$

Uncertainty in adiabatic cooling effectiveness is 3.85%

Error in Cooling Effectiveness, η at 0.6 = 0.6 ± 0.023

Similarly, for $\eta = 0.3$,

T_m = mainstream temperature, 303 K

T_{aw} = wall temperature, 281.4 K

T_c = coolant temperature, 231 K

$$\begin{aligned}\omega\eta &= 0.023365 \\ \frac{\omega\eta}{\eta} &= \frac{0.023365}{0.3} \\ &= 0.077882\end{aligned}$$

Uncertainty in cooling effectiveness is 7.79%

Error in cooling effectiveness, η at 0.3 = 0.3 ± 0.023365

II.3 Heat Transfer Coefficient

Heat transfer coefficient,

$$h = \frac{(K_1 * I^2 + K_2 * I)}{A(T_w - T_m)}$$

Where,

K_1, K_2 are constants from the voltage vs current curve (0.0030285, 0.0615805)

I is the current in Ampere, 176 A

T_{aw} is the surface temperature, 323 K

T_m is the mainstream temperature, 302 K

A is the area of the test surface, 0.041075 m²

ωT_m = uncertainty in mainstream temperature, ± 1 K

ωT_{aw} = uncertainty in surface temperature, ± 1.5 K

$\omega I = \pm 1.5$ A

$$\begin{aligned}h &= \frac{(K_1 * I^2 + K_2 * I)}{A(T_{aw} - T_m)} \\ \frac{\partial h}{\partial I} &= \frac{(2K_1 * I + K_2)}{A(T_{aw} - T_m)} \\ \frac{\partial h}{\partial T_{aw}} &= \frac{(K_1 * I^2 + K_2 * I)}{A(T_{aw} - T_m)^2} \\ \frac{\partial h}{\partial T_m} &= \frac{(K_1 * I^2 + K_2 * I)}{A(T_{aw} - T_m)^2}\end{aligned}$$

$$\omega h = \left[\left(\frac{\partial h}{\partial I} \omega I \right)^2 + \left(\frac{\partial h}{\partial T_{aw}} \omega T_{aw} \right)^2 + \left(\frac{\partial h}{\partial T_m} \omega T_m \right)^2 \right]^{\frac{1}{2}}$$

$$\omega h = \left[\left(\frac{(2K_1 * I + K_2)}{A(T_{aw} - T_m)} \right) \cdot \omega I \right]^2 + \left(\frac{(K_1 * I^2 + K_2 * I)}{A(T_{aw} - T_m)^2} \cdot \omega T_{aw} \right)^2 + \left(\frac{(K_1 * I^2 + K_2 * I)}{A(T_{aw} - T_m)^2} \cdot \omega T_m \right)^2 \right]^{\frac{1}{2}}$$

$$\omega h = 10.59802$$

$$h = 121.3216$$

$$\frac{\omega h}{h} = \frac{10.59802}{121.3216}$$

$$= 0.087355$$

Uncertainty in heat transfer coefficient is 8.74%

Error in heat transfer coefficient, h at 121.3216 = 121.32 ± 10.598 W/m²k

II.4 Coolant Mass Flow Rate

An orifice plate having a hole diameter of 20.13 mm is fixed in the coolant line to measure the coolant mass flow rate through the cooling holes. Orifice plate pressure tapings are made at the locations of Dp and Dp/2 at the upstream and downstream of the orifice respectively. Based on BS 1042 standards, mass flow calculations are carried out using the formulae mentioned and simplified to the below equation.

$$\dot{m} = 0.121198 * \sqrt{(P_{up1} - P_{down}) * (P_{up2} + 680)}$$

P_{up1} = upstream pressure in mm of H₂O, 1635.4 mm of H₂O

P_{up2} = upstream pressure in mm of Hg, 120.25 mm of Hg

P_{down} = downstream pressure in mm of H₂O, 1544.25 mm of H₂O

Uncertainty in pressure measurements are,

$\omega P_{up1} = \pm 0.101972$ mm of H₂O

$\omega P_{up2} = \pm 0.007501$ mm of Hg

$\omega P_{down} = \pm 0.101972$ mm of H₂O

At a coolant mass flow rate of 32.733 kg/hr, and for the above pressure values uncertainty is calculated and as follows.

$$\dot{m} = 0.121198 * \sqrt{(P_{up1} - P_{down}) * (P_{up2} + 680)}$$

$$\frac{\partial \dot{m}}{\partial P_{up1}} = \frac{0.121198 * (P_{up2} + 680)}{2 * \sqrt{(P_{up1} - P_{down}) * (P_{up2} + 680)}}$$

$$\frac{\partial \dot{m}}{\partial P_{down}} = \frac{-0.121198 * P_{up2} + 680}{2 * \sqrt{(P_{up1} - P_{down}) * (P_{up2} + 680)}}$$

$$\frac{\partial \dot{m}}{\partial P_{up2}} = \frac{0.121198 * (P_{up1} - P_{down})}{2 * \sqrt{(P_{up1} - P_{down}) * (P_{up2} + 680)}}$$

$$\omega \dot{m} = \left[\left(\frac{\partial \dot{m}}{\partial P_{up1}} * \omega P_{up1} \right)^2 + \left(\frac{\partial \dot{m}}{\partial P_{down}} * \omega P_{down} \right)^2 + \left(\frac{\partial \dot{m}}{\partial P_{up2}} * \omega P_{up2} \right)^2 \right]^{\frac{1}{2}}$$

$$\omega \dot{m} = \left[\left(\frac{0.121198 * (P_{up2} + 680)}{2 * \sqrt{(P_{up1} - P_{down}) * (P_{up2} + 680)}} * \omega P_{up1} \right)^2 + \left(\frac{-0.121198 * (P_{up2} + 680)}{2 * \sqrt{(P_{up1} - P_{down}) * (P_{up2} + 680)}} * \omega P_{down} \right)^2 + \left(\frac{0.121198 * (P_{up1} - P_{down})}{2 * \sqrt{(P_{up1} - P_{down}) * (P_{up2} + 680)}} * \omega P_{up2} \right)^2 \right]^{\frac{1}{2}}$$

$$\omega \dot{m} = \pm 0.025894 \text{ kg/hr}$$

$$\dot{m} = 32.733 \text{ kg/hr}$$

$$\frac{\omega \dot{m}}{\dot{m}} = \frac{0.025894}{32.733}$$

$$= 0.000791$$

So, at mass flow rate of 32.733 kg/hr, the uncertainty is 0.08% i.e. 32.733 ± 0.02589

List of Publications based on the Ph.D Work

Sl. No.	Title of the Paper	Authors	Name of the journal/Conferences/ Symposium, Vol., No., Pages	Month & Year of publication	Category*
1	Experimental and Numerical Investigation of Effusion Cooling Performance over Combustor Liner Flat Plate	Felix J, Rajendran R, Kumar G N, Giridhara Babu Y, Karthik M K and Ramesha D K.	Heat Transfer Engineering, https://doi.org/10.1080/01457632.2018.1460935 , Published Online: 23 Apr 2018.	Apr 2018	1
2	Experimental Study of Adiabatic Cooling Effectiveness on an Effusion Cooled Test Plate with Machined Ring Geometries	Felix J, Rajendran R, Kumar G N and Giridhara Babu Y.	Heat Transfer Research, 49 (9), 865-880. DOI: 10.1615/HeatTransRes.2018021461	Issue 9, 2018	1
3	Experimental and Numerical Investigation of Effusion Cooling Performance over Combustor Liner Flat Plate	Felix J, Rajendran R, Kumar G N, Giridhara Babu Y, Karthik M K and Ramesha D K.	Paper No. IHMTC2015- 1036, Proceedings of the 23rd National Heat and Mass Transfer Conference and 1st International ISHMT-ASTFE Heat and Mass Transfer Conference, IHMTC2015, Thiruvananthapuram, India.	December 17-20, 2015	3
4	Experimental Investigation of Overall Cooling Effectiveness on Combustion Chamber Liner with and without Impingement Holes	Felix J, Rajendran R, Kumar G N, Giridhara Babu Y, Vivek S and Sinith P.	GTINDIA2015-1377, Proceedings of the ASME 2015 Gas Turbine India Conference, GTINDIA2015, Hyderabad, India.	December 1-3, 2015	3

BIODATA

NAME: J. FELIX

DATE OF BIRTH: 20-05-1980

Mobile No.: +91 9448905736

Email: felix@nal.res.in, felix_thomas@rediffmail.com

ADDRESS:

Res: Flat No: 103, DS-Max Seasons Apartment, Annasandrapalya, Bangalore -560017.

Off: Propulsion Division, CSIR-National Aerospace Laboratories, Kodihalli, Bangalore -560017.

QUALIFICATION:

B.E (Mechanical Engineering) – P.S.N.A College of Engineering and Technology, Dindigul, TamilNadu. (Passed out - Apr 2001)

M.E (Thermal Engineering) – Karunya Institute of Technology, Coimbatore, TamilNadu. (Passed out - Dec 2002)

EXPERIENCE:

1. 01 Year as Lecturer at Sethu Institute of Technology, Madurai, TamilNadu.
2. 01 Year as Project Post Graduate Trainee at CSIR-National Aerospace Laboratories, Bangalore.
3. 01 Year as Project Assistant at CSIR-National Aerospace Laboratories, Bangalore.
4. 12 Years as a Scientist at CSIR-National Aerospace Laboratories, Bangalore.

PUBLICATIONS:

International Journal Papers	:04
International Conference Papers	:20
NAL Project Documents	:28
M. Tech Projects Guided	:04